Electrochemical synchronization of cell spreading on solid surfaces

Marius Socol

UNIVERSITÉ DE GRENOBLE

THÈSE

pour obtenir le grade de

DOCTEUR d'Université de Grenoble

préparée au Laboratoire des Matériaux et du Génie Physique (LMGP) et au Laboratoire d'Electrochimie et de Physicochimie des Matériaux et des Interfaces (LEPMI)

Spécialité* : *« Physique pour Sciences du Vivant »

présentée et soutenue publiquement
par

Marius SOCOL

le 20 May 2010

La synchronisation électrochimique de l'étalement cellulaire sur des surfaces solides

Thèse dirigé par **M. Franz BRUCKERT** et
co-dirigé par **M. Didier DELABOUGLISE**

Jury

Jacques Derouard	Président
Annie Viallat	Rapporteur
Pierre Cosson	Rapporteur
Jean-Paul Rieu	Examinateur
Didier Delabouglise	Examinateur
Franz Bruckert	Examinateur

Remerciements

Je tiens tout d'abord à remercier infiniment mes directeurs de thèse, Messieurs **Franz Bruckert** et **Didier Delabouglise**, deux grands Professeurs et leur grand coeur.

Je remercie spécialement Madame **Marianne Weidenhaupt**, pour sa gentillesse, ses bonnes idées et conseils scientifiques et aussi pour son aide pour la correction de la thèse.

Un grand merci a mon meilleur ami, **Mihai Miron**, qui m'a convaincu de venir en France, pour toute son aide, morale, financière et scientifique: réalisation de lamelles recouvertes avec Ti, Pt et Au et les discussions en physique.

Je remercie beaucoup les personnes qui m'ont aidé pour la mesure du potentiel Zeta: **Eric Chainet**, **Carole Pernel** et **Guillaume Costa**.

Je remercie **Alain Denoyelle** et **Christine Lefrou** pour leurs conseils et discussions dans le domaine de l'électrochimie.

Je remercie les personnes suivantes, qui m'ont beaucoup aidé: **Bertrand Fourcade (CNRS), Gérard Klein, Laurence Aubry** et **Michel Satre (CEA)**.

Je remercie **Annie Viallat, Pierre Cosson, Jean-Paul Rieu, Jacques Derouard,** d'avoir bien voulu examiner ma thèse

Je remercie également l'**Ecole Doctorale de Physique de Grenoble et le soutien de la région (CPER, Macodev).**

Je remercie également mes collègues doctorants, **Sébastien Keller** qui m'a beaucoup aidé quand j'ai été stagiaire, **Renaud Cornut**, qui m'a beaucoup aidé dans les simulations en *Comsol*, **Mael Manesse**, **Paolo Actis, Laure Fourel, Ofelia Maniti, Germain Rey, Laurent Nault, Nicolas Chaban, Claire Holtzinger, Mouna Messaoud** et **Thomas Ballet** pour leur compagnie agréable et stimulante.

Je remercie tout particulièrement ma famille et spécialement mon épouse **Olga**, à qui je dédie cette thèse.

Présentation de la thèse

Le travail de cette thèse s'inscrit dans le cadre d'une recherche sur l'analyse biophysique de l'adhésion de l'amibe *Dictyostelium discoideum* sur son substrat.

Dictyostelium discoideum est une cellule eucaryote simple, qui possède un génome haploïde contenant un nombre de gènes égal à la moitié de celui du génome humaine et qui peut être manipulé avec des techniques standards de génétique moléculaire. Elle est capable d'adhérer et de s'étaler sur différents matériaux aux propriétés de surface assez variables. En conséquence, cette amibe est un très bon modèle expérimental pour étudier la formation de contacts cellule-surface.

Le contact d'une cellule avec une surface solide est un processus très complexe qui initie d'importants chemins de signalisation intracellulaire, conduisant à l'adhésion et l'étalement cellulaire, la polarisation, la motilité, la prolifération et parfois la différenciation.

Le nombre des protéines impliquées dans l'adhésion cellulaire est assez important et suppose beaucoup d'interactions moléculaires. En dépit de la connaissance de nombreux éléments qui jouent un rôle dans l'adhésion, leur hiérarchie temporelle et organisation spatiale ne sont que partiellement connues. Certaines protéines membranaires impliquées dans cette adhésion ont été découvertes. Quelques unes de ces protéines sont similaires aux intégrines qui interviennent dans l'interaction des cellules mammifères avec les protéines de la matrice extracellulaire. *Dictyostelium discoideum* possède aussi beaucoup de protéines connues comme faisant partie des structures d'adhésion chez cellules mammaliennes, comme par exemple la taline, la paxilin, la coronine, qui stimulent la polymérisation de l'actine et relient les microfilaments d'actine de la membrane plasmique.

En utilisant la «reflection interference contrast microscopy» (RICM), Sébastien Keller du groupe conduit par Franz Bruckert, a observé récemment que la cellule *Dictyostelium discoideum* s'étale avec une activité de protrusion périodique. La période des cycles d'activité est d'environ 11 secondes et les cycles persistent au moins durant l'étalement (approximativement 1 minute). Cette activité cyclique révèle une organisation temporelle très complexe des événements moléculaires qui conduisent à l'étalement.

C’est un défi d’identifier la formation successive des complexes protéiniques qui mènent à établir des contacts stables entre la surface et la cellule. Pour cela, il serait nécessaire de synchroniser le point de départ de l’étalement cellulaire pour avoir accès à différentes étapes de cette activité.

Notre objectif était de synchroniser le contact cellule-surface pour une population des cellules, ceci étant un élément déterminant pour préparer du matériel cellulaire enrichi avec des complexes des protéines actives après un certain temps après le contact.

Le mémoire de thèse commence par le chapitre **introduction** qui a deux parties. La première partie porte sur les paramètres biologiques qui influencent l’adhésion et l’étalement de l'amibe *Dictyostelium discoideum*, le modèle cellulaire utilisé tout au long de ce travail. Les mécanismes qui assurent l'adhésion des cellules sur leur substrat sont passés en revue. La deuxième partie donne un état de l’art de la manipulation des cellules avec des champs électriques. Les techniques existantes de manipulation des cellules sont exposées et leurs mécanismes physiques associés sont décrits par les concepts de base, les différentes forces et les grandeurs physiques mises en jeu.

Le chapitre deux est consacré aux **matériels et aux méthodes** et porte sur les méthodes expérimentales spécifiques développées pour synchroniser l’adhésion cellulaire des amibes. Les expériences d’électrochimie, les simulations numériques, les méthodes d’observation et les méthodes d’analyse y sont présentées. Cette description est accompagnée de considérations sur les bases physiques et biologiques des méthodes utilisées: principe de la double couche électrique et détail de la théorie de Gouy-Chapman, potentiel Zeta, théorie DLVO et modèle de l’adhérence cellulaire sur des surfaces chargées en fonction de la force ionique.

Le troisième chapitre est consacré aux **résultats**. Le premier sous chapitre concerne l’adhésion non synchrone (étalement des cellules sous l’influence de la gravité). On y confirme les études précédentes qui montrent que *Dictyostelium discoideum* s’étale avec une activité de protrusion périodique, associée à une polymérisation de l’actine (suivie par microscopie de fluorescence en utilisant des cellules marquées avec $LimE^{\Delta coil}$-GFP) selon des périodes similaires. L’influence du champ électrique sur des cellules adhérentes sur différents matériaux (ITO, Ti, Pt et Au) est ensuite étudiée. Des potentiels positifs mais aussi négatifs ont été testés. Cette partie est suivie d'une description des

paramètres pouvant être manipulés afin de contrôler l'adhésion et l'étalement cellulaire (notamment la force ionique et la charge de surface), afin de définir comment des cellules vivantes peuvent être maintenues en lévitation à une certaine distance d'une surface par le jeu des propriétés électrostatiques des cellules et des surfaces. La polymérisation de l'actine sur des cellules en lévitation a été aussi étudiée dans ce sous-chapitre.

Deux méthodes sont ensuite analysées pour synchroniser l'adhésion cellulaire: l'augmentation de la concentration du tampon utilisé, par diffusion ionique et l'application d'un pulse électrique. Le volet suivant des résultats concerne la synchronisation de cellules qui se trouvent d'abord en lévitation puis adhérent de manière synchrone par diffusion ionique. Dans ce cas là, le temps de synchronisation obtenu a été trop long par rapport à la période de polymérisation de l'actine. Le dernier sous chapitre des résultats décrit comment la synchronisation a été obtenue avec succès sur un substrat d'ITO en appliquant des pulses électriques très courts (5V pendant 0.1 s). Les conditions expérimentales testées sont récapitulées dans des tableaux et celles qui induisent le plus de cellules adhérentes sont retenues. La synchronisation a été démontrée en étudiant l'activité de polymérisation de l'actine pendant l'étalement d'une population de 14 cellules induit par pulse électrique.

Enfin, une **discussion** des résultats est proposée dans le quatrième chapitre. Les résultats concernant les distances entre cellules et substrat sont estimés par observation en RICM et comparées avec les valeurs obtenues théoriquement à l'aide de modélisations appropriées. Une figure synthétise ces résultats.

En **conclusion,** nous estimons que nous avons obtenu, pour la première fois, la synchronisation de l'étalement cellulaire d'un groupe de cellules grâce à une méthode électrochimique. Ceci pourrait permettre, en faisant une analyse biochimique appropriée, d'identifier les événements moléculaires qui conduisent à l'adhésion cellulaire. Nous estimons que les connaissances acquises au cours de cette étude pourraient également servir de base à d'autres études sur les mécanismes contrôlant l'adhésion cellulaire, soit en servant de modèle d'étude de mutants affectant diverses protéines cellulaires, soit en permettant des analyses plus fines des paramètres biophysiques mis en jeu.

Summary

I. Introduction

1.1 *Dictyostelium discoideum*: lifestyle and importance as a model organism to study cell spreading and adhesion mechanisms

Dictyostelium discoideum is a soil-living amoeba belonging to the phylum Mycetozoa (Raper, 1935). *D. discoideum*, commonly referred to as slime mold, is a primitive eukaryote that is able to differentiate from unicellular amoebae into a multicellular organism and then into a fruiting body within its lifetime.

In the wild, *D. discoideum* can be found in soil and moist leaf litter. The primary diet of *D. discoideum* consists of bacteria, which are found in the soil and decaying organic matter. The amoebae feed on bacteria by phagocytosis.

When nutrients are available, *Dictyostelium discoideum* lives, divides and grows as single-cell amoebae (with an averaged diameter of 10 μm, if it is considered spherical). This growth phase is called vegetative stage (Fig. 1.1).

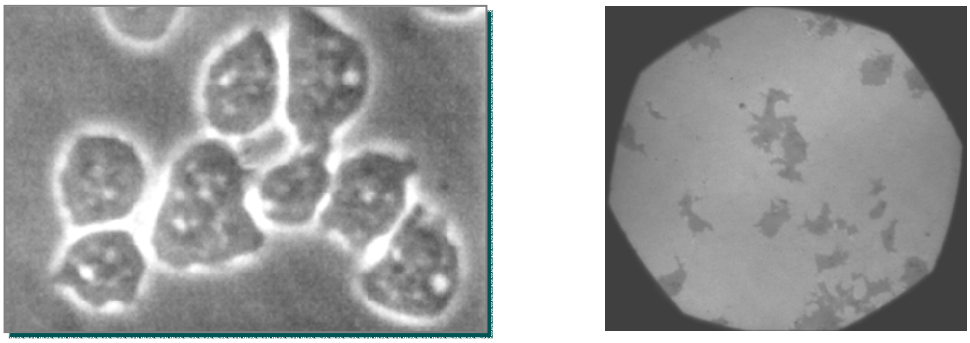

A **B**

Fig. 1.1 A. Phase contrast image and **B.** Reflection Interference Contrast Microscopy image of unicellular amoebae in vegetative stage.

The asexual life cycle of *D. discoideum* begins upon exhaustion of food sources, when vegetative cells aggregate to become multicellular (Aubry, 1999). *D. discoideum* has a multicellular development cycle (social cycle) that consists of four stages: vegetative, aggregation, migration, and culmination. Selected life stages are shown in Fig. 1.2 (Sameshima, 2001).

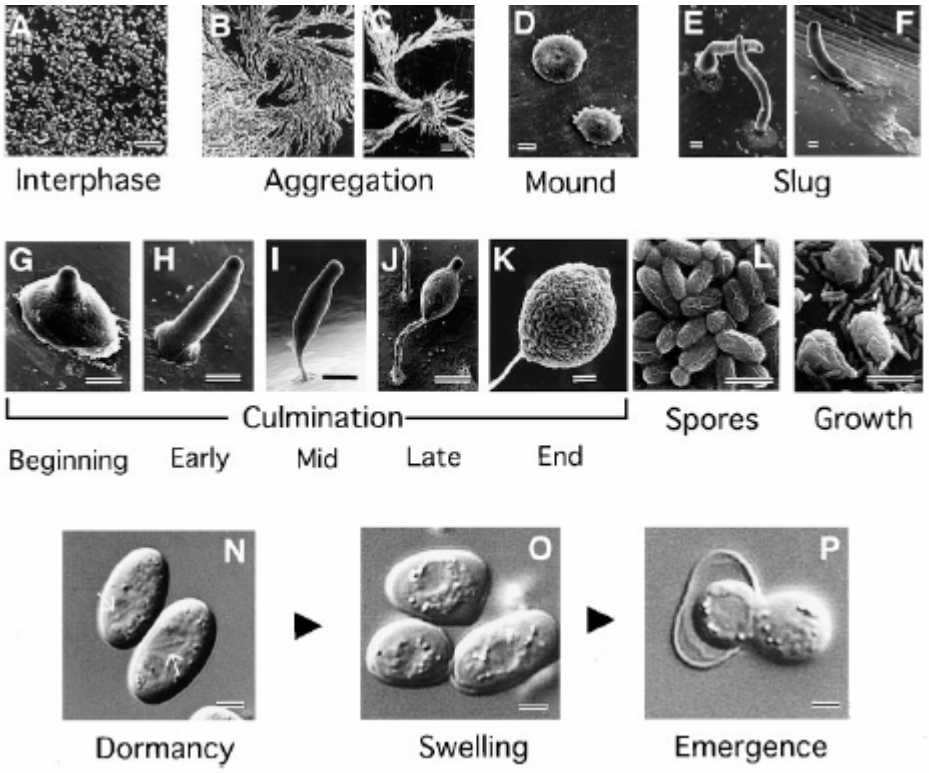

Fig. 1.2 Scanning electron micrographs of the asexual life cycle (A–M) and germination process observed by differential interferential contrast (DIC) (N–P) of *D. discoideum*, strain NC-4. (**A**) Interphase. (**B, C**) Aggregation stage. (**D**) Mound. (**E**) Nascent slug. (**F**) Migrating slug. (**G–K**) Beginning, early, mid, late, and end of culmination stage, respectively. At the end of the culmination stage, fruiting body formation is complete. (**L**) Spores in sorus. A part of **K** was enlarged. (**M**) Amoebae feeding on bacteria. (**N**) Dormant spores. (**O**) Swollen spores. (**P**) Emergence of nascent amoeba. Scale bar, 100 μm (**C**), 50 μm (**A**, **B**, **D–J**), 20 μm (**K**), 10 μm (**L**, **M**), 2 μm (**N–P**) (Sameshima, 2001).

Lab cultivation

D. discoideum's ability to be easily cultivated in the lab (Tyler, 2000) adds to its appeal as a model organism. The isolation of mutants that were able to grow axenically (Watts, 1970) made it possible to grow *Dictyostelium* in liquid nutritive medium without bacteria organisms. Organisms *D. discoideum* can be grown either in shaken liquid culture (e.g., HL5 medium) or on a bacterial lawn in Petri dishes. The cultures grow best at 22°-24°C (room temperature) and generation time is 8-12 hours in HL5 medium and 4-6 hours on a bacterial lawn.

D. discoideum cells can be fed on *E. coli*, which is adequate for starting the life cycle. When the food supply is diminished, the amoebae will aggregate. Soon, the dish will be covered with various stages of the social life cycle or sexual life cycle.

The establishment of a transformation system (Nellen, 1984) paved the way for the genetic manipulation of this organism.

Use as a model organism to study cellular adhesion

During their vegetative stage, *D. discoideum* cells adhere, move, emit and react to chemical signals and are able to differentiate. These processes present characteristics similar to cell migration in invasive cancer. The National Institute of Health (NIH) has been proposing amoeba as an attractive model for cancer research. Its genetic background cycle makes *D. discoideum* a valuable model organism to study genetic, cellular, and biochemical processes in more advanced organisms (see www.nih.gov/science/models/d_discoideum).

It can be observed at organism, cellular, and molecular levels primarily because of the restricted number of cell types, behaviors, and their rapid growth (Tyler, 2000). It is used to study cell differentiation, chemotaxis and programmed cell death, which are all natural cellular processes. It is also used to study common physiological phenomenon including cell sorting, pattern formation, phagocytosis, motility, and signal transduction (www.dictybase.org).

D. discoideum has a haploid genome with about half the number of genes of human beings, which can be manipulated by standard molecular genetic techniques. It carries similar genes and pathways making it a good candidate for gene knockout (Nag, 2008).

The entire genome of *D. discoideum* was sequenced (Eichinger, 2005) and is accessible in a public database called *dictyBase* (www.dictybase.org). Individual cell behavior accounts for many phases of health and disease. This is portrayed in *D. discoideum* in many different ways. Cytokinesis acts as part of immune response, tissue maintenance, and cancer, in the form of cell proliferation. Chemotaxis is involved in inflammation, arthritis, asthma, lymphocyte trafficking, and axon guidance. Phagocytosis is used in immune surveillance and necessary for antigen presentation, while cell-type determination, cell sorting, and pattern formation are basic features of embryogenesis.

D. discoideum is therefore a good model organism to study general cell biology problems such as the coupling between plasma membrane adhesion and the cytoskeleton or cell polarization during explorative motility.

1.2 Biological parameters that influence cell adhesion and spreading

Dictyostelium discoideum cells adher directly (no extra cellular matrix necessary) on different surfaces, hydrophilic or hydrophobic ones that exhibit different atomic or molecular structures at the interface with a liquid medium. Thus, we are strongly interested in cell surface charge, since plasma membrane lipids and proteins carry net charges, and how this aspect could influence cell adhesion. In addition, we are interested in mechanisms of cellular adhesion (adhesion proteins, distance interactions between cell membrane and surface molecules, signaling pathways).

1.2.1 Plasma membrane lipids and proteins: the main source of surface charge

An eukaryote is an organism whose cells contain complex structures enclosed within membranes. Many living organisms, including all animals, plants, fungi, etc. are eukaryotes. The defining membrane-bound structure that differentiates eukaryotic cells from prokaryotic cells is the nucleus, which gives these organisms their name. They have a variety of internal membranes and structures, called organelles, and a cytoskeleton composed of microtubules, microfilaments, and intermediate filaments, which play an important role in defining the cell's organization and shape. Eukaryotic DNA consists of several linear DNA molecules associated to specific proteins (histones), called chromosomes. During cell division a microtubules spindle assemble that helps to separate the chromosomes.

Given that in our present study, we used solutions very different from the usual culture medium (very low ionic strength, extreme pH values) and we applied electrical pulses in solutions containing cells, we are interested in electrical and chemical properties of the cell membrane determinated by its composition and architecture. In figure 1.3 we offer a simple illustration of an eukaryotic plasma membrane.

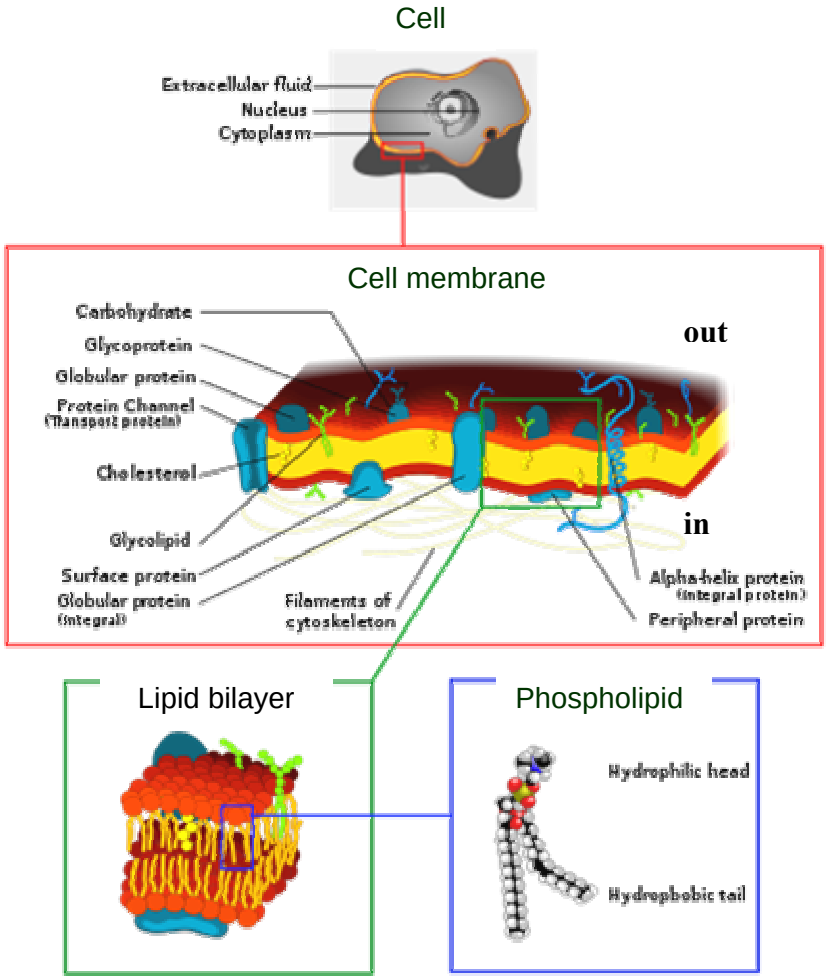

Fig. 1.3 Schematic representations of a eukaryotic cell membrane and some components (Alberts, 2008)

Despite their differing functions, all biological membranes have a common general structure: they are made of a very thin film of lipids and proteins held together by hydrophobic interactions. It is a continuous double layer approximately 5 nm thick, and in many membranes the two layers have a different composition. Lipid molecules constitute about 50% of the mass of most animal cell membranes, nearly all of the remainder being proteins. There are about 10^9 lipid molecules in the plasma membrane of a small animal cell (10 μm in diameter) and about 50 lipid molecules for each protein molecule in the cell membrane (lipid molecules are small compared with protein molecules) (Alberts, 2008).

Cell membranes are dynamic, fluid structures, intrinsically impermeable for most water-soluble molecules, and most of their molecules move about in the plane of the membrane. This basic fluid structure of the membrane is provided by the lipid bilayer.

The amount of each lipid depends upon the cell type (Lodish, 2004). The most abundant membrane lipids are phospholipids (phosphoglycerides, sphingolipids, see Fig. 1. 4), cholesterol and glycolipids (galactocerebroside and ganglioside that always contain one or more negatively charged sialic acid residues).

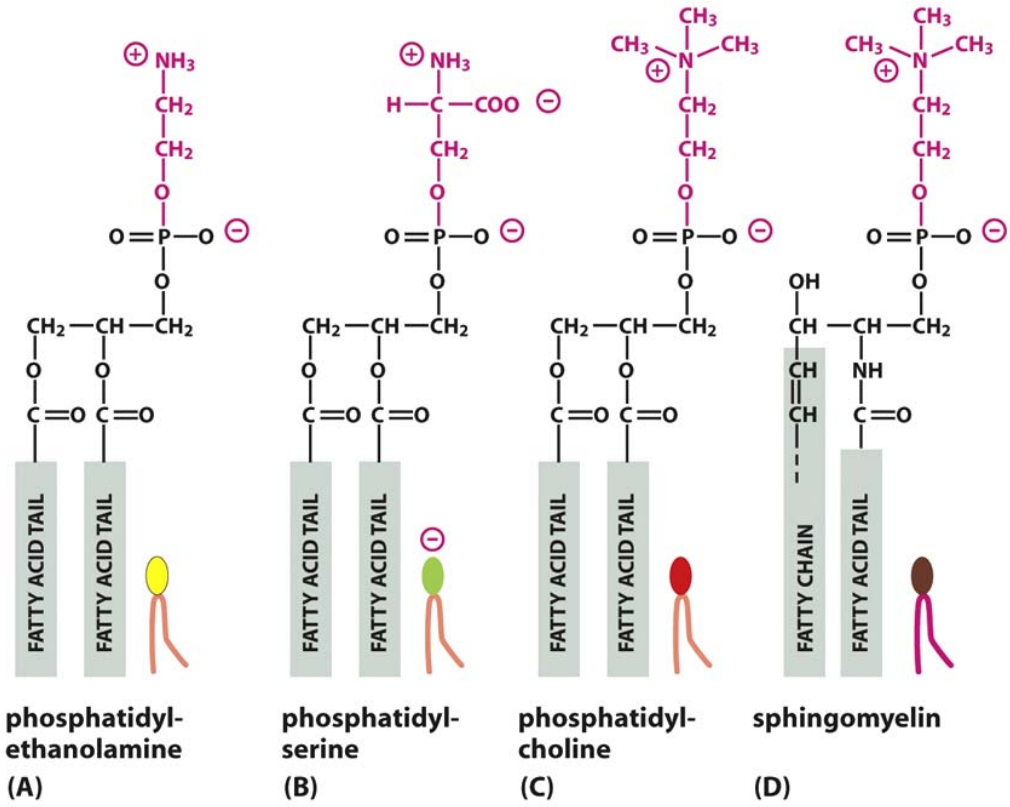

Fig 1.4 Four major phospholipids of the mammalian plasma membrane. The lipid molecules shown in **A-C** are phosphoglycerides, which are derived from glycerol. The molecule in **D** is sphingomyelin, which is derived from sphingosine and is therefore a sphingolipid. Note that only phosphatidylserine carries a net negative charge, the other three are electrically neutral at physiological pH, carrying one positive and one negative charge (Alberts, 2008).

Table 1.1 compares the lipid composition of several biological membranes.

Table 1.1 Appoximate lipid composition of different cell membranes

LIPID	PERCENTAGE OF TOTAL LIPID BY WEIGHT					
	LIVER CELL PLASMA MEMBRANE	RED BLOOD CELL PLASMA MEMBRANE	MYELIN	MITOCHONDRION (INNER AND OUTER MEMBRANES)	ENDOPLASMIC RETICULUM	*E. COLI* BACTERIUM
Cholesterol	17	23	22	3	6	0
Phosphatidylethanolamine	7	18	15	28	17	70
Phosphatidylserine	4	7	9	2	5	trace
Phosphatidylcholine	24	17	10	44	40	0
Sphingomyelin	19	18	8	0	5	0
Glycolipids	7	3	28	trace	trace	0
Others	22	13	8	23	27	30

Protein molecules that span the lipid bilayer (transmembrane proteins) mediate nearly all of the other functions of the membrane, transporting specific molecules across it, for example, or catalyzing membrane-associated reactions such as ATP synthesis (Curran, 2003). In the plasma membrane, some transmembrane proteins serve as structural links that connect the cytoskeleton through the lipid bilayer to the extracellular matrix (if it exists), a solid substrate or an adjacent cell (cell-cell adhesion), while others serve as receptors to detect and transduce chemical signals in the cell's environment (Sheetz, 2001).

Many membrane proteins are glycosylated (Lodish, 2004). These carbohydrates appear as oligosaccharide chains (fewer than 15 sugars) covalently bound to membrane proteins (glycoproteins). Another group, proteoglycans, which consist of long polysaccharide chains linked covalently to a protein core, is found mainly outside the cell, as part of the extracellular matrix. In the vegetative stage of *Dictyostelium discoideum,* the extracelullar matrix is missing (Traynor, 1992).

The membrane is selectively permeable and able to regulate what enters and exits the cell, thus facilitating the transport of materials needed for survival (electrically-neutral and small molecules pass the membrane easier than charged or large ones). There are two classes of membrane transport proteins: transporters and channels. Both form continuous protein pathways across the lipid bilayer. Whereas transmembrane movement mediated by transporters can be either active (pumps, using ATP hydrolysis, for example, see fig. 1.5) or passive (spontaneous), solute flow through channel protein is always passive (Gouaux, 2005).

The membrane also maintains the cell membrane potential, with the inside usually negative with respect to the outside. A membrane potential arises when there is a difference in the electrical charges on the two sides of a membrane. Such charge differences can result from active electrogenic pumping (see fig. 1.5) and from passive ion diffusion through ion protein channels.

The concentration gradient and the potential difference across the membrane (membrane potential) combine to form a net driving force, the electrochemical gradient, for each charged solute (Alberts, 2008). The electrochemical gradient influences the charged solute transport through the ion protein channels.

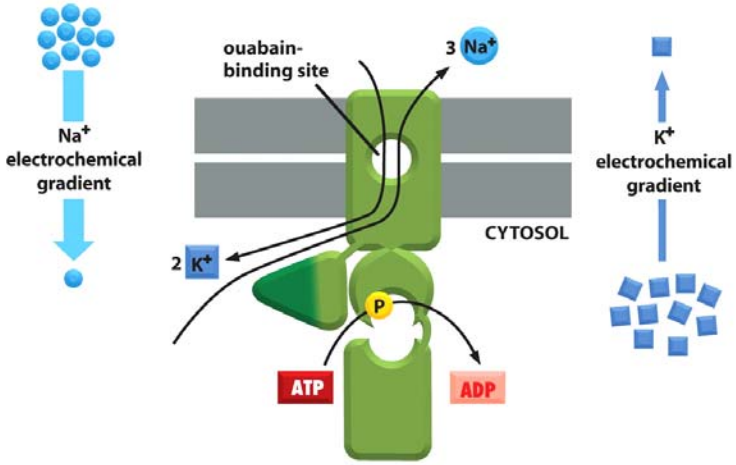

Fig. 1.5 The Na^+-K^+ pump. This transporter actively pumps Na^+ out and K^+ into a cell against their electrochemical gradient. For every molecule of ATP hydrolyzed inside the cell, three Na^+ are pumped out and two K^+ are pumped in (Alberts, 2008).

However, the electrogenic effect of the pumps, contributes only for approximately 10% to the membrane potential. The rest is attributed to the function of ion channels (narrow protein pores) that allow specific inorganic ions, primarily K^+, Na^+, Ca^{2+}, or Cl^-, to diffuse rapidly, with a rate of 100 million ions each second, down their electrochemical gradients across the lipid bilayer (Millhauser, 1988). In particular, nerve cells (neurons) have made a speciality of using ion channels to receive, conduct and transmit signals.

Only a small number of ions must move across the plasma membrane to set up the membrane potential (Fig. 1.6), which varies for an animal cell between 20 and 120 mV, depending on the organism and cell type. Thus, the membrane potential arises from movements of charges that leave ion concentrations practically unaffected and result in only a very slight discrepancy in the number of positive and negative ions on the two

sides of the membrane (fig. 1.6, Alberts, 2008). Knowing that the membrane capacitance for most animal cells is 1 $\mu F/cm^2$ one deduces that the movements of 173.000 K^+ ions across 300 μm^2 of membrane (surface of a spherical cell with diameter of 10 μm) which represent 1 positive charge per 180 nm^2, will carry sufficient charge to shift the membrane potential by about 100 mV. Moreover, these movements of charge are generally rapid, taking only a few milliseconds or less.

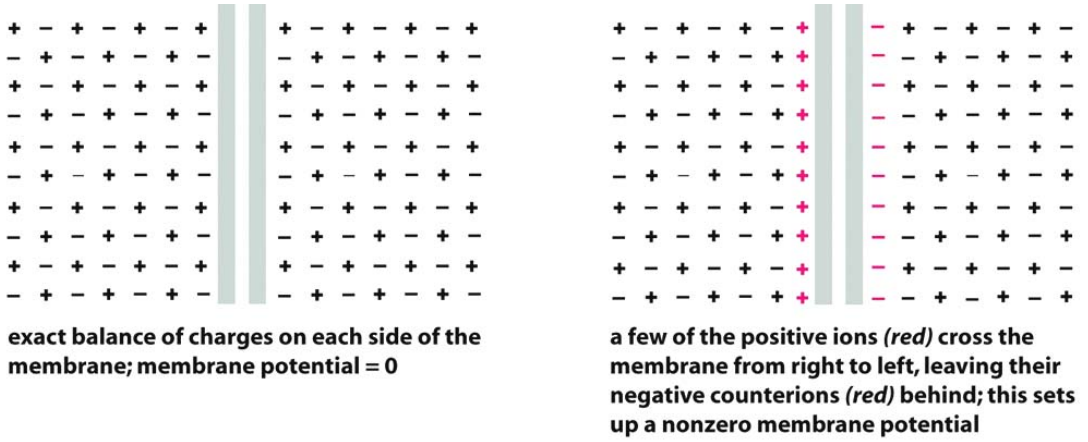

Fig. 1.6 The ionic basis of a membrane potential. A small flow of ions carries sufficient charge to cause a large change in the membrane potential

Although the K^+ gradient always has a major influence on this potential, the gradients of other ions (and the disequilibrating effects of ion pumps) also have a significant effect: the more permeable the membrane for a given ion, the more strongly the membrane potential tends to be driven toward the equilibrium value for that ion (Jacquez, 1971). Consequently, changes in a membrane's permeability to ions can cause significant changes in the membrane potential according to the Goldman equation (Goldman, 1943). This is one of the key principles relating the electrical excitability of cells to the activities of ion channels.

Mainly due to the presence of phosphatidylserine, ganglioside glycolipid and transmembrane proteins charges, but also to all hydroxyl groups in transmembrane glycoproteins, glycolipids, sphingomyelin, phosphatidylinositol, cholesterol, etc., the surface charge of an eukaryotic cell membrane is supposed to be negative in physiological conditions (pH~6-7) (Lakshminarayanaiah, 1975). Moreover, the membrane potential may influence the surface charge, especially when the extracellular

medium is lacking the inorganic ions. For example, the K^+ ions that go to form the layer of charge at the external side of the membrane, although their number is not significant, reduce the negative charges of the bilayer constituents.

A theoretical estimation of cell surface charge is very difficult to make and it widely differs in function of the cell type, including also here the influence of the membrane potential. Considering only phosphatidylserine and ganglioside glycolipid carrying negative charges, and additionaly supposing a symmetrical distribution in the two lipid layers of the membrane, we could estimate, on average, a minimum charge density of 1 negative elementary charge per 40 nm^2. For example, experimentally, the average values of the effective charge density present on the giant axon of the squid, frog muscle and barnacle muscle in their normal ionic environment, correspond to 1 negative charge per 2.22, 1.03 and 1.95 nm^2 respectively of the membrane area (Lakshminarayanaiah, 1975).

1.2.2 *Dictyostelium* adhesion proteins

There is less known about cell-substrate adhesion, the proteins involved and how motion and adhesive forces work together in *Dictyostelium* cells than in mammalian cells. Cell-substrate adhesion is a major aspect of amoeboid movement in the social amoeba *Dictyostelium* as well as certain mammalian blood and tumor cells. Cell-substrate adhesion is a crucial step in many biological processes such as development, wound healing, metastasis and phagocytosis (Fey, 2002). In mammalian cells, several proteins are involved in cellular adhesion, in particular cell-surface receptors, signaling molecules and components of the actin cytoskeleton. Integrin-mediated cell adhesion is one of the most widely studied adhesion mechanism. Integrins are heterodimeric type I transmembrane proteins composed of one α-subunit and one β-subunit, which bind to the extracelullar matrix by their extracellular domain and control cell spreading, migration, proliferation and survival (Schwartz, 2001).

In *Dictyostelium*, several proteins (glycoproteins) that mediate cell-cell adhesion during specific stages of development have been identified (e.g., gp 150, gp 130, gp 80, gp 24). Gp 24 protein (DdCAD-1) is a small, secreted but membrane anchored glycoprotein with similarities to vertebrate cadherins, expressed in the initial stages of

development (Brar, 1993). To date, it seems that only one of these molecules (glycoprotein gp 130) has been directly implicated in binding to substrate (Chia, 1996). It also plays role in phagocytosis.

To identify the molecular mechanisms involved in phagocytosis, Cornillon and colab. generated random insertion mutants of *Dictyostelium discoideum* and selected two mutants (phg1-1 and phg1-2) defective for phagocytosis (Cornillon, 2000). Both were characterized by insertions in the same gene, named *PHG1*. This gene encodes a polytopic membrane protein with an N-terminal luminal domain and nine potential transmembrane segments. Homologous genes can be identified in many species. Disruption of *PHG1* caused a selective defect in phagocytosis of latex beads and *Escherichia coli*, but not *Klebsiella aerogenes* bacteria. This defect in phagocytosis was caused by a decrease in the adhesion of mutant cells to phagocytosed particles. These results indicate that the Phg1 protein is involved in the adhesion of *Dictyostelium* to various substrates, a crucial event of phagocytosis.

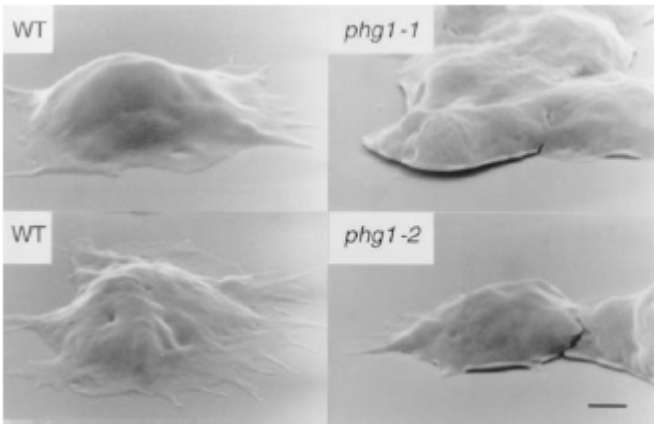

Fig. 1.7 Adhesion of wild-type (WT) and phg1 mutant cells to their substrate. Cells were grown on sterile glass plates for 3 days, fixed, dehydrated, and coated with gold. They were visualized in a scanning electron microscope. Scale bar = 1 μm (Cornillon, 2000).

Upon more prolonged culture in HL5 medium, phg1 mutant cells did adhere to their substrate. However, examination of the cells by scanning electron microscopy revealed distinct differences between adherent wild-type and mutant cells. Whereas wild-type cells adhered tightly to the glass coverslip, phg1 cells did not spread as extensively and local detachment zones could be seen (Fig. 1. 7).

In 2002 Fey reported the finding of a novel adhesion receptor, a protein named SadA localized to the cell surface, with nine putative transmembrane domains and three conserved EGF-like repeats in a predicted extracellular domain (Fey, 2002). Cornillon et al. identified in 2006 a new adhesion molecule in *Dictyostelium*. The SibA protein, (Cornillon, 2008), is a type I transmembrane protein, and its cytosolic, transmembrane and extracellular domains contain features also found in integrin β chains. Genetic inactivation of SibA affects adhesion to phagocytic particles, as well as cell adhesion and spreading on its substrate but it does not visibly alter the organization of the actin cytoskeleton, cellular migration or multicellular development. Still, no homologues of α-integrins were found in the *Dictyostelium* genome.

Table 1.2 The adhesion proteins found in *Dictyostelium*:

Protein	*Higher Eukaryote homologs*
Glycoprotein gp 130	Vertebrate cadherins
Phg1 transmembrane protein	9TM-αH protein
SadA transmembrane protein	9TM-αH protein
Sib(A-E) transmembrane proteins	β integrin homologue (5 isoforms)

1.2.3 The cell Cytoskeletons

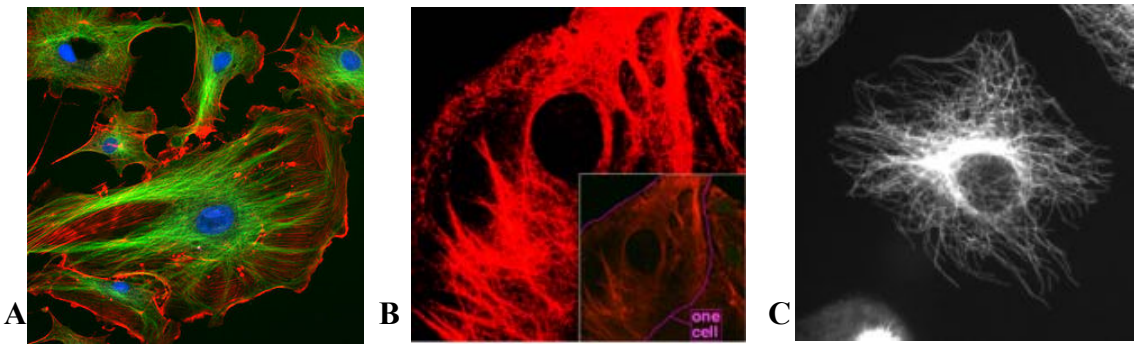

Fig 1.8 The eukaryotic cytoskeleton. **A.** Actin filaments are shown in red, microtubules in green, and the nuclei are in blue. **B.** Microscopy of keratin filaments inside cells. **C.** Microtubules in a fixed cell.

The cytoskeleton is found underlying the cell membrane in the cytoplasm and provides scaffolding for membrane proteins to anchor to (see Fig. 1.8). It exerts mechanical forces that deform the plasma membrane and form protrusions that extend from the cell. Indeed, cytoskeletal elements interact extensively and intimately with the

cell membrane (Doherty, 2008). The cytoskeleton is able to form appendage-like organelles, such as cilia, which are microtubule-based extensions covered by the cell membrane, and filopodia, which are actin-based extensions involved in stabilizing pseudopodia on the substratum (Heid, 2005). These extensions are closed in membrane and project from the surface of the cell in order to sense the external environment and/or make contact with the substrate or other cells. The concept and the term (*cytosquelette*, in French) was first introduced by French embryologist Paul Wintrebert in 1931.

Eukaryotic cells contain three main kinds of cytoskeletal filaments, which are microtubules, intermediate filaments, and microfilaments.

Microtubules

Microtubules are hollow cylinders about 23 nm in diameter (lumen = approximately 15 nm in diameter), most commonly made of 13 protofilaments which, themselves are polymers of alpha and beta tubulin. They are commonly organized by the centrosome and they have a very dynamic behaviour, binding GTP for polymerization: in the cell, the "minus" end is bound to the centrosome and therefore stable most of the time. Tubulin GTP binds to the "plus" end and hydrolysis the GTP into GDP. The microtubule alternates between slowly elongation and rapidly disaggregating phases. The growth phase lasts as long as a "cap" of tubulin GTP is present at the "plus" end.

In several cell types, an intriguing correlation exists between the position of the centrosome and the direction of cell movement: the centrosome is located behind the leading edge, suggesting that it serves as a steering device for directional movement (Ueda, 1997). In *Dictyostelium*, however Ueda et al. demonstrated that the extension of a new pseudopod in a migrating cell precedes centrosome repositioning. The microfilament network therefore dictates the positioning of the microtubules network.

Microtubules play key roles in:

- intracellular transport (associated with dyneins and kinesins, they transport organelles like mitochondria or vesicles).
- the axoneme of cilia and flagella.
- the mitotic spindle.
- synthesis of the cell wall (in plants).

Intermediate filaments

These filaments, around 10 nm in diameter, are more stable (strongly bound, two anti-parallel helices, forming tetramers) than actin filaments. Like actin filaments, they function in the maintenance of cell-shape by bearing tension (microtubules, by contrast, resist compression. It may be useful to think of micro- and intermediate filaments as cables and of microtubules as cellular support beams). Intermediate filaments organize the internal tridimensional structure of the cell, anchoring organelles and serving as structural components of the nuclear lamina and sarcomeres (Blumenthal, 2004). They also participate in some cell-cell and cell-matrix junctions. Different intermediate filaments are:

- made of vimentins, being the common structural support of many cells.
- made of keratin, found in skin cells, hair and nails.
- neurofilaments of neural cells.
- made of lamin, giving structural support to the nuclear envelope.

In *D. Dictyostelium* there are no intermediate filaments.

Actin filaments / Microfilaments

Around 6 nm in diameter, this filament type is composed of two intertwined actin chains (double helix structure) (Bamburg, 1999). Microfilaments are most concentrated just beneath the cell membrane, and are responsible for resisting tension and maintaining cellular shape, forming cytoplasmic protuberances (pseudopodia, filopodia, lamelipodia and microvilli- although these by different mechanisms). They are involved in phagocytosis and in some cell-to-cell or cell-to-matrix associations. They are also important for cytokinesis (formation of the cleavage furrow, specifically for cell division in suspension, (Neujahr, 1997, Zang, 1997)) and, along with myosin, for muscular contraction. Actin/Myosin interactions also help produce cytoplasmic streaming in most cells (Eichinger, 1999).

We are interested in the actin protein because its polymerization drives cell spreading and movement. Microfilaments are very dynamic structures: actin monomer polymerize and depolymerize leading to plasma membrane deformation.

1.2.4 Formation of microfilaments

Actin is one of the most highly conserved protein throughout evolution, being that it interacts with a large number of other proteins. It has 80.2% sequence conservation at the gene level between *Homo sapiens* and *Saccharomyces cerevisiae* (a species of yeast), and 95% conservation of the primary structure of the protein product. It is found in all eukaryotic cells where it may be present at concentrations between 10 and 200 μM. In *Dictyostelium* its plasma concentration as intermediate, is 100 μM (Podolski, 1990).

The actin monomer, known as globular actin (G-actin, 375 amino acids, 42 kDa), consists of two domains which can be further subdivided into two subdomains. ATP or ADP is located in the cleft between the domains with a calcium ion bound (Kabsch, 1990) (Fig 1.9A, black arrow). G-actin subunits assemble into long filamentous polymers called F-actin. Two parallel F-actin strands must rotate 166 degrees in order for them to layer correctly on top of each other (Fig. 1.9B). This gives the appearance of a double helix and, more importantly, gives rise to microfilaments of the cytoskeleton (Eichinger, 1999). Microfilaments measure approximately 7 nm in diameter with a loop of the helix repeating every 37 nm (Bamburg, 1999).

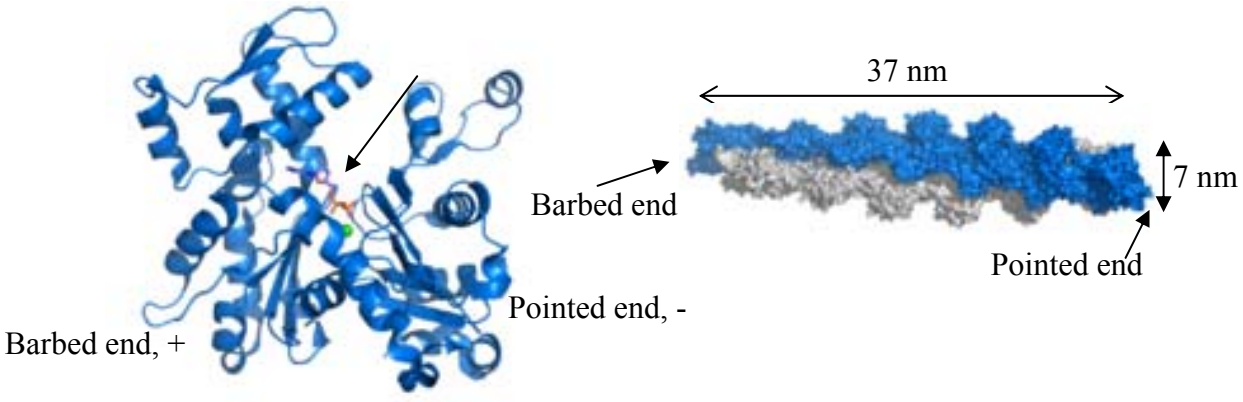

Fig. 1.9 A. Ribbon model of asymetric G-Actin molecule, ATP and the divalent cation are pointed by the black arrow; **B.** F-Actin; surface representation of 13 subunit repeat.

The actin molecule is polarized due to its structural asymmetry. Consequently, upon actin polymerization, every filament exposes its two extremities different protein domains that have different properties. The two extremities are called barbed end (+) and pointed end (-) (Fig. 1.9).

The polymerization of protein can be considered like a bimolecular reaction, where a monomer in solution binds to the extremity of a filament containing *n* actin subunits to form a new filament with *n+1* monomers of G-actins (Fig. 1.10A). Also, the rate constants, k_{on} and k_{off} respectively, are not the same at the two extremities of the filament: at the barbed end, the association and disassociation constants are higher than at the pointed end ($k_{on+} > k_{on-}$ and $k_{off+} > k_{off-}$ respectively; Fig. 1.10B), mainly due to the difference in electrostatic interactions at the filament extremities (Sept, 1999).

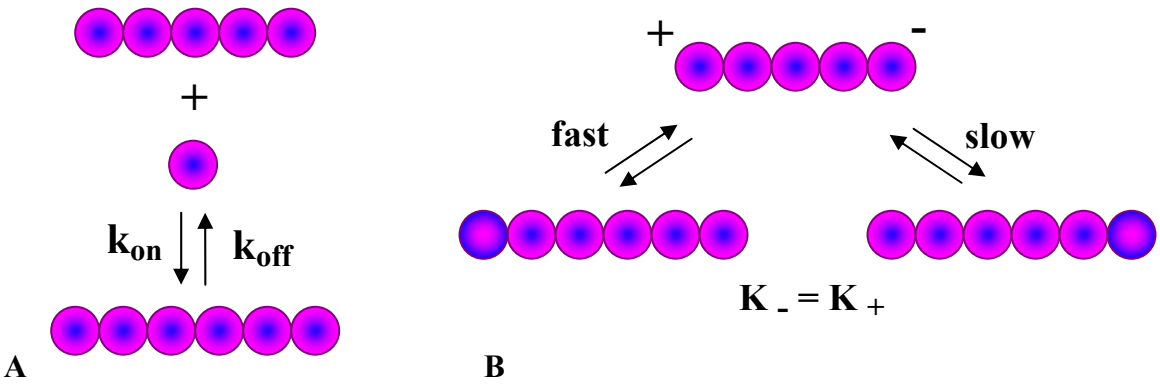

Fig. 1.10 A. Scheme of actin polymerization: k_{on} stands for association constant ($\mu M^{-1} \cdot s^{-1}$) and k_{off} represents the dissociation constant (s^{-1}) **B**. the rate constants (k_{on+}, k_{off+} and k_{on-}, k_{off-} respectively) are different at the two ends of filament: fast kinetics, at the barbed end (+) and slow kinetics, at the pointed end (-).

The general chemical reaction equation can be written as:

$$A_n + A_1 \underset{k_{off}}{\overset{k_{on}}{\Leftrightarrow}} A_{n+1} \qquad \text{Eq. 1.1}$$

where A_1 represents the actin monomer and A_n, A_{n+1} are the filaments with *n* and *n+1* monomers respectively.

The rate of polymer formation is given by:

$$\frac{d[A_{n+1}]}{dt} = \frac{d[A_1]}{dt} = k_{on+} \cdot [A_n][A_1] - k_{off+} \cdot [A_{n+1}] \qquad \text{Eq. 1.2}$$

for the barbed end, and by:

$$\frac{d[A_{n+1}]}{dt} = \frac{d[A_1]}{dt} = k_{on-} \cdot [A_n][A_1] - k_{off-} \cdot [A_{n+1}] \qquad \text{Eq. 1.3}$$

for the pointed end.

At the chemical equilibrium, $\frac{d[A_{n+1}]_{eq}}{dt} = 0$, which implies that:

$$K_+ = \frac{k_{on+}}{k_{off+}} = \frac{[A_{n+1}]_{eq}}{[A_n]_{eq}[A_1]_{eq}} \text{ and } K_- = \frac{k_{on-}}{k_{off-}} = \frac{[A_{n+1}]_{eq}}{[A_n]_{eq}[A_1]_{eq}} \quad \text{Eq. 1.4}$$

It can be noticed that the concentrations ratios from Eq. 1.4 are equal, resulting in the equality of the equilibrium constants ($K_+ = K_-$).

Moreover, in a polymerization reaction, for $n \geq 3$ (up to the nucleation phase), the number of free extremities is approximately the same at any moment (the gain of an extremity site is made on the base on the loss of other one, having also the same kinetics characteristics). Thus, we can appreciate that:

$$[A_n] = [A_{n+1}] = c \quad \text{Eq. 1.5}$$

It results immediately that the rate of polymerization, *r*, becomes:

$$r = \frac{d[A_{n+1}]}{dt} = k_{on} c \cdot [A_1] - k_{off} c = k'_{on} \cdot [A_1] - k'_{off} \quad \text{Eq 1.6}$$

We can find now the actin concentration for which the chemical equilibrium is reached ($r = 0$):

$$[A_1]_{eq} = \frac{k'_{off}}{k'_{on}} = \frac{k_{off}}{k_{on}} = \frac{1}{K} \quad \text{Eq 1.7}$$

This concentration is called "critical concentration" (C_c). Above this concentration, the filaments (at the barbed or pointed extremities) start to extend and below this concentration, the filaments decrease in length.

The critical concentration varies if the actin monomer is bound to ATP or ADP: 0.12 μM and 2μM respectively. When the monomer concentration lies between these two critical concentrations, net assembly occurs at the barbed end and net disassembly occurs at the pointed end, a process called treadmilling (see fig. 1.11). Thus, at steady state, the barbed end is the favoured site for ATP–actin addition whereas the pointed end is the favoured site for ADP–actin loss, both in vitro and in cells. In cells, actin turnover is enhanced more than 100-fold by actin-binding proteins that sever filaments, enhance subunit disassembly from the pointed end and facilitate ATP-for-ADP nucleotide exchange on free actin subunits (Pollard, 2003).

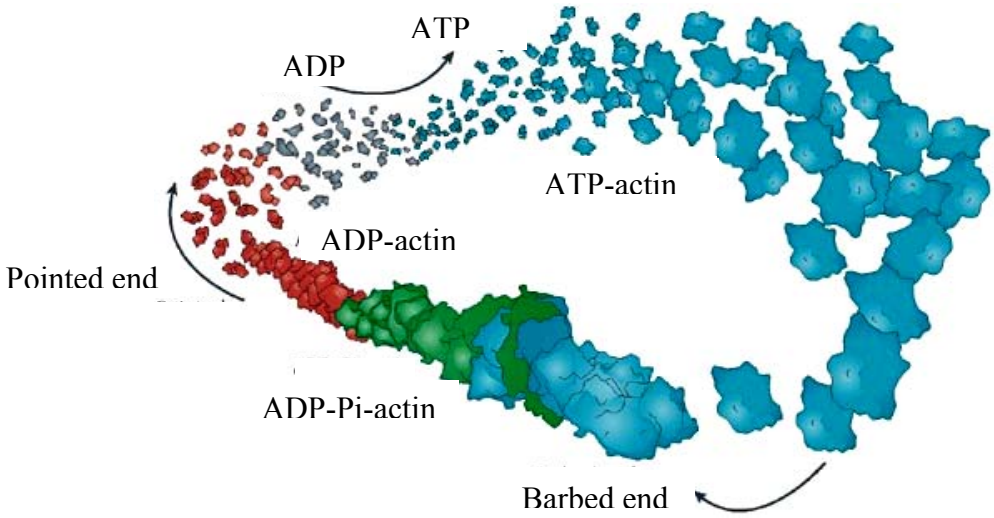

Fig. 1.11 Actin treadmilling model (Chi Pak, 2008)

ATP–actin complexes are preferentially added to the barbed end of actin filaments. Shortly after subunit incorporation, the non-covalently bound ATP is hydrolysed into ADP–P_i; subsequent release of the P_i occurs much more slowly. ATP hydrolysis occurs on average ~1–2 seconds after incorporation, whereas, in purified actin, P_i release occurs on average ~ 10 minutes after hydrolysis; however, both processes actually occur stochastically for each subunit. Thus, even when the monomer pool consists only of ATP–actin complexes and is given a sufficient amount of time, an actin filament can eventually consist of three types of actin–nucleotide complex: ATP–actin, ADP–P_i–actin and ADP–actin (Chi Pak, 2008).

Actin filament formation can be observed with the help of fluorescent actin monomers. Actin was directly labeled with a fluorescent dye (tetramethylrhodamine-5-maleimide) and was visualized by total internal reflection fluorescence microscopy (Fig. 1.12) (Fujiwara, 2002).

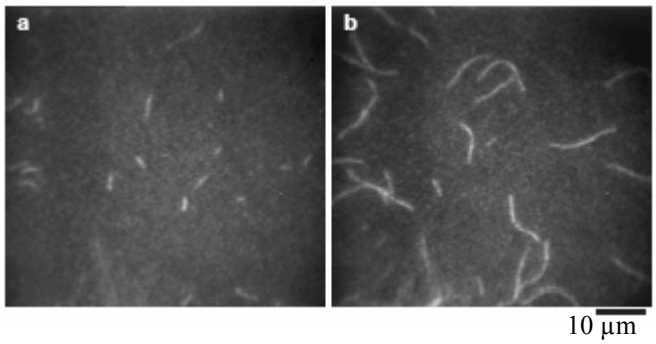

Fig. 1.12 Fluorescence micrographs of actin(Ca) polymerization taken 6 min (**a**) and 34 min (**b**) after the addition of 30 mM potassium chloride, 2 mM magnesium chloride, 4 mM ATP, 20 mM MOPS at pH 7.0, 10 mM DTT. (Fujiwara, 2002)

1.2.5 Actin polymerization leads to cell membrane deformation

The *Dictyostelium* cell is capable to reorganize its cytoskeleton in a few seconds (Eichinger, 1999, Condeelis, 1993). Thus, in vivo, there are regulation systems of actin polymerization. Indeed, actin forms molecular assemblies by interacting with many proteins, in both forms, G-actin and F-actin. These assemblies command cell adhesion, spreading, migration and motility, by providing an efficient pushing force against the plasma membrane. Different stages and their respective proteins are shown in Fig. 1.13.

Signaling pathways converging on WASp/Scar proteins regulate the activity of Arp2/3 complex, which mediates the initiation of new filaments as branches on preexisting filaments (Schafer, 1998; Bretschneider, 2002; Carlier, 2003a; Diez, 2005) (Fig. 1.13; see also Fig. 1.16).

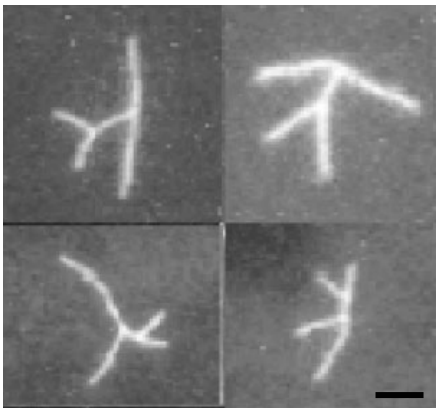

Fig.1.13 Gallery of branched actin filaments polymerized in the presence of N-WASP and Arp2/3 complex. Actin (4 mM) was polymerized in the presence of 100 nM N-WASP and 30 nM Arp2/3 complex. Filaments were polymerized for 3 minutes, then supplemented with 3 mM rhodaminelabeled phalloidin, diluted 500-fold and observed using a fluorescence microscope. Scale bar 5 μm (Carlier, 2003a).

After a brief spurt of growth, the capping protein terminates the elongation of the filaments, this being in favour of a more dense actin cytoskeleton and allows to exert more important forces against the plasma membrane (Eddy, 1996). After filaments have matured by hydrolysis of their bound ATP and dissociation of the γ phosphate, ADF/cofilin proteins promote debranching and depolymerization (Theriot, 1997). Profilin catalyzes the exchange of ADP for ATP, refilling the pool of ATP actin monomers bound to profilin, ready for elongation (Fig. 1.14, Pollard, 2003).

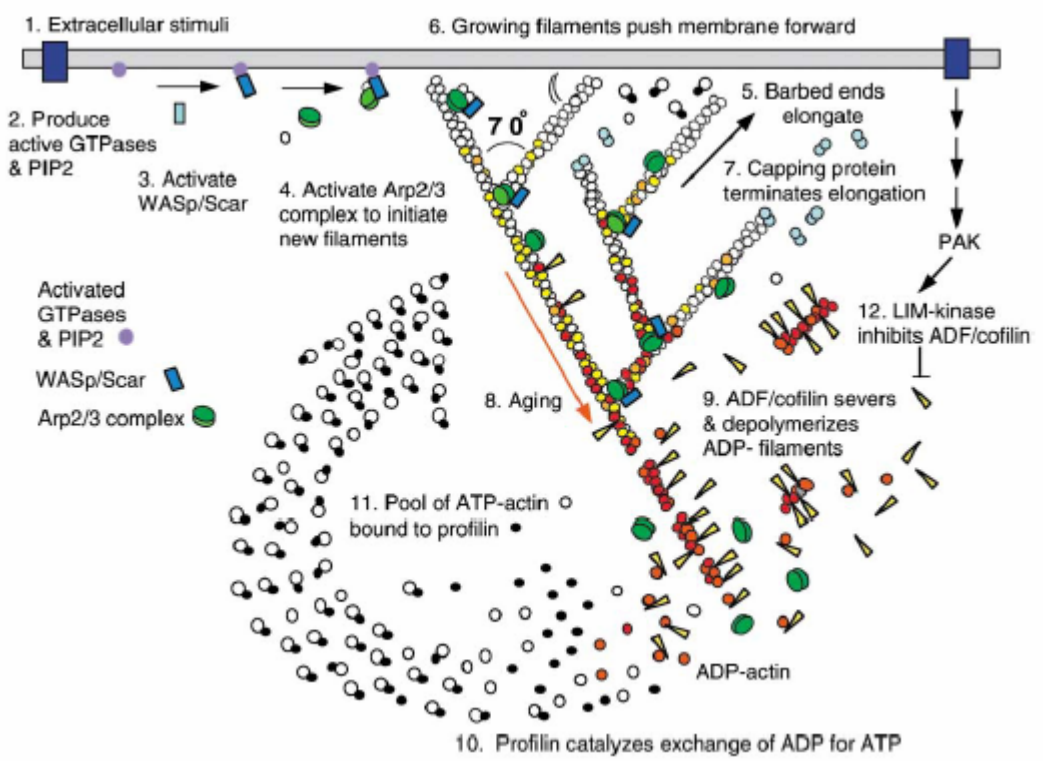

Fig.1.14 Dendritic Nucleation/Array Treadmilling Model for Protrusion of the Leading Edge
(1) Extracellular signals activate receptors. (2) The associated signal transduction pathways produce active Rho-family GTPases and PIP2 that (3) activate WASp/Scar proteins. (4) WASp/Scar proteins bring together Arp2/3 complex and an actin monomer on the side of a preexisting filament to form a branch. (5) Rapid growth at the barbed end of the new branch (6) pushes the membrane forward. (7) Capping protein terminates growth within a second or two. (8) Filaments age by hydrolysis of ATP bound to each actin subunit (white subunits turn yellow) followed by dissociation of the _ phosphate (subunits turn red). (9) ADF/cofilin promotes phosphate dissociation, severs ADP-actin filaments and promotes dissociation of ADP-actin from filament ends. (10) Profilin catalyzes the exchange of ADP for ATP (turning the subunits white), returning subunits to (11) the pool of ATP-actin bound to profilin, ready to elongate barbed ends as they become available. (12) Rho-family GTPases also activate PAK and LIM kinase, which phosphorylates ADF/cofilin (Pollard, 2003).

Motile cells extend a leading edge by assembling a branched network of actin filaments that produces physical forces as polymers grow beneath the plasma membrane. A core set of proteins including actin, Arp2/3 complex, profilin, capping protein, and ADF/cofilin can reconstitute the process in vitro, pushing the micrometric beads (Fig. 1.15, Carlier, 2003a). Mathematical models of the constituent reactions predict the rate of motion (Dikinson, 2002).

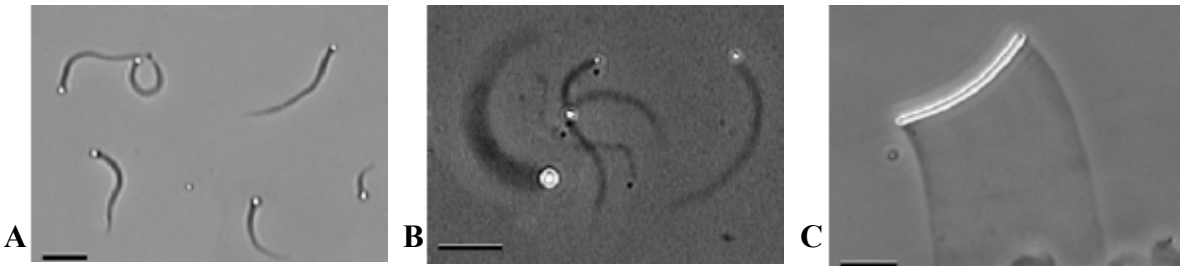

Fig. 1.15 Biomimetic motility assay: Examples of actin-based motility of functionalized particles in the reconstituted motility medium. **A.** N-WASP-coated beads (2 µm in diameter) generate actin tails and undergo propulsion in the medium. **B.** Beads of three different diameters (3, 1, and 0.5 µm) move at the same rate in the medium but display actin tails of different thickness. **C.** A glass rod (1 µm diameter, 30 µm in length) generates a lamellar actin array and moves mimicking lamellipodium extension (Carlier, 2003a).

Marcy et al. (Marcy, 2004) developed a micromanipulation experiment, in which a comet growing from a coated polystyrene bead is held by a micropipette while the bead is attached to a force probe. By pulling the actin tail away from the bead at high speed, they measured the force necessary to detach the tail from the bead (0.25 $nN/\mu m^2$). In addition, many authors present different experimental and theoretical methods for quantification of traction forces exerted by different types of migrating single cells, finding values between 0.1 $nN/\mu m^2$ (for Dictyostelium) and 5.5 $nN/\mu m^2$ (for fibroblastes) (Fukui, 2000; Balaban, 2001; Barentin, 2006).

1.2.6 Morphological structures of *Dictyostelium* actin cytoskeleton

Dynamic actin networks generate forces for numerous types of movements such as lamellipodia protrusion, filopodia protrusion (Fig. 1.16), pseudopod protrusion, uropodia, or the motion of endocytic vesicles (Marcy, 2004). These mechanisms require the barbed ends of actin filaments to be held close to the surface being pushed (Borisy, 2000). These filaments differ in shape, size and functionality.

Pseudopodia are temporary three-dimensional structural projections of eukaryotic cells. Pseudopodia extend by the reversible assembly of actin subunits into microfilaments. The pseudopodium extends until the actin reassembles itself into a network. This is the mechanism by which amoebae moves, as well as some animal cells, such as white blood cells.

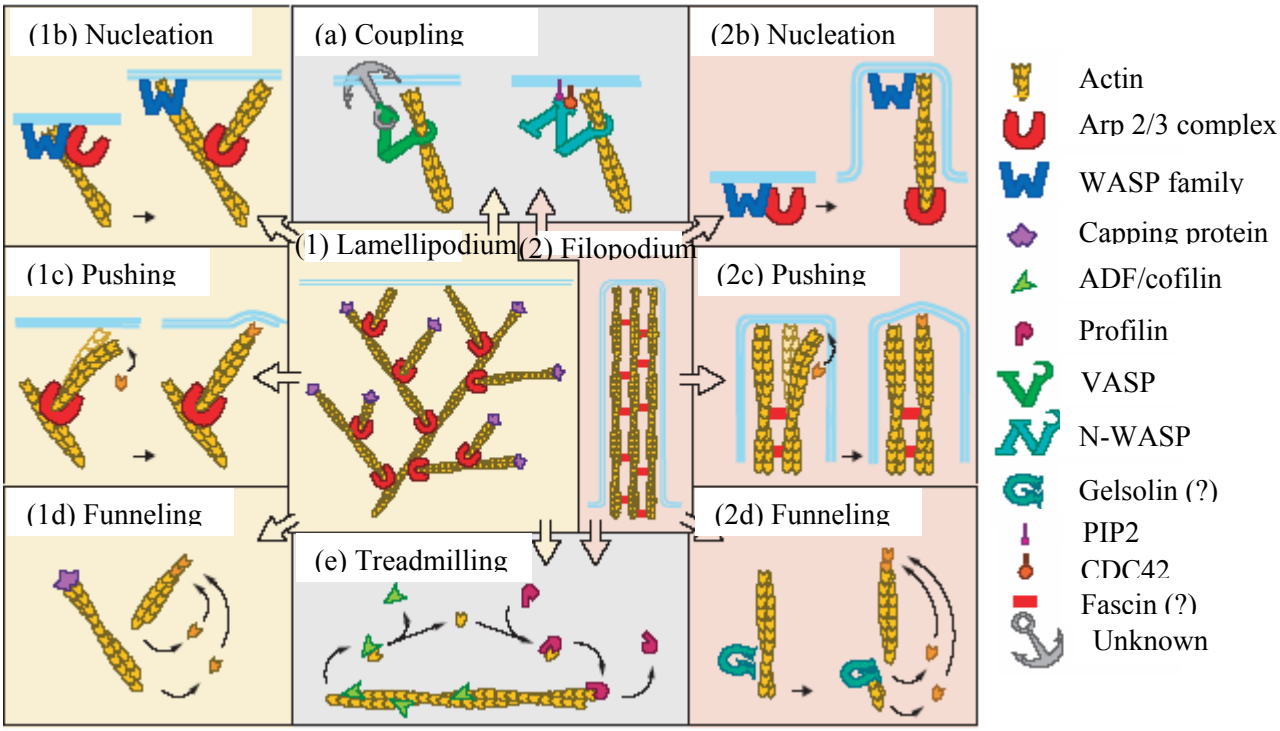

Fig. 1.16 Functional steps for the two major protrusive structures of crawling cells, lamellipodia (1) and filopodia (2). (a) VASP is involved in coupling the actin filament and the membrane, through an as yet unidentified molecule. An additional coupling pathway is provided by N-WASP, which binds PIP2 and is triggered by Cdc42. Members of the WASP family activate the Arp2/3 complex and nucleate formation of actin filaments on pre-existing filaments. **(1b)** In lamellipodia, activation and nucleation are repeated to generate a dendritic array of filaments; **(2b)** in filopodia, activation and nucleation need only occur once. Actin filaments are thought to push against the surface by an elastic Brownian ratchet mechanism **(1c, 2c)**. Nucleation followed by capping of barbed ends in lamellipodia **(1d)** or severing, followed by capping of barbed ends in filopodia **(2d)**, produce an excess of free pointed ends compared to barbed ends, leading to a more rapid growth of remaining barbed ends (known as funneling). The intrinsic low rate of treadmilling of actin filaments is accelerated by the synergistic action of cofilin and profilin **(e)**. (Borisy, 2000).

The functions of pseudopodia include locomotion and the capture of prey. Pseudopodia are critical in sensing prey that can then be engulfed; the engulfing pseudopodia are called phagocytosis pseudopodia. In this way, a well known example of related-behaviour with amoeboid cell is the human white blood cell (leukocytes).

The lamellipodium is a cytoskeletal actin projection on the mobile edge of the cell. It contains a two-dimensional actin mesh which pushes the cell membrane across a substrate. The lamellipodium is created by actin nucleation at the plasma membrane of the cell (Alberts, 2008) and is the primary area of actin incorporation or microfilament

formation in some cells. Lamellipodia are found primarily in very mobile keratocyte in the skin, which are involved in rapid wound repair, crawling at speeds of 10-20 μm/minute over epithelial surfaces. Lamellipodia are a characteristic feature at the front, leading edge, of motile cells.

The uropodium is a rigid membrane projection with related cytoskeletal components at the trailing edge of a cell in the process of migrating or being activated, found on the opposite side of the cell from the lamellipodium.

Filopodia are finger-like extensions of the cell surface that are involved in sensing the environment, in attachment of particles for phagocytosis, in anchorage of cells on a substratum (Heid, 2005), and in the response to chemoattractants (Diez, 2005), or other guidance cues. Filopodia represent an excellent model for actin-driven membrane protrusion of *Dictyostelium* cells (Medalia, 2006).

The implication of different key regulators of cellular activities (e.g. Ras family-small G proteins that have many effectors, Rac, Cdc42-two Rho family GTPases or VASP, WAVE and Arp2/3 complexes) in signaling transduction pathways (mediating downstream signaling) and their connections with cell motility and morphology was widely studied (Dumontier, 2000; Chen, 2000; Han, 2002; Steffen, 2006; Para, 2009). For example, in Fig. 1.17 it is shown that dominant RasG inactivation results in the reduction of filopodia (Chen, 2000).

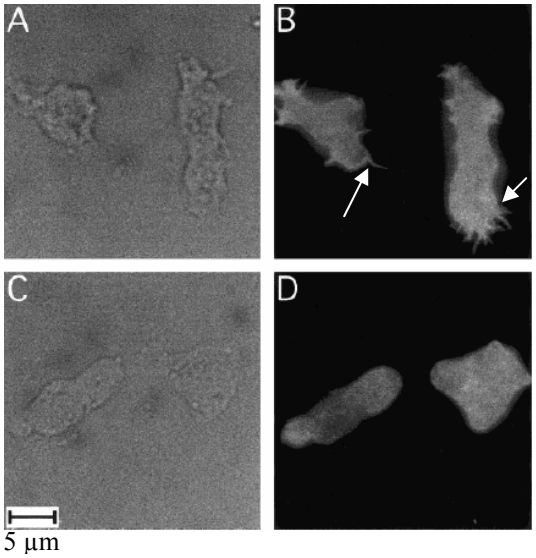

Fig. 1.17 Visualization of filopodia (pointed by white arrows) on wild type cells and RasG(G12T) transformants. F-actin was stained with rhodamine-phalloidin after fixation of vegetative *Dictyostelium* amoebae on a glass surface. **A, B:** wild type KAX-3 cells; **C, D:** RasG(G12T) transformants. Scale bar 5 μm (Chen, 2000)

In their natural environment, *Dictyostelium* cells migrate on or within three-dimensional (3D) complex substrates such as soil particles, fragmented leaves, and debris

of very different physicochemical properties. The cells are able to adhere and to move on humid as well as on dry substrates. Consequently, amoeboid migration must be a very robust process that is resistant to many adverse events. Cell movement is a cycling multistep process that requires the integration of complex biochemical and biophysical cell functions. Using protein micropatterning techniques to control cell environment at the micrometer scale, it has been shown that cell morphology and internal organization is influenced by the geometry of cell-surface contact zones (Jiang, 2005). An elusive question is the molecular identity of the dynamic signaling pathways translating the adhesive environment into a polarized response. As for mammalian cells, these pathways remain also partially known in the case of *Dictyostelium* amoebae. One possibility is that a biochemical signal is synthesized by adhesion receptors upon contact with the surface, which subsequently diffuses throughout the cell. In function of how the receptors are activated and which key regulators are activated (which signal transduction pathway is "used"), different organizations of actin cytoskeleton can be induced (Ridley, 1993). A more sophisticated mechanism is that mechanoreceptors sense mechanical constraints due to cell adhesion to the surface (Thery, 2006a).

Different cells solve this challenge differently, which leads to differences in migration strategies. The hallmarks of amoeboid movement include a simple polarized shape, dynamic pseudopod protrusion and retraction (Russ, 2006), flexible oscillatory shape changes, and rapid low-affinity crawling (Friedl, 2001). These morphological oscillations are not random and they appear to be associated with intrinsic physicochemical oscillations of actin polarization leading to pseudopodal extensions and retractions (Killich, 1993). Excitation waves of F-actin assembly develop and propagate for several micrometers at up to 26 μm/min. Wave propagation and extinction coincide with the initiation and attenuation of pseudopodium extension and cell advance, respectively (Vicker, 2000).

1.2.7 Focal adhesion/contact and adhesion sites in *D. discoideum*

In order to efficiently exert forces on a substrate, the cell has to attach on it, such that actin filaments transmit traction forces to the substrate at cell-substrate adhesion sites.

Cell adhesion is essential for cell migration, tissue organization and differentiation, therefore playing central roles in embryonic development, remodeling and homeostasis of tissue and organs, metastasis, phagocytosis. Cells usually adhere to extracellular matrix molecules, and a few of them (platelets, blood monocytes, osteoclasts, amoebae) also adhere to plain or coated solid materials. Adhesion dependent signals control the actin cytoskeleton assembly and cooperate with other signaling pathways to regulate biological functions such as cell survival, cell proliferation and cell differentiation. Cell migration and invasion are integrated processes requiring the coordinated assembly and disassembly of integrin-mediated adhesions and their coupling to the actin cytoskeleton dynamics (Delon, 2007; Vicente-Manzanares, 2009; Block, 2008).

Cellular adhesive structures consist of transmembrane adhesion molecules linked to the actin cytoskeleton and a signal transduction machinery aiming to assemble and disassemble it. In mammals, **focal adhesions** (FA; Fig. 1.18A) contain adhesion receptors, called integrins, cytoskeletal and signaling molecules in multimolecular complexes of 0.5–2 μm in diameter. Integrins bound to extracellular ligands (fibronectin) become linked to the actin cytoskeleton via several adapter and signaling proteins, such as talin, vinculin, α-actinin (not shown), filamin, focal adhesion kinase (FAK), and paxilin. FAK phosphorylates tyrosine domains of some signaling proteins, its activity being monitored the presence of phospho-tyrosines (Fig. 1.18B). In the mammals, the hallmark of FA is the presence of actin stress fibers parallel with the substratum that connects the FA.

Fully matured focal adhesions are formed at the leading extending edge of the cells and represent relatively stable cell-substrate interactions that persist as long as the cells are attached to the substrate (Friedl, 2001, Bukahrova, 2005).

The **focal contact** is smaller, less developed, and more transient compared to focal adhesions (Burridge, 1996). Focal contacts contain smaller clusters of adhesion receptors and a reduced array of cytoskeletal and signaling elements, which are not linked to stress fibers but rather to a more diffuse cortical F-actin (Burridge, 1996). Focal contacts are thought to represent more dynamic junctions predominantly under the control of Rac and Cdc42 signaling proteins (Nobes, 1999).

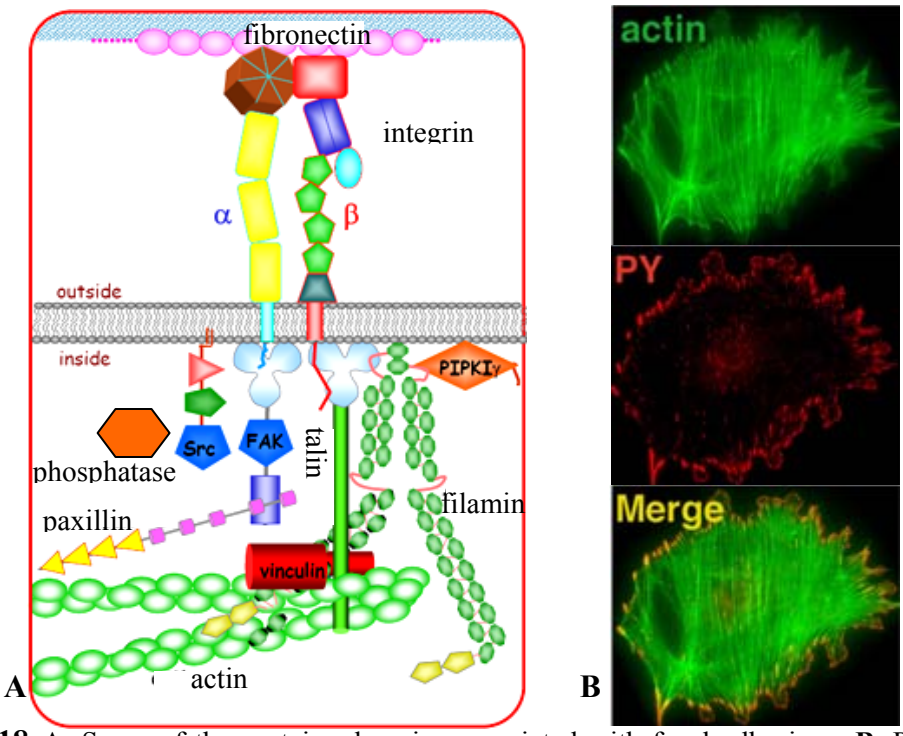

Fig. 1.18 **A**. Some of the proteins domains associated with focal adhesions. **B**. Porcine aortic endothelial cells, double-labeled for actin (green) and phospho-tyrosine (PY, red). Notice focal complexes at the cell edge and focal adhesions at the ends of actin cables (Geiger, 2001).

Dictyostelium cells are similar to leukocytes, in that they are fast-moving cells with an irregular shape. No structure similar to actin stress fiber has been found in *Dictyostelium*. Nevertheless, in *Dictyostelium*, several plasma membrane proteins (described above) have been identified that mediate adhesion. Some of these proteins are similar to β-integrins (SibA), which mediate interaction of higher eukaryotic cells with extracellular matrix proteins (Cornillon, 2006; Cornillon, 2008). In adition, *D. discoideum* also possesses many proteins known to be part of adhesion structures in higher eukaryotes, such as talinA, talin B (Niewohner, 1997; Tsujioka, 2008), paxillin (Bukahrova, 2005; Duran, 2009), coronin (de Hostos, 1991; Gerisch, 1993), ERMs, FAK, certain myosins (Patel, 2008), phg1, phg2 (Gebbie, 2004), Src-like tyrosine kinase (Moniakis, 2001). They stimulate actin polymerization (not all, some stimulate depolymerization) and link the attachment of actin microfilaments to the plasma membrane.

TalA$^-$ cells show reduced adhesion to the substrate and slightly impaired cytokinesis in the vegetative stage, while the development is normal (Tsujioka, 2008).

Phg2 seems to play a specific role in signaling actin polymerization/depolymerization at places where the amoeba comes into direct contact with a substrate (Gebbie, 2004). Paxillin is a key regulator component of focal adhesion sites, implicated in controlling cell-substrate interactions and cell movement (Bukahrova, 2005).

Two actin-containing structures have been proposed to act as ”feet” in *Dictyostelium* cells (adhesion sites). One of the candidates is the **eupodium** (Fig. 1.19), but this appears only in cells that are under the pressure of the agar sheet (Fukui, 1999). Eupodia are F-actin containing cortical structures similar to vertebrate podosomes (for example, in lymphocytes) or invadopodia found in metastatic cells. Eupodia are rich in actin binding proteins such as α-actinin, myosin I B/D, ABP120, cofilin, coronin, and fimbrin, but not a homologue of talin. There is a precise spatiotemporal coupling between F-actin assembly in eupodia and lamellipodial protrusion. When a lamellipodium advances to invade a tight free space, additional rows of eupodia (0.5 – 1 μm) are sequentially formed at the base of that lamellipodium.

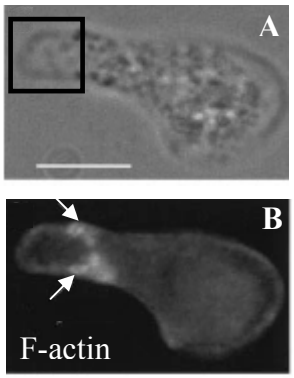

Fig 1.19 Immunofluorescence localization of actin in eupodia. The cells were prepared by the agar-overlay method. The cells migrate toward the left of the field. **A.** Phase-contrast image of a single active cell. The lamellipodium (black square) appears to be invading a space between the glass coverslip and the agarose overlay. **B.** The bright dots at the base of the lamellipodium (arrows) are eupodia. Scale bar, 5 μm.

The other is **actin foci**, which are observed on the ventral membrane of freely migrating cells (Yumura, 1990). When the cells are stained with ConcanavalinA protein which covalently bound the oligosaccharide chains of the glycoproteins, distinct patterns of dots and short fibers, which are referred to as cellular tracks (CTs), are observed behind the cells (Uchida, 1999). Since the dots in CTs contain actin and α-actinin, it is conceivable that they are derived from actin foci.

Actin foci are very dynamic structures that appear and disappear at the surface on the substratum during cell migration (Bretschneider, 2004). The velocity of the cells is inversely proportional to the number of actin foci (Uchida, 2004). Reflection interference

microscopy revealed that the ventral cell membrane was closer to the substratum at sites of actin foci (Uchida, 2004). Furthermore, some actin foci are incorporated into the retraction fibers, ripped off from the cells and eventually shed on the substratum after the cells move away (Uchida, 2004). These authors measured the traction force using a silicone substratum and demonstrated that the traction force was transmitted to the substratum through actin foci. They also found evidence suggesting that changing step is regulated in a coordinated manner during cell migration. Several lines of evidence strongly suggest that actin foci function as the active "feet" of *Dictyostelium* cells.

Figure 1.20A and B show live observations of GFP-actin expressing cells by fluorescence microscopy and the appearance of several fluorescent dots, present on the ventral cell membrane. The diameter of the fluorescent dots ranges from 0.3 to 1.0 μm, with an average diameter of 0.53±0.12 μm (for n = 30 fluorescent dots). Interestingly, the appearance of actin foci was transient (~20 s) and their positions on the substratum were unchanged during this time (Fig. 1.20C).

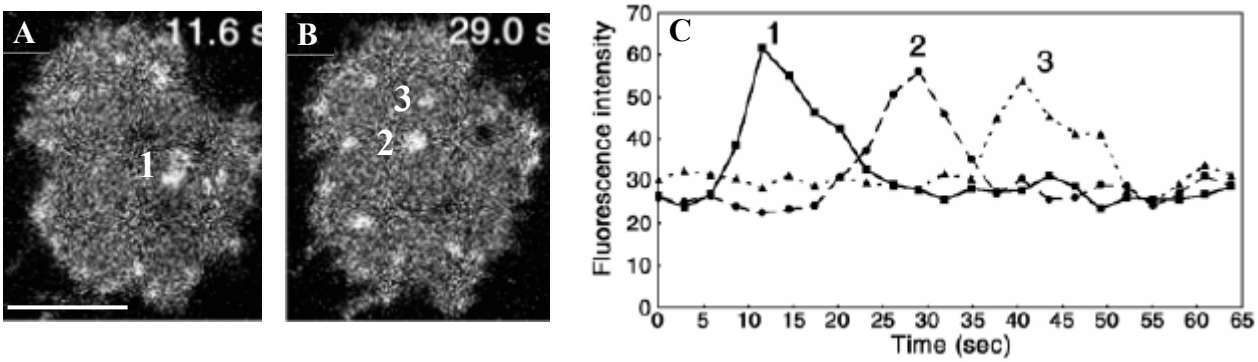

Fig. 1.20 A, B. Dynamics of actin foci in live cells as seen by fluorescence microscopy using actin GFP. The ventral membrane of a quiescent *Dictyostelium* cell was analyzed at various time points, as indicated. **C** Time course of fluorescence intensity of the three actin foci indicated in A and B. (Uchida, 2004)

To investigate whether these actin spots co-localize with the areas of paxilin enrichment, Bukahrova et al. (Bukahrova, 2005) produced a cell expressing both PaxB-GFP and a red fluorescent actin binding domain of ABP120 protein (a protein which appears in actin foci; Bretschneider, 2004). Observation of the actin foci and PaxB foci showed that the actin foci were much more dynamic (with half-life approximately 9 s) and, in general, did not coincide with the paxillin foci (Fig. 1. 21). The PaxB foci originated at the leading edge of the cell and stayed present during the time the surface

was in contact with the substrate (these structures look like authentic focal adhesion sites), while the actin foci could arise anywhere and be disassembled, while the surface was still in contact with the substrate. This indicates that these PaxB and actin foci may serve different functions (Bukahrova, 2005). Actin foci underneath the cell ventral surface could be sites of pseudopodia and may have a roll in cell positioning, force transmitting and stability on the substrate.

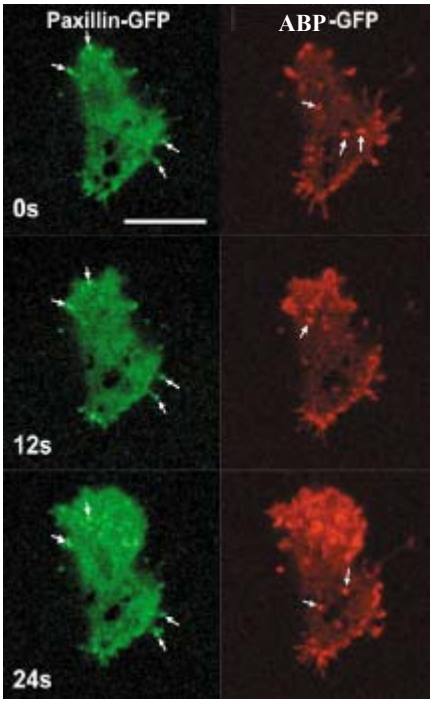

Fig. 1.21 Co-localisation of PaxB-GFP and ABP120-GFP. Confocal time series of vegetative wild-type AX2 cell expressing PaxB-GFP and ABP120-GFP. PaxB-GFP (green) localizes to long live stationary contact sites at the cell/substratum interface as indicated by the arrows that mark the same contact sites at different time points. ABP120-GFP (red) accumulates at very short-lived contact sites as indicated by the arrows. Scale bar, 10 μm.

Moreover, the active structures of dynamic pseudopodium extension and cell advance, respectively, are the short-lived actin rich-spots of short-life with different sizes and shapes (half life of 9 s; Bretschneider, 2004) which appear at the cell edges.

1.2.8 Dictyostelium spreading

An understanding of how adhesion and actin polymerization are coordinated is fundamental to physiological and pathological situations, like wound healing, the infiltration of macrophages into tissues in chronic inflammatory diseases or cancers.

In order to separate protrusion from retraction, Keller et al. (Keller, submitted) studied the temporal and spatial dynamics of *D. discoideum* cell-surface contact area

during spreading and their results support the physical model of spreading proposed by Chamaraux (Chamaraux, 2005). They provided evidence that, despite size, shape and speed variability, cells possess common spreading characteristics. Protrusion activity exhibits quasi-periodic variations, even in the presence of very low retraction activity, with a conserved 11 s period. They also studied the effect of external calcium on the morphology and kinetics of spreading.

The spreading process is presumably initiated by a first contact with a surface (Stossel, 1999). It comprises five steps: (1) In initial actin nucleation, extern signals are integrated by G-proteins and phosphoinositols (PIPs) leading to local actin polymerization. (2) during filament growth, as a result of actin polymerization, a pseudopod is formed and protruded; the development of a pseudopod results from elongation and cross-linking of polymerized actin to a viscous gel and unilateral swelling, prompting the outward pushing of the plasma membrane, extension of one or several leading pseudopods, and acquisition of a polarized cell shape. (3) during attachment, the pseudopods establish an interaction towards the underlying substrate by adhesion mechanisms that, in the case of *Dictyostelium*, remains to be defined on a molecular level. (4) contraction by filament sliding occurs after attachment of the cell to the substrate and elongation of the cell body; this contraction provides the force for translocation, and contractile force is putatively provided by myosin motors and additional mechanisms. (5) the spreading is terminated when retraction and detachment of the cell rear occurs, during which localized release of adhesive bonds at the trailing edge allows the detachment and retraction of the rear end into the advancing cell body.

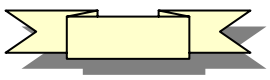

Dictyostelium discoideum are simple eukaryotic cells able to adhere and spread on plain materials (hydrophilic and hydrophobic) of surprisingly variable surface characteristics.

The contact of cells with a solid surface is a complex process and triggers important intracellular signalization pathways, leading to cell spreading, polarization, motility, proliferation and eventually differentiation. The number of proteins involved in

cell adhesion is quite large and involves many molecular interactions (Geiger, 2001). Despite our knowledge of many elements that play a role in adhesion, their temporal hierarchy and spatial organization is only partially understood. It is challenging to identify the successive formation of protein complexes leading to stable cell-surface contacts. Synchronizing cell-surface contact is a prerequisite for the preparation of cell material enriched in protein complexes active at a given time after contact. A biochemical analysis will be profitable when an entire cell population (minimum one million cells) will make the first contact point with a surface at the same time, starting the actin polymerization process in a synchronized way for all cells.

It would therefore be useful to synchronize the onset of cell-surface spreading, to get access to the different phases of this activity. In view of this, we investigated the possibility to modulate electrostatic repulsion between cells and a surface (glass, ITO, etc.) to control the formation of an initial cell-substrate contact. Moreover, electric fields could be used to diminish the repulsion between cells and a conductive surface.

1.3 Cell manipulation using electric fields

1.3.1 Electroactive substrates to control cell adhesion

Cell adhesion to material surfaces and the subsequent cell activities (spreading, focal adhesion, migration and proliferation) firstly depend on the presence and the location of specific extracellular matrix molecules and are highly sensitive to the surface chemistry and its physical environment. This includes the stiffness of the materials, and the topography of the surfaces on which cells adhere, as well as the geometry of chemical patterns on surfaces (Simon, 2006). Adsorption of macromolecules and surface functionalization are therefore essential. On the long term, remodelling of the extracellular matrix, secretion or storage of growth and differentiation factors, proper material stiffness will be determinant. A complete characterization of material properties is thus necessary. Mastering these processes is crucial for the good integration of substituting biomedical materials and for the compatibility between medical implants and

living tissues. It is also important for research in biology, since eukaryote cells are often grown on material surfaces. Furthermore, as the interaction between cells and materials extends over different scales, from nm (typical size of macromolecules), to several μm (cell geometry), micro- and nanotechnology are therefore well suited to engineer material surfaces for biological use, in order to provide cells in precise and well characterized conditions.

Material surfaces can be engineered not only to selectively control cell adhesion in a persistent manner, but also to switch from a non-adhesive to an adhesive state. A range of surfaces have been developed, whose hydrophobicity can be controlled either electrically (Lahann, 2003), electrochemically (Wang, 2003), thermally (Moran, 2006), or photoactively. Surface hydrophobicity is an interesting parameter to modulate cell adhesion because most proteins, including extracellular matrix ones, bind more strongly on hydrophobic surfaces than on hydrophilic ones (which is not the case for *Dictyostelium*, because amoebae adheres on plenty materials either hydrophobic or hydrophilic ones). However, large changes are necessary to significantly modify protein adsorption. Therefore, surface switching often relies on other physico-chemical mechanisms to change cell adhesion. In addition, caution should be exerted when using physical forces since living cells are very sensitive to their environment. Electrowetting for instance, requires large electric voltages to be effective in physiologically relevant solutions, which may trigger electrophysiological responses. In the same way, strong UV illumination is necessary for photo-induced wetting, which is harmful to cells. Consequently, these techniques have not yet been employed to control cell adhesion. Electrochemical and thermal switching are more cell-friendly techniques and several researchers have already demonstrated promising applications.

Thermal switching is based on hydrogels that are film-coated over the surface and exhibit a transition between a collapsed and a swollen structure at a critical solution temperature (LCST). An example of such a thermo-responsive polymer is poly(N-isopropylacrylamide or PNIPAAm, whose LCST is in the range of 32-35°C. This surface can interchange between hydrophobic, above the LCST, and hydrophilic, below the LCST. The LCST of PNIPAAm and its copolymers is at a physiologically relevant temperature, thus allowing the surface to be developed as a novel substrate for cell

culture and recovery without the use of harmful proteolytic enzymes such as trypsin or dispase (Moran, 2006). Cells adhere, spread and grow well on PNIPAAm hydrogels at 37°C, since the dehydrated polymer surface is hydrophobic which allows strong extracellular matrix protein binding. Reducing the temperature below LCST makes the surface hydrophilic and swelling exerts large mechanical forces, which induce detachment of a cell sheet including an intact extracellular matrix (Moran, 2006). This substrate is not adapted for *Dictyostelium* cells, since they have no extracellular matrix and also they do not survive at 37°C.

Electrochemical switching can be achieved in different ways. One possibility is to change the redox state of a molecule grafted to the material surface. The resulting surface voltage change exerts repulsive or attractive forces on adsorbed or covalently bound molecules, which drives a conformational change. Wang et al. (Wang, 2003) tethered bipyridinium molecules through an alkylated linker to an electrode and showed that redox modification of the bipyrinidium group bended the linker towards the surface, exposing the most hydrophobic part of the molecule (Fig. 1. 22). A reversible, but modest, surface energy change accompanies voltage application.

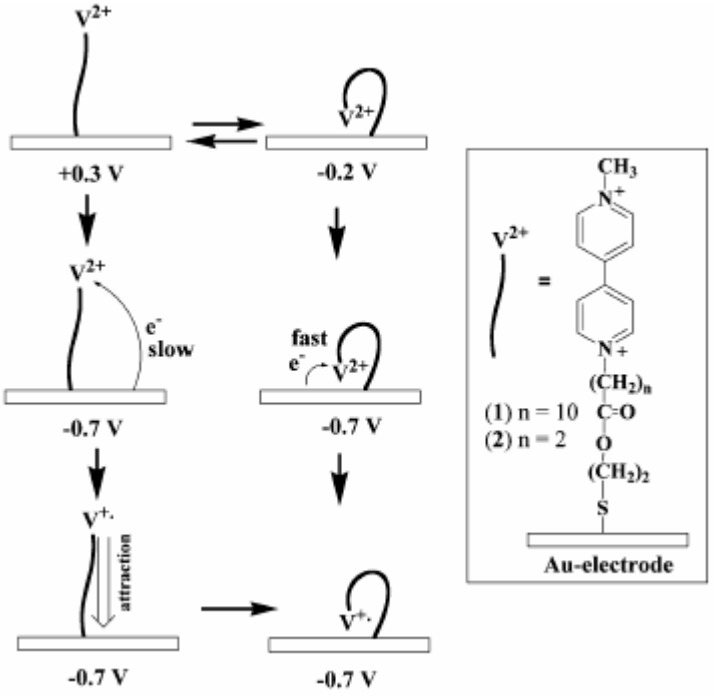

Fig 1. 22 Potential-induced molecular motion and redox-transformation of a bipyridinium monolayer associated with an electrode surface. (Wang, 2003)

Another approach is to release or bind biomolecules from or to the surface. For example, thiol chemistry on gold surfaces can be used for electrochemically bind or release a self-assembled monolayer. Yousaf et al. (Yousaf, 2001) reported the development of an electroactive mask that permits the patterning of two different cell populations to a single substrate. The key element in this method is to be able to turn on selected regions of a substrate. The authors use a self-assembled monolayer (SAM) that presents hydroquinone groups among a background of penta-(ethylene glycol) groups (Fig. 1. 23).

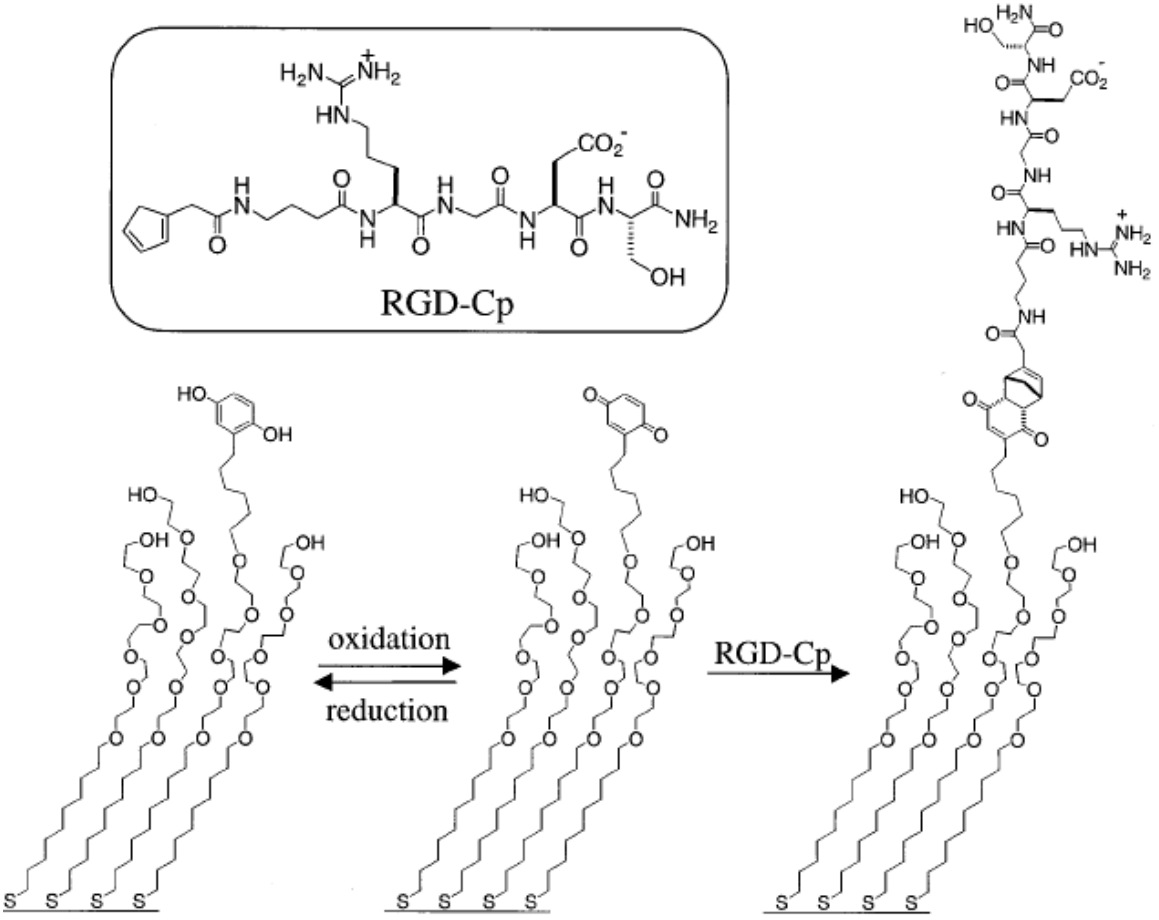

Fig. 1. 23 Molecular strategy for creating substrates that can be electrically switched to permit cell attachment. A monolayer presenting a mixture of hydroquinone groups and penta(ethylene glycol) groups (Left) is converted to a monolayer presenting the corresponding quinone groups (Center) by application of a potential to the underlying gold (500 mV versus Ag/AgCl). Both monolayers are inert to the attachment of cells. Addition of a conjugate of cyclopentadiene and the peptide Gly-Arg-Gly-Asp-Ser-NH2 (RGD-Cp) to the monolayer presenting the quinone group results in the Diels-Alder-mediated immobilization of peptide (Right). 3T3 fibroblasts attach and spread on the resulting surface. Monolayers presenting the hydroquinone group are unaffected by the treatment with RGD-Cp and remain inert to cell attachment (Yousaf, 2001).

The hydroquinone group undergoes oxidation when an electrical potential of 500 mV versus Ag/AgCl is applied to the underlying gold film to give the corresponding benzoquinone. This benzoquinone (but not the hydroquinone) then undergoes a selective and efficient Diels-Alder reaction with cyclopentadiene to form a covalent adduct. They used conjugates of cyclopentadiene and the peptide Gly-Arg-Gly-Asp-Ser-NH2 (RGD-Cp). Because this peptide is a ligand that binds to integrin receptors and mediates cell adhesion, the immobilization of this conjugate gives a surface to which cells can attach efficiently. The penta-(ethylene glycol) groups of the monolayer are critical to this design because they prevent the attachment of cells (they are inert to the nonspecific adsorption of protein) (Yousaf, 2001).

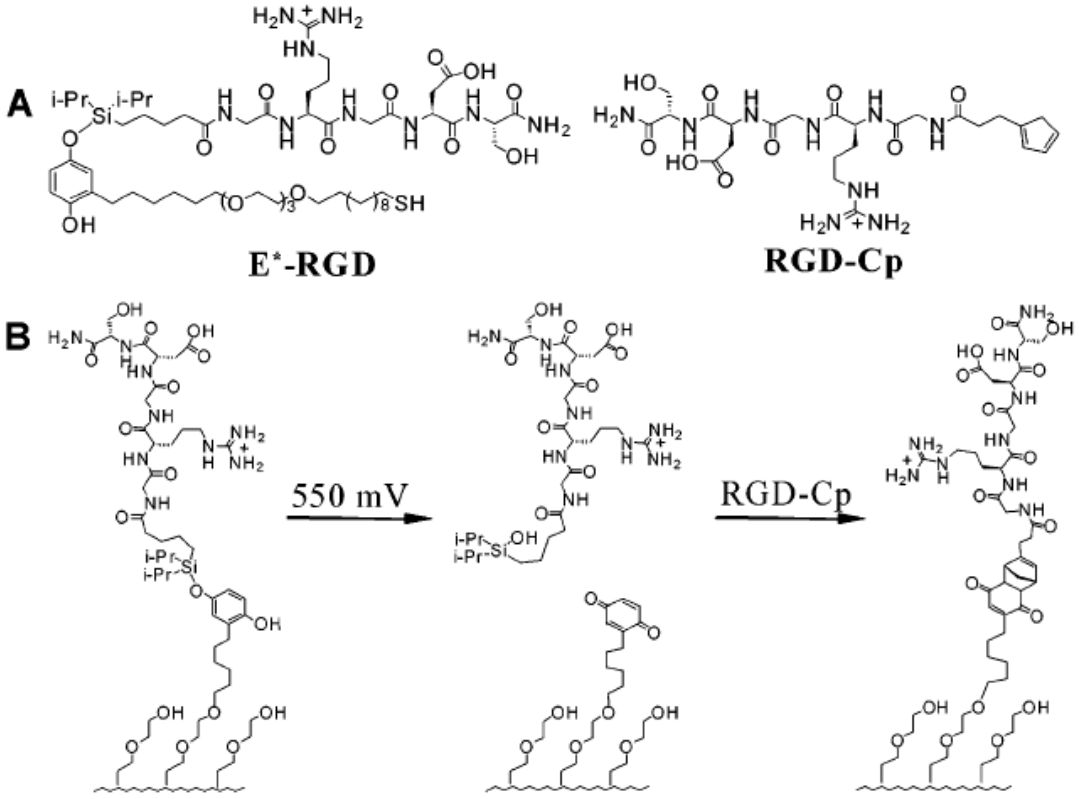

Fig. 1. 24 (A) Structures for the functionalized alkanethiol used to prepare dynamic substrates (E*-RGD) and the cyclopentadiene moiety (RGD-Cp) used to selectively immobilize ligand. (B) A monolayer presenting the *O*-silyl hydroquinone undergoes electrochemical oxidation to give a benzoquinone, with hydrolysis of the silyl ether and selective release of the RGD ligand. The resulting benzoquinone reacts with RGD-Cp by way of a Diels-Alder reaction, which selectively immobilizes the second ligand. The RGD peptide mediates the adhesion of cells (Yeo, 2003).

Yeo et al. (Yeo, 2003) prepared an electroactive self-assembled monolayer presenting an RGD peptide linked to an O-silyl hydroquinone group (E^*-RGD, Fig. 1.24) and allows for selective release of the adhering cells (swiss 3T3 fibroblast).

Applying for 5 minutes an electrical potential (550 mV versus Ag/AgCl) to the substrate oxidized the hydroquinone and released the RGD group, resulting in the detachment of cells attached to the RGD moiety. Subsequent treatment of the surface with diene-tagged RGD peptides (RGD-cp) restores cell adhesion after several hours (Fig. 1. 25).

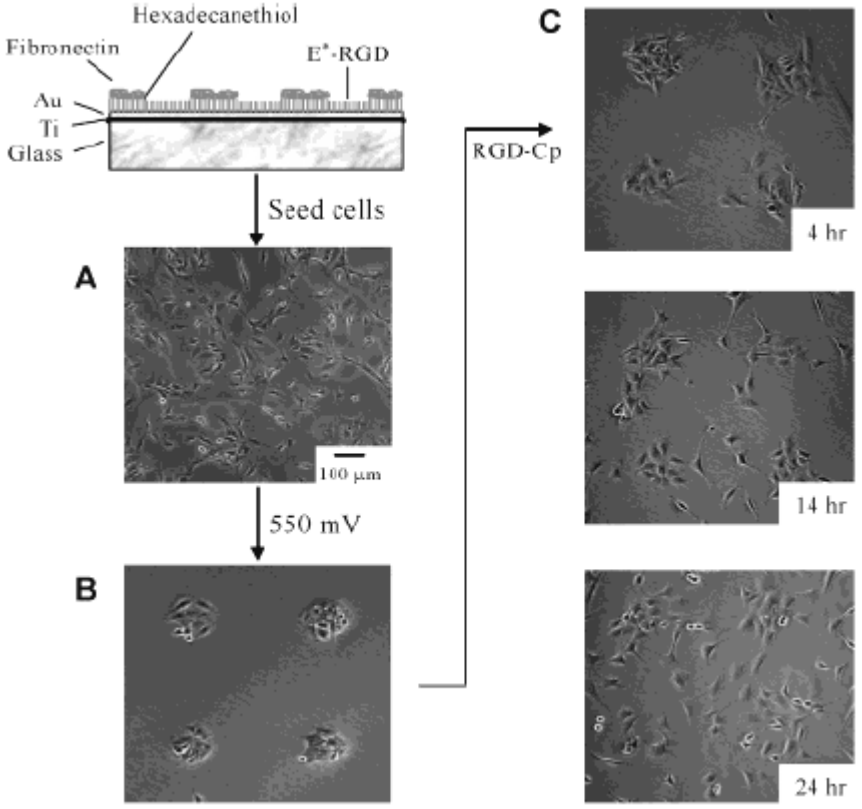

Fig. 1.25 Demonstration of a substrate combining two dynamic properties: (i) the release of RGD ligands and, thus, the release of cells, (ii) the immobilization of RGD ligands and, hence, migration and growth of cells. A monolayer was patterned into circular regions that present fibronectin and surrounded by RGD ligands tethered by way of an electroactive linker (E*-RGD). (A) Swiss 3T3 fibroblast cells adhered and spread evenly over entire substrate. (B) An electrical potential of 550 mV was applied to the substrate for 5 min, and the substrate was incubated for 4 h. Cells were efficiently released only from the E*-RGD regions. (C) Treatment of the monolayer with RGD-Cp resulted in ligand immobilization and initiated cell migration from fibronectin regions onto remaining regions. After 24 h, cells were distributed evenly over the substrate (Yeo, 2003).

Inversely, Tang et al. (Tang, 2006) coated an indium tin oxide microelectrode array with a protein-resistant (poly-lysine)-graft-polyethylene glycol copolymer. Application of a positive electric potential resulted in localized polymer desorption, thanks to the positively charged PLL moiety and freed the ITO surface for subsequent protein binding. It should be noted that this technique is relatively slow, since 24 s are required to fully remove adsorbed molecules from the electrodes. This electrochemical switching is therefore only applicable to cells that spread or move rather slowly.

Mali et al. (Mali, 2006) demonstrated that proteins undergo similar electrochemical transformations: they could be patterned on addressable gold electrodes and selectively released from them.

1.3.2 Influences of electrical field on the cells and cell-size model membrane systems (liposomes)

1.3.2.1 Electrotaxis

There is a long history of the use of electrical stimulation in medicine. For instance, the romans used the discharge from electrical fish to treat a number of pathologies, including gout and sick headache. More recently, we have become aware that many tissues generate their own electrical signals (physiological endogenous electric fields of 42-100 mV/mm (Barker, 1982)) which are present generally in the extracellular spaces, for minutes, hours, even days. It is thought that a host of basic cell behaviours such as cell shape, cell migration, cell division, and cell proliferation may be all controlled by these small electrical signals during normal development (McCaig, 2005). Motile cells could detect gradients in electrical potential and show directional migration (*electrotaxis*) towards the wound centre, when an external (exogen) DC electric field is applied. The applied electric field has strength comparable to the strength of endogenous wound electric fields (Fig. 1.26c). Very short (<200 μs) high voltage stimulations (100-500 V) can also be applied, both methods applying without the occurring of significant electrochemical reactions at the electrodes (Alon, 1987; Franek, 2000).

Following damage in several systems, steady electrical signals re-appear and again seem to regulate a range of coordinated cell activities. In epithelial tissues such as

skin and cornea, there is direct evidence for electrical regulation of the axis of cell division, the rate of cell proliferation and the direction of cell migration (Zhao, 2002a). These events need to be coordinated for successful wound healing to occur. Since there is evidence that these electrical signals may be the earliest to appear at a wound and that they may override coexisting chemical signals (Zhao, 2002b), they could act as a master regulator signal to quick start an integrated array of coordinated cell behaviours (Zhao, 2006, Fig. 1.26a, b).

The mechanisms underlying the generation of these signals and the varying mechanisms by which electrical signals direct nerve guidance and cell (epithelial, cancer, etc.) migration are widely explored. In the case of electronic stimulation of neuronal activity, a displacement current across electrolyte-oxide-semiconductor (EOS) capacitors gives rise to a voltage across the cell membrane that opens ion channels (Fromherz, 2008). How are electric migration cues relayed into cellular responses? Because all cell types and intracellular organelles maintain transmembrane electrical potentials owing to asymmetric ion transport, wounding results in strong and directional ion flow after disruption of epithelial cell layers (Barker, 1982).

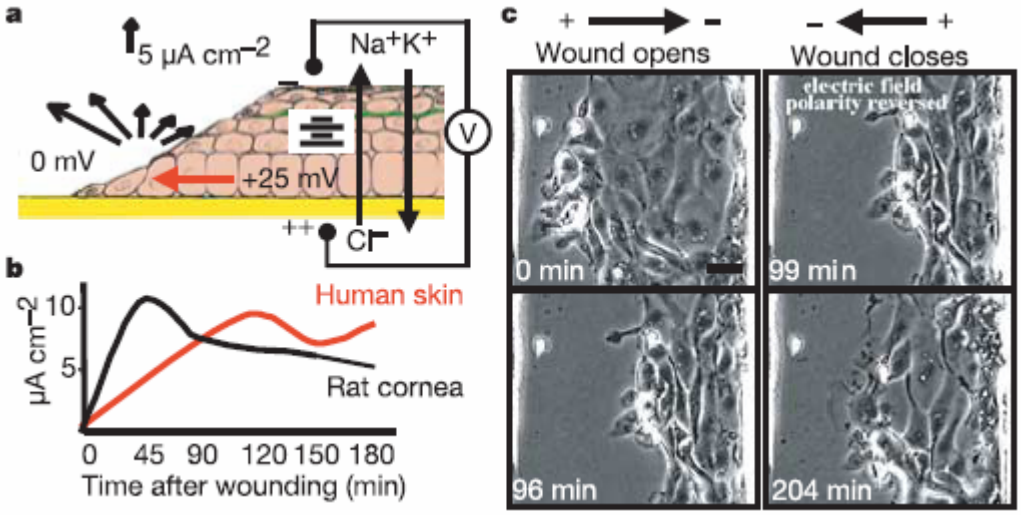

Fig. 1.26 Electrical signals direct cell migration in wound healing and activate selected signalling pathways. a) Wounding induces lateral electric fields directed towards the wound centre (red arrow), by collapsing the local transepithelial potential difference (V). Black arrows represent sizes and directions of currents. b) Directly measured currents increase over time in rat corneal and human skin wounds. c) An electric field (EF) directs migration of corneal epithelial cells in a monolayer model of wound healing (150 mV/mm). Scale bar in c) 20 μm (Zhao, 2006).

To identify possible mediators that couple electric stimuli to intracellular responses, Zhao et al. (Zhao, 2006) tested the role of ion transporters in the electrotactic response. In particular, the Na/H exchanger 1 (NHE1) has been implicated in directional cell migration (Denker, 2002). Testing two different types of NHE1 inhibitors, Zhao et al. found a decrease in the directedness of cell migration in electric fields. These results suggest that directional Na^+/H^+ transport by the NHE1 ion exchanger might relay the electric signal to PI(3)K activation with subsequent directional migration. In addition to Na^+/H^+ exchangers, it is likely that other ion channels such as Cl^- channels are also involved in electrotactic cell migration. Additionally, they found that electric stimulation triggers activation of Src and inositol–phospholipid signalling which polarizes in the direction of cell migration. Notably, genetic disruption of phosphatidylinositol-3-OH kinase-γ (PI(3)Kγ) decreases electric-field-induced signalling and abolishes directed movements of healing epithelium in response to electric signals. Deletion of the tumour suppressor phosphatase and tensin homolog (PTEN) enhances signalling and electrotactic responses. These data identify genes essential for electrical-signal-induced wound healing and show that PI(3)Kγ and PTEN control electrotaxis. Moreover, cathodally directed migration of corneal epithelial cells involved induced asymmetry of membrane lipids and associated EGF receptors, modulation of integrins, membrane surface charge (Rajnicek, 2008) and also asymmetric activation of MAP kinase signaling shown by leading edge asymmetry of dual phosphorylated extracellular signal–regulated kinase (Zhao, 2002a).

D. discoideum shows robust electrotaxis and migrates cathodally in an applied electric field (EF). Electrotaxis of *Dictyostelium* is voltage dependent, directedness increased with increasing field strength (Fig. 1.27) and the threshold voltage inducing directional migration is between 3 and 7 V/cm (300-700 mV/mm) (Zhao, 2002b).

Zhao et al. (Zhao, 2002b) concluded that reception and transduction of the electrotaxis signal are largely independent of G protein–coupled receptor signaling and that the pathways driving chemotaxis and electrotaxis do not use the same signaling elements. However, chemotaxis and electrotaxis intersect downstream of heterotrimeric G proteins to invoke cytoskeletal elements since actin was polymerized at the leading edge of cells during electrotaxis.

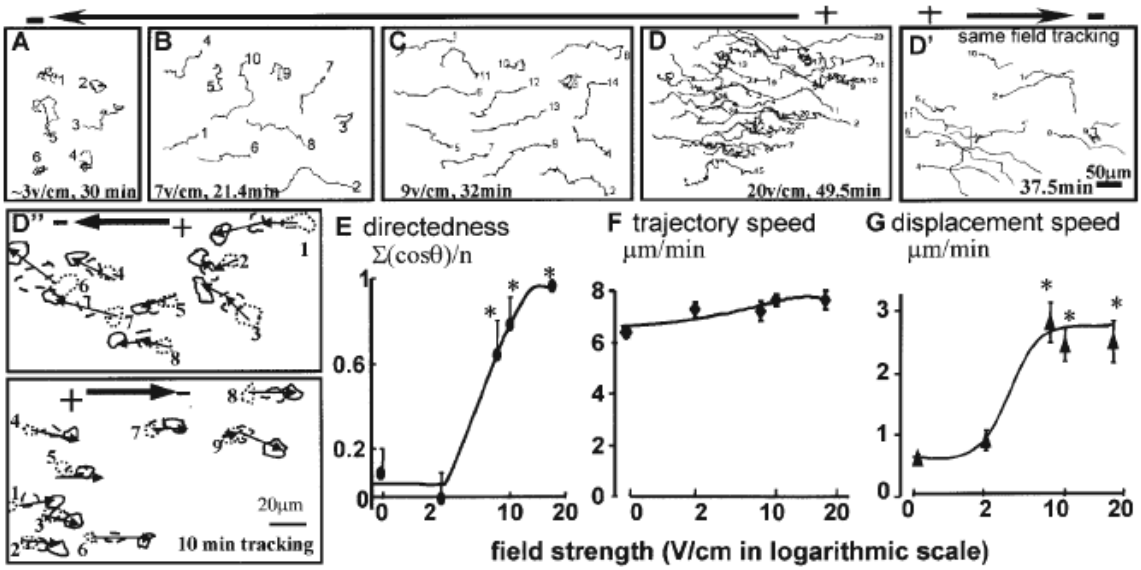

Fig. 1. 27 Wild-type *Dictyostelium* cells migrate cathodally (left) in a direct current (DC) EF as shown by trajectories mapping the cell centers starting from the numbered ends (B, C, and D). Electrotaxis depended on field strength (A–E and G). Reversal of field polarity reversed migration direction (D, D', and D''). D' is the same field tracking of D. D shows cell movements during 10 min field application pointing to the left and 10 min after reversing the field polarity. (E) Voltage dependence of electrotaxis (for directedness). Trajectory speed was similar between no field control and at different voltages (F), but movement in an EF was more persistent in one direction (G) (Zhao, 2002b).

1.3.2.2 Electrical forces (and their effects) for manipulating cells at the microscale

The main electrical forces for manipulating cells at the microscale are electrophoresis (EP) and dielectrophoresis (DEP). Electrophoretic forces arise from the interaction of a cell's charge and an electric field, whereas dielectrophoresis arises from a cell's polarizability. Both forces can be used to create microsystems that separate cell mixtures into its component cell types or act as electrical "handles" to transport cells or place them in specific locations (Voldman, 2006). In addition, two phenomena are able to reversibly modify the cell surface: electroporation and electrodeformation.

Electroporation and electrofusion are electric field–membrane coupled mechanisms (Teissie, 1986) related with EP or DEP, but more violent (usually 600-1600 V/cm for 0.1 ms to 5 ms at 1 Hz or 10-90 KV/cm nanopulses for tens of nanoseconds) (Beebe, 2005; Nuccitelli, 2009). Cell electroporation is routinely used in cell biology for protein, RNA or DNA transfer into the cells and was first described by Neumann almost

three decades ago (Neumann, 1982). Its clinical applications are under development for gene therapy and targeted intracellular drug delivery (especially for drugs with high toxicity), reducing the exposure time, doses of the administrated drug and associated side-effects. Nevertheless, the molecular mechanism supporting the induction of permeabilizing defects in the membrane assemblies remain poorly understood (Teissie, 2005; Kanduser, 2009).

Due to their molecular composition, in uniform or nonuniform fields, the cells and cell-sized vesicles will also experience an electrodeformation force proportional to $|E|^2$, where E is the electric field intensity (Riske, 2006). This force is usually negligible, but can be used intentionally to enhance cell electroporation and electrofusion. Riske and Dimova (Riske, 2005) used fast digital imaging to study the deformation and poration of cell-sized giant vesicles subjected to electric pulses (Fig. 1. 28). They revealed for the first time the dynamics of response and relaxation of the membrane at micron-scale level with a time resolution of 30 μs. Above a critical transmembrane potential the lipid bilayer ruptures and macropores (diameter ~2 μm) with pore lifetime of ~10 ms have been formed. The pore lifetime has been interpreted as interplay between the pore edge tension and the membrane viscosity.

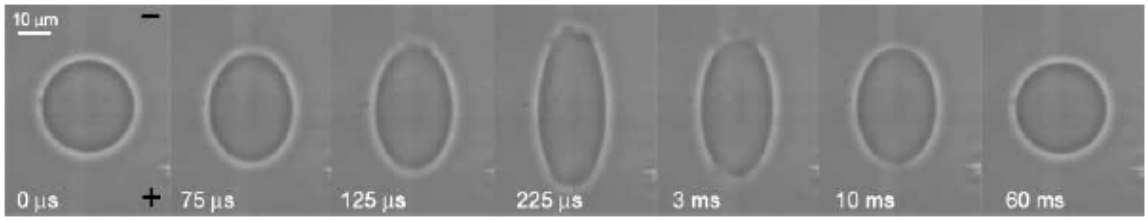

Fig. 1.28 A snapshot sequence of a vesicle subjected to a pulse, E = 2 kV/ cm, t_p = 200 μs. The image acquisition rate was 50 ps. Macropores are first visualized in the third frame (t = 125 μs). The electrode's polarity is indicated with a plus (+) and a minus (-) sign on the first snapshot. (Riske, 2005).

General characteristics of EP and DEP

As we have mentioned above, most cells are covered with negatively charged functional groups at neutral pH (Mehrishi, 2002). Because the cells are charged, they can be acted upon by electric fields. In water, the cells will move at a velocity given by the balance of the Coulomb ($\mathbf{F} = q \cdot \mathbf{E}$, where q is the net charge on the object and E is the applied electric field) and viscous drag forces, a process known as electrophoresis-EP (Figure 1. 29A, left).

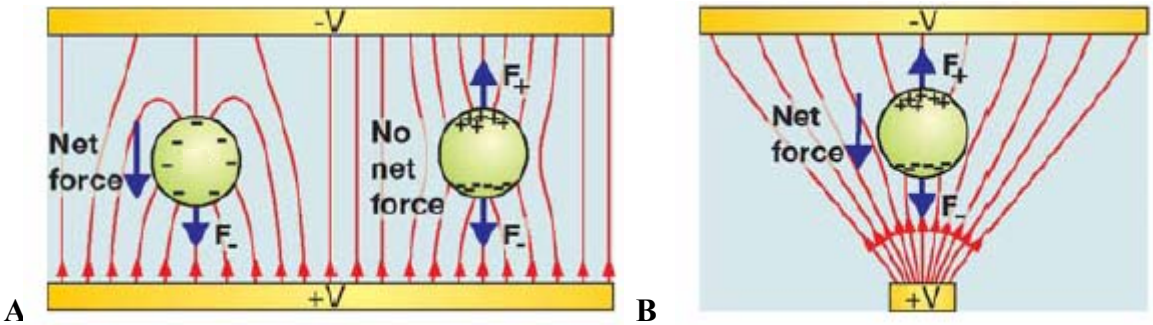

Fig. 1. 29 EP and DEP. **A)**. Charged and neutral particle in a uniform electric field. The charged particle (left) feels an EP force, whereas the dipole induced in the uncharged particle (right) will not result in a net force ($F_- = F_+$). **B)**. A neutral, polarized particle in a non-uniform electric field. The particle will experience a net force toward the electric-field maximum because the field magnitude is different at each end of the particle ($F_- > F_+$).

The electrophoretic mobility (μ) relating electric-field intensity (E) to velocity (v), ($v = E \cdot \mu$) is, to first order, given by $\mu = \varepsilon_m \xi / \eta$, where ε_m is the permittivity of the liquid, η is the liquid viscosity, and ξ is the zeta potential, which is primarily related to the particle's charge density and the ionic strength of the liquid (see Material and Methods). For most biological cells, the EP mobility is ~ 10^{-4} cm^2/Vs, or 1 μm/s in a field of 1 V/cm (Mehrishi, 2002). Any use of EP, therefore, to separate different cell types is therefore dependent on the zeta potential difference between cells.

Dielectrophoresis or DEP (in its simplest form) is due to the interaction of an induced particle's dipole and the spatial gradient of the non-uniform electric field. All particles (charged or not) exhibit dielectrophoretic activity in the presence of electric fields. However, the strength of the force depends strongly on the medium and particle electrical properties (permittivities, conductivities), on the particle shape and size, as well as on the frequency of the electric field. Consequently, fields of a particular frequency can manipulate particles with great selectivity. This has allowed, for example, the separation, the orientation and manipulation of cells (Wang, 1995; Gascoyne, 1997).

To obtain a practical force expression, we need to determine the dipole moment *p*. For cells, the dipole moment is induced by the applied electric field. When cells (and other polarizable particles) are placed in an electric field, a dipole is induced to satisfy the boundary conditions on the electric field. This induced dipole can be created by free charge, by polarization charge (e.g., water), or in general by a combination of the two.

The exact constitution of the dipole will be related to the frequency of the applied field. At low frequencies (down to DC) free-charge dipoles dominate, whereas polarization-charge dipoles dominate at high frequencies. One typically uses AC fields (rather than DC) for DEP because that will damp out EP-induced motion while minimizing physiological impact on the cells and any electrochemical reactions at the electrodes (Voldman, 2006). One general form of its expression is: $\mathbf{F}_{DEP} = \mathbf{p}\nabla\mathbf{E}$, (Washizu, 1992) where p is the particle dipole moment. One sees that the gradient of the electric field ($\nabla\mathbf{E}$) must be nonzero for the force to be nonzero, which can be explained with reference to Fig. 1.29. Here we see that if each half of a dipole sits in the same electric field (Fig. 1.29A, right), then the cell will experience equal opposing forces ($F_- = F_+$) and no net force. If, however, each half of the dipole is in a field of different magnitude ($F_- > F_+$, Fig. 1.29B), then the net force will be nonzero, driving the particle up the field gradient. We also note that if the dipole is not oriented along the field, then a nonzero torque will be created, forming the basis of electrorotation (Washizu, 1992).

In this regard, one finds that the imposed fields can exist within the cell membrane or the cytoplasm. At the frequencies used for electrical manipulation—DC to tens of MHz—the most probable route of interaction between the electric fields and the cell is at the membrane (Tsong, 1992). This is, as we have seen, because electric fields already exist at the cell membrane, generating endogenous transmembrane voltages in the tens of millivolts, and these voltages can affect voltage-sensitive proteins (e.g., voltage-gated ion channels (Catteral, 1995)). The imposed transmembrane voltage, which is added onto the endogenous transmembrane voltage, can be approximated at DC and low frequencies, as $1.5|\mathbf{E}|\mathbf{R}$ (where E is the electric field intensity and R is the radius of the cell). Therefore, at DC a 10 μm cell in a 10 kV/m field will experience a 75 mV imposed transmembrane potential, approximately equal to the endogenous potential (Voldman, 2006). In the context of DEP, some studies have been dedicated to measuring or estimating the induced transmembrane potentials at the cells (Glasser, 1998), but these have been difficult to measure, especially because the intrinsic nonuniformity of the electric field in DEP makes it impossible to assign it a unique value. In most studies, however, researchers have found no measurable effects due to field exposure (Glasser, 1998; Fuhr, 1994; Docoslis, 1999). Thus, DC fields-such as used in EP-will impose the

greatest stress on the cell membrane, whereas use of DEP in conditions under which the transmembrane loads and cell heating are small (KHz-MHz frequencies), is more benign.

1.3.2.3 Cells characterization, separation and handling using EP and DEP

At the microscale, there have been few reports using EP to separate, characterize cells, or for cell handling. This is perhaps due to the fact DC fields could be harmful to certain types of cells, limiting, thus, the fields that one can use. Nevertheless, there are reports that show that one can distinguish subtle phenotypic differences in mammalian cells, such as apoptosis (Guo, 2002) or different bacterial cell types (Armstrong, 1999) using EP. Moreover, the charged cells can move toward an electrode in an EP system. This points to one of the advantages of EP cell handling, which is that one can create electric fields, and thus transport cells, over large distances (up to centimeters). Portinga et al. (Portinga, 2001) described bacterial desorption and adsorption to indium tin oxide (ITO) electrode surface in a parallel plate flow chamber. If a high (≥65 μA) cathodic current was applied by adjusting the potential between -0.4 and -0.5 V, adhering bacteria were stimulated to desorb with desorption probabilities increasing with increasing current density. When a high (1.8 V; 2 mA) positive electrode potential was applied for 5 minutes, bacteria were forced to adhere and then, adhering bacteria could hardly be forced to desorb, indicating strong, irreversible adhesion.

If the field is nonuniform, the particles experience a translational force, known as the dielectrophoretic force (DEP), of a magnitude and polarity dependent on the electrical properties of the particles and their surrounding medium. This force is also a function of the magnitude and frequency of the applied electric field. For a spherical particle of radius R in an imposed electric field E (in V/m) of angular frequency ω, the magnitude of the dielectrophoretic force, F_{DEP} (in N), is given by the expression (Washizu, 1992):

$$F_{DEP} = 2\pi\varepsilon_m R^3 \, \mathrm{Re}\,(K^*)\nabla E^2_{rms} \qquad \text{Eq. 1.8}$$

where K^* is the complex Clausius–Mossotti factor, defined as:

$$K^* = \frac{\varepsilon_p^* - \varepsilon_m^*}{\varepsilon_p^* + 2\varepsilon_m^*} \text{ where } \varepsilon_p^* = \varepsilon_p - j\,\frac{\sigma_p}{\omega} \text{ and } \varepsilon_m^* = \varepsilon_m - j\,\frac{\sigma_m}{\omega} \qquad \text{Eq. 1.9}$$

The Clausius–Mossotti factor provides a measure of the strength of the effective polarization of a spherical particle as a function of particle and medium permittivity (ε) and conductivity (σ). The subscripts *p* and *m* refer to the particle and medium, respectively. Complex quantities are denoted with asterisks. *Re* stands for 'the real part of' the factor. The term ∇E^2_{rms} defines the average local nonuniform field strength and gradient (in V^2/m^3*)*. If the real part of the Clausius–Mossotti factor is positive, the dielectrophoretic force is positive (pDEP). This means that the particle experiences a translational force directed towards regions of high electric field strength, such as the electrode edge. On the other hand, if the Clausius–Mossotti factor is negative, a negative dielectrophoretic force (nDEP) will direct it away from the high-field regions (Florez-Rodriguez, 2004; Huang, 2002; Haddrell, 2006), leading to the particle levitation. In the case of passive levitation, a negative dielectrophoretic force can balance a net gravitational force pointed in the opposite direction (Fig. 1.30). The net gravitational force, F_g, is determined by the difference between the gravitational force on the particle and the buoyancy force (Florez-Rodriguez, 2004).

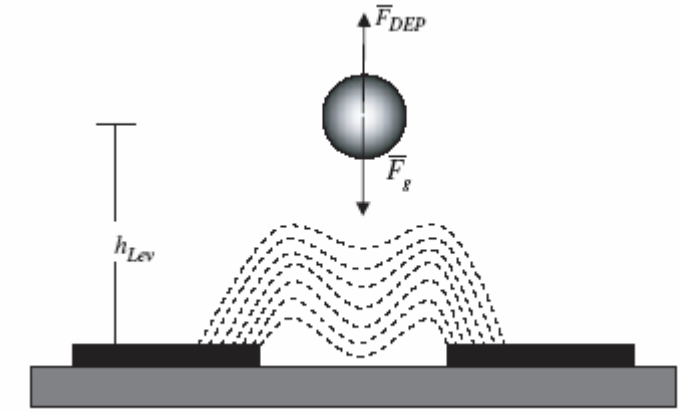

Fig. 1. 30 DEP levitation of particles above microelectrodes. The particles levitate to a height at which the DEP force, F_{DEP}, is equal and opposite to the net gravitational settling force, F_g.

Since both the DEP force and the gravitational force are dependent on R^3, particles with the same dielectric properties and density but different sizes can be expected to levitate to the same height. On the other hand, particles with differing dielectric properties will levitate to different heights in the chamber, irrespective of their size. Levitation has found many applications in particle characterization, separation, manipulation and trapping (Huang, 2002; Oblak, 2007; Vahey, 2008). The use of levitation reduces problems associated with particles adhering to the electrode surface,

steric hindrance and interparticle interactions that occur when the particles are confined to the two-dimensional electrode plane. Also, it prevents exposure to the possibly damagingly high fields and field gradients at the electrode surfaces. To achieve the optimum levitation height or trapping efficacy, it is often desirable to obtain the highest dielectrophoretic force for a given voltage. Experimentally, this is most easily achieved by raising the conductivity of the medium or its permittivity (or both) (Florez-Rodriguez, 2004).

For cells with very different electrical phenotypes, one can find a frequency and solution conductivity where one population of cells experiences pDEP and another nDEP. This allows for an easy separation, where one cell type will be attracted to the electrodes and the other repelled (Markx, 1994) (Fig. 1.31). This approach has been used to characterize, separate or transport live versus dead cells (Li, 2007), different species and cell types from each other (Huang, 2002) and cancer cell lines from dilute whole blood.

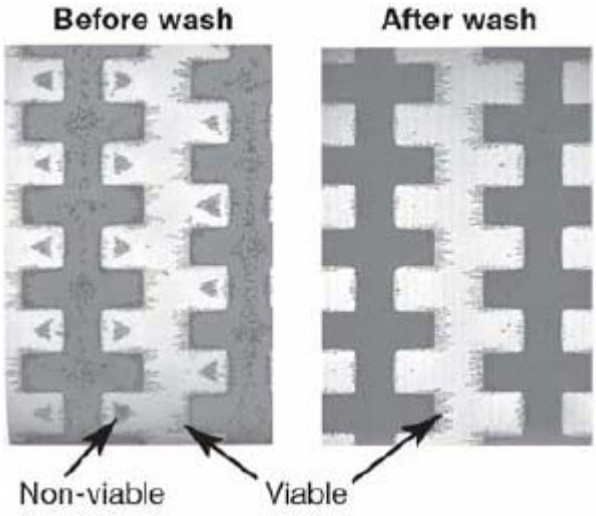

Fig. 1.31 Separation of viable and nonviable yeast. The left panel shows viable (experiencing pDEP) cells collecting on the electrodes and nonviable yeast (experiencing nDEP) collecting in between the electrodes. The nonviable cells can be removed by applying a fluid flow (right).

The primary technique which takes into account the magnitude of DEP, introduced in the late 1990s, is a type of field-flow fractionation-FFF (Vahey, 2008), where a perpendicular force (in this case, the nDEP force) moves cells to different heights in a parabolic flow chamber, where they then experience different drag forces and separate into bands (Fig. 1.32; Yang, 2000). The nDEP forces are balanced by the weight of the cell, resulting in a uniquely defined height.

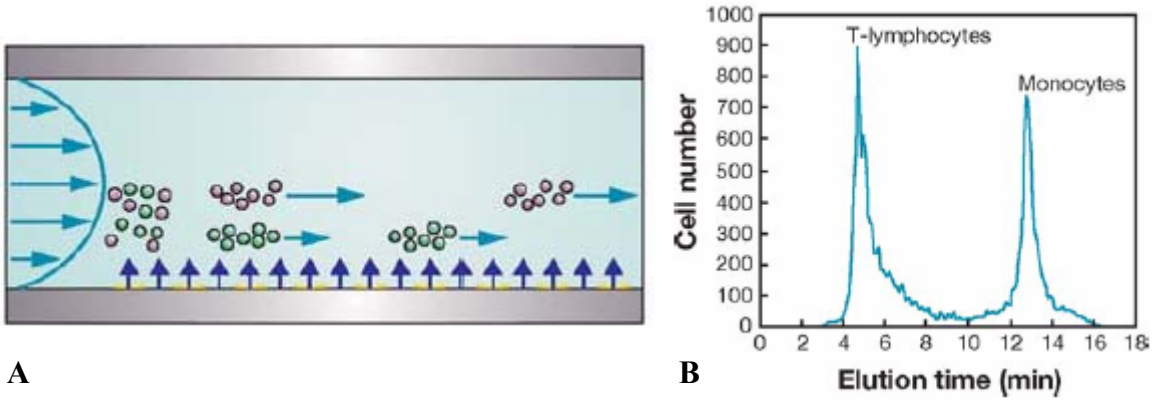

Fig. 1.32 A. Schematic of DEP-FFF (side view), showing that two cell populations, levitated to different heights by a DEP force, separate along the direction of flow in parabolic flow. **B** Separation of a mixture of human T-lymphocytes from monocytes using DEP-FFF. The monocytes are levitated to a lower average height and thus elute later than the T-lymphocytes.

Alternatively, static non-uniform electrical fields can be achieved under a DC electric field by specially designed features, such as obstruction or hurdles using electrically insulating materials. Some interesting applications of DC-DEP for particle separation in microsystems have been reported recently (Kang, 2006; Kang, 2008).

DC-Dielectrophoresis (DC-DEP), the induced motion of the dielectric particles in a spatially non-uniform DC electric field, is applied to separate biological cells by size. The cells experience a nDEP force at the corners of the hurdle where the gradient of local electric-field strength is the strongest. Thus, the moving cells deviate from the streamlines and the degree of deviation is dependent on the cell size. Kang et al. (Kang, 2008) demonstrated by using this method that, combined with the electroosmotic flow, mixed biological cells of a few to tens of micrometers difference in diameter can be continuously separated into different collecting wells (Fig. 1.33).

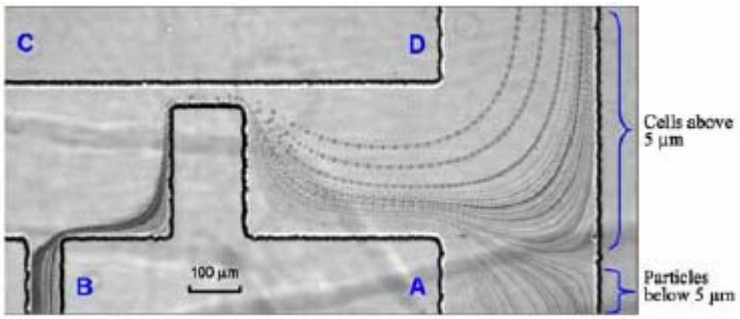

Fig. 1.33 Separation of the white blood cells: 5 µm threshold separation, V_A=102 V, V_B=191 V, V_C=343 V, V_D=0 V

For separating target cells of a specific size, all that is required is to adjust the voltage outputs of the electrodes.

DEP has been used extensively to handle cells, both for positioning and for transporting cells. Cell positioning typically uses stationary traps that may be turned ON or OFF in time. It is used either to create long term (more than several hours) patterns of cells on a substrate or for short term (minutes to hour) observation of cells in specific locations. Both pDEP and nDEP and many different geometries can be used for these purposes. In general, pDEP traps are easier to create than nDEP traps because it is easier to hold onto a particle by attracting it than repelling it. For example, Taff et al. (Taff, 2005) used the ring-dot geometry consisting of an outer ring electrode and an inner round "dot" electrode on a separate metal layer (Fig. 1. 34).

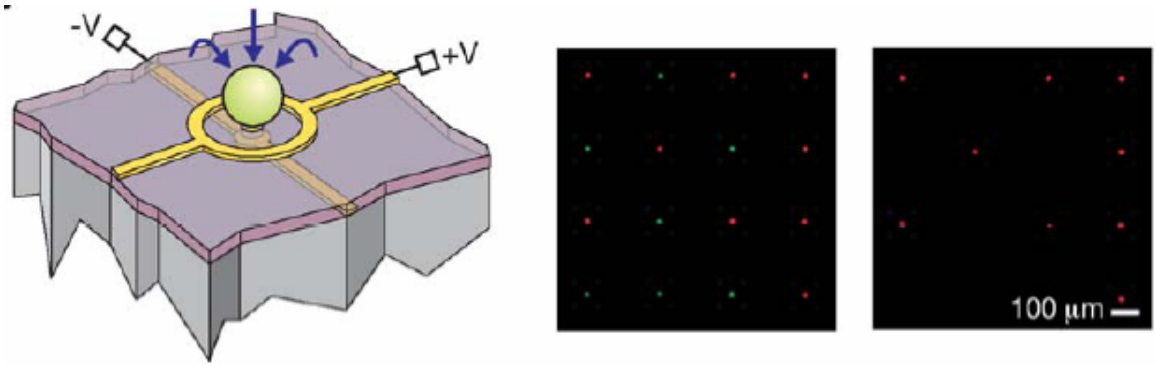

Fig. 1.34 Schematic (left) of ring-dot geometry, along with two images (right) showing addressable removal of green-labeled human HL-60 cells from a 4×4 trap array.

Cells are attracted via pDEP to the field maximum at the dot. Using this geometry they developed a scalable addressable trapping array for observing many single cells and then sorting out desired cells.

Electrical approaches to manipulating cells at the microscale have already shown great promise. This is primarily due to the favorable scaling of electrical forces with system size and the ease of fabricating microscale electrodes. Looking ahead, an upcoming goal for EP and DEP-based separations will be the demonstration of systems with specificity sufficient to enable separation of a few cells. Luckily, engineers continue to innovate in both DEP and EP separation and handling. It is however not possible to control thousands of cells simultaneously.

1.4 Objectives

In order to synchronize the onset of cell-surface spreading, we first investigated the possibility to modulate electrostatic repulsion between cells and a glass surface to control the formation of an initial cell-substrate contact.

We studied the formation of cell-surface contact as a function of ionic strength, then we show that it is possible to synchronize cell spreading either by changing the ion concentration around the cells or by electrochemical means.

We show in subchapter 3.1 that *Dictyostelium* cells spread using a periodic protrusion activity. Moreover, the actin polymerization activity, which drives membrane protrusions, is also oscillatory with almost the same period.

In the next subchapter, we will analyze the effect of an applied potential on the cells that are deposited on a conductive material. Using different conductive materials (ITO, Ti, Pt and Au) we tried to detach the adhering cells in 17 mM and 1.7 mM buffer solutions or to impair their contact with the surface by imposing a negative potential (current) at the material surface while they are sedimenting. Even the highest supportable potentials of materials and cells, did not allow to reach our aims.

In order to synchronize cell spreading, a new approach was taken into consideration and analyzed in the subchapter 3.3: to keep the living cells in suspension at a certain distance from the surface, despite the apparent gravity, using electrostatic properties of the cells and surfaces when we vary the ionic strength. Thus, by decreasing the ionic strength we can prevent cell adhesion using electrostatic repelling forces. We also use $LimE^{\Delta coil}$-GFP to monitor actin polymerisation activity. These experiments reveal that fluctuating actin polymerization occurs even in the absence of cell spreading.

In the last two subchapters, we analyze two different methods of adherence stimulation: using an experimental diffusion setup (subchapter 3.4) and an electrochemical method (subchapter 3.5).

Since *D. discoideum* adhesion is sensitive to ionic strength, we envisioned controlling this parameter in order to synchronize cell-surface contact. In subchapter 3.4 we show that by increasing the ionic strength we could induce cell adhesion and spreading. However, major drawbacks of this method are the unphysiological conditions

characterized by a high osmotic pressure reached in the chamber where the cells were levitating before concentrated solution diffused.

Using LimE$^{\Delta coil}$-GFP to monitor actin polymerisation activity, we finally show in subchapter 3.5 that synchronized cell spreading can be induced by a short electrical pulse (0.1 s) triggering a transient surface contact. As a consequence, the pulse-induced contact with the surface, triggers regular quasi-periodic actin polymerization, that is in phase in all the cells.

Chapter II. Materials and methods

2.1 Materials

2.1.1 Buffers and chemicals

Sörensen Buffer (SB) containing 2 mM Na_2HPO_4 (analytical grade) and 14.68 mM KH_2PO_4 (analytical grade) at pH 6.13 was used as a reference medium for the experiments. The theoretical osmolarity of this buffer is 36 mOsm and was experimentally measured with a Löser cryoscopy osmometer. The value of 34±3 mOsm was obtained.

Lowering buffer concentration was compensated for by adding osmotically equivalent amounts of D(+) sucrose. Solutions at a lower ionic concentration (phosphate sucrose buffers) were thus obtained by mixing appropriate volumes of SB and a 36 mM sucrose solution. Isotonic $CaCl_2$ solutions were prepared in the same way, using sucrose to maintain osmotic pressure.

Potassium hexacyanoferrate ($K_3Fe(CN)_6$), potassium nitrate, ferric chloride, anhydrous calcium chloride, hexahydrated magnesium chloride, sodium chloride, potassium chloride, cesium chloride, lithium perchlorate ($LiClO_4$), MES (2-(N-morpholino) ethanesulfonic acid, pKa = 6.09) and HEPES (4-(2 hydroxyetyl)-1-piperazineethane sulfonic acid, pKa = 7.67) and cysteine were analytical grade. The conductivity of hygroscopic ionic salt solutions was measured to ascertain their concentration. Aminopropyltriethoxysilane (APTES) and Latrunculin A were from SIGMA-ALDRICH (Saint Quentin Fallavier, France).

The solution conductivities were measured with an Analytical Radiometer, CDM 210, MeterLab apparatus.

2.1.2 *D. discoideum* culture and handling

D. discoideum AX2 cells were grown in agitated suspensions (180 rpm) in HL5 medium (FORMEDIUM, Norfolk, UK): peptone 14.3 $g.L^{-1}$, yeast extract 7.15 $g.L^{-1}$, maltose 18 $g.L^{-1}$, $Na_2HPO_4,12H_2O$ 1.28 $g.L^{-1}$, KH_2PO_4 0.48 $g.L^{-1}$, dihydrostreptomycin

sulfate 0.25 g.L^{-1}) at pH = 6. AX2 cells expressing a $LimE^{\Delta coil}$-GFP fusion protein (vector B12) (Diez, 2005) were grown in axenic medium supplemented with 20 µg/mL G418 (Sigma) in shaking suspensions. The plasmid was kindly provided by G. Gerisch.

D. discoideum cells were recovered by centrifugation (EPPENDORF 5415R, Hamburg, Germany) at 1000 x g, for 3 min at 4°C, washed once in SB and resuspended at 10^6 cells.mL^{-1} in diluted buffer before use.

When used, latrunculin A was added in the culture medium at 3 µM for 5 min before centrifugation and washes. Cells were used immediately after the treatment.

The zeta potential of *D. discoideum* cells and of surface-carboxylated fluorescent polystyrene beads (diameter 1 µm) was measured using a ZETASIZER 1000 (Malvern Instruments, Malvern, UK) and was found to be - 17±3 mV and -56±5mV in SB respectively.

2.1.3 Preparation of surfaces

Borosilicate glass cover slips for microscopy were used after cleaning with ionic detergent, rinsing with ethanol and deionized water.

Gold and platinum surfaces were obtained by vacuum deposition of 5 nm titanium on borosilicate glass and then 3 nm of gold or platinum, respectively.

Silanization of glass cover slips was performed as follows:

- Cleaning with ionic detergent, rinsing with ethanol and deionized water.
- Immersing in 14.5 M NaOH for 5 min and washing with deionized water.
- Immersing in a 1% APTES solution in 5 mM acetic acid for 20 minutes under agitation and washing with deionized water.
- Curing at 100°C for 15 minutes.

Silanized glass cover slips stored for some time in contact with air were decarbonated by a 0.1 M KOH solution.

2.1.4 Experimental chambers

Plastic frame that constitutes the chamber of a Labtek (Nalge Nunc Int. US) (volume = 0.7 cm^3, surface = 0.5 cm^2) were used to construct experimental chambers on different substrates (single-chamber setup). For diffusion experiments, a double chamber

setup was built, consisting of a thin lower chamber separated from the upper chamber by a polycarbonate membrane (MILLIPORE TMTP01300, Molsheim, France) 20 microns thick and 5 microns pore diameter, 10% porosity (see fig. 2.1A and B). The height of the lower chamber, *e*, was built using several layers of double adhesive tape (260 microns thick PVC ribbon covered with polyacrylic glue, 3M; e = 260n, where *n* is the number of double adhesive tape layers), cut out at the required dimensions.

These experimental setups are schematized in Fig. 2.2.

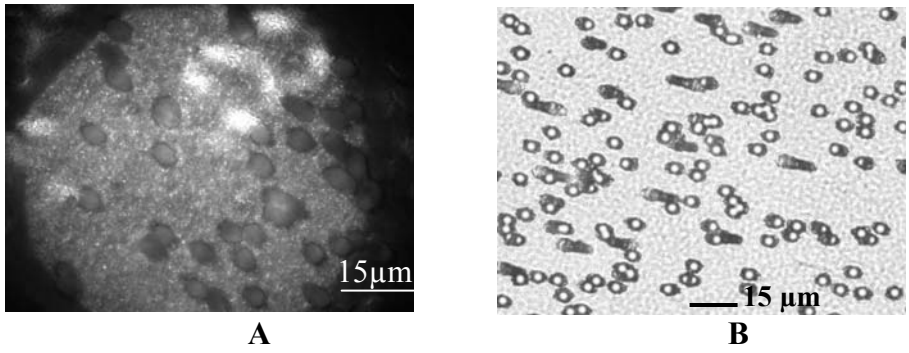

Fig. 2.1 Polycarbonate membrane images (**A**) RICM and (**B**) Phase Contrast. The 5-micron holes of the membrane can be seen.

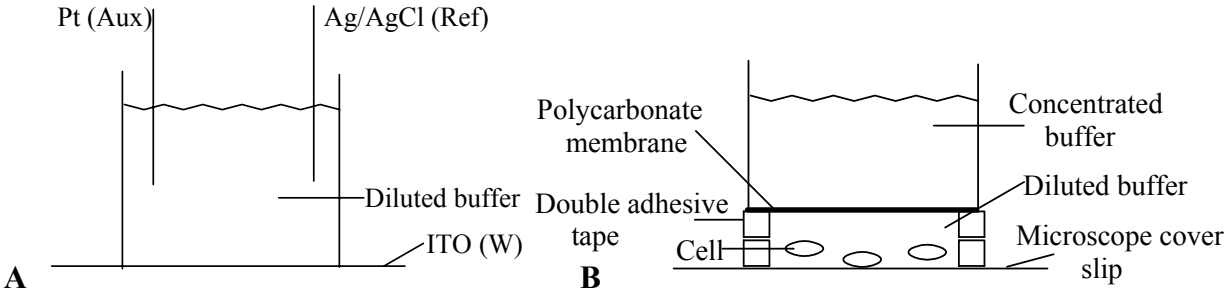

Fig. 2.2 (**A**) Single chamber and (**B**) double chamber setups. In (**A**) a three electrode experimental setup is shown: the platinum wire was the counter electrode (Aux), the ITO coated surface was used as the working one (W) and the reference was a Ag/AgCl pseudoelectrode (Ref.).

2.1.5 Electrochemical experiments

Transparent conducting surfaces were thin glass slides (0.145 and 0.175 mm thick) covered by Indium Tin Oxide (ITO, thickness 80 nm, resistance 20 ohms.cm) from PGO (Präzisions Glas & Optik Gmbh, Iserlohn, Germany). ITO belongs to the class of

transparent conductive materials with interesting optical and electrical proprieties (Laux, 1998).

For electrochemical experiments on gold or ITO coated surfaces, platinum and silver wires were attached in the upper chamber. The latter one was previously immersed in a ferric chloride aqueous solution, and used as a pseudo-reference electrode of Ag/AgCl type and named *Ref.* in the following. The platinum wire was the counter electrode and the ITO coated surface was used as the working one. We used a potentiostat (RADIOMETER DEA 332 Digital Electrochemical Analyzer controlled by VOLTALAB software, Villeurbanne, France) to carry out chronoamperometric and voltamperometric experiments.

In order to calibrate the electrochemical response of the ITO electrode with respect to local hexacyanoferrate concentrations, a 0.0 V/Ref. potential pulse (0.5 s) was applied, using the single chamber setup and the current response was measured as a function of known hexacyanoferrate concentrations.

In order to monitor the ionic diffusion kinetics in a double chamber setup, the lower chamber was first filled by a 0.5 M KNO_3 solution. 17 mM potassium hexacyanoferrate in 0.5 M KNO_3 was poured over the membrane. The concentration ratio between KNO_3 and $Fe(CN)_6^{3-}$ was 30 to avoid ionic migration of the hexacyanoferrate. At given times, a 0.0 V/Ref. potential pulse was applied for 0.5 s to the 50 nm gold surface and the current responses recorded to estimate the corresponding hexacyanoferrate concentration at the gold surface, using the calibration curve.

The diffusion coefficient, *D*, of $Fe(CN)_6^{3-}$ was determined by chronoamperometry (10 s) on a Pt flat disk surface using the Cottrell equation (Bard, 1980):

$$I(t) = nFSC_0 D^{0.5} (\pi t)^{-0.5} \qquad \text{Eq. 2.1}$$

where *n* is the number of exchanged electrons by the redox group (in this case n = 1), *F* the Faraday constant, *S* the Pt surface area and C_0 the initial concentration of $K_3Fe(CN)_6$. By plotting *I* as a function of $t^{-0.5}$, we obtained a diffusion coefficient comprised between 0.9 and 1.05 10^{-5} cm^2 s^{-1} for $Fe(CN)_6^{3-}$ which corresponds to published value (Robinson, 1970).

Electrochemically induced cell adhesion was carried out in a one-chamber setup (Fig. 2.2A) fitted with the reference and counter electrodes using an ITO-coated surface as working electrode. Cells were introduced in 0.17 mM phosphate sucrose buffer. After sedimentation, a potential pulse was applied for a certain time. In the case when we applied 2.5 V/Ref. for 2 s, the integrated electrical charge was 0.1 mC, corresponding to the production of 1 nmole of protons (according to Faraday's law), if all the current corresponds to water oxidation.

Potential pulses were generated with a TTi 10 MHz pulse generator (THURBLY THANDAR INSTRUMENTS, Huntington, UK) using a square-shaped 5 V pulse for given pulse durations. This voltage was applied between the ITO surface and the platinum counter electrode and is equal to the measured voltage between the working electrode and the counter electrode in the three-electrode setup.

2.1.6 Mathematical simulation of ion diffusion in the double chamber setup

In order to compare the experimental evolution of concentration at the surface in the double chamber setup (Fig. 2.2B) with a rather simple mass transport description, we solved Fick's second law considering planar diffusion (Equation 2.2). MATLAB (The Math Works, Natick, MA) software was used to numerically solve equation 2.2 for D = 10^{-5} cm^2 s^{-1} and e = 520 μm, considering a constant 17 mM concentration at the top of the lower chamber (the upper chamber can be considered as an infinite reservoir) and no flux condition at the glass surface.

$$\frac{\partial C(x,t)}{\partial t} = D\frac{\partial^2 C(x,t)}{\partial x^2} \qquad \text{Eq. 2.2}$$

with the boundary conditions: C(0, t) = 17 mM and $\left.\frac{\partial C(x,t)}{\partial x}\right|_{x=e} = 0$

The formula for the calculation of the diffusion coefficient for strong electrolytes (D_s), for example $A_{\nu_1}^{z_1} B_{\nu_2}^{z_2}$, is given by the well known Nernst relation (Robert, C. W., 1987):

$$D_s = \frac{RT}{F^2} \cdot \frac{(\nu_1 + \nu_2) \cdot (\lambda_1^0 \cdot \lambda_2^0)}{\nu_1 \cdot z_1 \cdot (\lambda_1^0 + \lambda_2^0)} = 2.66 \cdot 10^{-7} \cdot \frac{(\nu_1 + \nu_2) \cdot (\lambda_1^0 \cdot \lambda_2^0)}{\nu_1 \cdot z_1 \cdot (\lambda_1^0 + \lambda_2^0)} \text{ at T = 298 K; Eq. 2.3}$$

One denotes z_i and ν_i the ionic charge and its coefficient, respectively; λ_i^0 (in $cm^2 \cdot S/mol$) is the equivalent ionic conductivity at infinite dilution at 298 K.

For example, $D_{CaCl_2} = 1.33 \cdot 10^{-5} cm^2/s$, $D_{KH_2PO_4} = 1.21 \cdot 10^{-5} cm^2/s$

The diffusion coefficient of a single ion can be calculated regardless of the counter ion:

$$D_{ion} = \frac{RT}{F^2} \cdot \frac{\lambda^0}{z} = 2.66 \cdot 10^{-7} \cdot \frac{\lambda^0}{z} \qquad D_{Fe(CN)_6^{3-}} = 0.98 \cdot 10^{-5} cm^2/s \qquad \text{Eq. 2.4}$$

This value is in perfect agreement with the experimental value (see Materials and Methods) and with the literature (Bernard M., 1996).

For a mixture of salts, it is very difficult to calculate the average diffusion coefficient. For simplicity, the main contribution is attributed to the predominant salt, even though, in reality, there is a pair wise redistribution of negative and positive ions among the diffusing salts. In SB (Sörensen buffer or phosphate buffer), KH_2PO_4 is the predominant salt (14.68 mM).

2.1.7 Mathematical simulation of the pH in solution at the conductive surface

Concentration of the protons formed during an electrical pulse application is calculated using Comsol Multiphysics Modeling and Simulation software (EULA, COMSOL AB). Comsol is a finite element analysis and solver software package for various physics and engineering applications, especially coupled phenomena or multiphysics. The Chemical Engineering Module incorporates application models for the field of transport phenomena including ionic transport and multi component diffusion. The proton concentration in the ITO surface vicinity (the experimental setup is shown in Fig. 2.2A) is calculated, taking into account water electrolysis (the intensity of the current, the pulse application time) and, in the same time, its diffusion (the proton diffusion coefficient is $D_{H+} = 10^{-4}$ cm^2 s^{-1}) (Eq. 2.5). The proton migration is not considered, since the electrolyte concentration is higher than the proton concentration. Thus, we considered that the major contribution to the migration transport derives from electrolyte ions.

When the proton production is stopped, one considers only its diffusion in the bulk solution, increasing the pH close to the surface.

$$\frac{\partial C_{H+}(x,t)}{\partial t} = D_{H+}\frac{\partial^2 C_{H+}(x,t)}{\partial x^2} \text{ and } C_{H+}(0,t_s) = \frac{I \cdot t_s}{F \cdot S \cdot \Delta x} \qquad \text{Eq.2.5}$$

with boundary condition: $C_{H+}(\infty, t) = 0$. Where *F* is the Faraday constant, *S* the ITO surface area, *I* is the applied or measured intensity, t_s is the time of current application.

For an intensity of $4*10^{-5}$ A applied during 50 s, the concentration profile versus time is:

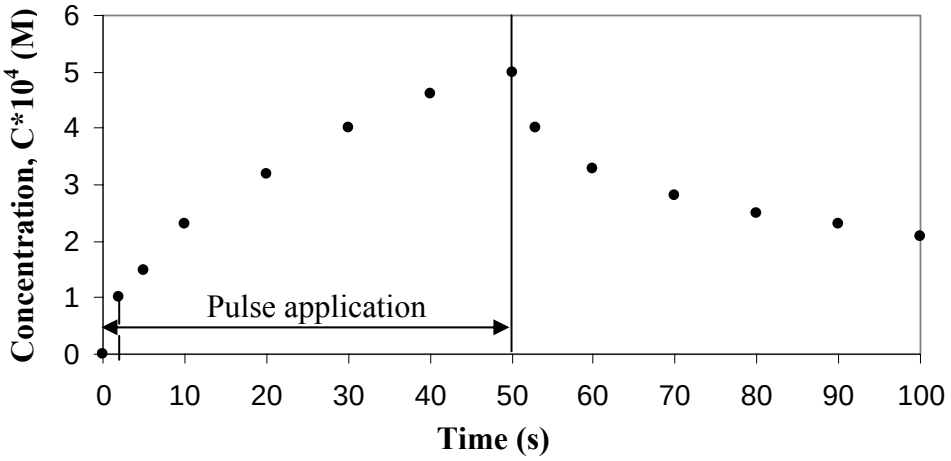

Fig 2.3 Theoretical proton concentration profile at the surface during and after a 50 s pulse

After applying the same current for 2 s, the pH is decreasing to 4 (see Fig. 2.3). For shorter current pulse, the pH increase is almost linear with the pulse duration. For a longer time application, the cell activity could be affected. In addition, the surface acidification was confirmed with a pH-sensitive dye.

2.1.8 Optical observation of cell spreading

To monitor the presence and spreading of *D. discoideum* cells, we used an inverted microscope (OLYMPUS IX71, Rungis, France, Fig. 2.4A) illuminated with a halogen lamp (transmitted light) and a mercury lamp (reflected light). Cells were imaged with an oil-immersed objective (60X magnification, 1.25 numerical aperture) by phase contrast (PC) and Reflection Interference Contrast Microscopy (RICM). For RICM, a green filter selected the 546 nm Hg emission peak and a semi-reflecting plate was set at

45° of the optical axis to illuminate the sample. Still images and movies (15 frames per s) were acquired by means of an Olympus DP30 CCD camera (Photonic Science, UK). For a better presentation in this thesis, some images were treated by transposing individual cells on a more clear background.

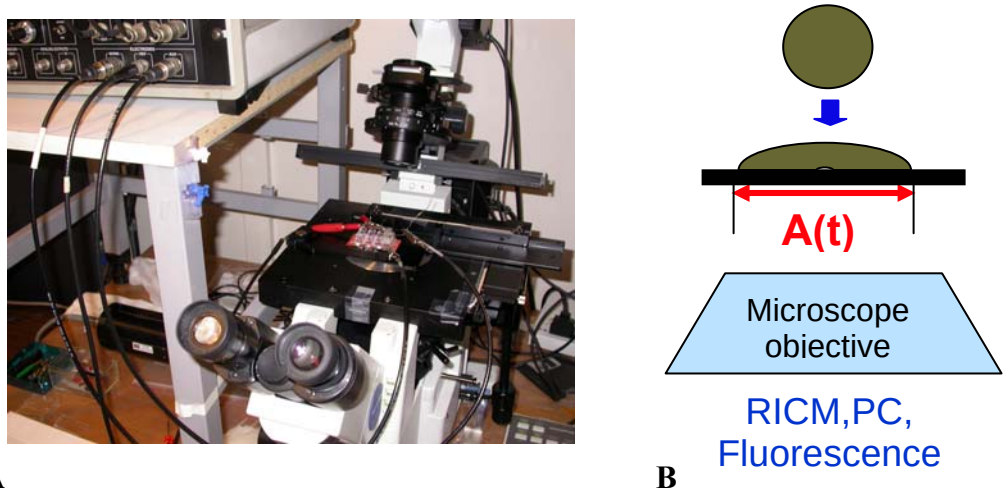

A **B**

Fig. 2.4 (**A**) photo in the laboratory of the experimental setup and (**B**) an explicative scheme for the observation of cell spreading by RICM, Phase Contrast (PC) or fluorescence.

RICM allows the analysis of living as well as fixed cells attached to a plain surface using reflection-type microscopes. The resulting image is determined by the relative reflectivity (RI) at different areas of the cell, and by interferences of the light reflected at different boundaries (Fig. 2.5, Bereiter-Han, 1979).

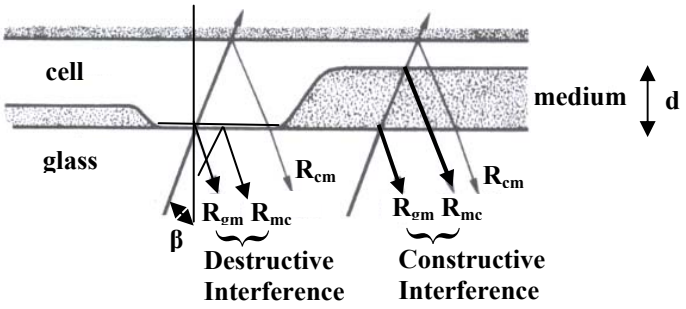

Fig 2.5 Schematic representation of the main reflecting interfaces in a cell preparation on a glass surface. The black arrows indicate the incident light beams and the reflected light beams with the relative intensity **R**. Suffixes indicate the optical media forming the interface (g, glass; c, cell; m, medium). The phase of $\mathbf{R_{gm}}$ is shifted for λ/2 at the reflecting surface. $\mathbf{R_{cm}}$ is normally not visible in thick cells. *β* is the angle of incidence of the illuminating beam and *d* stands for the geometrical distance between cell membrane and glass surface.

RICM is used to view cells in culture adhering to a plane glass surface. Extremely thin layers of protein or cytoplasm can be detected on a glass surface. Assuming that the

cytoplasm is optically homogeneous, three optical interfaces may occur (Fig. 2.5): glass/culture medium (gm), medium/cell (mc) or cell/medium (cm) (two thin layers on top of the glass). For Dictyostelium discoideum, which is a thick cell (average of 10 μm in diameter), R_{cm} is insignificant.

Light beams reflected from the various interfaces interfere with each other. The resulting intensities depend on the differences in optical path lengths (Δ) and RI at the boundaries. The optical path difference (Δ) between two reflected wave fronts is related to the geometrical distance (d), the refractive index (n) and the angle of incidence of the illuminating beam (for normal incidence, β = 0 and cosβ = 1) by the following equation:

$$\Delta = 2nd / \cos\beta \qquad \text{Eq. 2.6}$$

In the case of light reflection at an optically denser medium, the interference of the reflected light beams can occur. The calculated value of the intensity of the interfered light beam ($I_{interference}$) corresponds to the product of the amplitude ($E_{interference}$ or E) and its conjugated complex value ($E^*_{interference}$). Considering only two reflected wave fronts (R_{gm} and R_{mc}) one obtains:

$$E_{interfernce} = E_{gm} + E_{mc} = \sqrt{I_0} R_{gm} e^{i\frac{\lambda}{2}} + \sqrt{I_0} R_{mc} e^{i\Delta}, \qquad \text{Eq. 2.7}$$

where I_0 is the intensity of the incident light beam. The phase of R_{gm} is shifted for $\lambda/2$ at the reflecting glass surface.

$$I_{int\,erference} = E \cdot E^* = I_0[R_{gm}^2 + R_{mc}^2 + 2R_{gm}R_{mc}\cos(\Delta - \frac{\lambda}{2})] \qquad \text{Eq. 2.8}$$

It results that one obtains a maximum intensity, relative to the incident light intensity (constructive interference), if:

$$\cos(\Delta - \frac{\lambda}{2}) = \cos(\frac{2nd}{\cos\beta} - \frac{\lambda}{2}) = 1 \quad \Leftrightarrow \quad \frac{2nd}{\cos\beta} - \frac{\lambda}{2} = 2p\pi \cdot \frac{\lambda}{2\pi}$$
$$\Rightarrow \quad d = \frac{\lambda}{4} \cdot \frac{(2p+1)\cdot\cos\beta}{n} \qquad \text{Eq.2.9}$$

where $p \in N$.

When $\cos(\Delta - \frac{\lambda}{2}) = -1$ (destructive interference), it results:

$$d = \frac{\lambda}{4} \cdot \frac{(2p)\cos\beta}{n} \qquad \text{Eq.2.10}$$

In our experiments wavelength of the incident beam light is λ = 546 nm, the medium refractive index is considered n = 1.33 and the angle of incidence, β, is very close to 0 degrees. Regarding the equations 2.9 and 2.10, we obtain first maximum interference intensity (constructive interference) for $d \approx 100$ nm and the first minimum interference intensity (destructive interference) for $d = 0$ (putting $p = 0$).

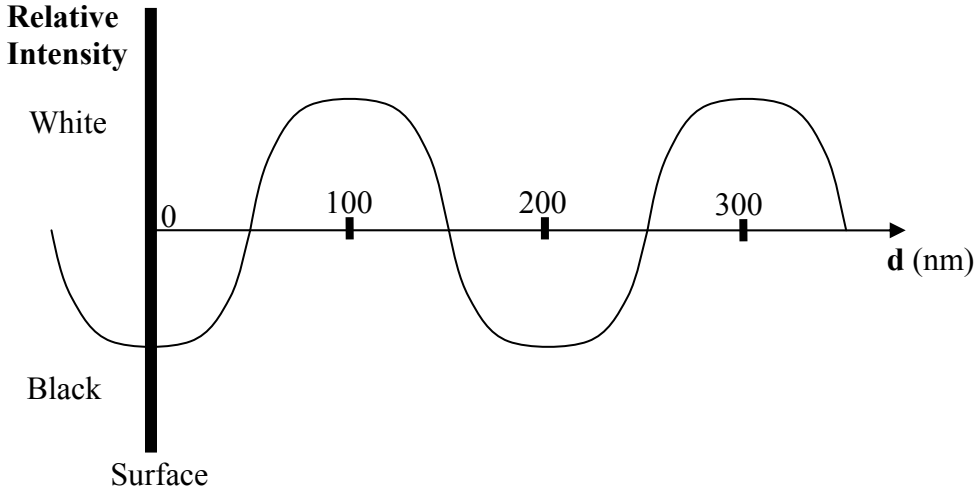

Fig 2.6 Schematic representation of interference contrast intensity relative to the background versus the geometrical distance between cell membrane and surface (d).

Thus, in areas where the cells are intimately attached with the glass, we can distinguish zones of close contact of the cells to the glass, which appear dark gray. Additionally, focal contacts are almost black (destructive interference, d = 0). The bright or white zones correspond to a maximum interference intensity (constructive interference, $d \approx 100 \cdot (2p+1)$ nm) (Fig. 2.6). Similar maximum interference intensities were obtained when transparent surfaces were thin glass slides (0.145 and 0.175 mm thick) covered by Indium Tin Oxide (ITO, thickness 80 nm).

Also, for a thin cell, at an angle of incidence of 30 degrees and with orange light (λ = 589 nm), cytoplasm with a refractive index of 1.4, a geometrical difference d of 100 nm is sufficient for maximum interference contrast (from maximum brightness to a dark contrast or viceversa, see also the Fig. 2.7). The brightness does not change considerably by changing either the wavelength or the angle of illumination but change sharply with d and n. RICM allows following very small changes and differences in distance between cell and surface (Bereiter-Han, 1998).

The refractive medium for SB and diluted buffer was measured with an Abbé refractometer: n = 1.333 for SB and n = 1.334 for diluted buffer solution containing sucrose.

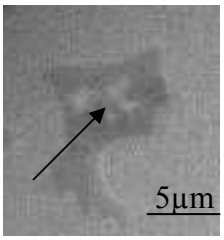

Fig 2.7 RICM image of a Dictyostelium discoideum cell spread on a glass; the bright zone indicates a membrane part that is at least at 100 nm distance from the substrate.

A *D. discoideum* cell was considered as attached when a dark contact area larger than 4 μm^2 lasted for more than 10 s and enlarged with time. Cells were considered fully spread when 90% of the maximum contact area was reached.

2.1.9 Analysis of cell spreading kinetics

Using the Image Pro Plus software (IPP, MediaCybernetics, Bethesda, MD, USA), RICM images were sub-sampled at 1 image per 1.2 seconds, the background was subtracted and flattened and the noise filtered. This generates a black and white movie showing the changes in contact area with time, where cell-surface contact areas appear white (pixel value 255) over a dark background (pixel value 0). White areas are quantified and plotted as a function of time, giving the spreading kinetics. Individual spreading kinetics are adjusted by the equation derived by Chamaraux *et al.* (Chamaroux, 2005):

$$A(t) = A_{max} \tanh(\alpha t) \qquad \text{Eq. 2.11}$$

where A_{max} is the maximum cell-surface contact area, α the inverse of the characteristic spreading time and the initial contact time is set at t = 0. In this model, the initial spreading slope is αA_{max}.

2.1.10 Analysis of LimE-GFP fluorescence

Epifluorescence images were obtained using an appropriate filter set to match Green Fluorescent Protein (GFP) characteristic excitation and emission spectra (λex =

481 nm, λem = 507 nm). GFP fluorescence was selected with a BGW cube (Olympus) and supplementary BG18 and BG28 excitation and emission filters (Melles Griot).

Green fluorescent protein (GFP) was first purified from *Aequorea victoria* in 1992 (Shimomura, 1962). GFP is a compact and globular protein composed of 238 amino acids (27 kDa) and has dimensions of 2.4 per 4.2 nm (Ormö, 1996). 30 years after its isolation, Douglas Prasher had the idea to use GFP like target in order to monitor the production and localization of a protein of interest. The gene of GFP was cloned in 1992 (Prasher, 1992). The first successful genetic expression of GFP in E. coli was realized in 1994 (Chalfie, 1994). The cells exhibit bright green fluorescence when exposed to blue light. The protein gets its fluorescent properties by an autocatalytic mechanism of fluorophore formation (Chalfie, 1994).

In our study we used a fluorescent version of the LimE protein (a GFP fusion construct with a fragment of LimE, $LimE^{\Delta coil}$-GFP (Schneider, 2003) which, will be noted simplest LimE-GFP) to visualize and measure the actin dynamics in *Dictyostelium*.

In our experiments, to quantify fluorescence variation with time, a threshold is set to identify actin polymerization active zones inside the cell. The threshold *T* is defined by the following formula: T = B+ 2(C-B) where *B* corresponds to background fluorescence outside the cell and *C* corresponds to the cytoplasmic fluorescence. An active zone is made of pixels in which significant fluorescence events occur over more than 3 consecutive frames and attain a minimum of 4 pixels (~1μm^2). The signal recorded is obtained by integrating the fluorescence over all the active zone. The time at which local fluorescence attains a maximum (peak values) was determined. Image Pro Plus software was used to quantify fluorescence.

2.2 Electrical phenomenon at the interface

2.2.1 Brief description of the electrical double layer

An electrode at which no charge transfer can occur across the metal-solution interface, regardless of the potential imposed by an outside source of voltage, is called an ideal polarizable electrode (IPE, for example, a mercury electrode in contact with a

deaerated KCl solution). Since charge cannot cross the IPE interface when the potential across it is changed, the behavior of the electrode-solution interface is analogous to that of a capacitor. In addition, a surface of an oxide material may be charged by dissociation of surface groups (for example, the silanol groups of glass surface) or by adsorption of charged ions or molecules from surrounding solution.

The solution side of the double layer is thought to be made up of several "layers". The one closest to the surface of the material (electrode or oxide material), the inner layer, contains solvent molecules and sometimes other species (ions or molecules) that are said to be specifically adsorbed (see Fig. 2.8). This inner layer is also called the compact, Helmholtz or Stern layer. The locus of the electrical centers of the specifically adsorbed ions is called the inner Helmholtz plane (IHP), which is at a distance x_1. The total charge density from specifically adsorbed ions in this inner layer is σ^i ($\mu C/cm^2$). Solvated ions can approach the solid material (M) only to a distance x_2. The locus of centers of these nearest solvated ions is called the outer Helmholtz plane (OHP).

The interaction of the solvated ions with the charged metal (or ionized surface groups) involves only long-range electrostatic forces, so that their interaction is essentially independent of the chemical properties of the ions. These ions are said to be nonspecifically adsorbed.

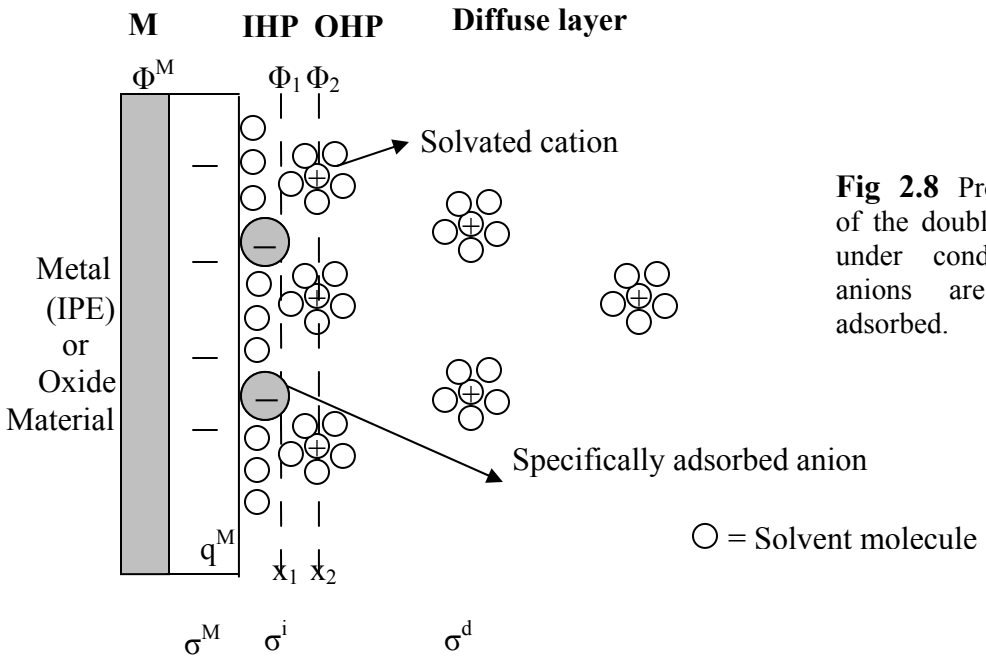

Fig 2.8 Proposed model of the double-layer region under conditions where anions are specifically adsorbed.

Because of thermal agitation in the solution, the nonspecifically adsorbed ions are distributed in a three-dimensional region called the diffuse layer, which extends from the OHP into the bulk of the solution (Bard, 1980). The excess charge density in the diffuse layer is σ^d, hence the total excess charge density on the solution side of the double layer, σ^S, is given by:

$$\sigma^S = \sigma^i + \sigma^d = -\sigma^M \qquad \text{Eq. 2.12}$$

The thickness of the diffuse layer depends on the total ionic concentration in the solution. For example for concentrations greater than 10^{-2} M (the Debye distance for a 1:1 electrolyte at 10^{-2} M is ~3 nm), the thickness is less than 10 nm.

2.2.2 The Gouy-Chapman Theory

Gouy and Chapman independently proposed the idea of a diffuse layer and offered a statistical mechanical approach to describe it. They considered the solution as being subdivided into laminae, parallel to the electrode, of thickness *dx*, starting from the electrode surface (x = 0). All these laminae are in thermal equilibrium with each other. However, the ions of every species *i* are not at the same energy in the various laminae, because the electrostatic potential Φ varies (its magnitude decreases from the electrode surface through the bulk solution). The laminae can be regarded as energy states with equivalent degeneracies; hence, the concentrations of species in two laminae have a ratio determined by a Boltzmann factor. If the reference is taken at the laminae far from the electrode, when every ion is at its bulk concentration n_i^0, then the population in any other laminae is:

$$n_i = n_i^0 \exp\left(\frac{-z_i e\Phi}{kT}\right) \qquad \text{and the charge density is } \rho(x) = \sum_i n_i z_i e \qquad \text{Eq. 2.13}$$

where Φ is measured with respect to the bulk solution. The other quantities are the electron charge, *e*, the Boltzmann constant, *k*, the absolute temperature, *T*, the (signed) charge, z_i of an ion *i* and ρ(x), the total charge per unit in any lamina.

From electrostatics, we know that ρ(x) is related to the potential at distance *x* by the Poisson equation:

$$\rho(x) = -\varepsilon\varepsilon_0 \frac{d^2\Phi}{dx^2} \qquad \text{Eq. 2.14}$$

which yields the Poisson-Boltzmann equation:

$$\frac{d^2\Phi}{dx^2} = -\frac{e}{\varepsilon\varepsilon_0}\sum_i n_i^0 z_i \exp\left(\frac{-z_i e\Phi}{kT}\right) \qquad \text{Eq. 2.15}$$

Equation 2.15 is treated by:

$$\frac{d^2\Phi}{dx^2} = \frac{1}{2}\frac{d}{d\Phi}\left(\frac{d\Phi}{dx}\right)^2 \qquad \text{Eq. 2.16}$$

$$\text{hence, } d\left(\frac{d\Phi}{dx}\right)^2 = -\frac{2e}{\varepsilon\varepsilon_0}\sum_i n_i^0 z_i \exp\left(\frac{-z_i e\Phi}{kT}\right)d\Phi \qquad \text{Eq. 2.17}$$

$$\text{Integration gives: } \left(\frac{d\Phi}{dx}\right)^2 = \frac{2kT}{\varepsilon\varepsilon_0}\sum_i n_i^0 \exp\left(\frac{-z_i e\Phi}{kT}\right) + C \qquad \text{Eq. 2.18}$$

and the constant *C* is evaluated by recognizing that at distance far from the electrode $\Phi = 0$ and $d\Phi/dx = 0$. Thus,

$$\left(\frac{d\Phi}{dx}\right)^2 = \frac{2kT}{\varepsilon\varepsilon_0}\sum_i \left[n_i^0 \exp\left(\frac{-z_i e\Phi}{kT}\right) - 1\right] \qquad \text{Eq. 2.19}$$

For a symmetrical electrolyte (z:z electrolyte) we obtain the following differential equation:

$$\frac{d\Phi}{dx} = -\left(\frac{8kTn^0}{\varepsilon\varepsilon_0}\right)^{1/2} \sinh\left(\frac{ze\Phi}{2kT}\right) \qquad \text{Eq. 2.20}$$

The equation 2.20 can be rearranged and integrated in the following manner:

$$\int_{\Phi_0}^{\Phi} \frac{d\Phi}{\sinh(ze\Phi/2kT)} = -\left(\frac{8kTn^0}{\varepsilon\varepsilon_0}\right)^{1/2} \int_0^x dx \qquad \text{Eq. 2.21}$$

where Φ_0 is the potential at x = 0 relative to the electrode surface. In the other words, Φ_0 is the potential drop across the diffuse layer. The result is:

$$\frac{2kT}{ze}\ln\left[\frac{\tanh(ze\Phi/4kT)}{\tanh(ze\Phi_0/4kT)}\right] = -\left(\frac{8kTn^0}{\varepsilon\varepsilon_0}\right)^{1/2} x \qquad \text{Eq. 2.22}$$

We obtain the potential profile in the diffuse layer:

$$\tanh(ze\Phi / 4kT) = \tanh(ze\Phi_0 / 4kT)\, e^{-\kappa x} \qquad \text{Eq. 2.23}$$

$$\kappa = \left(\frac{2n^0 z^2 e^2}{\varepsilon\varepsilon_0 kT} \right)^{1/2} \text{; for } \varepsilon = 78.49 \text{ at } 25^\circ\text{C } \kappa = 3.29 \cdot 10^7\, z\, C^{1/2}, \qquad \text{Eq. 2.24}$$

where *C* is the bulk z:z electrolyte concentration (M) and κ is given in cm^{-1}. 1/κ is the so-called Debye distance and is of the order of 3 nm for 10^{-2} M 1:1 electrolyte at 25ºC. For a 1:1 electrolyte, the Debye distance as a function of electrolyte concentration, is:

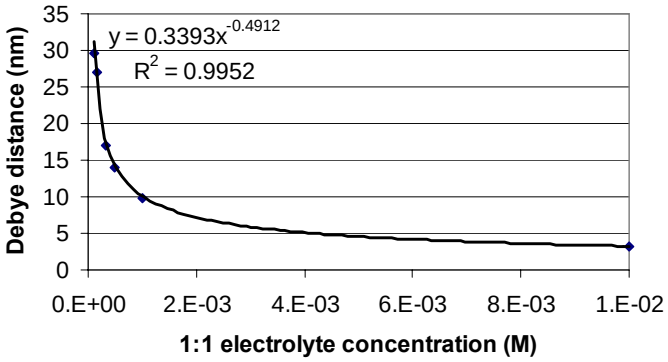

Fig. 2.9 Debye distance as a function of 1:1 electrolyte concentration.

In fact, the form is exponential in the limit of small Φ_0. If $\Phi_0 < 50/z$ mV at 25ºC, then we can approximate that: $\Phi = \Phi_0 e^{-\kappa x}$ Eq. 2.25

Suppose we now imagine a Gaussian surface in the shape of a box placed in our system (Fig. 2.10) with one end at the interface, the sides perpendicular to this end and extend far enough into the solution where the field strength dΦ/dx is essentially zero.

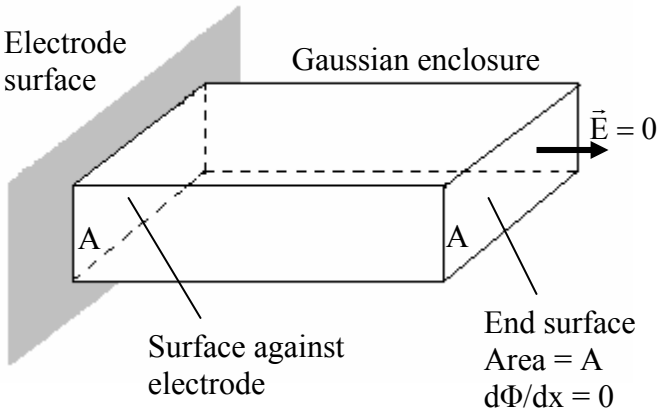

Fig. 2.10 A Gaussian box enclosing the charge in the diffuse layer contacting an area, A, of the electrode surface

The box therefore contains all the charge in the diffuse layer contacting the portion of the electrode surface adjacent to the end (charge conservation). From the Gauss law, this charge is:

$$q = \varepsilon\varepsilon_0 \oint_{surface} \vec{E} \cdot \vec{dS} = \varepsilon\varepsilon_0 \left(\frac{d\Phi}{dx}\right)_{x=0} \int_{surface}^{end} dS \qquad \text{Eq. 2.26}$$

Substituting from eq. 2.20 and recognizing that q/A is the solution phase charge density σ^S, we obtain the relation between charge density (σ^M) and Φ_0:

$$\sigma^M = -\sigma^S = (8kT\varepsilon\varepsilon_0 n^0)^{1/2} \sinh\left(\frac{ze\Phi_0}{2kT}\right) \approx 11.7 \cdot C^{1/2} \cdot \sinh(19.5z\Phi_0), \quad \text{Eq. 2.27}$$

where *C* is in mol/L and σ^M in $\mu C/cm^2$.

2.2.3 Tacking into account the finite size of electrolyte ions: the Stern modifications

The partial success of the Gouy-Chapman theory suggests that it has elements of truth, but also, indicates major defects. One of those defects is related to the finite size of the ions in an electrolyte.

For example, there is an unlimited differential capacitance with Φ_0 in the Gouy-Chapman model because the ions are considered as point charges that can closely approach the surface. Therefore, at high polarization, the effective separation distance between the metallic and solution phase charge zones decreases continuously towards zero. This view is not realistic. The ions have a finite size and cannot approach the surface any closer than the ionic radius. If they remain solvated, the thickness of the primary solution sheath would be added to that radius. Still another increment might be necessary to account for a layer of solvent on the electrode surface. In other words, we can envision a plane of closest approach for the centers of the ions at some distance x_2.

The Poisson-Boltzmann equation, and its solutions, still apply at distance $x \geq x_2$:

$$\tanh(ze\Phi / 4kT) = \tanh(ze\Phi_2 / 4kT)\, e^{-\kappa(x - x_2)} \qquad \text{Eq. 2.28}$$

The plane at distance x_2 from the surface electrode is an important concept and is called the outer Helmholtz plane (OHP, see Fig. 2.11 and 2.8). Between the electrode (x = 0) and OHP, there is no charge transport, therefore the potential Φ decreases linearly. The slope is given by Eq. 2.20, tacking $x = x_2$:

$$\left(\frac{d\Phi}{dx}\right)_{x=x_2} = -\left(\frac{8kTn^0}{\varepsilon\varepsilon_0}\right)^{1/2} \sinh\left(\frac{ze\Phi_2}{2kT}\right) \Rightarrow \Phi_0 = \Phi_2 - \left(\frac{d\Phi}{dx}\right)_{x=x_2} x_2 \quad \text{Eq.2.29}$$

resulting the total potential drop across the double layer (Φ_0).

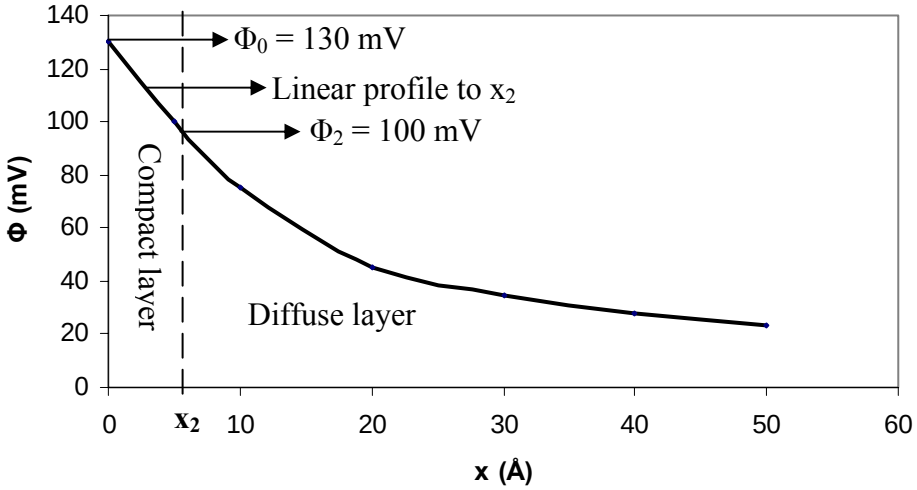

Fig 2.11 Potential profile through the solution side of the double layer, according to the Gouy-Chapman-Stern theory (GCS theory). Calculated from eq. 2.22 for 10^{-2} M 1:1 electrolyte in water at 25ºC (Bard, 1980).

From the streaming potential measurements, the shear plane, corresponding to the zeta potential, is very close to the OHP. Therefore, we can approximate the surface density charge (considering also the specifically adsorbed ions in the inner layer, if they exist) function of the zeta potential (ζ):

$$\sigma^M + \sigma^i = (8kT\varepsilon\varepsilon_0 n^0)^{1/2} \sinh\left(\frac{ze\Phi_2}{2kT}\right) = (8kT\varepsilon\varepsilon_0 n^0)^{1/2} \sinh\left(\frac{ze\zeta}{2kT}\right) \quad \text{Eq. 2.30}$$

$$\approx 11.7 \cdot C^{1/2} \cdot \sinh(19.5z\zeta)$$

2.2.4 Zeta potential measurements of surfaces

Zeta potentials were measured with a SurPass Anton Paar Electrokinetic Analyzer with the help of a SurPASS clamping cell (Fig. 2.12A). Polymethyl Methacrylate (PMMA-$(C_5O_2H_8)_n$) is the reference material in this method.

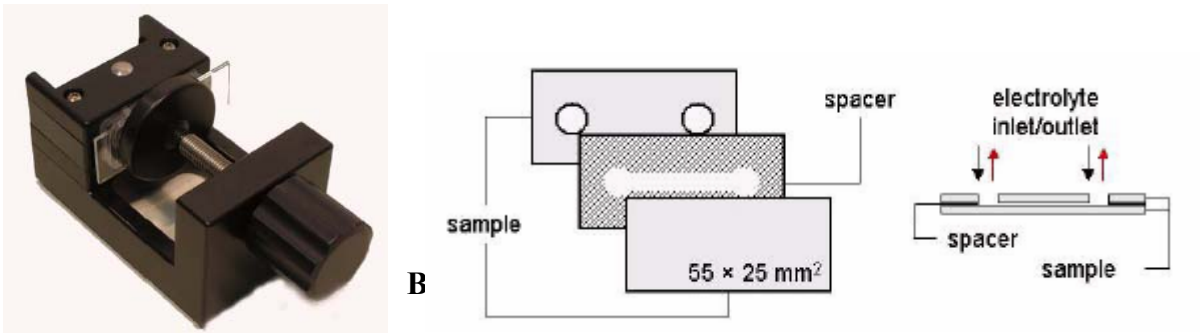

Fig. 2.12 A. SurPASS Clamping Cell with sample (glass slide) mounted; **B.** Schematic drawing of the sample stack in the SurPASS Clamping Cell (height: h; length: l and width: L)

A streaming current and streaming potential are an electric current and potential appearing when an electrolyte is driven by a pressure gradient ($P_1>P_2$; $\Delta P = P_2 - P_1<0$) through a channel or porous plug with charged walls (Fig. 2.12B). Adjacent to the channel walls, the charge-neutrality of the liquid is violated due to the presence of an electrical double layer: a thin layer of counterions is attracted by the charged surface. The transport of these counterions along with the pressure-driven fluid flow gives rise to a net charge transport: the streaming current (Fig. 2.13).

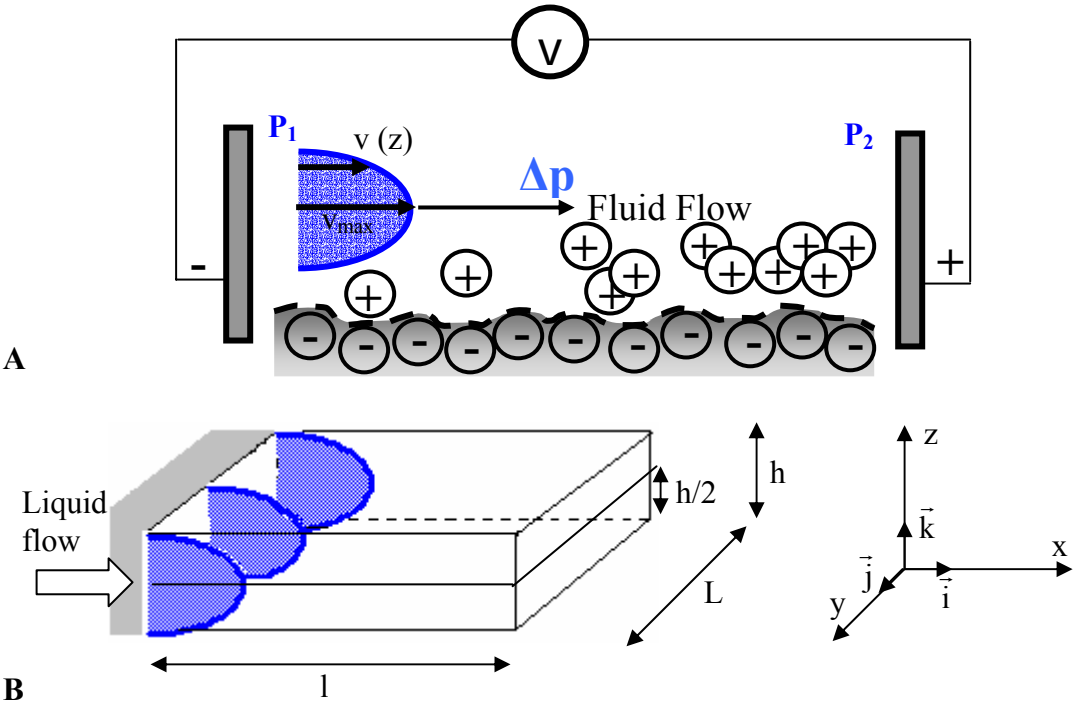

Fig. 2.13 A. Mechanism of streaming potential arising ($P_1>P_2$). **B**. Stationary flow in a clamping cell with dimensions: height (h), length (l) and width (L); h << L and h << l.

In order to find the streaming current and the streaming potential that arise when an electrolyte is driven by a pressure gradient through a space delimitated by two parallel planar surfaces, we employed the Navier-Stokes equation for the incompressible liquids and the Gouy-Chapman-Stern theory.

$$\rho\frac{\partial\vec{v}}{\partial t}+\rho\vec{v}\cdot\vec{\nabla}\vec{v}=-\vec{\nabla}P+\eta\Delta\vec{v} \qquad \text{Eq. 2.31}$$

where v stands for local speed of the fluid, ρ is the liquid density, η represents the dynamic viscosity of the liquid and P is the pressure.

One considers that the liquid flowing occurs in a stationary regime ($\frac{\partial\vec{v}}{\partial t}=0$) and only along the x axis between the two planar surfaces, in the other words the vector $\vec{v}$ is parallel with x axis: $\vec{v}(\vec{r})=v(z)\cdot\vec{i}$ (the height, h is very small in comparison with length and width). Thus, the divergence of speed vector variation is not zero only along z axis. It results the scalar product:

$$\nabla\vec{v}=\frac{\partial}{\partial x}\vec{i}\cdot v(z)\vec{i}+\frac{\partial}{\partial y}\vec{j}\cdot v(z)\vec{i}+\frac{\partial}{\partial z}\vec{i}\cdot v(z)\vec{k}=\frac{\partial v(z)}{\partial x}=0 \qquad \text{Eq. 2.32}$$

The Navier-Stokes equation becomes:

$$\eta\frac{\partial^2 v}{\partial z^2}=\frac{dP}{dx} \qquad \text{Eq. 2.33}$$

Tacking as reference the lower planar surface and considering that in vicinity of the walls the local speed of the liquid is null (v(0) = v(h) = 0, and for z = h/2 one has the maximum speed, v_{max}, (see Fig. 2.13), the speed has the following profile:

$$v(z)=k\cdot z(h-z) \qquad \text{Eq. 2.34}$$

where k is a constant which is found relaying the speed with the rate of fluid flow (D), which can be very easily experimentally determined:

$$D=\iint_{surface}\vec{v}\cdot d\vec{S}=\iint_{surface}v(z)\cdot dz\cdot dy=2kL\int_0^{h/2}z(h-z)=\frac{kLh^3}{6}$$
$$\Rightarrow\quad k=\frac{6D}{Lh^3}\quad\text{and}\quad v(z)=\frac{6D}{Lh^3}z(h-z) \qquad \text{Eq. 2.35}$$

Replacing the expression of v in Eq. 2. 33, one obtains:

$$-\frac{12\eta D}{Lh^3}\cdot dx = dP \Rightarrow -\frac{12\eta D}{Lh^3}\cdot\int_0^l dx = \int_{P_1}^{P_2} dP \Leftrightarrow -\frac{12\eta D\cdot l}{Lh^3} = \Delta P$$
$$\Rightarrow D = -\frac{\Delta P\cdot Lh^3}{12\eta\cdot l} \qquad \text{Eq. 2.36}$$

Replacing the expression of *D* from eq. 2.36 in Eq. 2.36 we get the local speed function of pressure difference:

$$v(z) = \frac{-\Delta P}{2\eta l}\cdot z(h-z) = \frac{|\Delta P|}{2\eta l}\cdot z(h-z) \qquad \text{Eq. 2.37}$$

Adjacent to the channel walls, the charge-neutrality of the liquid is violated due to the presence of an electrical double layer (see Gouy-Chapman-Stern theory): a thin layer of counterions is attracted by the charged surface. The transport of these counterions along with the pressure-driven fluid flow gives rise to a net charge transport, the streaming current (we note I_{str} equivalent of ions transported in time, for one surface):

$$I_{str} = \int_0^L\int_{z_2}^h \rho(z)\cdot v(z)\cdot dzdy = \frac{-\Delta P\cdot L}{2\eta l}\int_{z_2}^h \rho(z)\cdot z(h-z)dz \qquad \text{Eq. 2.38}$$

where z_2 is the outer Helmholtz plane coordinate and $\rho(z)$ is the charge density at distance z_2 from the surface. Considering that the thin layer of counterions is much smaller than the height of the chamber, we can approximate that $h\text{-}z \cong h$. It results:

$$I_{str} = \frac{-\Delta P\cdot Lh}{2\eta l}\int_{z_2}^h \rho(z)\cdot z\cdot dz \qquad \text{Eq. 2.39}$$

Tacking in account the Equation 2.14, we have:

$$I_{str} = \frac{-\Delta P\cdot Lh}{2\eta l}\int_{z_2}^h -\varepsilon\varepsilon_0\frac{d^2\Phi}{dz^2}\cdot z\cdot dz = \frac{\Delta P\cdot Lh}{2\eta l}\varepsilon\varepsilon_0\left(z\cdot\frac{d\Phi}{dz}\Big|_{z_2}^h - \int_{z_2}^h\frac{d\Phi}{dz}dz\right) \qquad \text{Eq. 2.40}$$
$$I_{str} = \frac{\Delta P\cdot Lh}{2\eta l}\varepsilon\varepsilon_0\left(h\cdot\left(\frac{d\Phi}{dz}\right)_{z=h} - z_2\cdot\left(\frac{d\Phi}{dz}\right)_{z=z_2} - \Phi(h) + \Phi(z_2)\right)$$

Knowing that $\Phi(h) = (d\Phi/dz)_{z=h} = 0$ and that the potential drop across the compact layer multiplied with its width, is negligible, we get:

$$I_{str} = \frac{\Delta P\cdot Lh}{2\eta l}\varepsilon\varepsilon_0\Phi(z_2) = \frac{\Delta P\cdot Lh}{2\eta l}\varepsilon\varepsilon_0\zeta \qquad \text{Eq. 2.41}$$

The tension that has to be applied for streaming current annulment, (the positive electrode-fig. 2.13-is placed against the fluid flow), considering that both surfaces are sources of counterions, is:

$$U_{str} = 2I_{str} \cdot R = 2 \cdot \frac{\Delta P \cdot Lh}{2\eta l} \varepsilon\varepsilon_0 \zeta \cdot \frac{l}{Lh \cdot K_L} = \frac{\varepsilon\varepsilon_0 \zeta}{\eta K_L} \cdot \Delta P \qquad \text{Eq. 2.42}$$

where U_{str} is streaming potential at zero net current conditions (V), R is the resistance of the bulk liquid (Ω), K_L is specific conductivity of the bulk liquid ($S \cdot m^{-1}$), ΔP is the pressure difference (Pa) and ζ stands as zeta potential (V).

Equation 2.42 (Helmoltz-Smoluchowski equation (Delgado, 2005)) is the basis of the experimental determination of zeta potential (see subchapter **2.2.7**).

2.2.5 Surface charge density and point of zero charge

When a solid is immersed in a polar solvent or an electrolyte solution, a surface charge develops through one or more of the following mechanisms:

1. Preferential adsorption of ions
2. Dissociation of surface charged species
3. Isomorphic substitution of ions
4. Accumulation or depletion of electrons near the surface
5. Physical adsorption of charged species onto the surface.

For a given solid surface in a given liquid medium, a fixed surface electrical charge density or electrode potential, *E*, will be established, which is given by the Nernst equation:

$$E = E_o + (R_g T/n_i F) \ln a_i \qquad \text{Eq. 2.43}$$

where E_o is the standard electrode potential at 1 M concentration of ions *i*, a_i is the chemical activity of specie i, n_i is the valence state of ions, R_g is the gas constant, *T* is the temperature, and *F* is the Faraday constant. Equation 2.43 clearly indicates that the surface potential of a solid varies with the concentration of the ions in the surrounding solution, and can be either positive or negative. The focus of the discussion here will be on non-conductive materials or dielectrics, more specifically on oxides.

The surface charge in oxides is mainly derived from preferential dissolution or deposition of ions, usually, by a chemical equilibrium. Ions physically adsorbed on the

solid surface determine the surface charge, and thus are referred to as charge determining ions, also known as co-ions.

The equilibrium determined by the proton concentration is as follows:

$$R-OH \Leftrightarrow R-O^{-}+H^{+} \qquad R-OH+H^{+} \Leftrightarrow R-HOH^{+} \qquad \text{Eq.2.44}$$

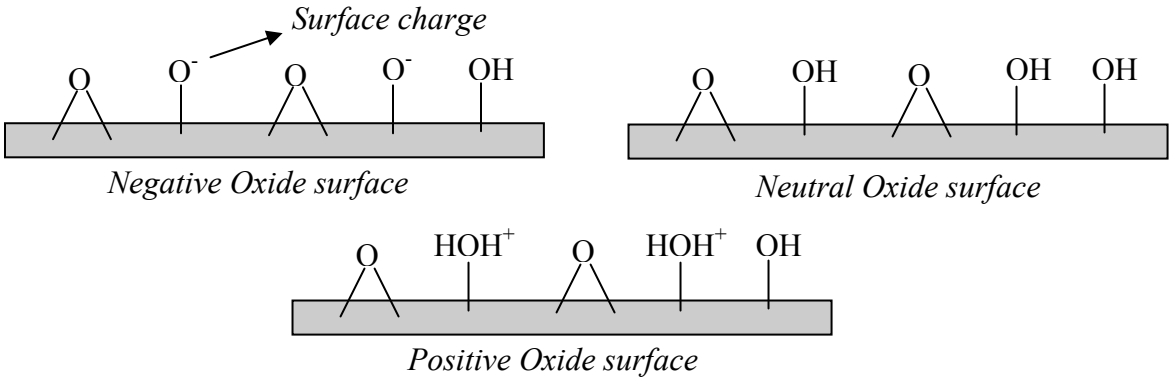

Fig. 2.14 Schematic distribution of the chemical surface groups on an oxide surface and charge surface group formation as a function of the pH.

In the oxide systems, the ions that determine charge are protons and hydroxyl groups and their concentrations are described by pH (pH = - log $[H^+]$; in water, $[H^+]\cdot[OH^-] = 10^{-14}$). They can bind to the surface groups R-O^- and R-OH (forming R-OH and R-HOH^+) or respectively extract a H^+ from the surface group R-OH (forming an R-O^- group at the surface) – see Fig. 2.14. As the concentration of charge determining ions varies, the surface charge density changes from positive to negative or vice versa (Parks, 1965; Hunter, 1981). The concentration of charge determining ions corresponding to a neutral or zero-charged surface is defined as a point of zero charge (p.z.c.) or zero-point charge (z.p.c.).

Table 2.1 gives a list of some p.z.c. values of selected oxides (Pierre, 1998). At pH > p.z.c., the oxide surface is negatively charged, since the hydroxyl group, OH^-, is the electrical determining ion. At pH < p.z.c., H^+ is the charge determining ion and the surface is positively charged. The surface charge density or surface potential, *E* in volts, can then be simply related to the *pH* and the Nernst equation (equation 2.43) can be written as (Pierre, 1998):

$$E = 2.303\, R_g T\, [(\text{p.z.c.}) - \text{pH}] / F \qquad \text{Eq. 2.45}$$

At room temperature, the above equation can be further simplified:

$E \approx 0.06\ [(p.z.c.) - pH]$ Eq. 2.46

Table 2.1 A list of p.z.c. of some common oxides in water

Solid	WO_3	V_2O_5	δMnO_2	βMnO_2	SiO_2	SiO_2 (quartz)	TiO_2	TiO_2 (calcined)
p.z.c.	0.5	1-2	1.5	7.3	**2.5**	**3.7**	6	3.2
Solid	Al-O-Si	ZrO_2	SnO_2	FeOOH	Fe_2O_3	Cr_2O_3	ZnO	Al_2O_3
p.z.c.	6	6.7	4.5	6.7	8.6	8.4	8	9

It can be noticed that for SiO_2 (silica is the main constituent of the glass), immerged in SB (pH = 6), the oxide surface is negatively charged. The same situation is met in the case of ITO (p.z.c. are included in the interval [3; 4.7] (Tobias, 2002)).

2.2.6 Water electrolysis

In a properly designed electrochemical cell, hydrogen will appear at the cathode (the negatively charged electrode, where electrons are pumped into the water), and oxygen will appear at the anode (the positively charged electrode). Assuming ideal faradaic efficiency, the generated moles of hydrogen is twice the moles of oxygen, and both are proportional to the total electrical charge that was exchanged through the solution. However, in many cells competing side reactions dominate, resulting in different products and non ideal faradaic efficiency.

Electrolysis of pure water requires a great deal of energy in the form of overpotential to overcome various activation barriers. Without this energy excess, the electrolysis of pure water occurs very slowly or not at all. This is in part due to the limited self-ionization of water. Pure water has an electrical conductivity about million times lower than 100 mM seawater. Many electrolytic cells do not behave as ectrocatalysts. The efficiency of electrolysis is increased through the addition of an electrolyte (such as a salt, an acid or a base) and the use of electrocatalysts.

In water at the negatively charged cathode, a reduction reaction takes place, with electrons from the cathode being given to hydrogen cations to form hydrogen gas (the half reaction balanced with acid):

Cathode (reduction): $2H^+(aq) + 2e^- \rightarrow H_2(g)$ $\quad E_{red}^0 = 0$ V

At the positively charged anode, an oxidation reaction occurs, generating oxygen gas and giving electrons to the cathode to complete the circuit:

Anode (oxidation): $2H_2O(l) \rightarrow O_2(g) + 4H^+(aq) + 4e^-$ $E_{ox}^0 = -1.23$ V

The same half reactions can also be written with base as listed below.

Cathode (reduction): $2H_2O(l) + 2e^- \rightarrow H_2(g) + 2OH^-(aq)$ $E_{red}^0 = -0.83$ V

Anode (oxidation): $4OH^-(aq) \rightarrow O_2(g) + 2H_2O(l) + 4e^-$ $E_{ox}^0 = -0.4$ V

Combining either half reaction pair yields the same overall decomposition of water into oxygen and hydrogen:

Overall reaction: $2H_2O(l) \rightarrow 2H_2(g) + O_2(g)$

The number of hydrogen molecules produced is thus twice the number of oxygen molecules. Assuming equal temperature and pressure for both gases, the produced hydrogen gas has therefore twice the volume of the produced oxygen gas. The number of electrons pushed through the water is twice the number of generated hydrogen molecules and four times the number of generated oxygen molecules.

Decomposition of pure water into hydrogen and oxygen at standard temperature and pressure is not favorable in thermodynamical terms. Thus, the standard potential of the water electrolysis cell is -1.23 V at 25 °C at pH 0 ($H^+ = 1.0$ M). It is also -1.23 V at 25 °C at pH 7 ($H^+ = 1.0 \times 10^{-7}$ M) based on the Nernst equation.

The negative voltage indicates the Gibbs free energy for electrolysis of water is greater than zero for these reactions. This can be found using the $\Delta G = -n F E$ equation from chemical kinetics, where n is the moles of electrons and F is the Faraday constant. The reaction cannot occur without adding necessary energy, usually supplied by an external electrical power source.

2.2.7 Electric proprieties of ITO material

Apart from its conductive property, indium-tin oxide (ITO) has many other advantages such as high optical transmittance in the visible and near-IR region, a robust chemically and mechanically nature, it can be easily patterned and has excellent adhesion property to many substrates (Moore, 2006).

Before testing the behavior of the living cells on the ITO surface in buffer solutions (17 or 1.7 mM), an electrochemical characterization of this substrate, was

required, (we employed 3 electrodes setup – Fig. 2.15A). We used cyclic voltammetry measurements for the characterization of ITO surfaces (Fig. 2.15B, in 1.7 mM phosphate sucrose buffer solution) with a scanning speed of 50 mV/s.

We obtained 3 potential (current) domains: below – 0.1 V/Ag,AgCl, the current (faradaic current) increases exponentially because of water reduction forming negative hydroxyl ions OH^-; between -0.1 and +0.8 V/Ag,AgCl, the current remains approximately constant and very low (0.5 μA, capacitive current); at more than 0.8 V/Ag,AgCl, the current increases exponentially because of water oxidation, resulting in the formation of positive H_3O^+ ions (faradaic current, Fig. 2.15B).

The quantity of produced charged ions (protons coordinated to a water molecule - H_3O^+ or hydroxyl ions, OH^- respectively) is directly proportional to the current intensity and to the duration of the current delivery (faradaic current); for ITO, the capacitive current, due to material polarization, is much less important than the faradaic one (see Fig. 2.15B).

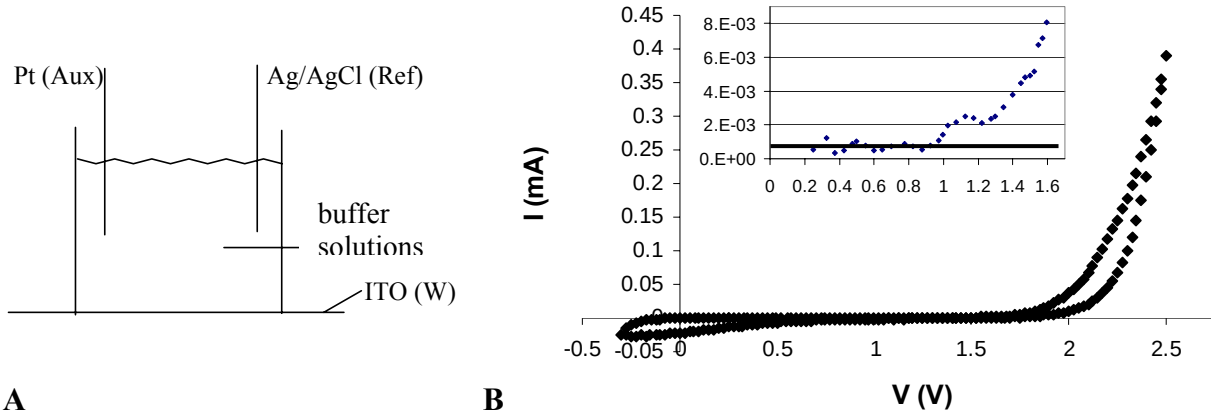

Fig. 2.15 A. Experimental setups for electrochemical characterization of ITO-glass surface as working electrode (W). **B**. Cyclic voltammetric curve obtained in 1.7 mM phosphate sucrose buffer solution (v = 50 mV/s); the insert presents the magnified [0.2 V-1.6V] window. The thick black line from the inset delimitate the capacitive current.

However, ITO is reduced and suffers an important deterioration when the negative potential falls below -1.5 V/Ag,AgCl for 30 s, (- 1.5 mC).

Since, during pulse application, the protons or hydroxyl ions accumulate at the surface, we measured the zeta potential of an ITO surface in 10 mM KCl at different pH (Fig. 2.16).

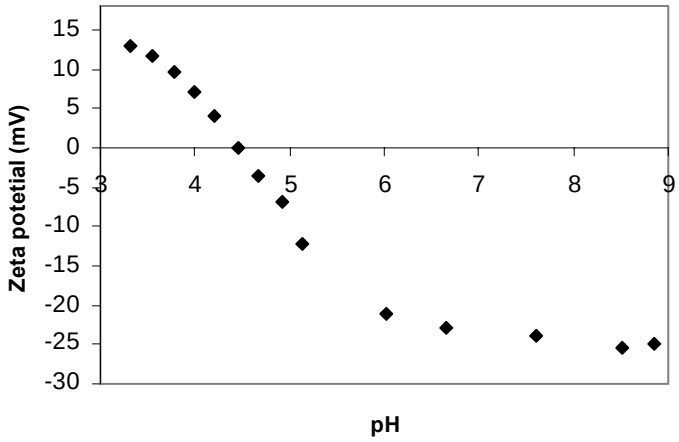

Fig. 2.16 ITO surface zeta potential versus pH of the electrolyte (10 mM KCl). It can be noticed that the p.z.c = 4.45.

At the surface of an oxide material, charged species depend on the pH. When the latter varies, the surface charge density changes from positive to negative or vice versa. The pH corresponding to a neutral or zero-charged surface is defined as the point of zero charge (p.z.c.). It can be found immediately that the p.z.c. of ITO surface is 4.45 (Fig. 2.16). This experimental value fits with the reported values in literature in the interval [3; 4.7] (Tobias, 2002).

2.2.8 Interactions between two charged particles: DLVO theory. Applications to the situation: one charged particle and a charged surface

The total energy interaction between two particles (Φ), which are electrostatically stabile, is the combination of van der Waals attraction (Φ_A) and electrostatic repulsion (Φ_R):

$$\Phi = \Phi_A + \Phi_R \qquad \text{Eq. 2.47}$$

Interactions between particles are complex. One of the interactions between particles is directly associated with the surface charge and the electric potential adjacent to the interface. The electrostatic repulsion between two particles arises from the electric surface charges, which are attenuated to a varied extent by the double layers. When two particles are far apart, the double layers do not overlap and electrostatic repulsion between two particles is zero. However, when two particles approach each other, the double layers overlap and a repulsive force develops. An electrostatic repulsion between

two spherical particles of the different radius (r_1 and r_2) and the same surface charge, is given by (Hiemenz, 1997):

$$\Phi_R = 4 \pi \varepsilon_r \varepsilon_o (r_1 r_2 / r_1 + r_2) \Phi_0^2 \exp(-\kappa S) \quad \text{Eq. 2.48}$$

where Φ_0 is the surface potential, κ is given by Eq. 2.24 and S is the particles separation distance (see Fig. 2. 17).

In approximation Debye-Hückel (small surface potentials, $\Phi_0 < 50/z$ mV at 25ºC), for a spherical particle of radius r near a flat surface ($r_{surface} = \infty$), the electrostatic repulsion is given by:

$$\Phi_R = 4 \pi \varepsilon_r \varepsilon_o r \Phi_0^{surface} \Phi_0^{particle} \exp(-\kappa S) \quad \text{Eq. 2.49}$$

with the same symbolisms like above.

When particles are small, typically micrometric or less, and are dispersed in a solvent, van der Waals attraction force and Brownian motion play important roles, whereas the influence of gravity becomes negligible. Van der Waals force is a weak force and becomes significant only at a very short distance (Å). Brownian motion ensures the particles colliding with each other at all times. The combination of van der Waals attraction force and Brownian motion would result in the formation of agglomeration of the particles.

Van der Waals interaction between two particles is the sum of the molecular interaction in the surrounding medium such as solvent. Integration of all the van der Waals interactions between two molecules over two spherical particles of radius, r, separated by a distance, S, gives the total interaction energy or attraction potential (Hiemenz, 1997).

$$\Phi_A = - A/6 \{2r^2/(S^2+4rS) + 2r^2/(S^2+4rS+4r^2) + \ln[(S^2+4rS)/(S^2+4rS+4r^2)]\} \quad \text{Eq. 2.50}$$

where the negative sign represents the attraction nature of the interaction between two particles, and A is a constant termed *the Hamaker constant*, which has a magnitude in the order of 10^{-19} to 10^{-20} J, and depends on the polarization properties of the molecules in the two particles and on the medium which separates them.

Equation 2.50 can be simplified under various boundary conditions. For example, when the separation distance between two equal sized spherical particles are significantly smaller than the particle radius, i.e., $S/r << 1$, a simple expression of the van der Waals interaction energy is obtained:

$\Phi_A = - A\ r/12\ S$ Eq. 2.51

In the case of two spheres with different radius (r_1 and r_2) one obtains:

$\Phi_A = - A\ r_1 r_2/((r_1+r_2)\ 6\ S)$ Eq. 2.52

The van der Waals interaction energy between two particles is different from that between two flat surfaces. Furthermore, it should be noted that the interaction between two atoms ($\Phi_A \propto S^{-6}$) are significantly different from that between two particles.

The van der Waals interaction energy (Φ_A) and attraction force (F) for a sphere with a radius *r* near a planar surface ($r_{surface} = \infty$), as shown in Figure 2.17A, is given by:

$\Phi_A = -A_{123}\ r/6S$ and $F = A_{123}\ r/6S^2$ Eq. 2.53

where A_{123} is the Hamaker constant for substances "l" (sphere) and "2" (glass) in presence of medium "3" (for example, water) and *S* is the separation distance between spherical particle and surface (Israelachvili, 1992). The attraction force dependence on distance for a cell of radius $r = 5 \cdot 10^{-6}$ m and density $\rho = 1.0665$ g/cm^3 (like *Dictyostelium* amoebae; Fukui, 2000) near a glass surface ($A_{123} \cong 10^{-20}$ J), in aqueous solution, is drawn in Figure 2.17B.

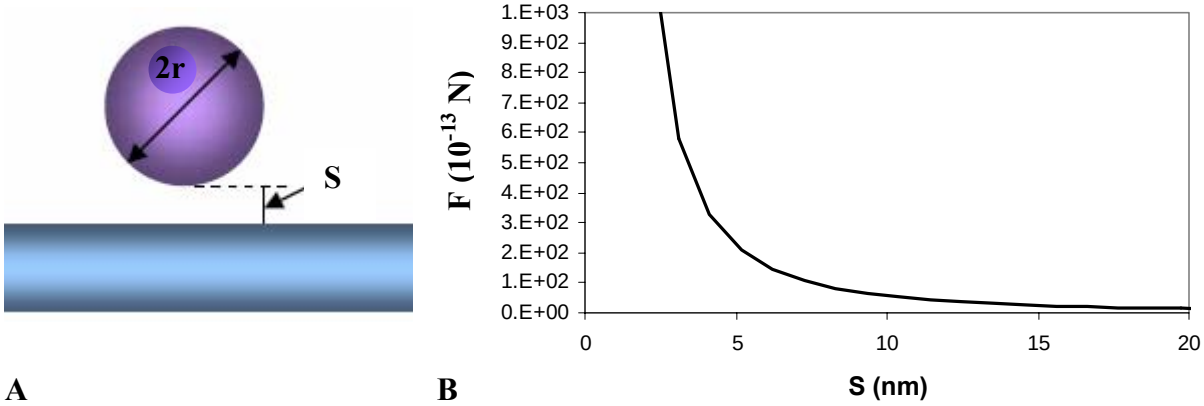

Fig. 2.17 A. Schematics of a particle near a flat surface. **B**. Attraction force (F) estimation for a cell ($r = 5\ 10^{-6}$ m) near a glass surface in aqueous solution versus distance separation (S).

For a distance $S = 100$ nm, the attraction force between a *Dictyostelium* cell and a glass surface is $5.3 \cdot 10^{-14}$ N, which is negligible comparatively with the apparent gravity ($3 \cdot 10^{-13}$ N).

Although the nature of the attraction energy between two particles is the same as that between two molecules, integration of all the interaction between molecules from two particles and from medium results in a very different dependence of the force on the

distance between particles. The attraction force between two particles decays very slowly and extends over distances of nanometers. As a result, a barrier potential must be developed to prevent agglomeration. Two methods are widely applied to prevent agglomeration of particles: electrostatic repulsion and steric exclusion.

The electrostatic stabilization of particles in a suspension is successfully described by the DLVO theory, named after Derjaguin, Landau, Verwey, and Overbeek (Overbeek, 1984). The interaction between two particles in a suspension is considered as the combination of the van der Waals attraction potential and the electric repulsion potential. There are some important assumptions in the DLVO theory:

- Infinite flat solid surface, uniform surface charge density and no re-distribution of surface charge, i.e., the surface electric potential remains constant.
- No change of concentration profiles of both counter-ions and surface charge determining ions, i.e., the electric potential remains unchanged and solvent exerts influences via dielectric constant only, i.e., no chemical reactions between the particles and solvent.

It is very clear that some of the assumptions are far from the real picture of two particles dispersed in a suspension. For example, the surface of particles is not infinitely flat, and the surface charge density is most likely to change when two charged particles get very close to each other. However, in spite of the assumptions, the DLVO theory works very well in explaining the interactions between two approaching particles, which are electrically charged, and thus is widely accepted in the research community of colloidal science.

At a distance far from the solid surface, both the van der Waals attraction potential and the electrostatic repulsion potential tend to zero. Near the surface is a deep minimum in the potential energy produced by van der Waals attraction. A maximum is located a little further away from the surface, as the electric repulsion potential dominates the van der Waals attraction potential (Hiemenz, 1997) (Fig. 2.18).

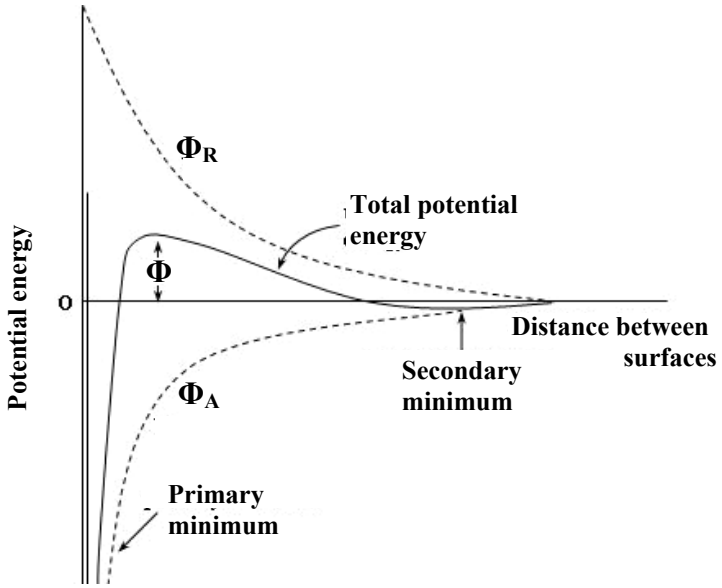

Fig. 2.18 van der Waals attraction potential (Φ_A), electric repulsion potential (Φ_R), and the combination of the two opposite potentials (continuous line, Φ) as a function of distance from the surface of a spherical particle

The maximum is also known as repulsive barrier. If the barrier is greater than ~10 kT, where *k* is the Boltzmann constant, the collisions of two particles produced by Brownian motion will not overcome the barrier and agglomeration will not occur. Since the electric potential is dependent on the concentration and valence state of counter-ions and the van der Waals attraction potential is almost independent of the concentration and valence state of counter-ions, the overall potential is strongly influenced by the concentration and valence state of counter-ions.

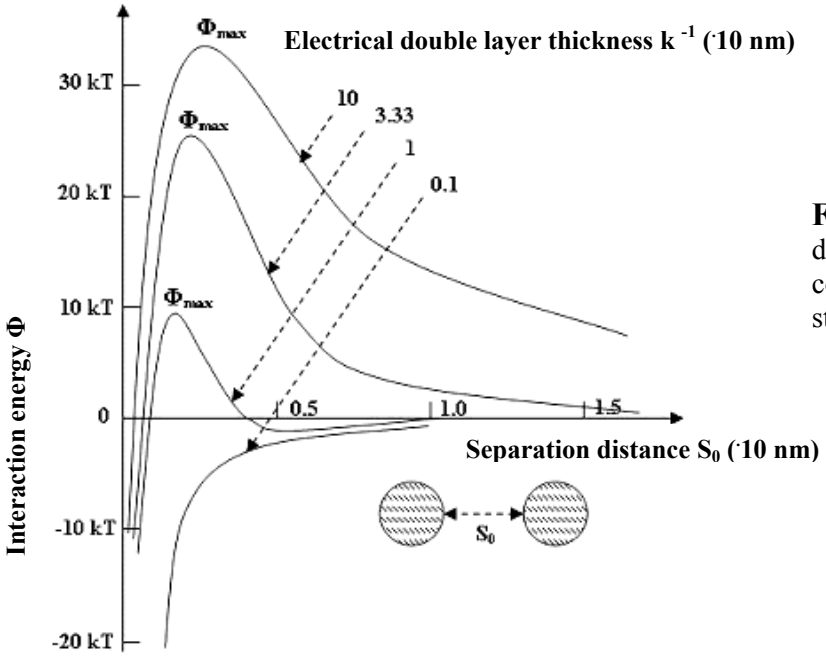

Fig. 2.19 Interaction energy dependence of the concentration and valence state of counter-ions.

An increase in concentration and valence state of counter-ions results in a faster decay of the electric potential as schematically illustrated in Fig 2.19 (Overbeek, 1984). As a result, the repulsive barrier is reduced and its position is pushed towards the particle surface. The secondary minimum observed in Fig.2.18 is not necessary to exist in all situations, and it is present only when the concentration of counter-ions is high enough. If a secondary minimum is established, particles likely associate with each other and form a colloid fluid, which is known as flocculation.

2.2.9 Model of cell attachment to charged surfaces as a function of ionic concentration

This kinetic model is based upon the observation that cell spreading is an irreversible process. When cells are able to reach the surface, so that a small visible contact is formed (about 4 μm^2), this contact extends and the cell spreads. The number of cells spreading as a function of time is thus given by a first order equation:

$$dN/dt = k(N_0 - N) \qquad \text{Eq 2.54}$$

The number of cells spreading at a given salt concentration is determined after τ =10 minutes, which is much longer than the sedimentation time of the cells (about 1 minute). The fraction of cells attached to the surface is thus linked to *k*, the rate of formation of cell-surface contact for a cell levitating at about 100 nm over the surface.

$$N(\tau)/N_0 = 1 - \exp(-k\tau) \qquad \text{Eq 2.55}$$

We assume that the rate of formation of cell-surface contact is thermally activated (Decave, 2003; Garrivier, 2002; Bell, 1984):

$$k = k_0 \exp\left(-\Delta G^* / k_B T\right) \qquad \text{Eq 2.56}$$

where k_0 is an intrinsic collision frequency between the cell membrane and the surface, ΔG^* is the energy of the activation barrier to overcome to form a stable cell-surface contact, and $k_B T$, the Boltzman thermal energy term. The potential energy of this interaction is maximal at a cell-surface distance *d* and the difference between this value and the minimum at longer distances constitutes the activation barrier.

ΔG^* is given by the DLVO theory (Atkins, 2006) and depends on the ionic concentration. It can be written as the sum of a term representing the electrostatic repulsion, ΔG_E, a term representing the activation energy at large ionic concentrations, ΔG^*_0, when electrostatic repulsion is negligible and a term representing van der Waals attraction potential, Φ_A, which also could be neglected for distances grater than 2.5 nm nanometers (Evans, 1995; see also fig. 2.19). For simplicity, we assume that the cell is round (radius r) and the surface is planar, and that both have identical surface potential Φ_0.

$$\Delta G^* \approx \Delta G_E = 4\pi\varepsilon_0\varepsilon_r r\Phi_0^2 e^{-\kappa d} \approx U_0 e^{-\kappa d} \qquad \text{Eq 2.57}$$

where ε_0 and ε_r are the vacuum and relative dielectric constants and κ^{-1} the Debye length. U_0/e is the electrostatic energy at the Debye length. The Debye length is inversely proportional to the square root of the ionic strength, the latter being proportional to the salt concentration:

$$\kappa d = bdC^{0.5} \qquad \text{Eq 2.58}$$

where C is the salt concentration. For monovalent salts, b = 0.31 $nm^{-1}M^{-0.5}$ and for divalent ones b = 0.54 $nm^{-1}M^{-0.5}$, with d in nm. From equations 2.24-2.28, it follows that the fraction of cells attached to the surface after 10 minutes is given by:

$$N / N_0 = 1 - \exp(-a\exp(-ce^{-bdC^{0.5}})) \qquad \text{Eq 2.59}$$

where $a = k_0\tau \exp(-\Delta G^*_0/k_BT)$ and $c = U_0/k_BT$.

The association rate of firm cell-surface contact formation k depends on the salt concentration as:

$$k = a / \tau \exp\left(-ce^{-bdC^{0.5}}\right) \qquad \text{Eq 2.60}$$

The curve relating k to C is sigmoidal. For $C < C_1 = \left[(bd)^{-1}\ln(c^{-1}\ln 10)\right]^2$, the association rate is less than 10% of its maximum. For $C_1 < C < C_2 = \left[(bd)^{-1}\ln(c^{-1}\ln 2)\right]^2$, the association rate increases almost linearly with C, and for $C > C_2$, it tends to a maximum value.

Chapter III Results

3.1 Unsynchronized adhesions

3.1.1 Dynamics of cell-substrate contact areas during spreading and motility

Recall of thesis work of S. Keller

Before a cell adheres on a surface, it has to make a first contact point with the substrate. A few seconds after, a significant cell adhesion area is visible and cells start to extend pseudopods in one or several directions. A succession of pseudopods follows, resulting in an anisotropic increase in cell-substrate contact area. After about one minute, the cell starts retracting part of its contact area. At this point, pseudopods still extend but their growth rate decreases to match the retraction activity. Once a balance between *gain (area increased)* and *loss (retracted area)* areas is reached, spreading is over and cells start to move on the surface in a given direction (Fig 3.1).

Globally, *Dictyostelium* cells spread fast (1-2 min), in an anisotropic manner. A representative example of cell spreading on a glass surface in SB (Sörensen buffer – see Materials and Methods), is shown in Fig. 3.1.

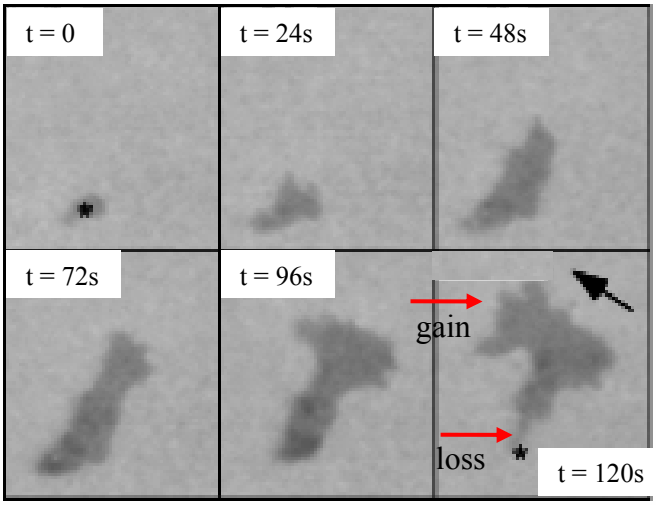

Fig. 3.1 RICM images of a *Dictyostelium* cell spreading on a glass surface in the presence of 500 µM $CaCl_2$. After full spreading, the cell starts moving in the direction indicated by the black arrow (t = 120s). The asterisk in the first and last frames indicates the initial contact point. The red arrows indicate the loss and the gain areas.

Cells were allowed to sediment on a glass surface in SB and cell-substrate contact areas were visualized by Reflection Interference Contrast Microscopy (RICM, see Materials and Methods). Cells had various forms, elongated or more rounded, spread rapidly or slowly, and reached different maximal area (example shown for 3 cells, Fig 3.2). However, for all cells one can distinguish two steps in spreading kinetics (total contact area as a function of time): a quasi-linear increase in contact area was followed by a plateau phase.

For each individual cell, recording time started when the cell made contact with the substrate, corresponding to a visible area of about 2 μm^2. For the cell of Figure 3.1, after the initial contact, cell-substrate contact area mainly increased in a single direction for about 60 sec, then a new spreading direction appears at 90° from the first one. At the same moment, the cell started retracting its initial contact area. Maximum cell-substrate contact area was reached at 100 sec (generally the average is 110 μm^2) and from that time, cell-substrate contact dynamics resulted in net cell movement.

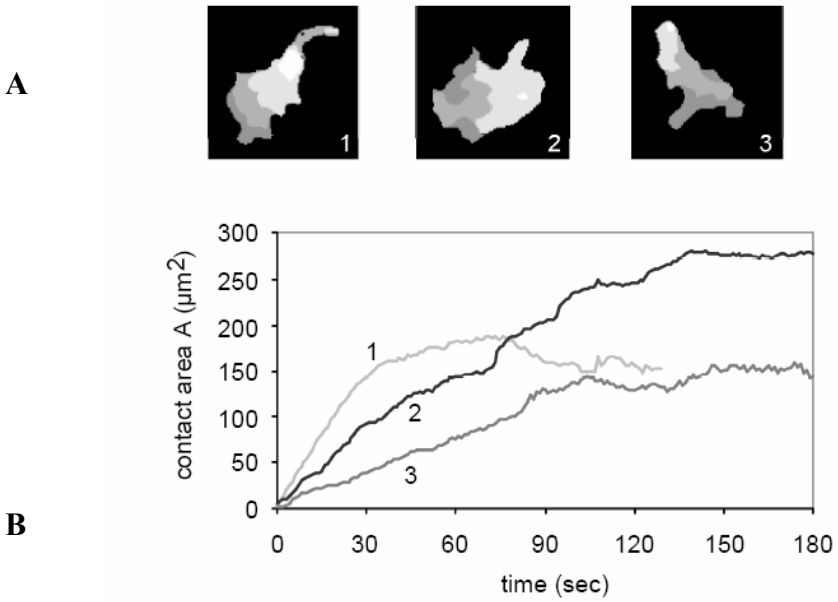

Fig. 3.2 Illustrative examples of *Dictyostelium* form variability during spreading
A: Composite picture showing in increasing greyscale, the area gained by the cells during 24 s at time intervals of 3 seconds. B: Spreading kinetics of the three cells shown in A: total contact area as a function of time.

Cells need actin polymerization for spreading

Chamaraux derived a very general expression, describing cell spreading (Chamareaux, 2005) (Eq.3.1):

$A(t) = A_{max} \tanh(\alpha t)$, where α is a characteristic spreading time constant Eq. 3.1

The hypothesis underlying this model is the control of cell spreading by actin polymerization, following two antagonist processes: i) stimulation of actin polymerization through a cell-substrate contact-induced signaling. ii) initiation of actin depolymerization by membrane tension, which increases with the contact area.

Cell spreading requires actin cytoskeleton remodeling. This is clearly shown by adding latrunculin A (3μM), a drug that promotes actin filament depolymerization. This drug strongly decreases the initial spreading of *D. discoideum* cells and makes that contact surface round (Fig.3.3).

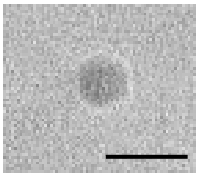

Fig. 3.3 RICM image of contact area of a cell in SB +3 μM Lantraculine on glass; the bar scale is 2 μm

Equation 3.1 contains two parameters: A_{max} (μm^2), the maximum area observed between the cell and the substrate, and α (s^{-1}), the characteristic spreading time. This equation was used to fit the spreading kinetics shown in Fig. 3.4 (A_{max} = 201 ± 6 μm^2; α = 0.0115 ± 0.0007 s^{-1}). The global shape of the spreading kinetics is in good agreement with the model's prediction. However, in details, experimental data sometimes vary significantly from the model curve, exhibiting alternatively faster and slower spreading events. In order to characterize better the details of the kinetics, cell-substrate area variations was decomposed *into gain and loss zones* (Fache, 2005).

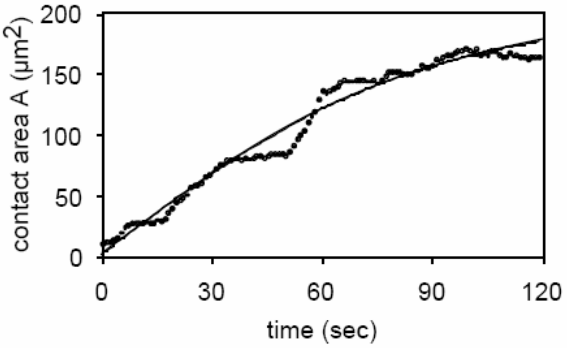

Fig. 3.4 Spreading kinetics of the cell shown in Fig. 3.1: total contact area as a function of time (black points). The solid line is a fit of the experimental data with Eq. 3.1.

Protrusion and retraction zones were defined as the area gained or lost over a 3 seconds time interval. Fig. 3.5A shows the areas gained during 20 seconds intervals for the considered cell. Protrusive and retractile activities (μm^2/sec) for the cell shown in Fig. 3.1 were plotted as a function of time in Fig.3.5B.

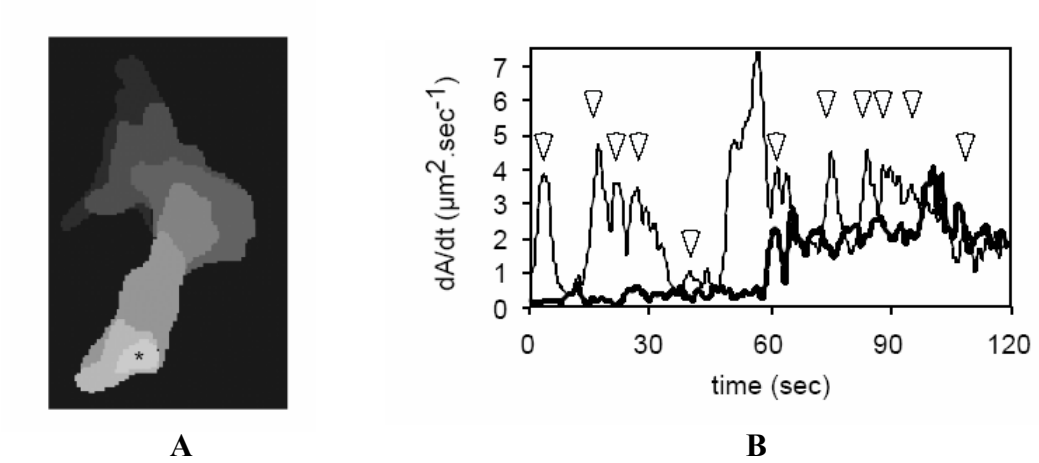

A **B**

Fig. 3.5 **A**. Composite picture showing in increasing greyscale the area gained by the cell shown in Fig 1, during successive time intervals for 24 s. The initial contact area appears in white.
B. Dynamics of cell-surface contact areas during spreading of the cell: gained area (thin line) and lost area (thick line) as a function of time. Arrowheads point to significant protrusion peaks.

As the cell reached the substrate, only protrusion activity was detectable, and retractions started only at 55 seconds. The end of spreading and the transition from spreading to motility corresponds to the moment when protrusion and retraction curves first cross. From the above figure, it is obvious that protrusive activity was not steady, but exhibited large peaks.

Plotting the time occurrence of successive significant protrusion peaks reveals that they appear regularly. For the cell under study, the mean period Δt was about 11.5 seconds (Fig. 3.6).

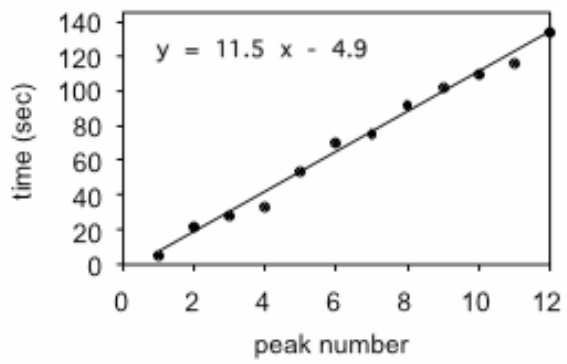

Fig. 3.6 Time occurrence of successive peaks in the kinetics of gained area shown in Fig. 3.5. The distribution can be linearly fitted, defining an average period of 11.5 s.

Keller studied a set of 15 cells spreading on a glass surface. For a given cell, a characteristic period *T* was determined by averaging Δt. This period does not significantly vary from cell to cell (<T> = 10.68±1.9 s), which shows that most variation indeed originates from intrinsic fluctuation of cell activity.

Furthermore, oscillations in protrusion activity are clearly visible. Quantitatively, the first maximum in the protrusion curve does not appear randomly, but occurs at 6.24 ± 2.64 seconds after cell-substrate contact. The uncertainty in the position of the first peak is due to the lack of precision in the determination of the initial time of contact with the substrate, since it corresponds to very small areas. Therefore, the contact with the substrate could trigger the first protrusion peak.

The uncertainty in the onset of spreading generates phase differences between cells that mask their common behavior. In order to phase cell contributions together, one can shift individual cell protrusion kinetics along time so that the first maximum occurrs at 6 seconds upon cell-substrate contact. This phasing procedure clearly increased the size of the oscillations seen on average protrusion kinetics (Fig. 3.7), supporting the existence of a common 10.8 seconds period.

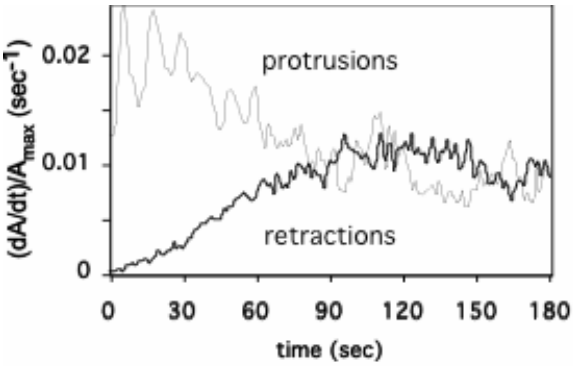

Fig. 3.7 Average of normalized gain and loss kinetics after alignment of kinetics on the first peak of gain activity (set at 6 s). The statistical error is 0.0022 s^{-1}. The averaged time interval between the 6 first peaks is 10.8 ± 2.0 s for 15 cells.

Oscillating protrusion activity is molecularly driven by actin polymerization. We therefore extended the work of S. Keller by monitoring the kinetics of actin polymerization near the surface that accompanies spreading.

3.1.2 Cyclic actin polymerisation activity during cell adhesion in SB

In order to verify the oscillating character of actin polymerization, epifluorescence microscopy was employed. LimE-GFP cells were used for fluorescent tracking of actin polymerization in SB. Here, we used a fluorescent version of Lim protein (a GFP fusion construct with a fragment of LimE, LimE-GFP) to display and to measure the actin dynamics in Dictyostelium.

In time course of the cell spreading LimE – GFP fluorescence appeared and disappeared locally (Fig. 3.8). We named these short-lived localized activities *fluorescence events*. They indicated a local actin polymerization followed by a depolymerization.

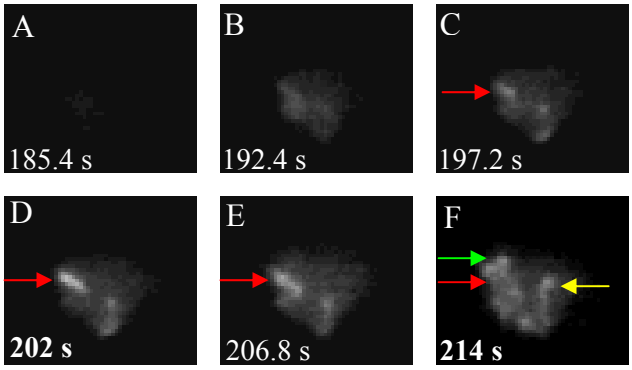

Fig. 3.8 Examples of LimE$^{\Delta coil}$-GFP fluorescence events during a *Dictyostelium* cell spreading on a glass surface. A and B, chronological images during cell sedimentation, one can observe the cell approaching to the surface; C, the red arrow point a zone with an increased fluorescence; in the same place the fluorescence will reach a maximum (D) and will decreases (E) until its total evanescence (F); in the same time in the other zones, an increase of fluorescence activities take place (F, green and yellow arrows). The intensity of fluorescent zones which are not pointed out by arrows were under the threshold established by us or were not localized at the cell edges (see Materials and Methods).

Focusing at glass surface, the first observed fluorescent event (Fig. 3.8 and Fig. 3.9 – at t = 202 s) indicated that the cell adhesion has already occurred. We do not know with exactitude when and where at the surface, the first contact point had taken place and if it coincides in time with the maxima of fluorescence event or in space with the event localization. Nevertheless, successive fluorescent events less or more regularly spaced in time were observed, indicating oscillating actin activity.

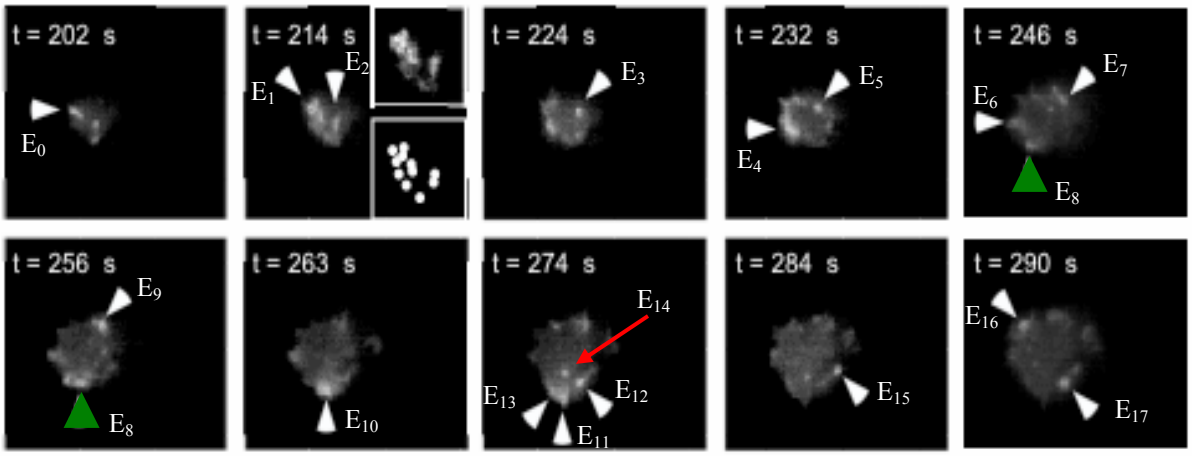

Fig. 3.9 LimE$^{\Delta coil}$-GFP fluorescence images of a *Dictyostelium* cell spreading on a glass surface. Arrows point to regions of significant actin polymerization (Event-E_i). At t = 214s, upper inset: brightness and contrast are changed to enhance the visibility of actin foci; lower inset: the position of individual actin foci is denoted by spots. The fluorescent zones which are not pointed by arrows are under the established intensity threshold or do not occur at the cell edges – e.g. red arrow (see Materials and Methods).

We employed the following technique for identifying the actin polymerization events: every fluorescent zone was quantified individually and they were plotted in the same graph using different colors, which allowed identifying individual events (Fig. 3.10). There are events that occur frequently at the same time. The events (E_i) are identifiable to the maxima of fluorescence observed in the images of Fig. 3.9.

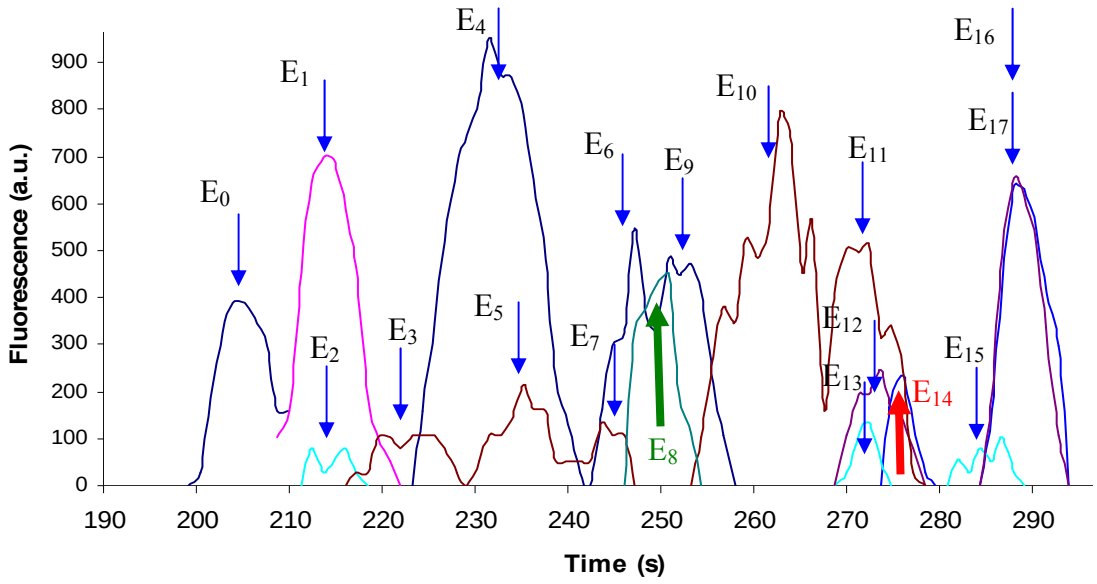

Fig. 3.10 Individual fluorescence in regions of significant fluorescence reinforcement (E_i), for the cell shown in Fig. 3.9. For sake of clarity, recordings corresponding to different regions are coloured differently. Green arrow correspond to an event seen in two images taken at 246s and 256 s shown in Fig. 3.9, and red arrow points an event which not occurs at the cell edge.

The first event (E_0) corresponds to the first fluorescence maxima when the cell began to contact the surface under gravity. The fluorescence activity is later reinforced approximately in the same zone, inducing the presence of two successive actin polymerization events only spaced in time.

Individual events often – but not always - match changes in cell protrusion direction. This is especially obvious for cells extending successive protrusions in different directions. Since actin polymerization maxima that are located in different areas of the cells appear simultaneously (see Fig 3.9 and 3.10, for example, E_1-E_2), one can infers that the actin cytoskeleton is organized globally.

It can be noticed that an oscillating process of actin polymerization occurs. This pulsatory process suggests that the first contact point with the substrate triggers actin polymerization that could deform the cell membrane and lead to the formation of successive contact points.

The time of occurrence of the maxima of the peaks appearing in Fig. 3.10 (without those pointed by the red arrow) was plotted against the corresponding peak number, considering the first event (Event0) as the origin. Thus, for the studied cell, we obtain the following representation of fluorescent maxima events number versus time (Fig. 3.11):

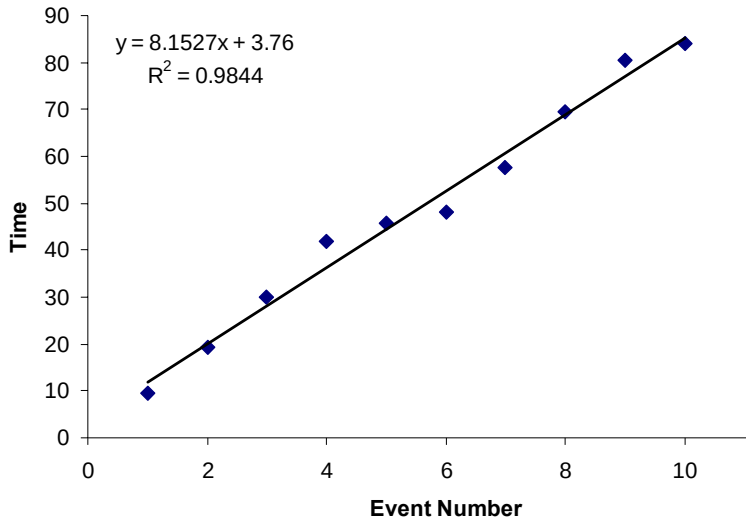

Fig. 3.11 Time occurrence of successive peaks during cell adhesion in SB; the distribution was linearly fitted, defining an average period of 8 s

We also can define an average period of maxima apparition.

From a group of *18* studied cells, *14* cells (78%) exhibit 6 or more, fluorescent event peaks within 65 s after the apparition of the first peak and *4* cells had less than 6

peaks after the apparition of the first peak. For the cells that had 6 or more fluorescent event peaks, the time interval between the maxima was 4-11 seconds (Fig. 3.12A). The probability of an event apparition after the first event (E_0), is another important parameter. Every probability was calculated by counting the cells that having a maximum in a given one-second interval, divided by the total number of analyzed cells (*14* cells) (Fig. 3.12B).

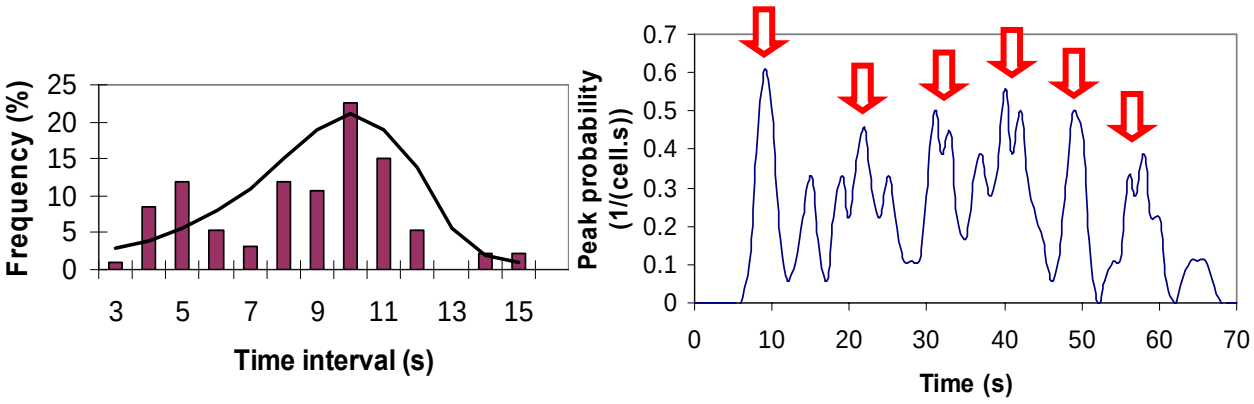

A **B**

Fig. 3.12 (**A**) Histogram of time intervals between adjacent peaks of LimE$^{\Delta coil}$-GFP fluorescence reinforcement. For all cells, the first peak is set to t = 0 s. The solid line represents the best fit of the experimental data with a normal distribution. (**B**) Frequency of appearance of LimE$^{\Delta coil}$-GFP fluorescence peaks, after the first peak, for 14 individual cells as a function of time. The data were expressed as probability of appearance of a peak per cell and per second.

Analysis of Fig. 3.12B shows that the probability for the second polymerization event to appear, for all the cells, between 10th and 11th seconds after the apparition of the first event (E_0), was approximately 0.6 $s^{-1}cell^{-1}$. If we integrate over a 3 seconds window, 72% of the cells would have the second peak between 8 and 11 seconds after the first one. Moreover, the probability that the cells have three peaks of activity at 9.5±1 s, 22±1 s and 31±1 s is higher than 0.2.

3.1.3 Cells that contact the surface under the action of gravity are not synchronized

In this experiment, the cells were not synchronized because they undertook the action of gravity, thus they were making the first contact points with the substrate at different times (Fig. 3.13). Moreover, the time of first contact with the surface (t_0) was not precisely known.

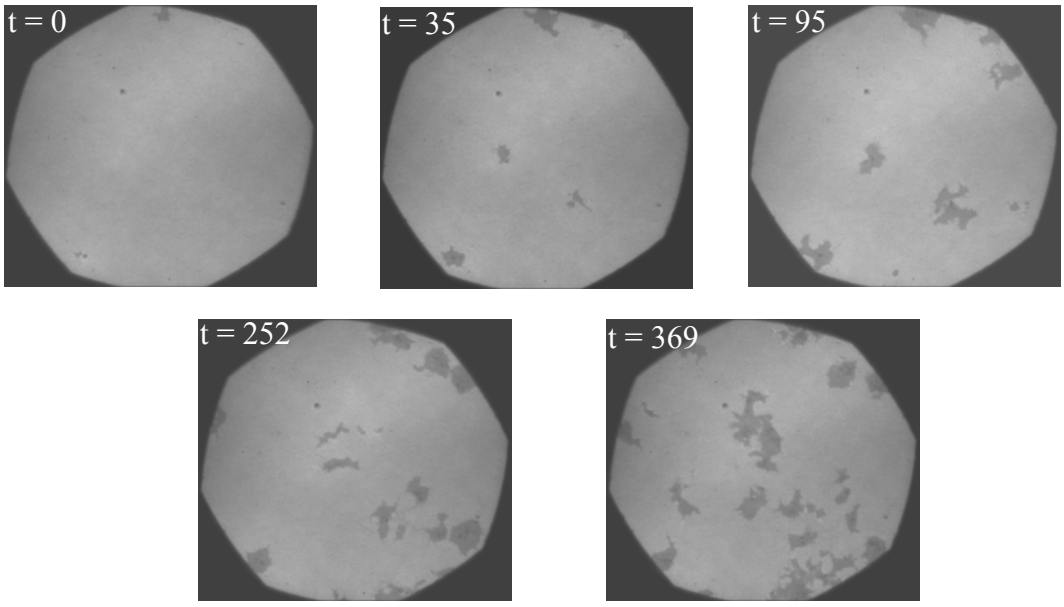

Fig. **3.13** Sequence of RICM images with the AX_2 cells sedimentation on glass surface under the action of gravity.

We denote here the *asynchrony* as the time difference between the moments at which the first and the last cell arriving on the surface started spreading. For the experiment shown in Fig. 3.13 asynchrony was 369 s.

A biochemical analysis would be profitable if an entire cell population (minimum of one million cells) would make the first contact point with a surface at the same time, starting the actin polymerization process in a synchronized way.

Conclusions:

We have shown in this subchapter that *Dictyostelium* cells spread using a periodic protrusion activity. Moreover, the actin polymerization, which drives membrane protrusions, is also oscillatory with almost the same period.

In the next subchapter, we will analyze the effect of an applied potential on the cells deposited on a conductive material, aiming to synchronize their spreading on the surface.

3.2 Electric field influence on adherent cells

3.2.1 Influence of the electric field on the cells deposited on the ITO material

Introduction

It is well known that *Dictyostelium discoideum* adheres to all kinds of treated or non-treated materials or substrates, in different buffers and in a wide range of buffer concentrations. We first used indium tin oxide (ITO, see Material and Methods) covered glass to test cell adherence in standard conditions and without the use of external current source. Thus, in 17 mM SB (SB - Sörensen buffer, see Material and Methods) and 1.7 mM phosphate sucrose buffer, cells falling under the action of gravity (G) adhere in identical way on both glass surface and ITO substrate (Fig. 3.14).

At the ionic strength of I = 24 mM and even less, I = 2.4 mM, the electrostatic repulsive force ($\mathbf{F_e}$) between the negative groups of the cell membrane and the negative charges of ITO oxides (Fig.3.15), appearing on the surface in contact with the buffer solution, is not sufficient to inhibit cell surface contact and spreading. Moreover, there is an attractive potential that can be taken into consideration (Evans, 1995), especially for small distances from the surfaces (less than 2.5 nm)-see DLVO theory (Overbeek, 1984).

The apparent gravity force (**Ga = G - Fa**) on a *D. discoideum* cell can be estimated from its volume (500 fL), its density (1.0665 g/cm^3) (Fukui, 2000) and taking into account the Archimedes force (**Fa**), to be 0.3 pN ($Ga = \Delta\rho \cdot g \cdot V = 0.066 \cdot 1000 \cdot 10 \cdot 500 \cdot 10^{-18} = 0.3 \cdot 10^{-12}$ N).

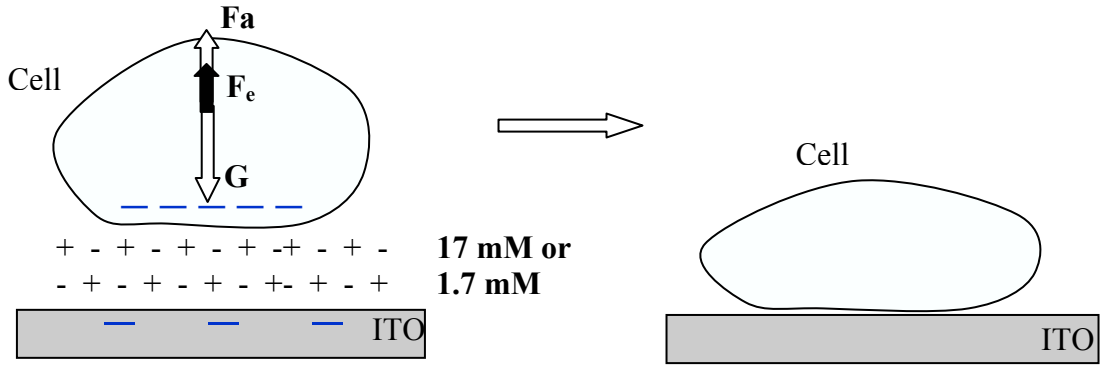

Fig 3.14 Schematic way of cell spreading; the electrostatic repulsion don't prevent the cell adhesion; **Fa** - Archimedes force, $\mathbf{F_e}$ - electrostatic repulsive force, **G** – gravity.

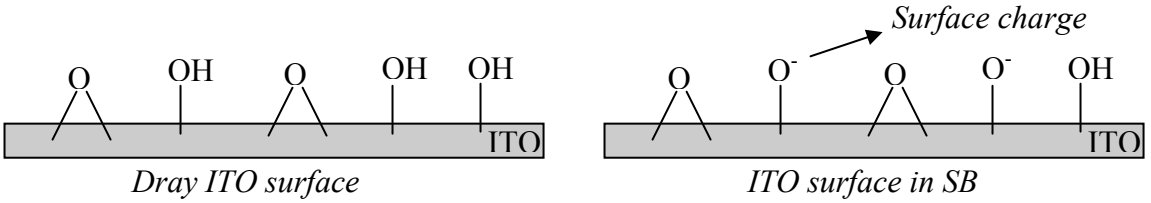

Fig. 3.15 (**A**) Schematic distribution of the chemical surface groups on a dry ITO surface; (**B**) charge surface groups formation after the surface immersion in electrolyte

Thus, if cells adhesion has to be prevented, a repulsive force of at least 0.3 pN must be applied.

Influence of positive potentials

In order to determine the influence of an imposed positive potential (current) on the cell activity, in 17 mM buffer solution (SB), we first employed the setup with 3 electrodes (see Materials and Methods). *Dictyostelium discoideum* cells were introduced in the electrochemical chamber (see Fig. 3.16A) in SB and after the cells had adhered to the surface, a potential was applied at the ITO surface. In all experiments, involving SB solution, we did not observed any effects on the cells activity, even for the highest potentials applied at the ITO surface.

It is very well known (see Materials and Methods) that the ionic screening effect is decreasing with the decrease of the ionic strength (Debye radius is inversely proportional to the ionic strength). In view of these, we diluted ten times the buffer solution obtaining a 1.7 mM phosphate sucrose buffer solution (see Materials and Methods).

All the results presented here were obtained for 1.7 mM phosphate sucrose buffer.

The first important result was the observation that when a minimal potential of +1.5 V/Ag, AgCl ($I = 10^{-3}$ mA for 20 s) was applied, the cell membrane became black (Fig. 3.16B, black arrow) as observed by RICM (see Material and Methods). Given RICM interferential laws we attributed this phenomenon to a close contact between cell membrane and the ITO surface, which could suggest an attraction phenomenon.

Moreover, during the potential application and even after, the contact surface decreased and became round. Moreover, the frequency and the number of protrusions were drastically diminished or even stopped for a definite period (*impairment or delay of dynamic activity*, see also Table 3.1). *Recovery time* is defined like the period between the end of the electrical pulse and the moment when the cells revival their initial dynamic activity. The dynamic activity impairment is shown by RICM images for a 1V potential pulse during 60 s (Fig. 3.16C) and by Phase Contrast (PC) images after 60 s for a 2V pulse application (60 s) (Fig. 3.16E).

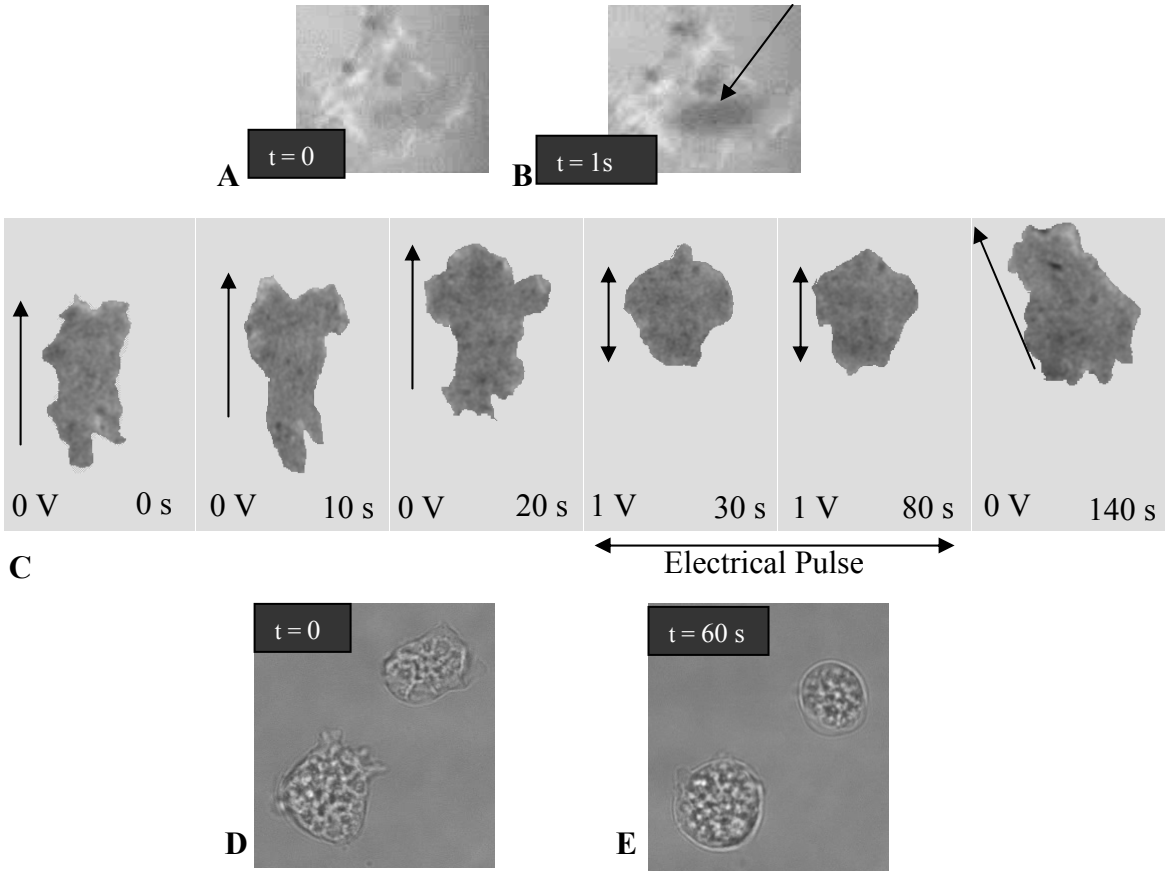

Fig. 3.16 Successive images (A, B) showing the close contact between the membrane and the surface; (C) RICM images of a cell showing the delay in cellular activity when 1V potential pulse during 60 s is applied (the arrows indicate the moving sense; double arrow indicate a stagnation); (D) and (E): successive phase contrast (PC) images before and after 60 s for a 2V pulse application (60 s).

We summarize the results of the experiments in two tables. The first one (Table 3.1) shows the cellular responses as a function of electrochemical parameters when a positive potential was imposed, in 1.7 mM phosphate sucrose buffer.

Table 3.1. Cellular response as a function of positive potentials at the ITO substrate

	1	2	3	4	5
	Imposed	Measured	Calculated	Observations	
	Potential (V/Ag, AgCl) and time of application (s)	*Current average intensity (mA)*	*Minimal pH value*	*Attractive electrostatic effect Attraction Max:+++*	*Cellular dynamics and motility*
1	+2.5 (2 s)	$+4*10^{-1}$	*3.1*	+ + +	*no delay of activity*
2	+2 (60 s)	$+3*10^{-2}$	*3.4*	+ +	*activity stopped, cells remain glued on the surface*
3	+1.5 (20 s)	$+5*10^{-3}$	*4.4*	+	*delay of activity, recovery after 150 s*
4	+1 (60 s)	$+1.5*10^{-3}$	*4.7*	no effect	*delay of activity, recovery after 60 s*
5	+1 (30 s)	$+1.5*10^{-3}$	*4.85*	no effect	*delay of activity, recovery after 17 s*
6	+0.8 (120 s)	$+5*10^{-4}$	*5*	no effect	*limit of delay of activity*

The minimal pH value reached during the potential pulse was calculated by Comsol simulation taking into account the diffusion of the generated protons ($D = 10^{-4}$ cm/s^2) but not considering the proton or hydroxyl migration in the created electric field (their concentration is lower than that of the salts composing the buffer). After application of the potential, the proton production is stopped and the system homogenizes by diffusion.

It can be observed that minimum value of the potential for which an effect on the cell's activity can be observed (Line 5) corresponds to pH = 4.85, which is close to the p.z.c of ITO surface.

If we compare lines 2-6, we observe that recovery time of cellular activity increases with the decrease of the minimum pH value. For short duration time of potential pulse (line 1), we notice that even for lower pH (so higher protons concentration), no sign of cellular dynamics impairment was observed. One can deduce that a longer exposure to an acidic pH affects cell activity more importantly (the activity can be stopped definitively, see line 2).

If we compare now column 1 and 4 one can notice that the membrane attraction to the surface increases with the value of the imposed potential. Regarding the calculated pH values, we can notice that the attraction force increase correlates with an increase of the maximal concentration of produced positive ions (protons). Thus, we suggest two factors who could contribute to this phenomenon: 1) The negative charges of ITO surface (pH depending, see fig. 2.16) and cell membrane are neutralized by the produced protons during the application of the positive potential; the repulsive force being diminished the cells could contact the surface. 2) The second factor takes into account the electrophoresis transport of charged microparticles (cells), the cells moving in the created electric field with much lower speed (1 μm/s in a 1V/m electric field for a cell of 10 μm in diameter (Gingell, 1976)) than lighter and more mobile negative charged ions (migration).

In conclusion, the cells seem to be attracted on the surface if the pH value is lower than 4.7 and seem to tolerate short (1 to 5 s) positive potentials.

The role of calcium in cell dynamic activity

The Ca^{2+} ions have an important role in the dynamic activity of the cells, as can be observed in the Table 3.2.

Table 3.2. Cellular response as a function of positive potentials at the substrate, in 1.7 mM phosphate sucrose buffer + 100 μM Ca^{2+}

1	2	3	4	5
Imposed	Measured	Calculated	Observations	
Potential (V/Ag, AgCl) and time of application (s)	*Current average intensity (mA)*	*Minimal pH value*	*Attraction electrostatic effect Max:+++*	*Cellular dynamics and motility*
+1.5 (20s)	$5*10^{-3}$	*4.4*	+	*no effect on the cell's activity*
+2 (50s)	$3*10^{-2}$	*3.45*	+ +	*delay of activity, recovery after 10 - 90 s*
+2.3 (50s)	$2*10^{-1}$	*2.6*	+ + +	*activity stopped, cells were glued on the surface, some cells recover after 10 minutes*
+2.5 (50s)	$4*10^{-1}$	*2.3*	-	*explosion of the cells*

In comparison with the Table 3.1, we can notice (see column 3 and 5, Table 3.2) that the cells in the presence of Ca^{2+} are more active after a long exposure to a low pH. Regarding the attraction force, it did not change with Ca^{2+} concentration (see column 1 and 4, Table 3.1 and 3.2). We can notice that if the pH value decreases under 2.5 and the cells were submitted to such low pH for longer time than 50 seconds, the cell membrane is destroyed.

Influence of the negative potentials

We have seen that positive voltage pulse induce blackening of the cell membrane. On the contrary application of a negative potential of -1 V/Ag, AgCl ($I = -10^{-2}$ mA for 5 s) results in white spots which appeared on the surface of the cells in the first two seconds during the application of the negative potential (Fig. 3.17B). When the potential application time was extended to more than 60 s (see Table 3.3), the cell activity was also impaired.

Based on the RICM laws, we attribute the apparition of the white zones to an uplifting of the cell membrane from the surface, which suggests the apparition of a repulsive force between cell membrane and the ITO surface. Note that this uplifting is a not uniform, large aria of cell membrane remains dark (Fig. 3.17B)

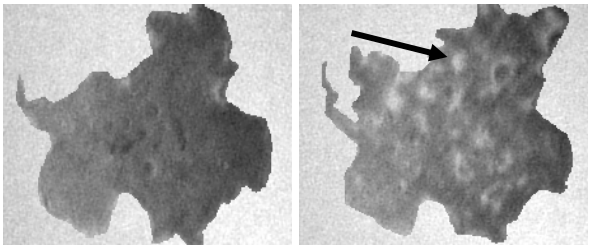

A B

Fig 3.17 Succession of RICM images before (A) and during (B) -1 V pulse application. In the first second of the pulse application white spots appeared (one of these is pointed by a black arrow) at the membrane-surface interface (B).

When a negative potential was applied, the cells in 1.7 mM phosphate sucrose buffer had different responses in function of the time of potential application (Table 3.3).

The minimum value of potential for which we obtained an effect on the cells dynamics was -0.5 V/Ag, AgCl, if the application time is greater than 60 seconds (line 1).

Table 3.3. Cellular response as a function of negative potential at the ITO substrate

	1	2	3	4	5
	Imposed	Measured	Calculated	Observations	
	Potential (V/Ag, AgCl) and time of application (s)	*Current average intensity (mA)*	*Maximal pH value*	*Repulsion electrostatic effect Max:+++*	*Cellular dynamics and motility*
1	-0.5 (60 s)	$-1*10^{-3}$	*9*	no effect	*delay of activity, recovering after 15 s*
2	-1 (100 s)	$-1*10^{-2}$	*10*	+	*delay of activity, recovering after 60 s*
3	-1 (5 s)	$-1*10^{-2}$	*9.6*	+	*activity is not affected*
4	-1.3 (5 s)	$-2.8*10^{-2}$	*10*	+ +	*activity is not affected*
5	-1.5 (5 s)	$-5*10^{-2}$	*10.3*	+ + +	*activity is not affected*

If we look at line 2 and 3, we can notice that for the same potential and current intensity value and for a significant difference of application times we obtained the same repulsion effect and an important delay of activity when the cells are exposed for a long time to a high pH (see column 3 and 5).

The repulsion of the membrane from the surface is related to the potential and current intensity values (line 3, 4 and 5).

For potential application times of a few seconds (1 to 5 s) and if the maximal pH value is smaller than 10.3 during the potential application, no visible cellular activity impairment was observed (see lines 3, 4 and 5, column 5).

We can attribute the membrane repelling from the surface to repulsive effect of negative surface charges and to electrophoretic force, helped by the rupture of adhering bonds by alkaline pH.

Are the cells affected by the positive or negative potential application?

In order to test the cell viability during the potential application on ITO surface, experiments with IP (propidium iodide) were performed. Thus, for maximal potential and

current intensity (+2.5 V/Ag, AgCl, I = $5 \cdot 10^{-1}$ mA for 5s and -1.5 V/Ag, AgCl, I = $-5 \cdot 10^{-2}$ mA for 30 s respectively) no damage of the membrane was observed. In both experiments, we identified one cell among 10^3 that was suspected for membrane damaging, similar percentages were found without using a potential pulse.

Can we prevent cell adhering on ITO using a negative potential and synchronize their spreading?

Even at the maximal value of the negative potential which can be imposed on ITO material (-1.5 V/Ag,AgCl for 30 s, $-5 \cdot 10^{-2}$ mA current), cells already adhering to the surface in 17 mM or 1.7 mM phosphate buffer could not be detached from the surface. Sedimenting cells also adhere despite a high negative potential which was applied on the ITO surface. So, the accumulation of negative charges of ITO surface (pH depending, see fig. 2.16) being less significant, also the electrophoretic effect was not sufficient to inhibit cell surface contact and spreading.

Thus, a new approach was taken into consideration: uses other conductive materials allowed us to impose higher potentials (and higher currents) in 1.7 mM phosphate sucrose buffer without destroying the substrate.

3.2.2 Influence of the electric field on the cells deposited on other conductive materials (Ti, Au and Pt)

Titanium surface

Deposited on a thin glass surface covered with Ti (see Materials and Methods), the cells in 1.7 mM buffer solution, were submitted to +2 V/Ag, AgCl (I = 10^{-1} mA, 1 minute). Even for long exposure time (1 minute), no cell attachment was observed but a very short delay of the cell dynamic appeared (Fig. 3.18C); we presume that in this case all faradaic current was mainly due to the titanium oxidation (the surface becomes transparent, fig. 3.18B) involving the following steps:

$$Ti - 2e^- \Leftrightarrow Ti^{2+} \quad E^0 = 1.63\ V/SHE$$

$$Ti^{2+} - e^- \Leftrightarrow Ti^{3+} \quad E^0 = 0.368\ V/SHE$$

$$Ti^{3+} + H_2O - e^- \Leftrightarrow TiOH^{3+} + H^+ \quad E^0 = 0.055\ V/SHE$$

In this case, protons are produced in a fourth lesser amount than when water electrolysis occurs on the ITO surface at the same potential difference. This could explain the absence of effect on cellular dynamics. A strong cell attraction effect was not observed because of the dissolution of the titanium film, which possibly created a natural convection effect, accelerating the dissipation of proton gradient.

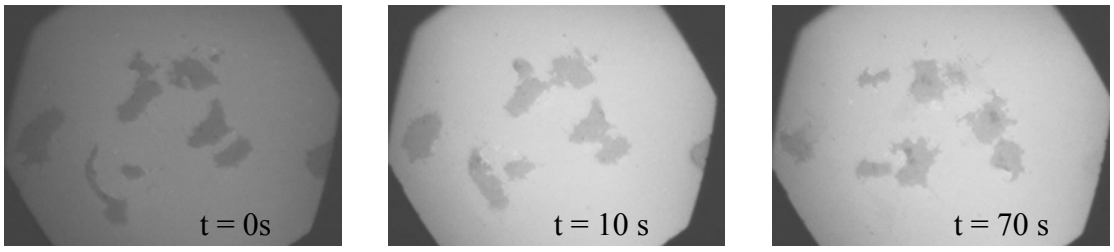

A **B** **C**

Fig. 3.18 RICM images showing the relative contrast changes during experiment. (**A**) adhered cells on Ti surface at the beginning of 2 V/Ref. pulse application (60 s) (**B**) only after 10 s it can be observed a contrast change (background becomes brighter) without effect on the cell dynamic (**C**) 70 s after the pulse, the cells are apparently no affected by the formed protons.

When we applied in 1.7 mM phosphate sucrose buffer, a negative potential (-3 V/Ag, AgCl, I = $-5 \cdot 10^{-1}$ mA for 1 minute), to the titanium surface, the inner zones were pushed away from the surface (Fig. 3.19B). 60 seconds after the pulse onset, the cell contact area on the substrate decreased very much, the cellular edges being pushed away from the surface (Fig. 3.19C). 30 seconds after the end of the potential application the cells restored their initial state and dynamics (Fig. 3.19D). A total detachment was not obtained. The cells did not explode despite a high current intensity. In addition, the point of zero charge (p.z.c.) of TiO_2 is 6 (Pierre, 1998). All these suggest a high capacitive current due to the thick porous oxide layer (Schneider, 2009). Thus, less HO^- ions are produced by applying a negative potential, compared to ITO. In the same time, the electrophoretic forces acted to detach the cells.

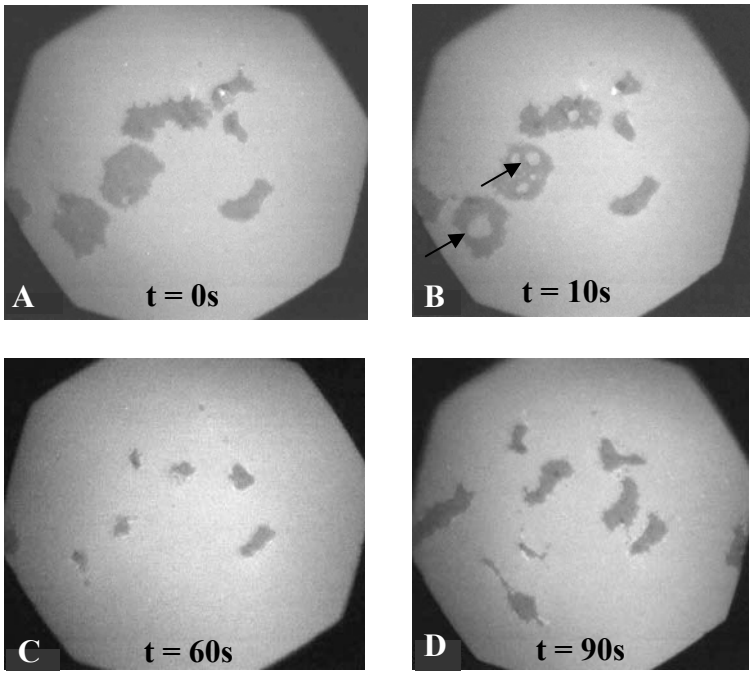

Fig. 3.19 RICM images for (**A**) before (**B, C**) during and (**D**) 30 s after the end of a -3 V/Ag, AgCl ($I = -5 \cdot 10^{-1}$ mA) negative potential pulse application on Ti surface (contrast was modified for a better visualization)

Platinum and gold surfaces

In order to increase the current intensity, so to increase the electrophoretic force, platinum and gold surfaces were prepared (see Materials and Methods). These materials indeed exhibit no oxide layer in standard conditions.

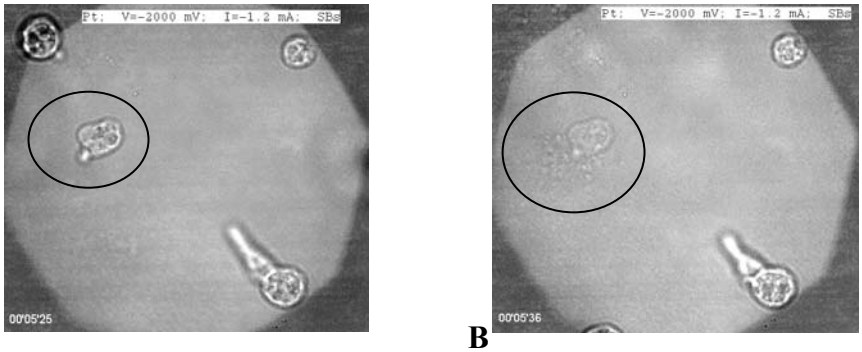

A **B**

Fig. 3.20 Phase contrast (PC) images (**A**) before and (**B**) during the cell explosion (ellipse); a -2 V/Ag,AgCl potential was applied on a Pt surface.

The cells were submitted to -2 V/Ag, AgCl negative potential, (I = 1.2 mA for 1 minute). Because of the high current intensity (platinum is a catalyst for water reduction), a large amount of HO^- is produced and, after only 1 minute, the adhered cells exploded (see figure 3. 21B, ellipse).

The same explosion effect was also observed when cells were submitted to a strongly basic NaOH 10^{-2} M solution during 1 minute.

Conclusions

Using different conductive materials (ITO, Ti, Pt and Au) we tried to detach the adhering cells in 17 mM and 1.7 mM buffer solutions or to impair their contact with the surface by imposing a negative potential (current) at the material surface while they are falling under the gravity. Even for the highest negative potentials the materials or the cells can support, we did not prevent cell adhesion.

In order to synchronize cell spreading, a new approach was then taken into consideration:

- in a first step we will keep the living cells in suspension at a certain distance from the surface (*d*, in Fig. 3.21) by decreasing the ionic strength of the buffer solution (the osmotic pressure was kept at 36 mOsm by adding sucrose) and so, this will increase the repulsive force (F_e).

- in a second step we will induce cell contact and spreading on the surface either by increase of the ionic strength or by electrochemical means.

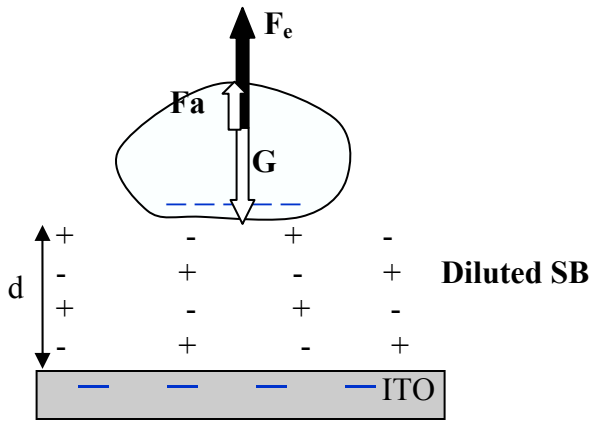

Fig. 3.21 Scheme of a levitating cell; the electrostatic repulsion prevents the cell adhesion.

3.3 Control of cellular adhesion by changing buffer concentration, salts nature or by surface chemical treatment

3.3.1. Electrostatic repulsion between *D. discoideum* cells and a glass surface

Introduction

In order to synchronize cell spreading, a new approach was taken into consideration: to keep the living cells in suspension at a certain distance from the surface, despite the apparent gravity (G_a). It is very well known that the ionic screening effect which decreases with decreasing of the ionic strength (Debye radius is inversely proportional to the ionic strength) influence cell adhesion (Gingell, 1976, 1982; Trommler, 1985). Wolf and Gingell (1983) studied the effect of dilution on unfixed red cells pre-adherent to glass in isotonic solutions and got interferometric evidence for spatially uneven separation on dilution. Cells that settle at low ionic strength make smaller and more uniform contacts with glass than do cells that initially settle at higher ionic strength and are then subjected to dilution.

Vigeant and Ford (1997) evaluated whether the attractive potential component considered in the DLVO method could explain the reversible adhesion of *E. Coli* bacteria to the glass surface. They did not find quantifiable changes with ionic strength for either the tendencies of individual bacteria to approach the surface or the overall times bacteria spent near the surface but, they did observed that the diameters of the circles which the smooth-swimming bacteria traced out on the glass increased in low ionic strength solution.

According to these results, decreasing the ionic strength of the buffer solution (the osmotic pressure being kept at 36 mOsm by adding sucrose), could increase the repulsion force (F_e) and then equilibrate the apparent gravity at a given distance *d* (Fig. 3.22).

The strength of ionic interaction forces in solution depends on the surface charge density and on the Debye radius (or Debye distance). The first one depends on pH for the oxide materials and the second one depends on the ionic concentration of the solution and on the nature of ions, at a given temperature.

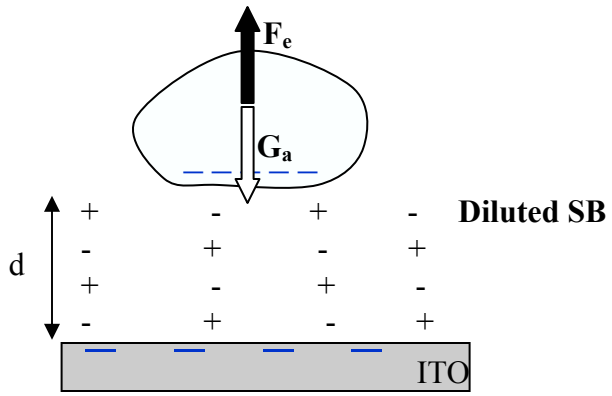

Fig. 3.22 Scheme of a levitating cell; the electrostatic repulsion prevents the cell adhesion; $G_a = G - F_a$.

Dilution effect on Dictyostelium cells

D. discoideum cells exhibit a negative charge in a physiological solution *ie* a phosphate buffer (SB, see Materials and Methods).

It is known that glass surfaces are also negatively charged (20). In order to quantify these surface charges we measured the zeta potential for the living cells and different surfaces in SB solution (Table 3.4). The zeta potentials for the surfaces were deduced from the measurements of the streaming potentials (see Materials and Methods). Although the method does not apply to conductive surfaces, our ITO material is a doped semiconductor with a resistance of 20 Ω·cm, for which zeta potential measurements in 10^{-2} M 1: 1 electrolyte solution reflect the real values with a good accuracy.

Table 3.4 Zeta potential of different substrates and for the *Dictyostelium* cells in SB (pH = 6.13)

Substrate	PMMA	APTES	Glass	NaOH Treated Glass	ITO	Active cells	Latrunculin-treated cells
Zeta Potential (mV)	-32±3	+1±2	-20±5	-31±4	-16±5	-17±3	-18±2

The glass surfaces treated with aminopropyltriethoxysilane (APTES) have a positive zeta potential which can be explained by the apparition on the surface of ammonium cations ($R\text{-}NH_3^+$) in contact with the electrolyte. The ITO material and the

borosilicate glass have approximatively the same negative zeta potential, thus the same negative surface charge due to hydroxyl groups (R-OH) which in contact with an electrolyte form negative groups ($R\text{-}O^-$) in equilibrium with the solution (pH depending). A chemical treatment of the glass substrate with NaOH 14.5 M for 5 minutes (see Materials and Methods) increases the number of surface hydroxyl groups. The polymethylmethacrylate (PMMA), the reference material in this method, exhibited the grater negative zeta potential.

In view of varying the electrostatic repulsion between the cell membrane and the surface, we first studied the effect of salt concentration, giving that the ionic screening effect decreases with the decrease of ionic strength. The latter depends both on the ionic ratio of the salt and on its concentration (Gingell D., 1982). We used sucrose to maintain a constant osmotic pressure (Materials and Methods).

Phase Contrast was used to localize cells and Reflection Interference Contrast Microscopy (RICM) to monitor their relative position to the glass surface.

On a glass coverslip, in 17 mM phosphate buffer containing mainly monovalent KH_2PO_4, all cells adhered to the surface (Fig.3.23A). It can be observed that they are surrounded by a bright fringe (inset of Fig. 3.23A, pointed by arrow)

At 0.17 mM phosphate concentration, we observed the presence of round spots that are brighter than the grey background and which are surrounded by a dark fringe (inset of Fig. 3.23B and cell **1** from Fig. 3.23C). Such effects suggest the presence of cell membranes at a minimum distance of 100 nm from the surface (impair multiple of a quarter of the wavelength of the incident light divided by the refractive index of cytoplasm, see Material and Methods). The bright spots were not fixed which indicate that the cells were submitted to Brownian motion, but on average, they remained on definite location and at definite distance from the surface. These cells can be easily displaced by moving the experimental setup or creating a small turbulence in the medium.

The brightness of these spots continuously changed between gray and white, showing that no adhesion takes place. Although the cells remained near the surface, they did not succeed to start the adhesion process. When decreasing five times the concentration of the 0.17 mM buffer solution, we obtained a different RICM image for the levitating cells, which is now darker than the grey background (cell **2** in Fig. 3.23C).

When decreasing ten times the concentration of the 0.17 mM buffer solution, RICM image (cell **3**) shows the almost the same optical characteristics like initially.

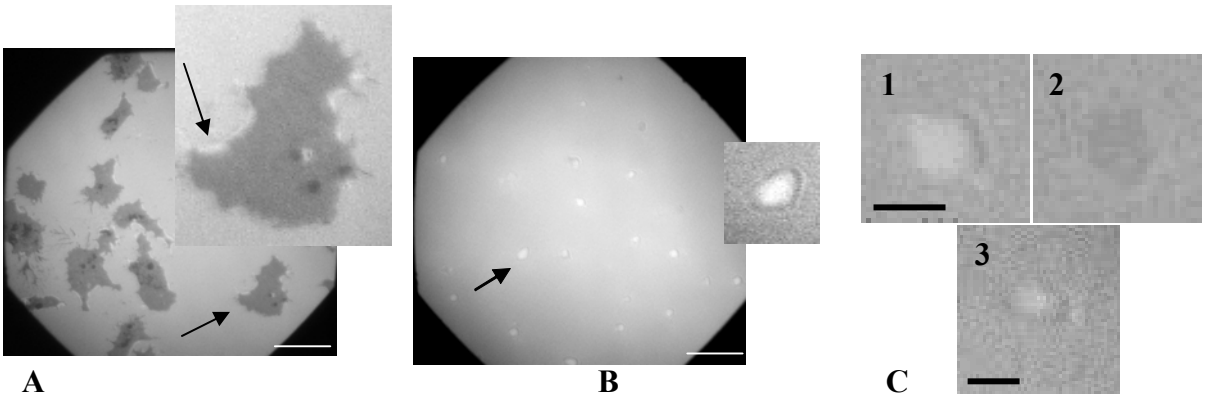

Fig 3.23 A, B: RICM images of *D. discoideum* cells on glass, in 17 mM (A) or 0.17 mM (B) phosphate concentration (insert : magnification of the area pointed by the arrow). Bar length = 20 μm. (C) levitating cells in 0.17 mM (cell **1**), 0.034 mM (cell **2**) and 0.017 mM (cell **3**), Bar length = 1 μm.

In the above figure, the RICM contrast difference of the levitating cells in the three buffer solution suggests that the distance between cell membrane and the substrate is different at 0.17 mM, at0.034 mM and at 0.017 (see Discussion).

Quantitative measurements of the percentage of adherent cells as a function of concentration and nature of the ions

When the ionic concentration was raised, cells were able to come into close contact with the surface and spread onto it, as revealed by the appearance of dark spots that enlarged gradually. The percentage of cells able to spread on the glass surface during 10 minutes increased sharply with the phosphate buffer concentration between 0.4 and 1.2 mM (Fig. 3.24).

Under a critical ionic concentration, 0.7 mM for SB, more than 50% of the cells levitate over the glass surface (Fig. 3.24). At 1.2 mM phosphate buffer, it takes 10 minutes for all cells to spread, and this time is reduced to 7 s at 1.7 mM.

Therefore, an increase in ion concentration speeds up cell spreading. On the other hand, the nature of the salt solution plays a significant role, as shown by the shift and the

steepness of the cell spreading response to $CaCl_2$ concentrations (Fig. 3.24, black diamonds).

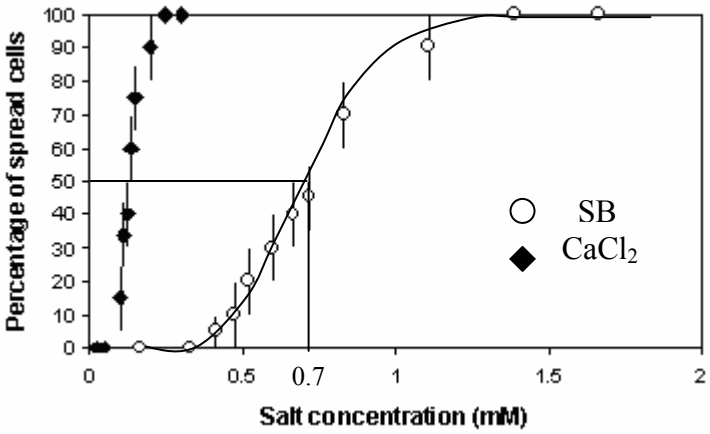

Fig 3.24 Percentage of *D. discoideum* cells spreading onto glass during a contact time with the surface of 10 minutes, as a function of calcium chloride concentration (full diamonds) and phosphate buffer concentration (open circles).

Divalent ions were more efficient than monovalent ones, since cells adhered at salt concentrations comprised between 0.05 and 0.25 mM $CaCl_2$.

When cells, previously spread on glass in 1.7 mM phosphate sucrose buffer (Fig. 3.25A), were submitted to a reduction of the surrounding ionic concentration down to 0.17 mM at a constant osmotic pressure, they remained attached to the surface, but the brightness of the contact area monitored by RICM slightly increased (Fig. 3.25B). Since the sucrose concentration is almost constant, the refraction index of the solution remains unchanged.

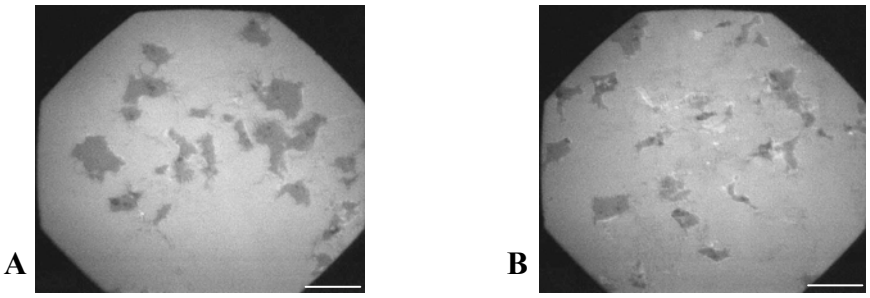

Fig 3.25 RICM images of *D. discoideum* cells on glass, in 1.7 mM phosphate sucrose buffer (**A**) and after dilution of the same sample to 0.17 mM (**B**). Bar length = 20 µm. Time between **A** and **B** is 150 s.

Therefore, the variation in the grey level is due to an increase in the distance between the cell and the surface (10-50 nanometers). Under these conditions, protrusive

activity still occurred along the cell margin, as indicated by the presence of fluctuating white areas around the central stable dark zone.

The extent of dark cell-surface contact area was slightly reduced, but all cells remained attached to the surface. Cells are even able to move on the surface, forming new contact zones despite electrostatic repulsion (figure 3.25A and B represent the same cells, B was taken 150 seconds after A). Taken together, these observations show that binding of the cell membrane to the surface, but not full detachment, is sensitive to the nature and the concentration of ions (Wolf, 1983).

In view of all these experiments, we examined whether, besides the existent electrostatic repelling between the cell membrane and a negative charged surface, the specific nature of ions or molecules in experimental solutions surrounding the cells also influence cell adhesion.

Is there a specific role played either by Na^+, K^+ or both cations ?

It could be envisaged that a specific ionic channel for Na^+ or K^+ could be responsible for cellular adherence. A specific role for H^+ channel is out of question because the two buffer solutions that fully allow or prevent cell spreading (17 mM phosphate buffer and respectively 0.17 mM sucrose phosphate buffer) have approximately the same pH (6.1 and 6.3, respectively). We, thus, prepared two buffer solutions that contain only one type of cation: one solution was made of NaH_2PO_4 and Na_2HPO_4 (we denominated it for simplicity, SB-Na) and the other one of KH_2PO_4 and K_2HPO_4 (SB-K) in the same ratio as for Sörensen buffer (SB). The pH values of SB-Na and SB-K were 6.07 and 6.00, respectively. The cells adhered normally in both 17 mM buffer solutions, whatever the nature of the cation is. Supplementary experiments with four completely dissociated salts were performed. These ones were composed of different types of cations and anions and do not contain the phosphate group: NaCl (pH = 5.85), KCl (pH = 5.6), CsCl and $LiClO_4$. In each case, the cells adhered normally. Thus, the hypothesis of the existence of a specific mechanism involving sodium, potassium or phosphate ions was rejected.

Therefore, in conclusion, the cellular adherence seems to be energy involved in close contact under the control of the electrostatic repulsion between cellular membrane and substrate and is not the consequence of a biochemical process involving specific ions or ion channels.

Could sucrose play a role in electrostatic repel ?

Another possibility would be the impediment of ion transport or cell movement by sucrose. Thus, we replaced the sucrose with a small organic molecule: a hydrophilic amino acid cysteine. We prepared a buffer solution of 0.17 mM diluted SB, maintaining osmotic pressure constant by using cysteine. As the cells were levitating in this buffer, we concluded that the sucrose did not interfere in cellular adherence.

Moreover, we choose two big organic molecules, soluble in water, to replace the sucrose and prepare 0.17 mM buffer solutions: MES (2-(N-morpholino)ethanesulfonic acid, pKa = 6.09) and HEPES (4-(2 hydroxyetyl)-1-piperazineethane sulfonic acide, pKa = 7.67) – Table 3.5, Column 3.

Table 3.5: **Organic zwitterionic salts replacing the sucrose**

Solution: type and composition	Inorganic Salt (C=17 mM)	Organic salts (concentration of inorganic salts 0.17 mM)		Combined solution
		HEPES [HEPES] = 36 mM	MES [MES] = 36 mM	MES+NaOH [NaOH] = 11 mM [MES] = 17 mM
Observations	The cells attach immediately	The cells didn't attach	Very few cells attached very slowly (after 2-3 minutes)	The cells attached immediately and exploded after 1-2 minutes

It can be noticed that the voluminous organic molecules could successfully replace the sucrose in view of maintaining constant osmotic pressure without helping the cellular adherence. The second column is shown as reference for the organic salts.

When we used MES + NaOH solutions, the cells become round and stopped to move because of the extreme pH values; the final concentration of NaOH ($5 \cdot 10^{-3}$) induced adhesion of all the cells on the surface (column 5).

3.3.2. Electrostatic attraction between D. discoideum cells and a APTES treated glass surface

In order to reverse the electrostatic interaction from repulsive to attractive we changed the glass surface charge by silanization (see Materials and Methods).

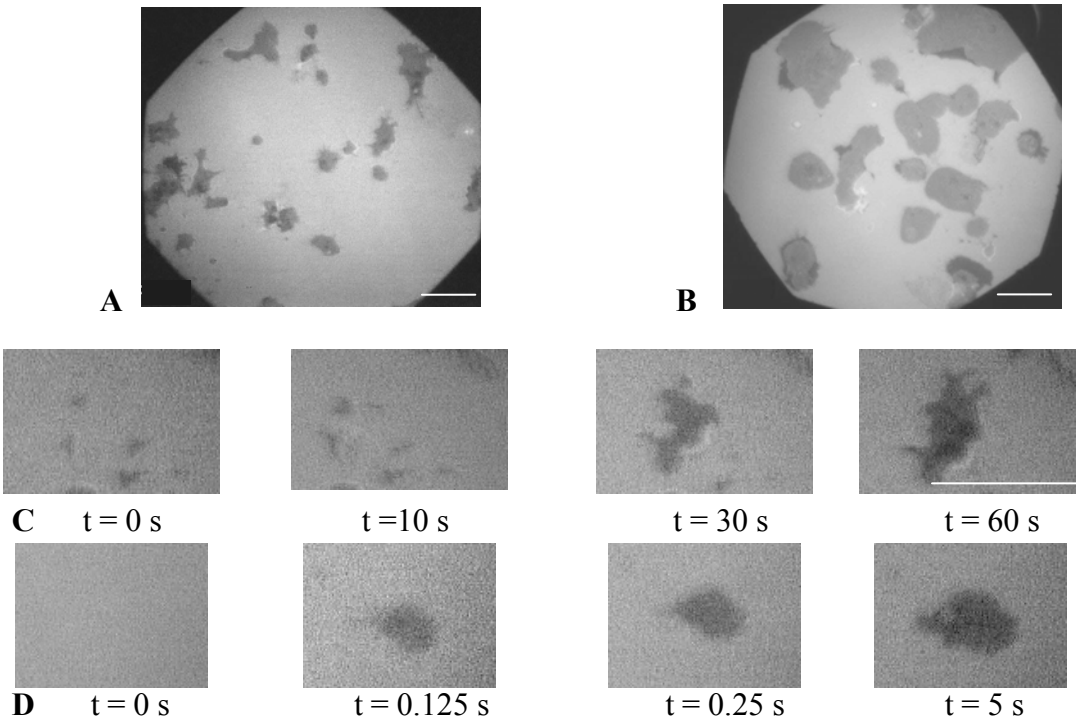

Fig. 3.26 Effect of ionic concentration on *D. discoideum* adhesion on aminopropyltrimethoxysilane treated glass. **A**, **B**: RICM images of *D. discoideum* cells on aminopropyltriethoxysilane (APTES) treated glass in 17 mM (**A**) or 0.17 mM (**B**) phosphate concentration. Bar length = 20 μm. **C**, **D**: Kinetics of cell spreading on aminopropyltriethoxysilane treated glass in 17 mM (**C**) or 0.17 mM (**D**) phosphate concentration. Bar length = 20 μm. The last image of each sequence is the maximal contact area of the spreading cells.

At physiological pH (6.1), aminopropyltriethoxysilane (APTES) replaced silanolate anions by ammonium cations. On this surface, cells spread whatever the ionic concentration is (Fig. 3.26A and B). Furthermore, at 0.17 mM, the cell-surface contact area increased faster than at 17 mM (Fig. 3.26C and D) and for most cells, the maximum area reached by the fully spread cell was larger (Fig. 3.26A and B). This shows that electrostatic interactions between the cell membrane and positively charged surfaces are significant at low ionic concentration and that they can be used to control cell adhesion.

As can be noticed, at low ionic concentration, positive surface charges exert forces strong enough to attract the cell to the surface and force spreading. After contact, about 20 μm^2 of cell membrane spread on the surface in less than 1 s, which is ten times the average spreading rate observed at physiological ionic concentration (Fig. 3.26D). This shows that electrostatic forces can be very strong at short distances, and thus be able to control cell adhesion.

3.3.3. Actin polymerization of *D. discoideum* cells in state of levitation

Is there an oscillating actin polymerization activity for levitating cells like in adherent cells ?

In order to follow the actin dynamics in LimE-GFP cells levitating over glass or ITO covered glass surface at 0.17 mM phosphate sucrose buffer, GFP fluorescence variations were recorded over time.

Fig. 3.27A shows sequential pictures highlighting different actin polymerization events (white arrows). Distinct fluorescence events appear randomly all over the cell and are moving with respect to the surface while visible. Fluorescence recording over time shows that actin polymerizes with peaks appearing more or less regularly (Fig. 3.27B).

The first three events are separated by 8.4 s whereas the time interval for the next event is 16.8 s, indicating that one event might be missing. Indeed, as the focal plane for fluorescence recordings was fixed, the levitating cell, which was continuously moving, was not fully accessible and fluorescence events out of this plane are not recorded. These experiments reveal that fluctuating actin polymerization occurs even in the absence of cell spreading. Some of these events might be related to endocytosis (see fluorescence peak at 55.2 s in Fig. 3.27A).

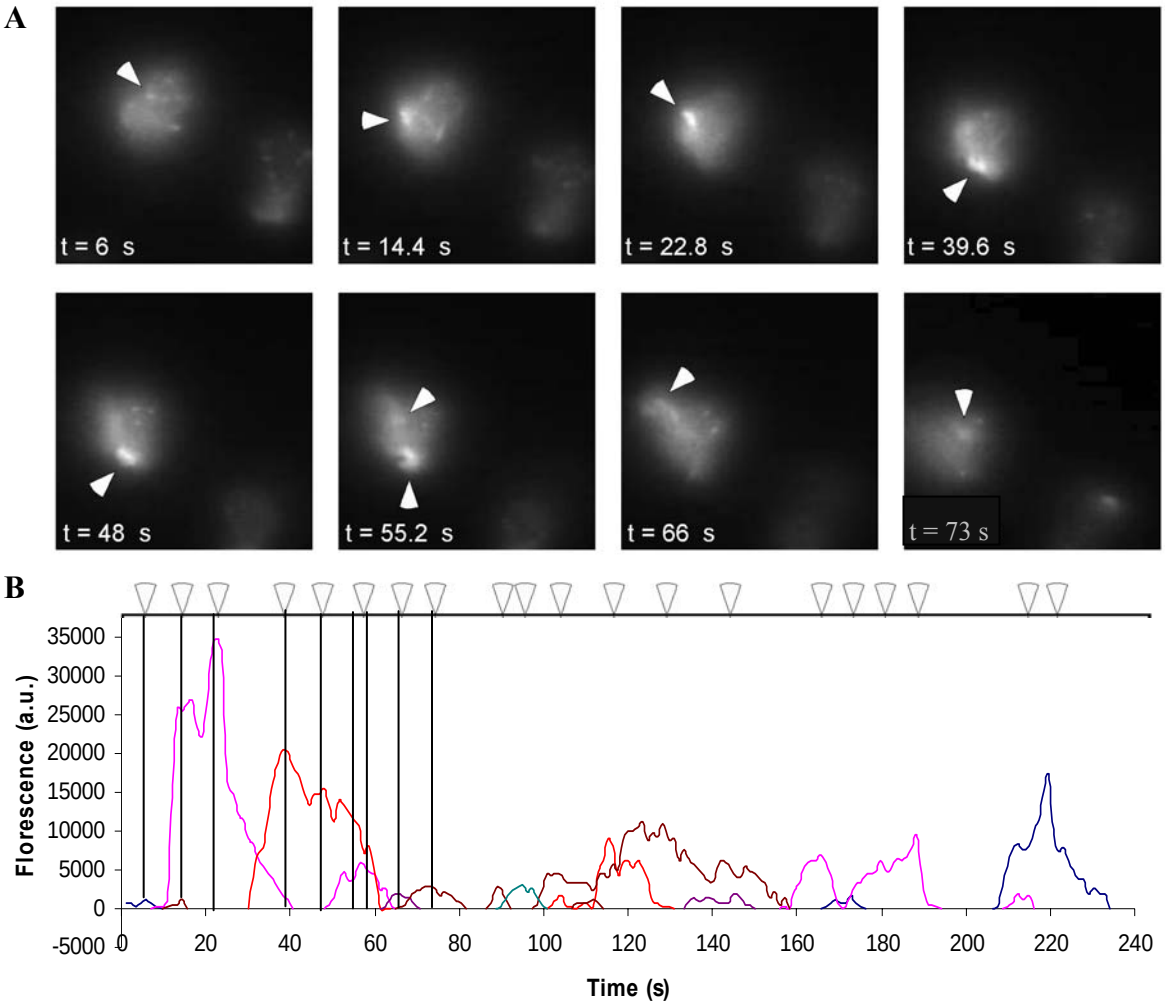

Fig. 3.27 LimE$^{\Delta coil}$-GFP fluorescence kinetics in levitating cells. **A**. Sequential images of *D. discoideum* expressing LimE$^{\Delta coil}$-GFP levitating in 0.17 mM phosphate sucrose buffer over a glass surface. Arrows indicate fluorescence maxima of individual events.
B. LimE$^{\Delta coil}$-GFP fluorescence variation as a function of time for the cell shown in (**A**). Vertical lines correspond to the same events highlighted in (**A**).

Analysis of 8 levitating cells, confirms more or less the existence of regular oscillatory actin polymerization activity during levitation. The origin of this activity will be discussed later.

In this subchapter, we showed how the living cells could be kept in suspension at a certain distance from the surface, despite the apparent gravity, using electrostatic properties of the cells and surfaces. In the following two subchapters, we analyze two different methods for adherence activation.

3.4 Synchronization by ion diffusion

3.4.1 Electrostatic control of *D. discoideum* adhesion by ionic diffusion

Experimental setup and diffusion parameters

In subchapter 3.3 we have shown how we can prevent cell adhesion using electrostatic repelling forces. Thus, by increasing the ionic strength one decreases the repelling force and thus, we could induce cell adhesion and spreading.

In view of synchronizing cell adhesion using ionic diffusion, we designed a two-chamber setup (Fig. 3.28). *D. discoideum* cells contained in *the lower chamber* levitate above a glass surface into 0.17 mM phosphate sucrose buffer (sucrose SB). The *upper chamber* was separated from the lower one by a 20 μm thick porous polycarbonate membrane. At t = 0 s, a concentrated salt solution was gently poured in the upper chamber and diffused through the pores (5 μm diameter) of the membrane, increasing the local ionic concentration around the levitating cells in the lower chamber. The diffusion distance corresponds to *the lower chamber thickness (e)*.

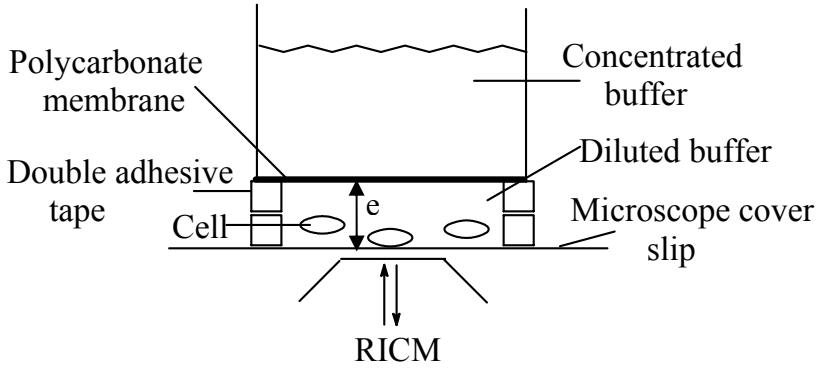

Fig 3.28 Experimental setup for cell adhesion. Relevant parameters: thickness *e* of the lower chamber, initial concentrations in the upper chamber and lower chamber.

Using the experimental setup with a flexible polycarbonate membrane settled at the distance, *e*, of 264 or 528 μm, the experiments were difficult to reproduce; when close to the surface, the polycarbonate membrane possibly stuck to the substrate and consequently pushed mechanically the cells on the glass surface, forcing them to adhere (Figure 3.29):

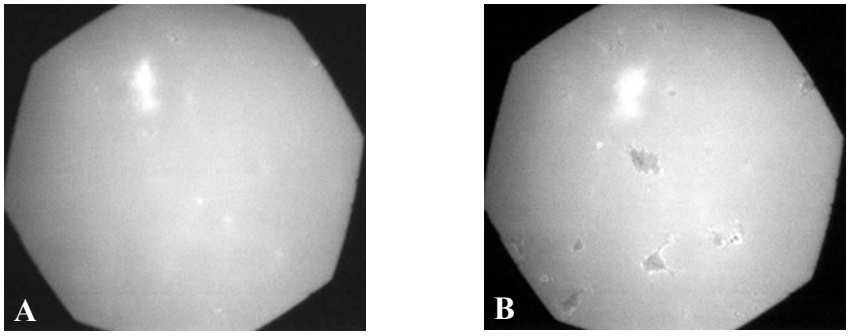

Fig. 3.29 Influence of mechanical pressure of the membrane on cells. (**A**) RICM image showing levitating cells in 0.17 mM phosphate sucrose buffer and (**B**) few cells are mechanically forced to adhere after adding the flexible polycarbonate membrane at a distance e = 264 µm.

The way the upper compartment was filled influenced the results. Indeed, when we pushed a concentrated buffer solution on the polycarbonate membrane, most of the suspended cells were displaced in the so created convection. The percentage of displaced cells decreased with an increase of the lower chamber thickness (e). Practically, we poured the concentrated buffer solution gently on the membrane in such a way that the cells remained levitating in stable positions.

Electrochemical experiments and determination of diffusion times

In order to record the ionic diffusion kinetics through the polycarbonate membrane, we performed electrochemical experiments on gold-coated glass (see Materials and Methods) with a 17 mM potassium hexacyanoferrate ($K_3Fe(CN)_6$) solution in an excess of KNO_3 added in the upper chamber. In these conditions, the hexacyanoferrate anion has a diffusion coefficient similar to phosphate buffer ($D \sim 1 \cdot 10^{-5}$ cm^2/s) (Bernard M., 1996) and exhibits a well-known electrochemical reduction reaction below + 0.2 V/Ag,AgCl. The reduction reaction is:

$$Fe(CN)_6^{3-} \overset{+1e^-}{\Leftrightarrow} Fe(CN)_6^{2-}.$$

The lower chamber was glued on the gold-coated glass acting as a working electrode and was filled with potassium nitrate solution (Fig. 3.30).

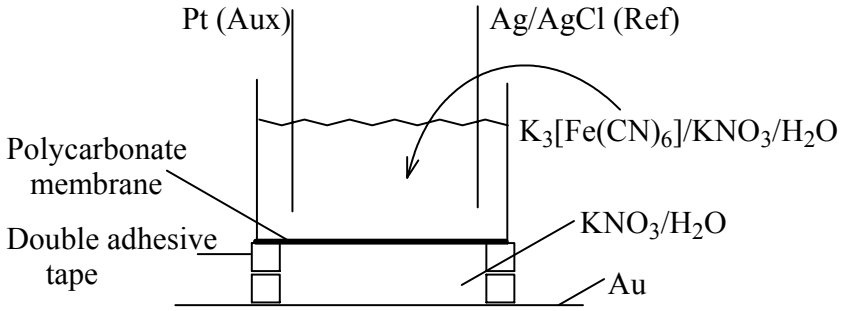

Fig. 3.30 Experimental setup for ionic diffusion control. Relevant parameters: thickness *e* of the lower chamber, concentration in the upper chamber.

The concentration of potassium hexacyanoferrate at the working electrode was monitored by short (0.5 s) potential pulses at 0.0 V/Ag,AgCl. The transiently induced electrochemical reaction did not change the overall salt concentration of the solution. The current intensities sampled at 0.05 s were proportional to the local hexacyanoferrate concentrations. The resulting curves are shown in Fig. 3.31, for three different lower chamber thicknesses *e*.

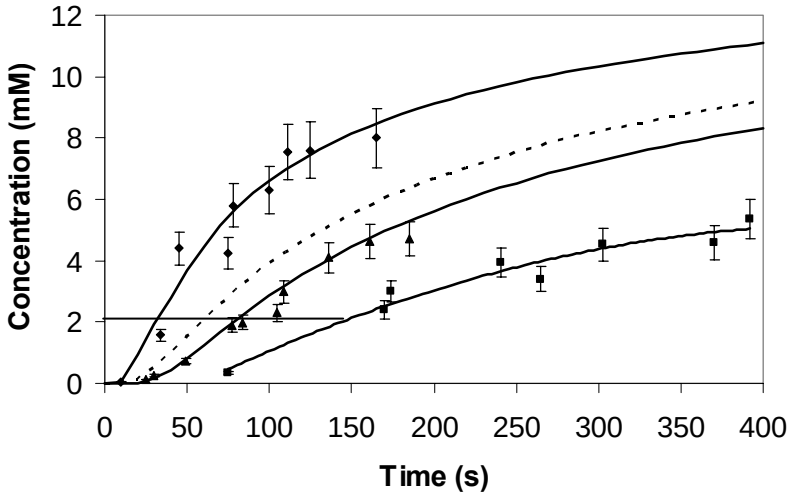

Fig. 3.31 Time evolution of $Fe(CN)_6^{3-}$ concentration at the conductive surface, for three different thicknesses of the lower chamber, e = 264 µm (diamonds), e = 528 µm (triangles), e = 1056 µm (squares) when the upper chamber concentration was 17 mM. Solid lines are provided as a guide for the eye. The dotted line is a MATLAB (The Math Works, Natick, MA) simulation of surface concentration with planar diffusion conditions, using the experimentally determined $Fe(CN)_6^{3-}$ diffusion coefficient ($1.0\ 10^{-5}$ $cm^2.s^{-1}$) and a lower chamber thickness of e = 520 µm. e.g. time for reaching 2 mM in the lower chamber is 55 and 70 in theoretical and respectively experimental approach.

After a delay, the hexacyanoferrate concentration rises and tends to 17 mM as the upper and lower compartment concentrations equilibrate. The calculated curve with MATLAB software (see Materials and Methods) for the 528 μm thick lower chamber is shown in figure 3.31 (dotted line).

It can be noticed that the theoretical curve is close to experimental data, which proves that diffusion controlled the increase of the salt concentration at the glass surface. For example, time for reaching 2 mM in the lower chamber is 55 and 70 in theoretical and respectively experimental approach, when e = 528 μm. The difference between theoretical and experimental curves could be attributed to: first a possible lateral diffusion contribution and surfaces reflection, second to the non-zero membrane thickness, third to reduced surface of the holes and delay of osmosis phenomenon through the holes caused by holes walls reflection, fourth to uncertainty in the lower chamber thickness and fifth to membrane deformation when concentrated salt solutions are poured over it. We indeed observed by interferential contrast monitoring of the membrane holes network, that the membrane bent by several tenths of micrometers during these experiments,.

Using the experimental curves, it can be anticipated that the ionic concentration around the cells increases from 0.4 to 1.1 mM (see Fig. 3.31) in about 20-30 s, for a chamber thickness e = 260 μm, when we added 17 mM solution in the upper chamber. Given that the rate at which the ionic concentration increases at the surface is proportional to the salt concentration added in the upper chamber, it is possible to accelerate this rate by using more concentrated salt solutions.

Time of salt diffusion and time of cellular reaction

The diffusion experiments using levitating cells in the lower chamber and different salt solutions added to the upper chamber are summarized in four figures.

For help, table 3.6 summarizes the different used and deduced of the experiments.

We define *the lag time* as the time interval between the beginning of ionic diffusion and initiation of spreading and the *asynchrony* as the time interval (Δt, see Fig. 3.13) between the onsets of spreading of the fastest and the slowest cells.

Table 3. 6 Schematic diffusion experimental setup parameters, observables and results

Variables	Observable	Results
Lower chamber thickness, ***e*** Added salt concentration in the upper chamber, C_u Sucrose buffer concentration of lower chamber, C_l	Lag time, ***t*** Asynchrony, Δt	Figures 4-7 Supplementary experiments Conclusions

In order to reduce the difference between the concentrations of the lower and the upper chamber, thus, to decrease the diffusion time, we initially used a 0.33 mM phosphate sucrose buffer (sucrose SB) for the cells in the lower chamber (Fig. 3.32).

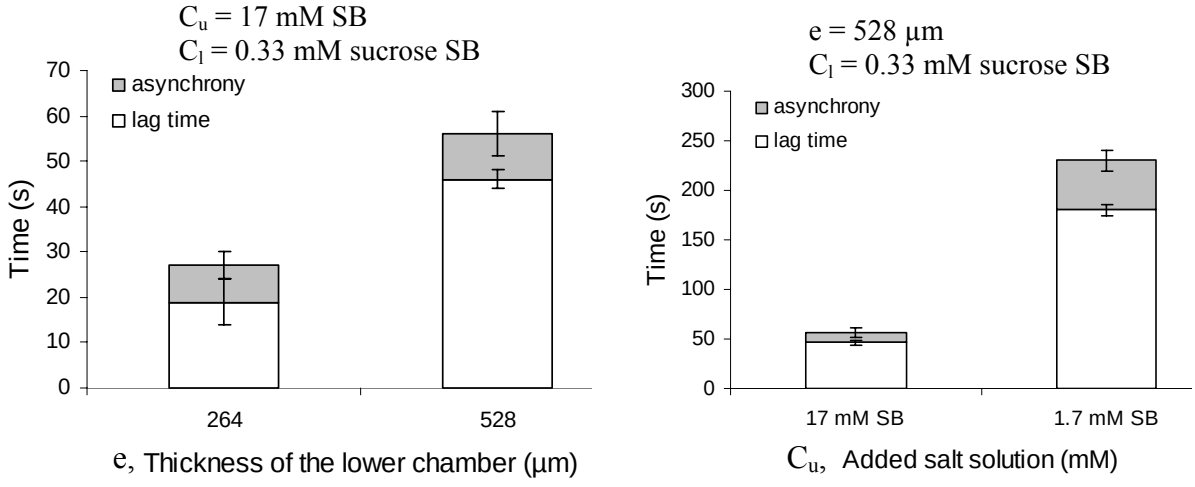

Fig 3.32 Lag time and asynchrony (respectively the lower and the grayed upper part of the bars) as a function of the (A) thickness of the lower chamber (SB: Sörensen phosphate buffer) and of the (B) added salt concentration in the conditions shown on the figures.

The lag time and asynchrony increase with the distance between the membrane and substrate and depend on the initial concentration of the solution added in the upper chamber, in agreement with diffusion laws.

We diluted the phosphate sucrose buffer (maintaining the osmotic pressure with sucrose), in which the cells were immersed in the lower chamber, to 0.17 mM. At the same time, trying to limit the diffusion distance, we maintained the lower chamber thickness *e* at 264 and 528 µm.

The minimal lag time and the best asynchrony were obtained when we added a ten times more concentrated SB solution (Fig. 3.33A). Even we expected to reduce time ten fold when compared to 17 mM SB, we reduced it only by a factor of approximately 2. This happens because of the already described limitations of our experimental setup (see also Fig. 3.37B)

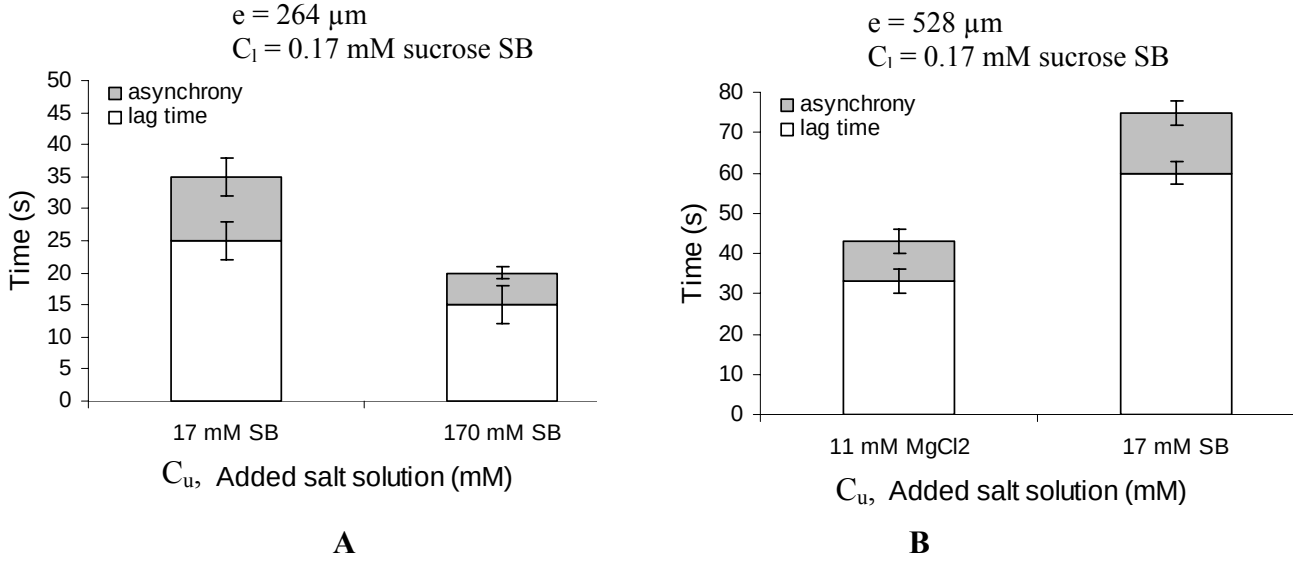

Fig 3.33 Lag time and asynchrony as a function of the (A) added phosphate buffer concentration and of the (B) nature of the added salt, in the conditions shown on the figures.

When we added a 1:2 electrolyte solution ($MgCl_2$) the lag time is shorter (32 s) than with SB (60 s), even though the concentration is smaller (11 mM, Fig 3.33B). The explanation could be the following: the divalent cations act more efficiently as electrostatic double-layer counterions than the monovalent ones, because they have twice the charge number per mole and could adsorb to the interacting surface (Gingell, 1982).

Using the experimental setup with a flexible polycarbonate membrane at 264 or 528 μm from the surface, the experiments are difficult to reproduce; moreover, the 0.33 mM concentration of the diluted buffer in the bottom compartment is at the limit of levitation conditions. In order to improve the experimental setup, we choose to place the membrane at 1056 μm and the cells were added in a diluted buffer of 0.17 mM SB. Figures 3.34 and 3.35 present respectively the effects of the ionic concentration of some

added salt solution and that of lower chamber thickness *e*, on the parameters defined above.

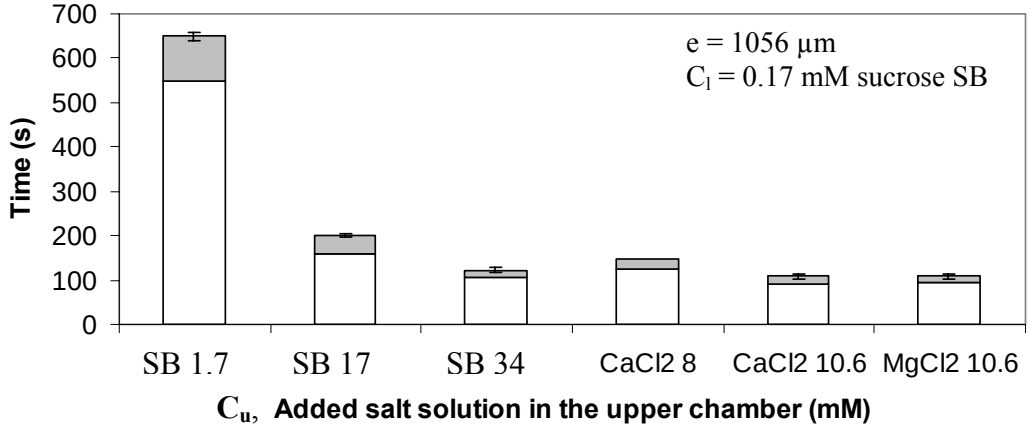

Fig. 3.34 Lag time and asynchrony (respectively the lower and the grayed upper part of the bars) as a function of the nature and concentration of the added salt in the upper chamber (SB: Sorensen phosphate buffer).

The asynchrony clearly decreases when the added salt concentration was raised (Fig. 3.34, compare SB solutions). The ionic environment around cells that levitate close to the surface changes therefore more rapidly from repulsive to adhesion-promoting conditions when the salt concentration in the upper chamber is higher. Also, the divalent cations screening out the negative surface charges more efficiently (Fig. 3.34).

This shows that it is possible to synchronize cell spreading by controlling the ion concentration of the medium surrounding the cells. Moreover, the experiments using the parameters e = 1056 µm and C_l = 0.17 mM phosphate sucrose buffer, are highly reproducible.

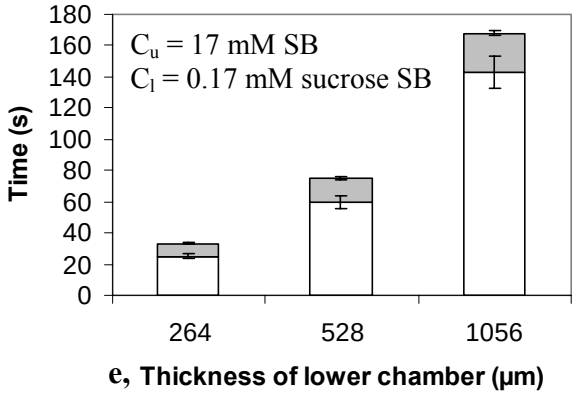

Fig. 3.35 Lag time and asynchrony (respectively the lower and the grayed upper part of the bars) as a function of lower chamber thickness, *e*, when 17 mM SB is added in the upper chamber. The error bars refer to the variability of these 2 parameters between independent experiments.

Using the previously experimental curves for mass transport phenomena (see Fig. 3. 31), we found that all the three lag time values reported in figure 3.38 correspond to the same phosphate buffer concentration of 2 mM. This is higher than the ionic concentration at which 50% of the cells spread in ten minutes (0.7 mM, Fig. 3.24, subchapter 3.3). The discrepancy reflects that the kinetics of successful cell surface contact formation increases with the salt concentration. At a given ionic concentration, the time for a cell to start spreading is the sum of the one to establish a contact with the surface and the one to start the biochemical reactions (probably very rapid, 1 to 3 s) that allow spreading. The kinetic of the first one gradually increases with salt diffusion to the lower compartment whereas the second one remains approximately constant and is insensitive to ionic concentration.

The asynchrony clearly decreases when the polycarbonate membrane is closer to the glass surface. The ionic environment around cells that levitate close to the surface changes therefore more rapidly from repulsive to adhesion-promoting conditions when the polycarbonate membrane is close to the cells.

3.4.2 Synchronization of *D. discoideum* cells using ionic diffusion

We investigated how cell spreading was synchronized when a concentrated salt solution from the upper chamber diffuses through a polycarbonate membrane into the lower chamber containing *D. discoideum* cells in 0.17 mM phosphate sucrose buffer. A representative example is shown in Fig. 3.36, using a salt concentration of 170 mM in the upper chamber, and a thickness of lower chamber e = 260 μm.

D. discoideum cells started spreading 15 s after adding the concentrated salt solution, and all cells had begun spreading at t = 20 s. In this case, the lag time was 15 s and asynchrony was 5 s.

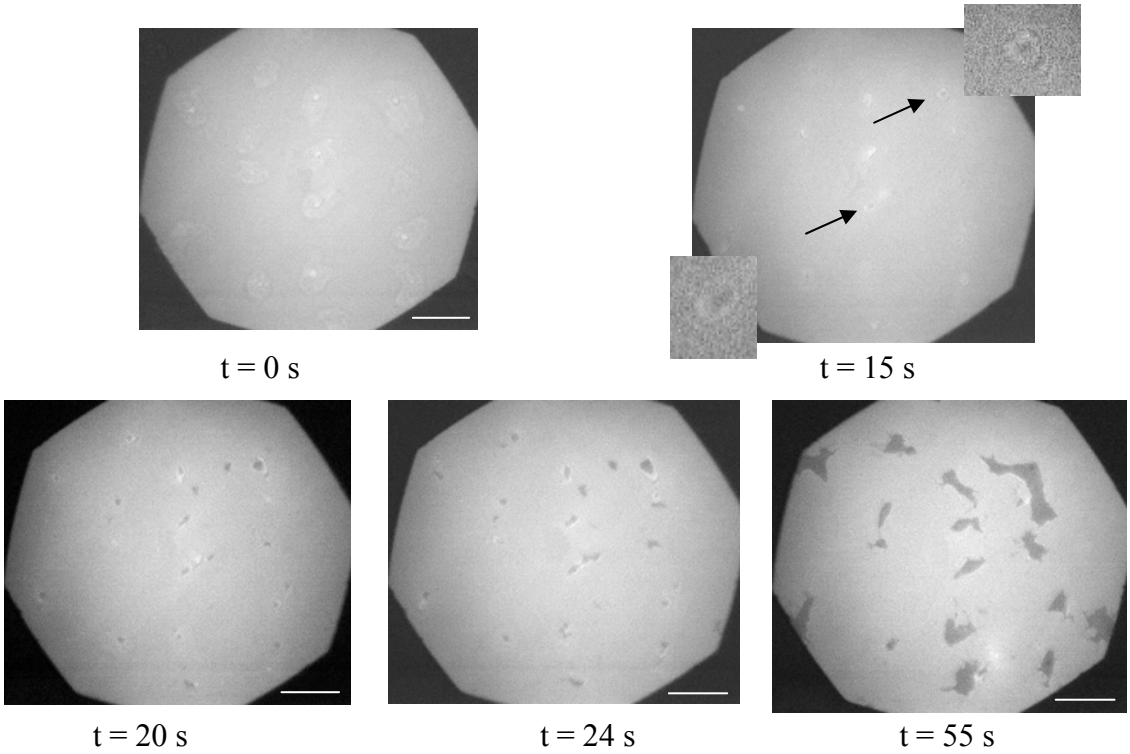

Fig. 3. 36 Example of synchronous contact of *D. discoideum* cells with a glass surface, induced by the diffusion of a 170 mM phosphate buffer solution through a polycarbonate membrane set at e = 260 µm from the glass surface. *D. discoideum* cells do not spread on glass in 0.17 mM SB (t = 0). At t = 0 s, 500 µL of the concentrated salt solution (170 mM) is gently poured in the upper chamber. Cell spreading is monitored at the indicated time by RICM (inserts: magnifications of area pointed by the arrows). Bar length = 20 µm.

Adding a 170 mM phosphate buffer solution we obtained the smallest asynchrony time Δt = 5s; although this is a very good result, the continuous salt diffusion from the upper chamber trough the polycarbonate membrane, increased the osmotic pressure and could affected cell viability. In consequence, using this experimental approach, the upper solution should be diluted after one minute of salt diffusion.

In Figure 3.37A, individual cell spreading kinetics are analyzed and normalized to the maximal contact area of each cell (see Materials and Methods). The maximal cell surface contact area was 190±95 μm^2, which is similar to that obtained for unsynchronized cells (Keller, submitted). Figure 3.37A shows averaged spreading kinetics of 17 cells, fitted with the model of Chamaraux (Chamaraux, 2005): $A(t) = A_{max} \tanh(\alpha(t-t_0))$.

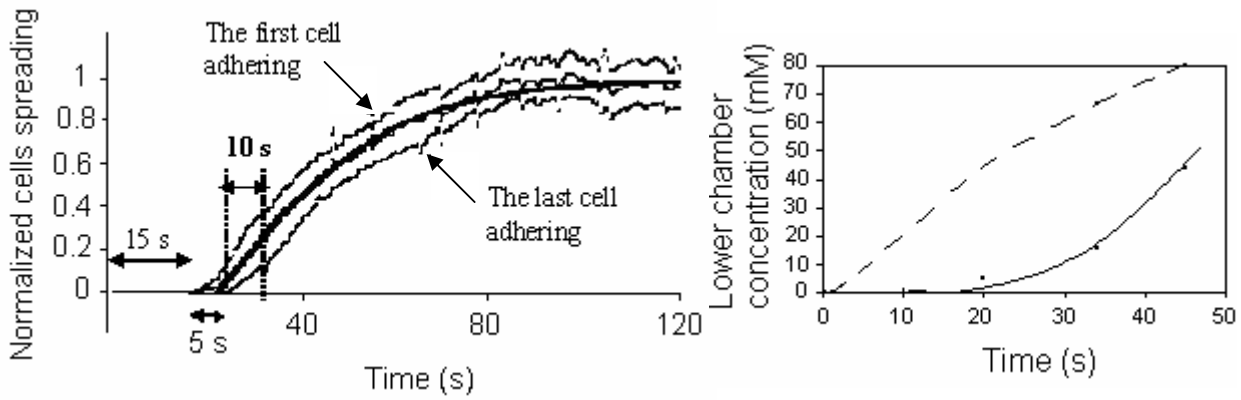

Fig. 3.37 A. Synchronization of *D. discoideum* cell spreading on a glass surface (experimental conditions similar to Fig. 3.35). Averaged normalized spreading kinetics of 17 cells (corresponding to two individual experiments) were fitted to the model of Chamaraux (thin line); maxima and minima of error bars are connected by dotted lines; t = 0 beginning of ionic diffusion, lag time (15 s), the asynchrony (5 s) and the minimal synchronization window (10 s) are shown (↔). **B** Time evolution of $Fe(CN)_6^{3-}$ concentration at the conductive surface, for e = 264 µm (squares) and C_u = 170 mM. The solid line is provided as a guide for the eye. The dotted line is a MATLAB (The Math Works, Natick, MA) simulation of surface concentration with planar diffusion conditions, using the experimentally determined $Fe(CN)_6^{3-}$ diffusion coefficient ($1.0\ 10^{-5}\ cm^2.s^{-1}$)

The spreading rate α used in the fit was 0.015 ± 0.001 which is very close to the value obtained for unsynchronized cells (Keller, submitted). Representing standard deviations of the spreading kinetics allows defining a synchronization window, which is the minimal time interval between the maxima and the minima of the standard error bars. Thus, in our experiment, cells were best synchronized in a 10 s window, 30 s after the first observed surface contact. The lag time was 15 s. From the data of Fig.3.37B, 10 s after gently pouring on the membrane 170 mM SB, C_l was only 0.5 mM, which can explain the lag time value (the cells start to adhere when lower chamber concentration is around 2 mM).

Actin polymerization speeds up the formation of the initial cell-surface contact.

In order to determinate if the decrease in electrostatic repulsion is the only parameter to promote cell adhesion, in other words, if this is only a passive phenomenon, we reproduced the diffusion experiment with latrunculin-treated cells (Fig. 3.38).

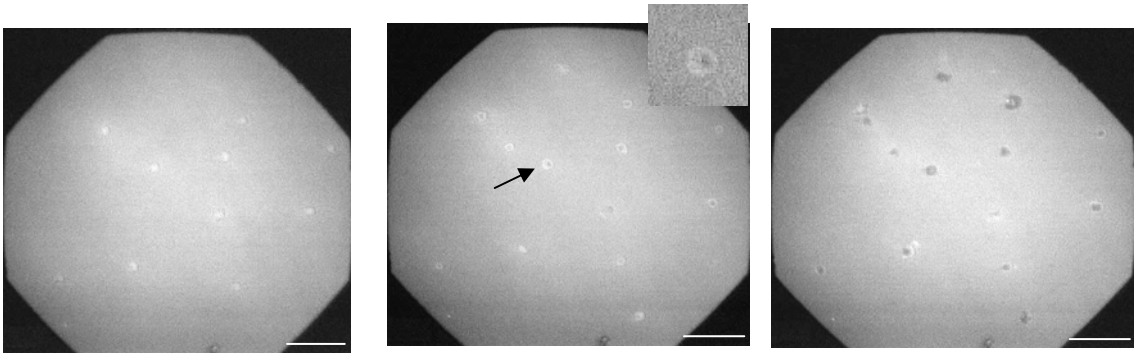

t = 0 s t =100 s t = 230 s

Fig. 3.38 Example of synchronous contact of latrunculin-treated *D. discoideum* cells on a glass surface, induced by the diffusion of a 17 mM phosphate buffer solution through a polycarbonate membrane set at 528 μm from the glass surface. RICM observations at the indicated times. Cells start contacting the surface100 s after addition of concentrated buffer (insert: magnification of the area pointed by the arrow). Bar length = 20 μm.

Latrunculin A prevents actin polymerization (Coue, 1987), but does not change the cell surface potential (see Table 3.4, subchapter 3.3). Indeed, it is well known that actin polymerization is necessary for efficient cell spreading.

A 528 μm thick lower chamber was used for these experiments. The phosphate concentration in the lower chamber was 0.17 mM and contained *D. discoideum* cells exposed to 3 μM latrunculin A in the culture medium (see Materials and Methods). Latrunculin-treated cells were spherical, immobile and levitate (Fig. 3.38, t = 0). When the concentration of the salt solution increases at the glass surface, dark contact areas that slowly increased in size were observed by RICM (Fig. 3.38, t = 100 s).

Interestingly, the lag time was significantly higher in the presence of latrunculin (100 s) than in its absence (60 s, Fig. 3.33B), for identical lower chamber thickness (e = 528 μm). In the presence of latrunculin, cells therefore remain 40 s longer above the surface before starting visible spreading. This suggests that actin polymerization accelerates the formation of a stable contact with the glass surface.

In this subchapter, we showed how we could synchronize cell adhesion and spreading using an experimental diffusion setup. The minimal time interval for all cells to contact the surface and start spreading was 5 s when we added a 170 mM SB in the upper chamber. However, the major drawback of this method is the unphysiological conditions characterized by a high osmotic pressure in the lower chamber.

3.5 Synchronization by electrical pulse

3.5.1 Electrostatic control of *D. discoideum* adhesion by electrochemical means

In subchapter 3.4, we showed how we could synchronize cell adhesion and spreading using an experimental diffusion setup. In physiological conditions, the minimal time interval for all cells to contact the surface and start spreading was 8±3 s when we added 17 mM SB solution in the upper chamber, a 0.33 mM phosphate sucrose buffer being in the lower chamber (e = 264 μm). However, this time interval turns out to be insufficient for a good synchronization of biochemical processes in a cell population. Indeed, the period of actin polymerization oscillation is about 8 s (see subchapter 3.1).

Thus, a second method was developed to trigger the initial cell-surface contact by electrochemical means.

Since at low ionic concentration, *D. discoideum* adhesion is sensitive to surface charge, we envisioned controlling this parameter in order to synchronize cell-surface contact. To this purpose, a small plastic chamber was glued on a coverslip coated with a 80 nm thick conductive Indium Tin Oxide (ITO) layer. A pseudo reference Ag,AgCl (named *Ref.*) and a counter platinum electrode were fitted in the bulk volume of the chamber (Fig. 3.39).

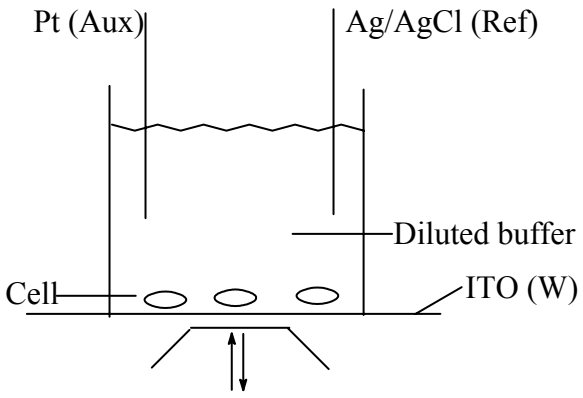

Fig 3.39 Experimental setup for electrochemical cell adhesion. Relevant parameter: concentration in the chamber (0.17 mM or 0.017 mM).

The ITO surface was used as a working electrode. The zeta potential average of the ITO-coated surface was -16 mV in SB. In order to electrically characterize this setup, cyclical current-potential curves were acquired in the range – 0.3 to + 2.5 V/Ref., in 0.17 mM phosphate sucrose buffer (Fig. 3. 40).

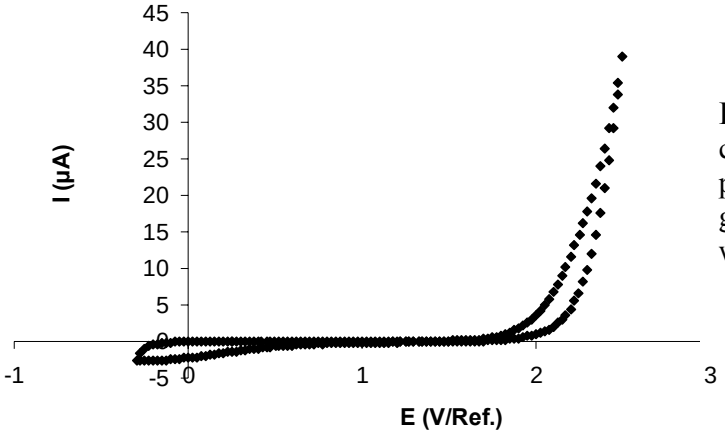

Fig.3.40 Cyclic voltamperometric curve obtained in 0.17 mM phosphate sucrose buffer with ITO-glass surface (around 0.8 cm^2) as a working electrode.

Between - 0.2 and + 1.8 V/Ref., the current is negligible, as expected for diluted salt solutions. The sharp rise in current for voltages higher than + 1.8 V/Ref. is due to water oxidation at the surface, producing H^+ ions.

D. discoideum cells, resuspended in 0.17 mM phosphate sucrose buffer, were introduced in this chamber and allowed to levitate above the ITO surface. We observe them like small round spots surrounded by a dark fringe (insert of Fig. 3.41A). The cells contrast change between whiter than the gray of the background and darker than the gray of the background, suggesting a movement in vertical plane, Fig. 3.41A – see also Fig. 3.23B, C). Potentials comprised between 0 and + 1.8 V/Ref. had no attracting effect on the levitating cells. In contrast, application of short (2 s or less) + 2.5 V/Ref. pulses resulted in the sudden and simultaneous formation of dark cell-surface contact zones (Fig. 3.41B).

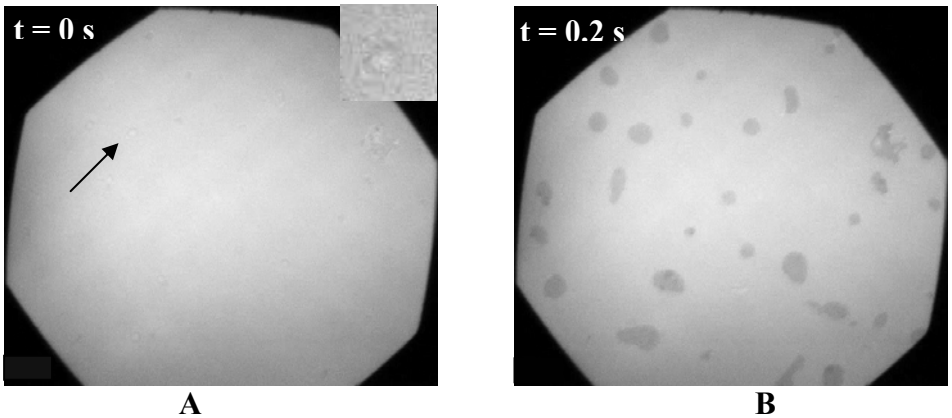

Fig. 3.41 RICM images of *D. discoideum* cells obtained (**A**) before and (**B**) after applying a 2.5 V/Ref. pulse for 0.2 s at the ITO surface. In (**A**) cells levitate over the surface in 0.17 mM phosphate sucrose buffer, identified by round spots, in center whiter than the background, (see also Fig. 3.23B,C, subchapter 3.3); insert: magnification of the area pointed by the black arrow (**B**). Dark cell-surface contact zones appeared during 0.2 s electrical pulse for 80% of cells.

The fast spreading kinetics in 0.17 mM phosphate sucrose buffer (0.1 - 0.2 s) is comparable to those observed on APS-treated surfaces (Fig. 3.26), suggesting the presence during the pulse, at the surface, of a positive charge attracting the negative ones of the cells membrane.

We also analyzed the attachment kinetics of the cells levitating in 0.034 mM phosphate sucrose buffer during 2 s application of + 2.5 V/Ref. pulse. In Fig. 3.42 we exemplify the attachment kinetics of a single cell:

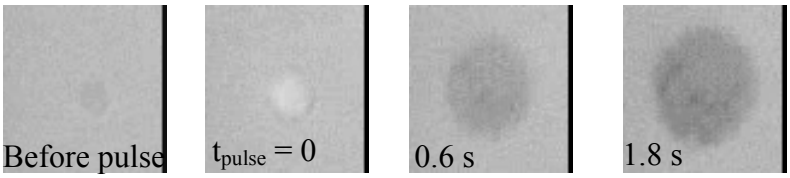

Fig. 3.42 RICM images of *D. discoideum* cells obtained before and after applying a 2.5 V/Ref. pulse for 2 s at the ITO surface in 0.034 mM SB. The cell RICM contrast changes from darker than the background for white and then, 0.6 s after the beginning of the pulse, to black.

In 0.034 mM, before pulse application, the levitating cell was darker than the background; at the onset of pulse, the centre of the cell became white surrounded by a dark fringe. After 0.6 s from the pulse onset, the cell became black very rapidly and its contact surface increases with time (Fig. 3.42). This fast contrast changing could be related to a breakdown of membrane-cytoskeleton assembly (in less then 0.2 s, for at least one cell). This rupture is random; the cells did not become all black at the same time: 15 from 21 cells became black between 0.4 and 1.6 s from the pulse starting (the pulse takes 2 s). Given the fact that the levitating cell was darker than the background and according to the sequence of RICM contrast changing, we estimated the distance between the substrate and the cell membrane, before pulse application, to be 200 nm (a white spot produced by an object stands 100 nm, see Materials and Methods).

We also observed a fast appearance of close cell-surface contact areas for latrunculin-treated cells. Tacking into account these observations, we concluded that the cellular attraction in electrical field is a passive phenomenon and involve no biochemical reactions at least in the early stages of pulse application (less than 2 s).

D. discoideum cells were not permeabilized by the voltage pulse, as judged by propidium iodide staining (subchapter 3.2). In contrast, latrunculin-treated cells in 1.7 mM or 0.17 mM SB often exploded after contact and released their content (Fig. 3.43), showing that very large mechanical forces were exerted on the plasma membrane during the positive voltage pulse (a process that could be catalyzed by the protons formed on the surface).

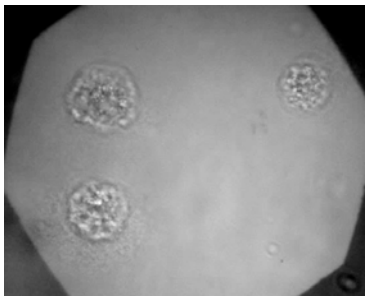

Fig.3.43 RICM and PC combined image of latrunculin-treated cells in 1.7 mM after a 2.1 V/Ref. pulse potential.

Cells in phosphate sucrose buffer, attached after an electric pulse (2 s or less), did not move away from the initial contact zone formed during the voltage pulse, even when the ionic concentration was raised to physiological values, as if the cells were stuck to the ITO surface (see Discussion). Ten or less minutes later, cells eventually moved away from this zone.

To explore gentler conditions, we then studied the effect of electric pulse duration (less than 0.25 s) on cell spreading. In these experiments, the reference electrode was removed, and a constant 5 V voltage was applied between the platinum electrode in the bulk solution and the ITO surface ($I = 4.10^{-5}$ A). This 5 V pulse corresponds to the actual voltage between the counter electrode and the ITO surface in the three electrode setup used above. When the pulse duration was reduced, two spreading modes could be distinguished during the same experiment observed by RICM. The first one was evidenced by dark contact areas (Fig. 3.44A black arrow) and corresponds to those described above. The second one was evidenced by white contact areas (Fig. 3.44A, white arrow), which indicated that cells were further away from the surface. Only the cells following the first mode (black cells) could by seen appearing during the pulse; in contrast, white contacts (white cells) appeared visible by RICM on a longer period (for example, of 5 to 15 s after a 0.1 s pulse). Using epifluorescence microscopy and focusing

at ITO surface, one observes that all cells (independently on their RICM appearance) approach to the surface making contacts with ITO surface during the pulse application (Fig. 3.44C). In Contrast Phase, is observed how cells stop their Brownian movement during and after the electrical pulse application. Consequently, these contacts triggered the onset of cell spreading.

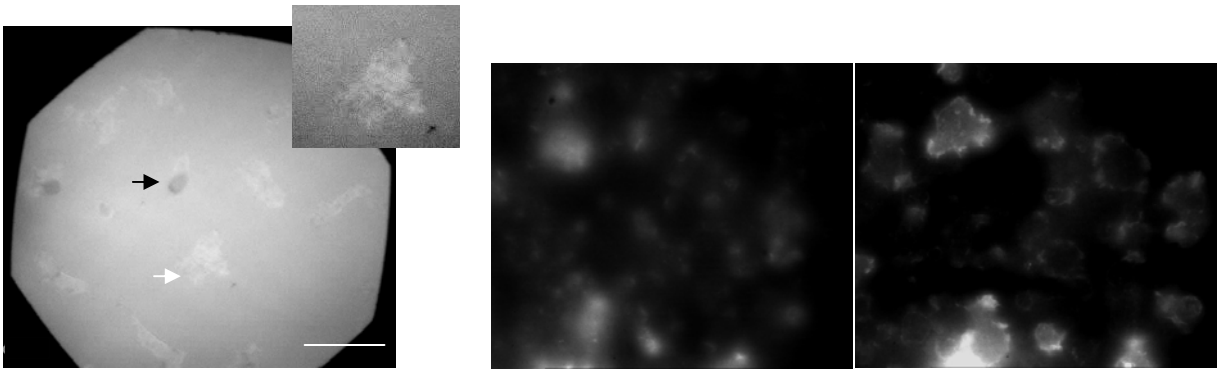

Fig. 3.44 A. RICM image obtained 30 s after applying a 0.1 s long 5 V pulse between the ITO surface and a platinum counter electrode, on *D. discoideum* cells levitating over the surface in 0.17 mM phosphate sucrose buffer. Scale bar = 20 μm. Black arrow: close cell-surface contact induced by the electric pulse. White arrow: cell spreading induced by the electric pulse. Insert: magnification of the area pointed by the white arrow. **B** and **C** Fluorescence images before (**B**) and during (**C**) 5 V pulse (0.1 s), focusing at ITO surface.

Addition of 200 μL diluted buffer showed that the cells were adherent because they were not removed by the flow.

When we added physiological buffer, the color of the contact zone turned grey which indicated a reduced distance to the surface; in contrast with the first mode (dark or black cells), cells spreading following the second mode (white cells), moved readily on the surface, away from the initial contact point. These cells therefore are not impaired by the electric pulse.

Figure 3.45 shows the percentage of spreading cells in both modes as a function of the pulse time for a constant 5 V potential pulse applied.

Below 0.03 s, 5 V electric pulses have no effect. The percentage of cells spreading with either mode increases with pulse time, but with independent evolutions. Above about 0.1 s, all cells reach the surface. The percentage of cells forming dark contacts

increases quasi-exponentially as a function of time. Above 0.23 s, all cells form dark contacts.

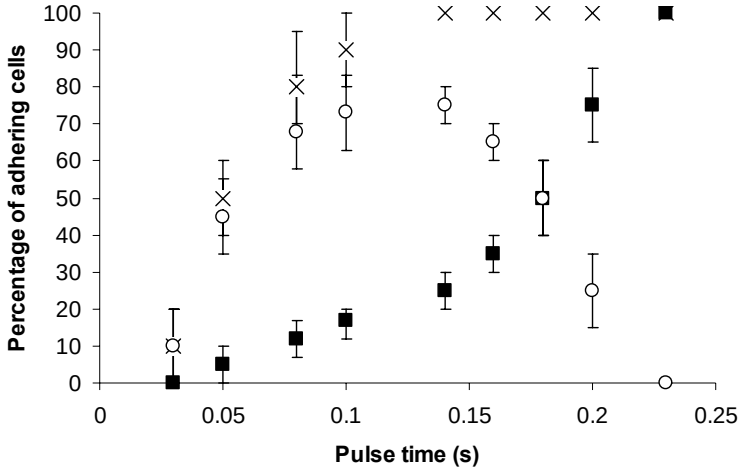

Fig 3.45 Efficiency of cell spreading as a function of pulse time. Circles: percentage of white cells. Squares: percentage of dark cells. X: percentage of adherent cells (black and white arrows in Fig. 3.44).

The optimum duration, that maximizes spreading in the second mode (white cells), is 0.1 s. Under these conditions, 90% of the cells form visible RICM contact areas within 15±5 s after the pulse and then spread and move over the surface, as in physiological buffer.

Interestingly, cells formed dark contacts immediately after the voltage was raised (< 60 ms, see Fig. 3.45 at t = 0.05 s appeared dark cells) and only during pulse application. In contrast, white contacts appeared visible by RICM on a period of 5 to 15 s after a 0.1 s pulse and with a period of 20 to 30 s after a 0.05 s pulse.

The cells approaching the ITO surface under the gravity action when the pulse was stopped, never spread. Moreover, the attachment kinetics of the black contacts was stopped at this time. This indicates that spreading was triggered only on cells close to the surface by events occurring during the pulse. The probability of spreading increased with the potential duration time, so with proton concentration at the surface.

In order to analyze the effect of a proton accumulation at the surface during the pulse application, we measured the zeta potential (Materials and Methods) of an ITO surface in 10 mM KCl versus solution pH (see Fig. 2.16).

At pH > p.z.c., the oxide surface is negatively charged, since the surface is covered with negative groups, R-O^-. At pH < p.z.c., R-HOH^+ is the charge determining group and the surface is positively charged. The chemical equilibrium at the surface, determined by protons concentration, is as follows (see also Fig. 3.46):

$$R-HOH^+ \xleftrightarrow{-H^+/H^+} R-OH \xleftrightarrow{-H^+/H^+} R-O^-$$

The negative surface charges of ITO were neutralized by the protons during the application of a positive potential and so, the repulsive force being diminished the cells could contacted the surface.

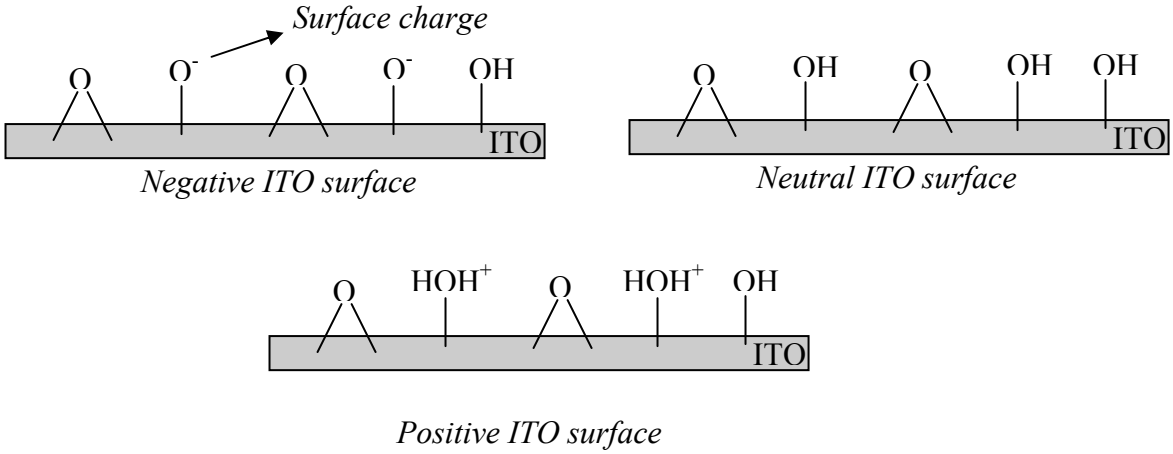

Fig. 3. 46 Schematic distribution of the chemical surface groups on a ITO surface and charge surface groups formation as a function of pH.

As we can see on table 3.7, when ITO surface was neutralized, the percentage of dark cells was 20% and when the surface became positive by decreasing the pH (longer pulse application), the percentage sharply increases at 75-100%. pH values were calculated using Comsol Multiphysics Modeling (see Materials and Methods). We measured the zeta potential in a 10 mM KCl solution and we calculated it for a 0.1 mM solution (see Materials and Methods). For more diluted electrolyte solutions, the measurements of zeta potential of a conductive material may induce big errors especially if they are bigger than 50 mV. Thus, the values should be deduced on the base on those found experimentally in 10^{-2}-10^{-3} M, 1:1 electrolyte solutions (Delgado, 2005).

Table 3.7 pH values and percentages of adherent cells as a function of pulse time

Pulse time (s)	Calculated pH	Experimental Zeta potential (10 mM)	Calculated Zeta potential (0.1 mM)	Percentage of dark cells	Percentage of white cells
0	6	-21	-110	0	0
0.033	4.814	-6	-68	0	10
0.05	4.717	-4	-42	10	45
0.1	4.55	-1	-10	15	70
0.143	4.452	0	0	20	75
0.2	4.36	2	20	75	25
0.23	4.33	2.5	27	100	0

In order to characterize these passive physico-chemical phenomena, we repeated the same experiment with surface-carboxylated fluorescent polystyrene beads (diameter 1 μm). Due to their negative zeta potential (-56 mV), the beads levitated over the ITO surface at 0.17 mM phosphate sucrose buffer. When a 5 V pulse was applied, the beads were rapidly attracted on the surface as observed by the change in focus using fluorescence microscopy (Fig. 3.47).

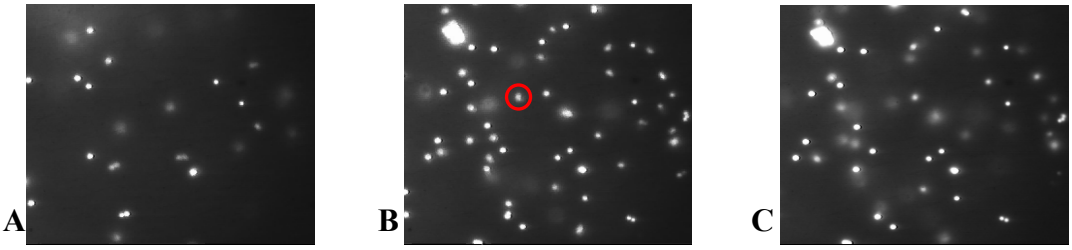

Fig.3.47 (**A**). Fluorescence beads before 5V pulse (3.2 s) in 0.17 mM phosphate sucrose buffer; some beads are deposited on the surface before the pulse application. (**B**) Beads were attracted to the surface during the pulse application (for example, the bead in the red circle). (**C**) A fraction of beads bind irreversibly to the surface.

We conducted experiments as a function of pulse duration (Fig. 3.48). This showed that beads were attracted for pulses longer than 0.5 s. Interestingly, for pulses longer than 1.5 s, a fraction of beads bind irreversibly to the surface. This fraction increased quasi-exponentially with pulse duration.

Beads that are not irreversibly attached left the focal plane immediately after the end of the electrical pulse. This showed that during the voltage pulse, forces over negatively charged objects close to the surface were involved. These forces lasted as long as the pulse was imposed. Some covalent ester bonds between the carboxylic functions of

the beads and the ITO surface likely formed and some ones became irreversibly bound to the surface.

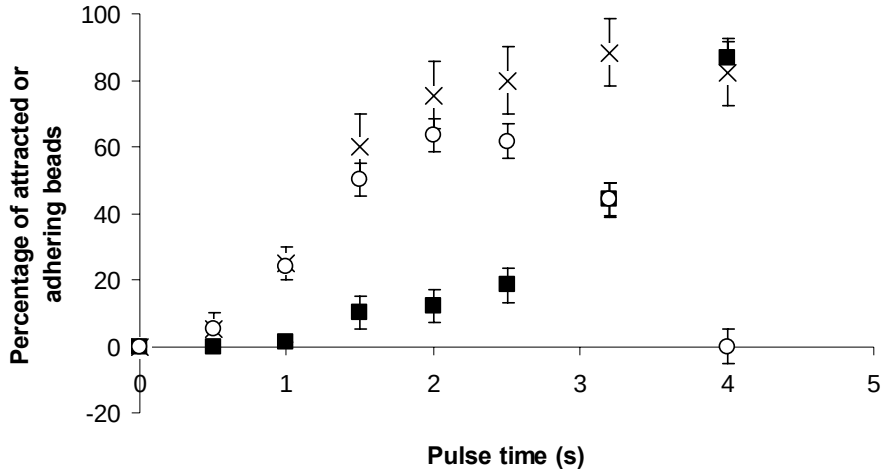

Fig. 3.48 Electrical and electrochemical effect of potential pulse on polystyrene beads as a function of pulse time. X : percentage of attracted beads. Squares: percentage of irreversibly attached beads. Circles: percentage of reversibly attracted beads.

3.5.2 Actin polymerization kinetics in electrochemically induced cell synchronization

Cyclic actin-polymerization events accompany spreading in *D. discoideum*, and cycles persist beyond cell spreading into random motility (see subchapter 3.1). This complex temporal organization can be tackled by controlling the onset of cell-surface contact; thus, cell synchronization allows statistically relevant quantification of molecular events accompanying spreading in a cell population.

RICM observations did not allow us to detect the actin polymerization activity in the earliest stages after a pulse application. We therefore used electrochemically induced surface contact experiments with *D. discoideum* AX2 LimE$^{\Delta coil}$-GFP cells to follow the evolution of cyclic actin polymerisation at the onset of the surface contact.

First, cells were allowed to levitate over an ITO covered glass surface in 0.17 mM phosphate sucrose buffer, the focal plane of the objective was settled to the ITO surface level (plane zero) and the fluorescence was recorded. In this case, the fluorescence intensity is very low or zero given that the cells are levitating at minimum 100 nm from the focal plane. If we focus to cell level, experiments reveal that fluctuating actin polymerization occurs even in the absence of cell spreading (see subchapter 3.3).

Levitating cells were subsequently submitted to a 5 V 0.1 s pulse to induce cell-surface contact and LimE$^{\Delta coil}$-GFP fluorescence was recorded (Fig. 3.49). About 2 s after the pulse, new immobile fluorescence events start to appear (pointed by the red arrow, see Fig. 3.50).

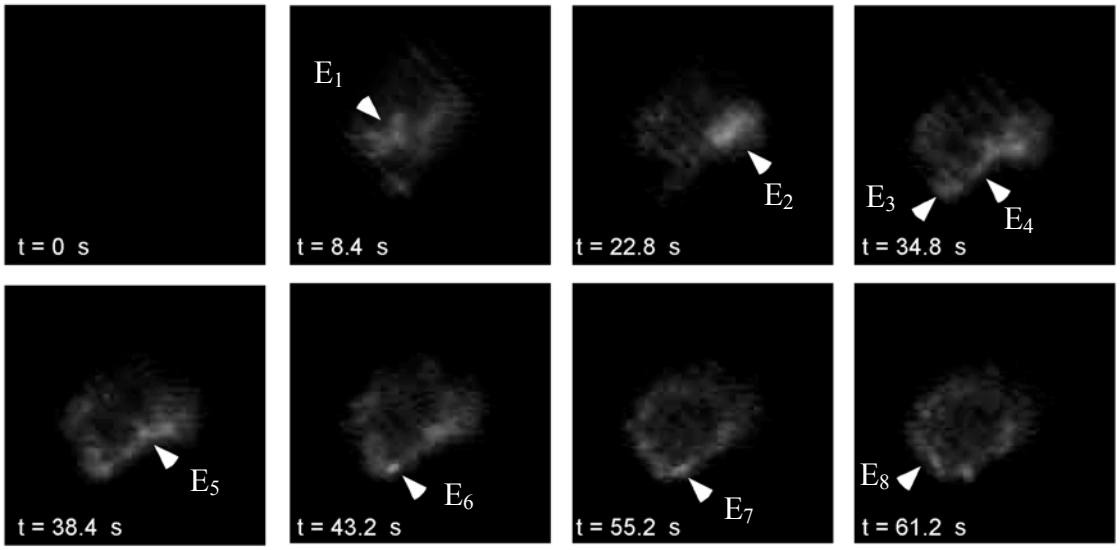

Fig. 3.49 Sequential images of *D. discoideum* expressing LimE$^{\Delta coil}$-GFP subjected to a 5V 0.1 s pulse while levitating in 0.17 mM phosphate sucrose buffer over an ITO-covered glass surface. Sequential frames were taken at different times after the pulse (t = 0 s). Arrows indicate fluorescence maxima of individual events.

For the studied cell, we obtain the following representation of fluorescent maxima events versus time:

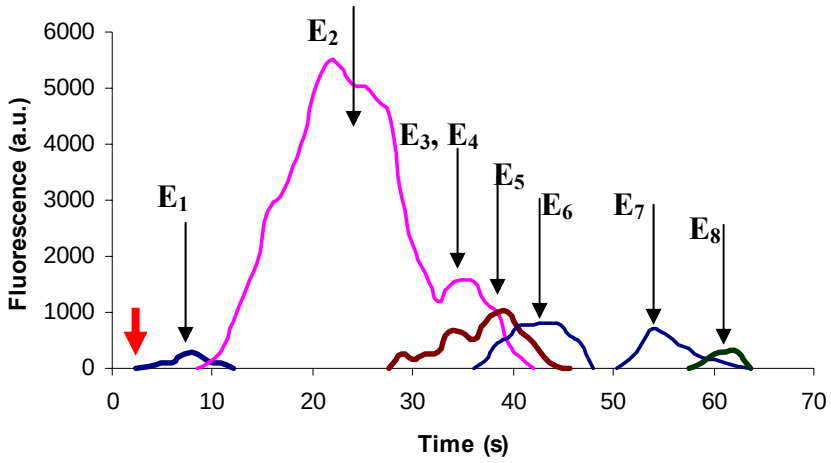

Fig. 3.50 LimE$^{\Delta coil}$-GFP fluorescence variation in active zones as a function of time for the cell shown in Fig. 3.49. Black arrows correspond to the events highlighted in Fig. 3.49. Red arrow point the beginning of the first event fluorescence, around 2 s after the pulse. The pulse was applied at t = 0.

The first event peak appeared 8.4 s after the pulse. As the cells spread, more and more actin foci appeared at the edge of the cells. Similarly to spreading in physiologic conditions (see subchapter 3.1), actin polymerization events appeared more or less regularly at 8.4, 22.8, 34.8, 38.4, 43.2, 55.2 and 61.2 s after the pulse.

Analyzing these individual fluorescence events for the cell presented in figure 3.50, a period of 8.27 ± 4.63 s (Fig. 3.51) can be measured which is very close to the averaged time of occurrence of the maxima of the peaks appearing in Fig. 3.10 (for a cell who spreads in SB).

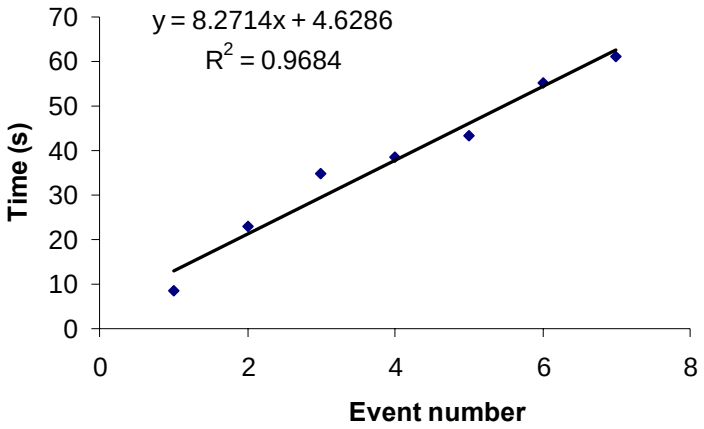

Fig. 3.51 Time occurrence of successive peaks during cell adhesion after the pulse application (Event 0, t = 0); the distribution is linearly fitted, defining an average period of 8.27 s

Fig. 3.51 Time occurrence of successive peaks during cell adhesion after the pulse application (Event 0, t = 0); the distribution is linearly fitted, defining an average period of 8.27 s

As we have seen, the cells make simultaneously contacts with the surface during the pulse and the onset of spreading in dilute buffer solution is also due to the electrical pulse application. One important question is whether the actin polymerization activity is synchronized immediately after the pulse (for example, within 20 s after the pulse). If, the majority of levitating cells exhibit the first fluorescent event peak randomly in time, after the electrical pulse, we can conclude that it did not trigger a synchrony internal signalization in cell population. Contrary, if the first peak appears for majority of the cells with a high probability in a restricted interval, we can affirm that the cells are synchronized.

We analyzed the probability of the apparition of the first peak, after the electrical pulse application, for *47* cells. We obtained the following results: *10* cells (20%) either did not have observable activity (even they were adhered) within 65 s after the pulse or

they were not spreading; *37* cells (80%) were active cells and started to spread, showing, more or less regularly spaced in time, oscillating actin polymerization activity. Remarkably, no maxima appeared before 7 s after the pulse application. *29* cells from *37* (79%) had the first peak within 4 seconds interval, between 7.5 s and 11.5 s and *8* cells exhibit an fluorescent event peak within 12-20 s interval, after the pulse (Fig. 3.52).

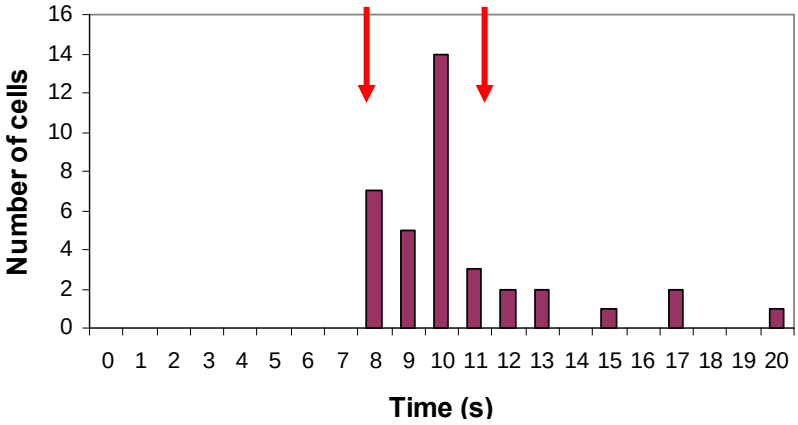

Fig. 3.52 Number of cells that exhibit the first fluorescent event peak after an electrical pulse application within one-second interval. One observes that majority of cells (29 cells) has the first peak between 7.5 s and 11.5 s (interval delimited by the red arrows). Total of compiled cells was 37 cells.

From the *29* cells that had the first peak within 4 seconds interval, between 7.5 s and 11.5 s (interval delimited by the red arrows in Fig. 3.52), *14* cells exhibited 6 or 7 fluorescent event peaks within 65 s after the pulse application and *15* cells had less than 6 peaks within 65 s after the pulse application. The distribution of the time intervals between individual fluorescent peaks was compiled for the *14* cells that exhibit 6 or 7 fluorescent event peaks within 65 s after the pulse application (Fig. 3.53A).

Most cells showed regular actin polymerization events separated by 10 ± 3.9 s (Fig. 3.53A). The probability of peak appearance was plotted as a function of time after the pulse (Fig. 3.53B). Remarkably, the first peak appears 9.4 ± 1.7 s after the pulse and two additional maxima appear at 23 and 34 s. If we integrate over a 3 seconds window, 86% of the cells would have the first peak between 7.5 and 10.5 seconds after the pulse application. Moreover, the probability that the cells have three peaks of activity at 9±1 s, 23±1 s and 34±1 s is higher than 0.2.

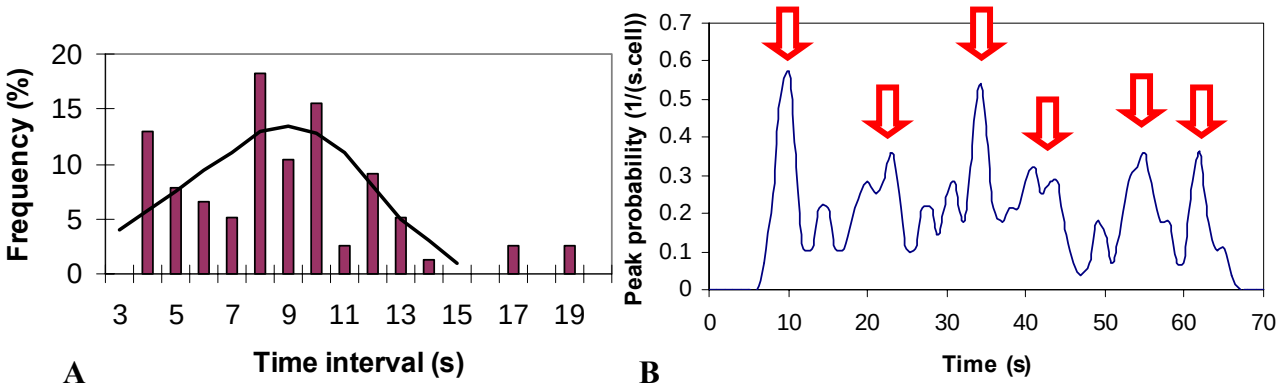

Fig. 3.53 A. Histogram of time intervals between adjacent peaks of significant actin polymerisation activity for 14 individual cells, which exhibit 6 or 7 consecutive actin polymerization events in the next 65 s after the pulse (during spreading). The solid line represents the best fit of the experimental data with a normal distribution (average = 10 s; standard deviation = 3.9 s).
B. Frequency of appearance of $LimE^{\Delta coil}$-GFP fluorescence peaks for 14 individual cells as a function of time after the pulse. The data are expressed as probability of appearance of a peak per cell and per second.

As a consequence, the pulse-induced contact with the surface, triggers quasi-periodic actin polymerization, for all active cells which spread in dilute buffer solution, after an electrical pulse application.

Moreover, the probability that the first peaks after the pulse appear within 4 seconds, for all active cells which spread in dilute buffer solution, is 0.79 (see Fig. 3.52). We consider that spreading is therefore synchronized.

IV Discussion

4.1 Actin polymerization at actin foci: does it require contact with the surface ?

D. discoideum cells have various forms, elongated or more rounded, spread faster or slower, and reach different total areas.

Despite these cell-to-cell variations, the dynamics of cell-surface contact zones during spreading of D. discoideum reveal common features: a few seconds after contact with the surface, cells start to extend pseudopods in one or several well-defined directions. A succession of pseudopods follows, resulting in an anisotropic increase in cell-surface contact area. After about 50 s, the cell starts retracting part of its contact area, initiated at the point where the initial contact area was formed. At the same time, pseudopods still extend but their size decreases to match the retraction activity. Once a balance between gain and loss of area is reached, spreading is completed and cells start to move on the surface.

In the subchapter 3.1 we present the results of periodic protrusion activity during *Dictyostelium* spreading and motility. The reported time period (10.68 ± 1.9 s for all RICM experiments) is almost the same during shear flow induced cell motility (Fache, 2005) and spreading.

During spreading, actin polymerization at the cell margin is also quasi-periodic, with a 10-11 s time period for the variations of $LIM^{\Delta coil}$-GFP fluorescence. The periodic formation of close contacts between the cell and the surface is therefore accompanied by the periodic activation of actin foci or clusters of actin foci at the cell margin. This may correspond to traveling actin waves observed before, that resemble self-organized chemical waves in dissipative, physico-chemical systems (Vicker, 2000; 2002a, b; Gerisch, 2004; Bretschneider, 2009). It is therefore possible that the intermittent movement of the cell margin corresponds to the activation and deactivation of adhesion receptors controlling local actin polymerization. Actin polymerization at the cell margin induced by activation of adhesion receptors would put nearby adhesion receptors into contact with the surface, starting a new cycle, supporting the hypothesis that this periodic

activity seems to be set by the contact with the surface. Lowering the actin polymerization rate would thus extend the duration of this cycle.

We also showed (see subchapter 3.3) that fluctuations in actin polymerization activity occur in the absence of any stable cell surface contact, as cell levitate over repulsive surface (Fig. 3.27). Further, the movie analysis reveals that even under these conditions, as the cell is agitated by continuous Brownian movement, it makes transient immobile punctuated contacts with the surface that last at least 8.4 seconds and which are similar to actin foci (Fig. 4.1). In this example, it can be seen that the cell rotates around the fixed fluorescent dot (1 μm in diameter), indicating that adhesion was minimum. This was evidenced using of LIM$^{\Delta coil}$-GFP fluorescence and phase contrast observation, as RICM images were not controlled to resolve such small contact sites. Also, phase contrast observations reveal the randomly pseudopodia formation when cell levitate. Additionally, actin polymerization activity still occurs in suspended cells in isoosmotic sucrose solution (36 mM sucrose in deionized water).

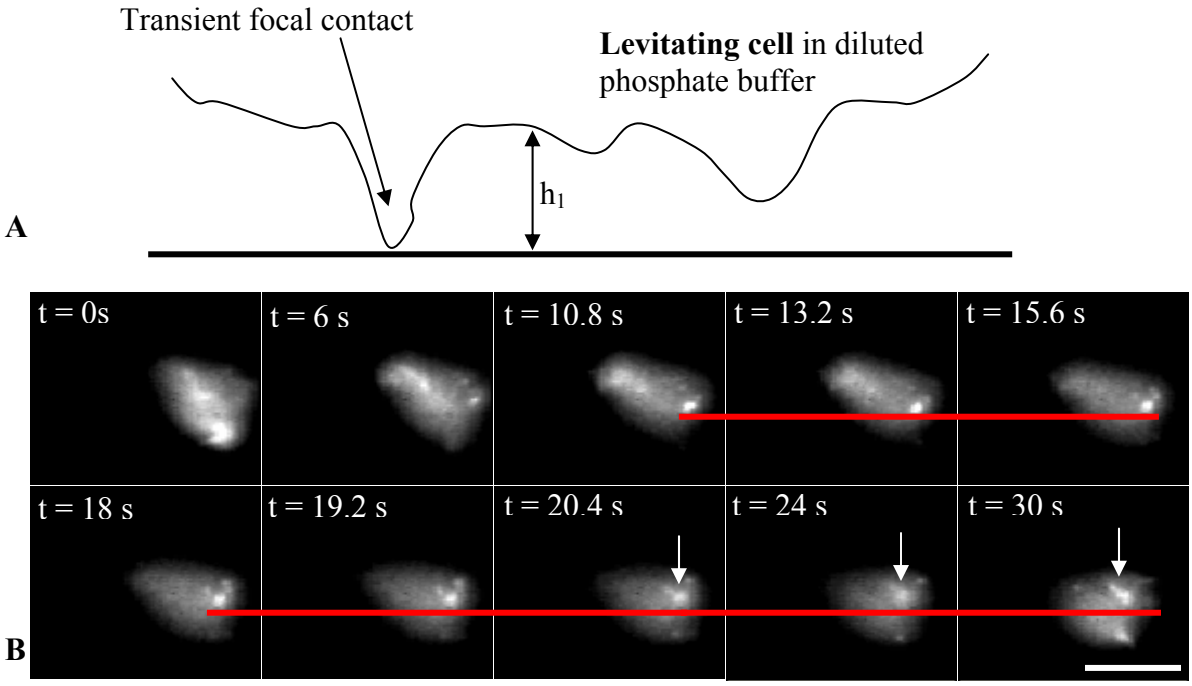

Fig. 4.1 LimE$^{\Delta coil}$-GFP fluorescence kinetics in levitating cells. **A**. Schematic representation of levitating cell in dilute phosphate buffer. The black arrow indicates a transient focal site. **B**. Sequential images of *D. discoideum* expressing LimE$^{\Delta coil}$-GFP levitating in 0.17 mM phosphate sucrose buffer over a glass surface. Red horizontal lines correspond to the same level on a glass surface and guide us to localize the fluorescent dot, corresponding to the transient focal site. Arrows indicate fluorescence dissipation of the fluorescent dot. Notice the rotation of the cell during this transition. Scale bar: 10 μm.

How is it possible for a cell to make contacts with the surface, in the presence of such repelling force field? We propose two explanations: 1) it is posible that the electric fields are not homogenous due to the non-uniform distribution of the negative or positive discrete surface charges (maybe for both surfaces, but more probable for cell surface). Therefore, thin cell membrane deformations could appear in zones where the repulsive electric field is less important. An observation supporting this assumption is that some micrometric negatively charged fluorescent beads (supposing that they do not have defaults) stick to the surface even in very dilute medium. 2) an internal mechanism of actin polymerization exists, which does not require any contact; this could push the membrane in a pseudo-periodic way, resulting in the formation of contacts with the surface.

Interestingly, periodic membrane blebing has recently been reported for spreading fibroblasts that gives rise to 10-15 s periodic fluctuations of membrane velocity (Dubin-Thaler, 2008). Furthermore, adhesion spots form and disaggregate at the membrane margin of CHO cells with about the same kinetics, close to that of *Dictyostelium* actin foci (Choi, 2008). *Dictyostelium* and higher eukaryotes are therefore likely to share molecular mechanisms of spreading.

In addition, we showed that electrochemically-induced cell-surface contact triggers periodic activity (suchapter 3.5). It seems therefore that an internal clock is involved in cell spreading and movement, and is sensitive to cell-surface contact. Spatial control of *Dictyostelium* spreading can be achieved by microengineered adhesion patterns (Tzvetkova, 2008). In subchapter 3.5, we showed that applying an electrochemical pulse on a conductive material can synchronize *Dictyostelium* spreading, thus providing temporal control.

Almost periodic activity of *Dictyostelium* motility has already been observed in previous works. Analysis of cell contour observed by time-lapse video microscopy revealed the existence of periodical cell movements, at the minute time scale (Killich, 1993). Quasi-periodic behaviors in the velocity and shape of migrating Dictyostelium cells have also been reported (Uchida, 2003; Wessels, 1998; Shenderov, 1997). In addition, the shear stress exerted by the cell to the surface also exhibits approximately periodic phases of protrusion and retraction activities, each lasting about 50 s (Del Alamo,

2007). These phases start once spreading is completed and modulate the level of protrusion and retraction activities (Killich, 1993). At least two time scales are therefore present in the complex amoeboid motility.

4.2 Estimation of the repulsive electrostatic forces and distances between the cells and surfaces as a function of ionic concentrations

4.2.1 The effect of ionic concentration on the electrostatic repulsion and attraction

We investigated the effect of ionic concentration on the electrostatic repulsion between negatively charged *Dictyostelium* cells and a negatively charged glass (or ITO) surface. These forces influence the kinetics of efficient cell-surface contact formation.

Our results show that the variation of the ionic concentration affects the time to contact the surface but not the spreading time once an efficient contact is established. Indeed, on glass, at constant intermediate ionic concentrations (0.5 - 0.7 mM), cells that are able to make a successful contact, spread in about 1-2 minutes, as observed in physiological conditions (Fig. 3.1). At concentrations smaller than 0.25 mM in SB, the screening effect of the negative charges of glass surface and cells is decreased enough such that the electrostatic repulsion prevents cell adhesion. The distance between surface and *Dictyostelium* cells depends on the surface composition and nature and concentration of the ions found in the medium solution.

Electrostatic repulsive forces are not sufficient to detach cells that already form large contact areas with the surface but can displace the cell membrane locally. When the salt concentration is changed, variations in the grey level of the interior of the cell-surface contact area can be observed (Fig. 3.25). We interpret the variation in reflected light intensity as a change in the distance between the plasma membrane and the surface, because the refractive index of the buffer solutions is almost unchanged when the salt concentration is varied. Similarly, application of a negative voltage pulse on ITO coated glass, sufficient to locally produce OH^- ions, also results in a whitening of the cell-surface contact in the interior of the cell and transiently reveals the presence of a few close contact points with the surface (Fig. 3.17). These adhesion structures are likely to be actin

foci, first observed by Yumura *et al*. in *D. discoideum* (Uchida, 2004; Yumura, 1993). This shows that cell attachment is stronger at the margin of the cell than in its centre, as postulated by earlier theoretical and experimental studies (Garrivier, 2002; Decave, 2002).

Moreover, when cell-surface contact is triggered by an electrochemical pulse, they spread at low ionic strength in about 1 minute which is remarkably close to cells sedimenting and spreading in physiological buffer (Keller, submitted; Chamaraux, 2005). Once a successful contact is formed, cells are thus able to spread against electrostatic repulsion using actin polymerization as a driving force. We presume that, at the margin of the cell, the actin cytoskeleton exerts a torque around the adhesive edge perpendicular to the membrane of the cell in the direction of the surface. This allows the cell to overcome repulsion locally and, once a contact has been established, to extent the contact zone on the surface, even in a low ionic strength environment.

Conversely, at low ionic concentration, positive surface charges (APS or pulse time > 0. 1 s) exert forces strong enough to attract the cell surface and induce spreading. About 20 μm^2 of cell membrane spread on the surface in less than 1 s, which is ten times the average spreading rate observed at physiological ionic concentration (Fig. 3.26). Actin cannot polymerize as quickly. It is therefore likely that in these conditions, the plasma membrane detaches from the underlying cytoskeleton over a large zone (dark contact zone), which is later filled by actin. A similar mechanical situation was reported in micropipette experiments, when suction is applied to detach the plasma membrane from the cytoskeleton. Macroscopically, the magnitude of such forces is a few nN (Boulbitch, 2002; Merkel, 2002). This shows that electrostatic forces can be very strong at short distances, and thus be able to control cell adhesion.

In the next paragraph, we will develop a simple model based on the the Gouy-Chapman-Stern theory of the double layer (see Materials and Methods) to evaluate the electrostatic repulsive forces.

4.2.2 Electrostatic repulsive forces estimations

Using RICM we can estimate the surface area of an object (adherent cell) and the distance between the object and the focused planar surface. However, there is some uncertainly in the determining of distances in *z* axis (the reflected light intensity varies between white and black and can only indicate a multiple of a quarter or less of wavelength, depending also of the refractive index, see Materials and Methods). Our model intends to estimate the distance between the surface and a levitating cell on the basis on the cell and substrate surface charges and on the buffer concentration.

Surface charge density of the ITO and cell surfaces

As we have seen, the charge density at 25ºC of a planar surface immerged in z:z electrolyte could be calculated with eq. 2.30 (see Materials and Methods): $\sigma^M + \sigma^i \approx 11.7 \cdot C^{1/2} \cdot \sinh(19.5z\zeta)$, where *C* is the bulk solution concentration (M), σ_M is ITO surface charge density, σ_i represents the charge density of specifically adsorbed ions in the inner layer ($\mu C/cm^2$) and ζ is the zeta potential in absolute value, in Volts.

First, we make the following approximation: SB solution contains only 1:1 electrolytes.

It is very known that, in general, σ_i ($\mu C/cm^2$) is negligible in front of σ_M ($\mu C/cm^2$), and particularily, considering that the nature of ions composing SB solutions suggests a low number of ions adsorbed at the surface, the above equation becomes:

$$\sigma^M \approx 11.7 \cdot C^{1/2} \cdot \sinh(19.5\zeta) \text{ in } \mu C/cm^2 \qquad \text{Eq. 4.1}$$

The averaged zeta potential of ITO surface at 25ºC, in 10^{-2} M KCl (pH = 5.6) is -21 mV (moreover, the values of zeta potential for ITO and glass surface are close; see Table 3.4 and 3.7). We can now calculate the ITO charge density in these conditions:

$$\sigma^M \approx 11.7 \cdot 0.1 \cdot \sinh(19.5 \cdot 21 \cdot 10^{-3}) = 0.482\ \mu C/cm^2 \qquad \text{Eq. 4.2}$$

which is equivalent with one negative charge ($1e^- = 1.6 \cdot 10^{-19}$ C) for 33 nm^2 at pH = 5.6.

Applying the same equation for a living cell (ζ = -17 mV in SB, pH = 6.1, Table 3.4) we obtain the charge density of *Dictyostelium* cell at pH = 6.1 (σ_{cell}):

$$\sigma_{cell} \approx 11.7 \cdot 0.13 \cdot \sinh(0.3315) = 1.52 \cdot 0.337 = 0.512\ \mu C/cm^2 = 5.12 \cdot 10^{-15}\ C/\mu m^2 \qquad \text{Eq. 4.3}$$

which represents one negative charge ($1e^- = 1.6 \cdot 10^{-19}$ C) for 31 nm^2. For a spherical cell of 10 μm diameter (cell surface = $S_{cell} = 4\pi r^2 = 314\ \mu m^2 = 3.14 \cdot 10^8\ nm^2$), the surface charge, Q_{cell}, is therefore $1.61 \cdot 10^{-12}$ C at pH 6.1 (approximately 10^7 negative elementary charges/cell). Measurements made in 10^{-2} M KCl solution at different pH (5.8 and 5.2) have shown unchangeable value of zeta potential (-21 mV).

Electrostatic Model

Solving the Poisson equation considering Debye- Hükel approximation and expressing the Laplace operator in spherical polar coordinates and assuming that the potential *V(r)* at a point **r** in the vicinity of a positive ion is spherically symmetric we got (Hoppe, 1983):

$$V(r) = \frac{q}{4\pi\varepsilon\varepsilon_0} \cdot \frac{e^{-\kappa r}}{r} = \frac{ze}{4\pi\varepsilon\varepsilon_0} \cdot \frac{e^{-\kappa r}}{r} \qquad \text{Eq. 4.4}$$

where $\kappa = \left(\frac{2n^0 z^2 e^2}{\varepsilon\varepsilon_0 kT} \right)^{1/2}$; for ε = 78.49 at 25ºC, $\kappa = 3.29 \cdot 10^7 \cdot z \cdot C^{1/2}$ (Eq. 2.24, see Materials and Methods) where *C* is the bulk z:z electrolyte concentration (M) and κ is given in cm^{-1}. $r_D = 1/\kappa$ is the so-called Debye distance and is of the order of 30 nm for 10^{-4} M 1:1 electrolyte at 25ºC. The $e^{-\kappa r}$ factor is the screening term of the charge *q* due to its counterions. The potential therefore decreases following $e^{-\kappa r}$ and *κ* (inverse of Debye distance) strongly modulates its value.

In the same reasoning, we can consider the surface of the cell like a discrete distribution of point charges, relative to the semi-infinite planar electrode; thus, the potential at a point **r** in vicinity of the cell is:

$$V(r) = \frac{1}{4\pi\varepsilon\varepsilon_0} \cdot \sum \frac{Q^i_{cell} e^{-\kappa r_i}}{r_i} = \frac{1}{4\pi\varepsilon\varepsilon_0} \cdot \int_{S_{cell}} \frac{\sigma_{cell} e^{-\kappa r_i}\, dS}{r_i} \qquad \text{Eq. 4.5}$$

where Q_{cell}^i is the charge on the surface of the cell at a distance r_i from the point **r**, S_{cell} is cell surface and σ_{cell} is density charge of the cell.

In the case considered in this work, cells with a negative surface charge come near a planar surface of ITO that also possesses a surface negative charge at physiological pH (see Fig. 4.2). When cells levitate at a distance **r** = 100-300 nm and therefore are placed

in the electric field of the surface (ψ), the repelling force between the two objects could be written as:

$$F_e = \sum_i \frac{\psi(r) \cdot Q^i_{cell} e^{-\kappa r_i}}{r_i} = \int_{S_{cell}} \frac{\psi(r) \cdot e^{-\kappa r_i} \cdot \sigma_{cell} dS}{r_i} \qquad \text{Eq. 4.6}$$

where ψ(r) is the potential at the distance *r* from the planar surface, due to its superficial charges (Materials and Methods, Eq. 2.28).

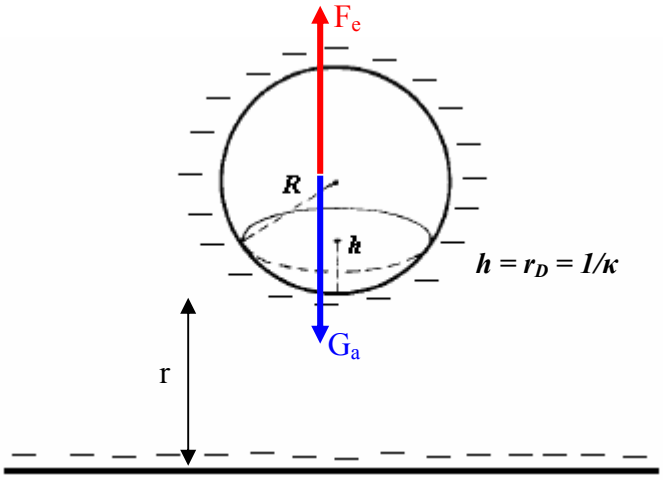

Fig. 4.2 A Schematic representation of a spherical levitating cell of radius R, repelled by a substrate with negative charge surface in SB diluted. The discrete negative surface charges is represented by "-". A cap with the surface S = 2πRh = 2πR/κ is also marked (see explication below). Electrostatic repulsion force (F_e) is balanced by the apparent gravity (G_a) and are represented by red and blue arrow respectively (intentionally not centered); we neglected the van der Waals attraction contribution. The solution ions (including the counterions) are not shown.

We consider now that the main contribution to the repelling force is due to the charges located on a sphere cap with $\boldsymbol{h = r_D = 1/\kappa}$ which is the closest surface on the ITO planar substrate (Fig. 4.2). Contribution of the charges situated on the upper part of the sphere is negligible, comparative with those situated at distance ***r***, because of the exponential screening term, $e^{-\kappa r}$, which is dependent on Debye distance. Thus, the repelling force becomes:

$$F_e = \psi(r) \frac{\sigma_{cell} S \cdot e^{-\kappa r}}{r} = \psi(r) \frac{Q^S_{cell} \cdot e^{-\kappa r}}{r} \qquad \text{Eq. 4.7}$$

where *S* is the cap surface and Q_{cell}^S is the charge situated on the cap surface.

The cap surface depends on the Debye distance and has the following formula:

$$S = 2\pi R/\kappa \qquad \text{Eq. 4.8}$$

where *R* is the cell radius and 1/κ is Debye distance.

Knowing the surface charge density of the cell ($5.12 \cdot 10^{-15}$ C/μm^2) from zeta potential measurements, the repelling force becomes:

$$F_e = 5.12 \cdot 10^{-15} \cdot \frac{2\pi R}{\kappa} \cdot \frac{\psi(r) e^{-\kappa r}}{r} \qquad \text{Eq. 4.9}$$

Now, the potential at distance *r* from the ITO surface, *ψ(r)*, could be written on the base on Eq. 2.28, in function of the zeta potential (in absolute value) of the ITO surface, in a majority 1:1 electrolyte, at 25ºC and $\kappa = 3.29 \cdot 10^9 C^{1/2}\ m^{-1}$:

$$\tanh(e\psi(r)/4kT) = \tanh(e\psi_2/4kT)\, e^{-\kappa(r-x_2)} \cong \tanh(e\zeta_{ITO}/4kT)\, e^{-\kappa r} \qquad \text{Eq. 4.10}$$
$$\Leftrightarrow \quad \tanh(11 \cdot \psi(r)) \cong \tanh(11 \cdot \zeta_{ITO}) \cdot e^{-\kappa r}$$

Zeta potential of ITO surface was measured experimentally in a 10 mM KCl solution (-21 mV, see Table 3.7) and will be estimated theoretically for each SB diluted solution.

Considering that for a levitating cell, this force is compensated by the apparent gravity force (Fig. 4.2) estimated for a *Dictyostelium* cell at $3 \cdot 10^{-13}$ N, (at a distance **r** = 100-300 nm electrostatic repulsion potential dominates the van der Waals attraction potential, see Materials and Methods) we have the following equality:

$$5.12 \cdot 10^{-15} \cdot \frac{2\pi R}{\kappa} \cdot \frac{\psi(r) e^{-\kappa r}}{r} = 3 \cdot 10^{-13} \qquad \text{Eq. 4.11}$$

4.2.3 Distance calculation

For a cell levitating in 0.17 mM phosphate sucrose buffer

To express the potential *ψ* at a distance *r* from ITO surface, we need to know the potential drop along the diffuse layer, ψ_2, and therefore the zeta potential in a refernce solution (see Eq. 4.10). We measured the zeta potential in a $C_0 = 10^{-2}$ M KCl solution (ζ_0 = -21 mV, see Table 3.7) and we calculate it for a 0.17 mM solution, using eq. 2.30. We assume that ITO charge surface does not significantly change with the solution ionic strength, because we deal with dilute solutions (the activity coefficients involved in dissociation constants of surface groups are influenced by ionic strength), but only with pH (see Materials and Methods). In this approach, we also excluded the specific adsorption that could be influenced by dilution.

In buffer solution like SB, even at large dilution, the pH indeed remains around 6.1-6.3. For electrolyte solutions with a concentration lower than 10^{-3} M, the

measurements of zeta potential of a conductive material may induce big errors especially if they are bigger, in absolute value, than 50 mV. Thus, the values should be deduced on the base on those found experimentally in 10^{-2}-10^{-3} M 1:1 electrolyte solutions (Delgado, 2005).

Hypothesis: Surface charge (σ_M) does not significantly change with dilution, but only with pH. It result that:

$$\sigma^M \approx 11.7 \cdot \sqrt{C_0} \cdot \sinh(19.5 \cdot \zeta_0) = 11.7 \cdot \sqrt{C} \cdot 10^{-2} \sinh(19.5 \cdot \zeta_C) \quad \text{Eq. 4.12}$$

where ζ_i is the absolute value of zeta potential of the ITO surface immersed in a 1:1 electrolyte solution with concentration C_i. For $C = 1.7 \cdot 10^{-4}$ M solution, it results:

$$\sigma^M \approx 11.7 \cdot 10^{-1} \cdot \sinh(19.5 \cdot 0.021) = 11.7 \cdot \sqrt{1.7} \cdot 10^{-2} \sinh(19.5 \cdot \zeta) \quad \text{Eq. 4.13}$$

It follows immediately that ζ = -0.097 V. For comparison, for a non conductive material, like glass, for which we measured the zeta potential without significant errors, in $1.7 \cdot 10^{-4}$ M sucrose phosphate buffer solution, we obtained –0.095 V (this also indicates close values of surface charge for both surfaces).

Now, we can develop the eq. 4.10:

$$\tanh(11 \cdot \psi(r)) \cong \tanh(11 \cdot \zeta) \cdot e^{-\kappa r} = \tanh(1.067) \cdot e^{-\kappa r} = 0.788 \cdot e^{-\kappa r} \quad \text{Eq. 4.14}$$

For r > 100 nm and $r_D = 1/\kappa = 1/3.29 \cdot 10^9 \cdot C^{1/2}$ = 23 nm, $0.788e^{-kr} < 10^{-2}$ it results that:

$$\tanh(11 \cdot \psi(r)) \cong 11 \cdot \psi(r)$$

$$\Rightarrow \quad 11 \cdot \psi(r) = \tanh(11 \cdot \zeta) \cdot e^{-\kappa r} \quad \Rightarrow \quad \psi(r) = \frac{\tanh(11 \cdot \zeta)}{11} \cdot e^{-\kappa r} \quad \text{Eq. 4.15}$$

Replacing the new expression of the $\psi(r)$ in eq. 4.11, we got:

$$5.12 \cdot 10^{-15} \cdot \frac{2\pi R}{\kappa} \cdot \frac{\tanh(11 \cdot \zeta)}{11} \cdot \frac{e^{-2\kappa r}}{r} = 3 \cdot 10^{-13} \quad \text{Eq. 4.16}$$

For a cell of radius R = 5 μm in $1.7 \cdot 10^{-4}$ M SB ($r_D = 1/\kappa$ = 23 nm, considering the SB like 1:1 electrolyte), cup surface is $S = 2\pi R/\kappa$ = 0.722 μm^2. The eq. 4.16 becomes:

$$\frac{e^{-2\kappa r}}{r} = 1133.54 \quad \Rightarrow \quad r = 104 \text{ nm} \quad \text{Eq. 4.17}$$

The RICM experimental observations indicate that the cells, which levitate in 1.7 10^{-4} M SB either above a glass or an ITO surface, appear like white spots suggesting a distance around 100 nm (see Materials and Methods and Fig. 3.23B, C; see also Fig. 4. 5).

The similar RICM contrasts intensities obtained with both surfaces can be explained by the thick of ITO layer (80 nm), value that is close to that of a half wavelength shown in Fig. 4.2. Moreover, the distance between a cell and glass or an ITO surface should be very close considering the values of zeta potential for both surfaces.

A cell levitating in 0.034 mM phosphate sucrose buffer

The same reasoning like above is followed and we obtain: ζ = -0.137 V, $r_D = 1/\kappa$ = 52 nm, S = 1.633 μm^2 and,

$$\frac{e^{-2\kappa r}}{r} = 435.46 \Rightarrow r = 238\,nm \qquad \text{Eq. 4.18}$$

Experimental observations (Fig. 4.3A, Fig. 3.23C and Fig. 3.42-before pulse) indicate for most levitating cells a contrast darker than the background, corresponding to a distance around 200 nm from the surface (see Materials and Methods). We also analyzed the attachment kinetics of the cells levitating in 0.034 mM phosphate sucrose buffer during 2 s application of + 2.5 V/Ref. pulse (Fig. 4.3) We noticed that, before the cell-surface contact become black (Fig. 4.3C), the cells follow an intermediate contrast revealed by white spots (Fig. 4.3B), confirming that initial levitating distance was around 200 nm.

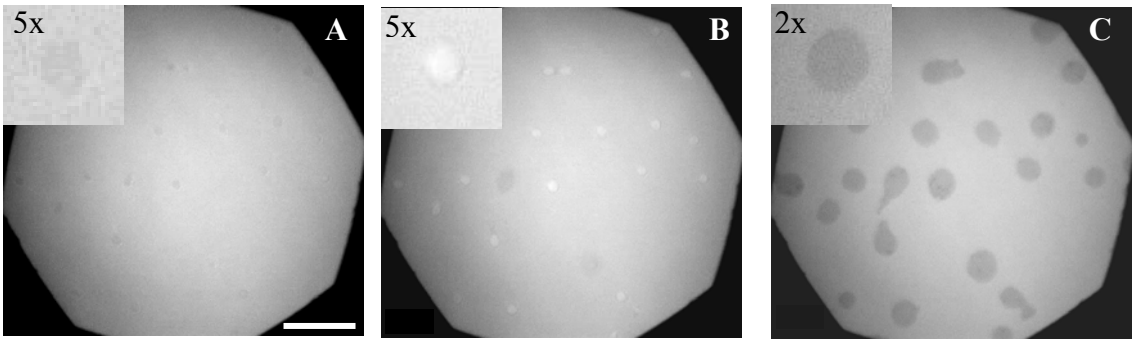

Fig. 4.3 RICM images of *D. discoideum* cells obtained before and after applying a 2.5 V/Ref. pulse for 2 s at the ITO surface in 0.034 mM SB. The cell RICM contrast changes from darker than the background (A) for white (B) and then, 2 s after the beginning of the pulse, to black (C). The inserts in A, B and C are magnified dark, white levitating cells and black contact respectively.

Before pulse application (Fig. 4.3A), most levitating cells (14 from 19) were darker than the background; at the onset of pulse, the centre of the cell became intensively white surrounded by a dark fringe (Fig. 4.3B). Most of the cells became black

after 0.6 s from the pulse onset and its contact surface increases with time (Fig. 3.42, Fig. 4.3 C-after 2 s). According to the sequence of RICM contrast changing, we estimated the distance between the substrate and the cell membrane, before the pulse, to be 200 nm (a black spot produced by an object standing at a pair multiple of 100 nm apart from the surface, see Materials and Methods).

A cell levitating in 0.017 mM phosphate sucrose buffer

In this case, we obtain: $\zeta = -0.154$ V, $r_D = 1/\kappa = 74$ nm, $S = 2.324\ \mu m^2$ and,

$$\frac{e^{-2\kappa r}}{r} = 298.8 \quad \Rightarrow \quad r = 340\ \text{nm} \qquad \text{Eq. 4.19}$$

The interpretation of the variation in reflected light intensity in RICM experiments (Fig. 4.4A and 3.23C) is that the cells levitate around 300 nm from the surface. We also analyzed the attachment kinetics of the cells levitating in 0.017 mM phosphate sucrose buffer during 1 s application of + 1.8 V/Ref. pulse (Fig. 4.4).

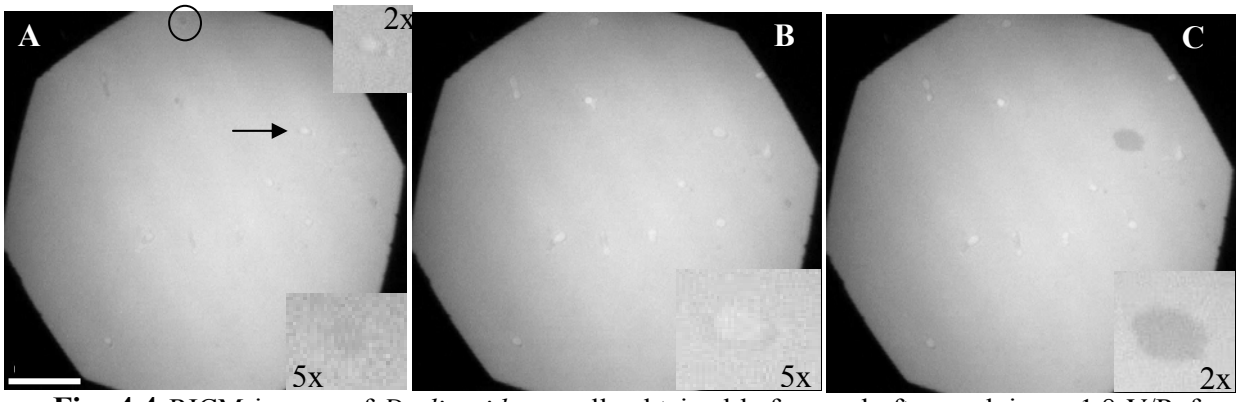

Fig. 4.4 RICM images of *D. discoideum* cells obtained before and after applying a 1.8 V/Ref. pulse for 1 s at the ITO surface in 0.017 mM SB. The cell RICM contrast changes from brighter than the background in the centre of the cell (A) for white (B) and then, for one cell, 1 s after the beginning of the pulse, to black (C). The inserts in A stand: up right, the magnified levitating cell pointed by the arrow; down right, the magnified levitating black cell from the circle. The inserts in B and C represent the same cell pointed by black arrow in A.

In 0.017 mM, before pulse application (Fig 4.4A), most levitating cells were in the centre brighter than the background (with some exceptions, one of these shown by the black circle) surrounded by a dark fringe; at the onset of pulse, the centre of the cell became intensively white, surrounded by a dark fringe (Fig 4.4A). After 1 s from the pulse onset, only one cell became black. The reason of this could be the low value of the applied potential. Given the fact that the levitating cell was brighter than the background

in the centre and according to the sequence of RICM contrast changing (Fig. 4.4A-C), we estimated the distance between the substrate and the cell membrane, before the pulse, to be around 300 nm (a white spot produced by an object standing to an impair multiple of 100 nm apart from surface, see Materials and Methods and Fig. 4.5). Unfortunately, we catch the sequence when the cells become darker than the background before they become intensively white only for two cells, maybe because of the initial fast cell movement, that could not be imaged by our camera for all cells.

Corrections to distance calculation

This model induces some errors in calculus of distances. The errors arise especially from the fact that we presumed that our solutions are 1:1 electrolyte solutions (which affect the Debye distance). In addition, we got errors from the estimation of the integral from eq. 4.6 and from the elimination of van der Waals attraction potential.

However, adapting our model for the real composition of SB solution (a mixture of 1:1 and 1:2 salts: 15 mM KH_2PO_4 and respectively 2 mM Na_2HPO_4) we can improve the distance calculation.

For a cell of radius R = 5 μm in 1.7 10^{-4} M SB ($r_D = 1/\kappa = 20.9$ nm), cup surface is $S = 2\pi R/\kappa = 0.656$ μm^2 and zeta potential, $\zeta = 0.092$ V. Additionally, $\sigma_{cell} = 5.6 \cdot 10^{-15}$ C/μm^2. The eq. 4.17 becomes:

$$\frac{e^{-2\kappa r}}{r} = 1179.4 \quad \Rightarrow \quad r = 96 \text{ nm} \qquad \text{Eq. 4.20}$$

For a cell of radius R = 5 μm in 0.34 10^{-4} M SB we obtain: $\zeta = -0.132$ V, $r_D = 1/\kappa = 46.9$ nm, S = 1.47 μm^2 and,

$$\frac{e^{-2\kappa r}}{r} = 458.44 \quad \Rightarrow \quad r = 217 \text{ nm} \qquad \text{Eq. 4.21}$$

For a cell of radius R = 5 μm in 0.17 10^{-4} M SB, we obtain: $\zeta = -0.149$ V, $r_D = 1/\kappa = 66$ nm, S = 2.07 μm^2 and,

$$\frac{e^{-2\kappa r}}{r} = 318 \quad \Rightarrow \quad r = 305 \text{ nm} \qquad \text{Eq. 4.22}$$

The obtained distances are resumed in Table 4.1.

Table 4.1 Estimated and calculated distances between *Dictyostelium* cell and ITO surface, for three different buffer solution concentrations

Solution concentration (mM)	**RICM distance estimations (nm)**	Calculated distance, r (nm), solution is considered formed by 1:1 electrolyte	Calculated distance, r (nm), for a mixed solution: 1:1 and 1:2 electrolytes
0.17	**75-125**	104	96
0.034	**175-225**	238	217
0.017	**275-325**	340	305

In Fig. 4.5 we offer a schematic representation of localization in *z* axis of levitating and adhering cells ("white" cells after the pulse), in dilute phosphate buffer, inspired by RICM observation of reflected light intensity.

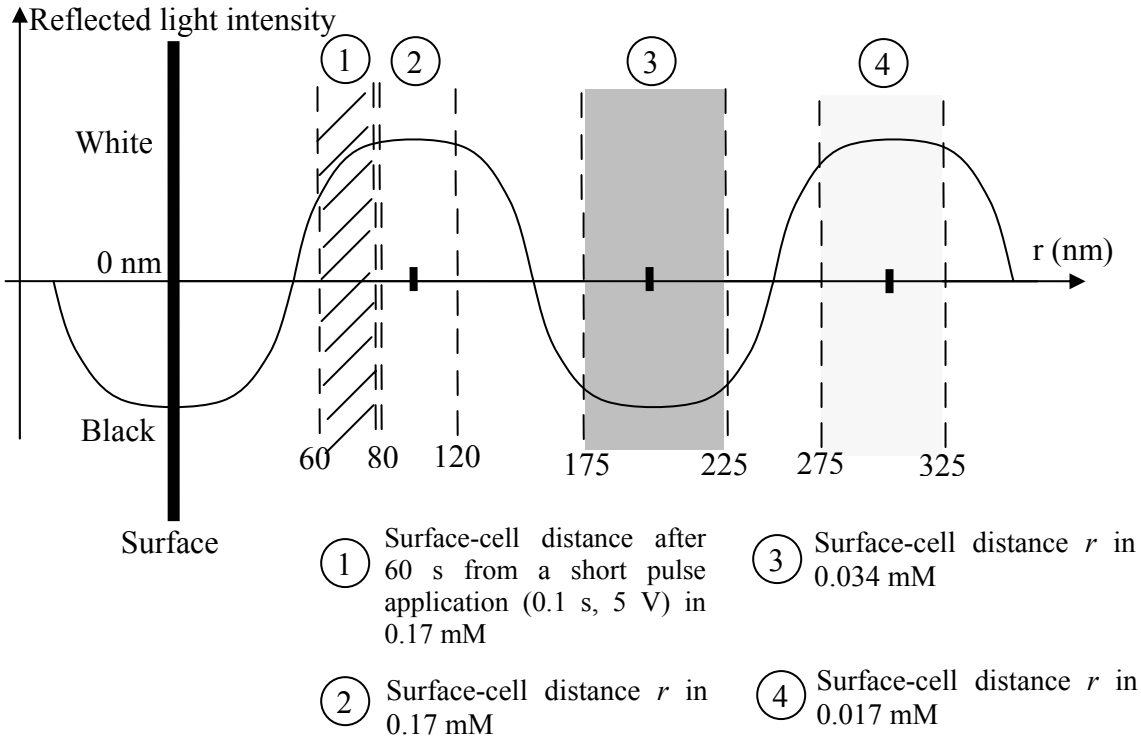

Fig. 4.5 Schematic representation of vertical localization of levitating and adhering cells ("white" cells after the pulse), in dilute phosphate buffer. The large bands represent the zones with high probability of occupancy in concordance with RICM estimations (see Materials and Methods).

The calculated values are very close to the RICM estimations. Anyway, the differences that appear are probably due to the fact that the living cells, even suspended, make some contacts with the surface (see Fig. 4.1), approaching on it and therefore, the real distance is smaller than the theoretical one.

We have to mention that the cells do not remain fixed at a certain distance from the surface, but they are in a continuous Brownian movement, laterally and in *z*-axis. This movement can be observed by following the RICM variations in reflected light intensity of the spots representing the levitating cells. For example, in 0.017 mM, for majority of the cells in most of the time, it can be seen in the middle of the ventral part a white zone surrounded by a dark fringe (see Fig. 3.23C and Fig. 4. 4). Its contrast can vary very much, reaching a black hue, which signifies that cells approach to a zone with a low contrast intensity (very probably to the 225 nm limit).

4.3 Which has the main contribution to cell attraction when a pulse is applied: the electrophoretic force (EP) or the change of surface charge?

This model could also determinate if the electrophoretic force (F_{EP}) plays an important role besides the change in surface chemical state (change of the surface charge due to the pH variation-water electrolysis).

In our experimental setup, the counter electrode is set out at a distance of 2.5±0.5 mm from work electrode, the ITO surface. Applying 5 V between the two electrodes, we got an average electric field intensity (E) of 20 V/cm.

The electrophoretic mobility (μ) relating electric-field intensity to velocity (v = μ·E) is given by (Mehrishi, 2002). For example, in 0.17 mM SB,

$$\mu = \frac{\varepsilon_r \varepsilon_0 \zeta}{\eta} = \frac{78.49 \cdot 8.85 \cdot 10^{-12} \cdot 40 \cdot 10^{-3}}{10^{-3}} = 2.77 \cdot 10^{-8}\ \mathrm{m^2/Vs} \qquad \text{Eq. 4.23}$$

where ε_r is the relative permittivity of the liquid, ε_0 is the electrical permittivity of the vacuum, η is the liquid viscosity, ξ is the zeta potential of the cell in 0.17 mM SB (constant during the pulse) and v is cell speed in a field E. It results that:

$$v = \mu \cdot E = 2.77 \cdot 10^{-8} \cdot 20 \cdot 10^{2} = 55.53\ \mu m/s \qquad \text{Eq. 4.24}$$

For example, the speed of a glutaraldehyde-fixed human red blood cell, placed in a field E = 20 V/cm, is experimentally estimated to 132 μm/s or $13.2 \cdot 10^4$ nm/s (μ =

$6.6 \cdot 10^{-8}$ $m^2/(V \cdot s)$; Gingell, 1976). The electrophoretic force is calculated considering that, in bulk solution, at equilibrium, is equal with the friction force in the liquid medium-F_v (Stokes relation). For *Dictyostelium* cell (10 μm in diameter), we obtain:

$$F_{EP} = F_v = 6\pi R\eta \cdot v = 6 \cdot 3.14 \cdot 5 \cdot 10^{-6} \cdot 10^{-3} \cdot 55.53 \cdot 10^{-6} = 52.33 \cdot 10^{-13} \text{ N} \quad \text{Eq. 4.25}$$

We will analyze the case of a cell which, before the electrical pulse, levitates in 0.17 mM phosphate sucrose buffer at a distance r = 117.5 nm (according to our calculus) from the ITO surface. The electrostatic repelling force is equal to the apparent gravity force ($3 \cdot 10^{-13}$ N).

Hypothesis: One supposes that the charged surfaces (cell and ITO surfaces) are not changing during 0.1 s pulse (5V).

At small pH variation (less than 0.5, for example, when we deal with very dilute solutions, e.g. 0.017 mM) the charge surface will not vary significatively during the 5 V electrical pulse. We can calculate the distance on which a cell can move against the surface repulsive field under the influence of electrophoretic force (F_{EP}), developed during the pulse application.

In 0.17 mM SB, during the positive electrical pulse, the cell move towards the surface until the repelling force felt by negatively charged cell in the double layer annihilates the sum of apparent gravity force and electrophoretic force ($55.33 \cdot 10^{-13}$ N).

$$F_e = G_a + F_{EP}$$

$$5.6 \cdot 10^{-15} \cdot 0.656 \cdot \frac{\psi(r)e^{-\kappa r}}{r} = 55.33 \cdot 10^{-13} \Rightarrow \frac{\psi(r)e^{-\kappa r}}{r} = 1507 \quad \text{Eq. 4.26}$$

where, F_e is the repelling force in the double layer, G_a is apparent gravity, F_{EP} is electrophoretic force, $1/\kappa = 20.9$ nm, $\zeta_{ITO} = 0.092$ V and following the same reasoning as above, we obtain $r = 68$ nm (to be compared to 96 nm).

As can be observed, in the absence of any surface transformation, at this electric field intensity, the electrophoretic force can move the cell against the ITO surface only by a 28 nm distance. Our calculus is supported by the following experimental observation: application of the same electric field intensity (20 V/cm) for 0.1 s, in 0.017 sucrose phosphate buffer, induce an insignificant change in ITO surfaces charge (due to a minimal pH variation; theoretical calculus assert a maximal pH value of 5.5 during pulse application) and no adhering cell was observed. This demonstrates that the forces inside

the diffuse layer act like a barrier and are too strong for cell displacement. Only a change at the surface level could induce a cell adhesion, by decreasing the negative surface charge of the ITO surface. Considering the dynamic process of the surface charge transformation (repelling force is decreasing exponentially in time), the electrophoretic force could determine, at the beginning of the onset of the electrical pulse when the production of protons is still low, a very rapid movement of the cells towards the repelling barrier, theoretically situated by us at 90-110 nm from the surface. Thus, this could explain why we never observed, during the pulse, the cells at distances upper to 90-110 nm from the surface (for example, the cells in 0.017 mM diluted buffer).

Adhesion force estimation

Our model could also provide a method to calculate adhesion forces. We will analyze the example of adhering cells in sucrose phosphate buffer after a 0.1 s electrical pulse (5V). During the pulse, the cells are attracted towards the ITO surface (which undergoes an electrochemical transformation) and consequently they could setup some initial adhesion sites on the surface. After approximately 60 s from the pulse application, cells are completely spread on the ITO surface with the same morphology and surface area (in average 110 μm^2) as in physiological buffer (SB) but with zones exhibiting a brighter contrast than the background in RICM analysis ("white" cells). We except the cells which are very strongly attracted on the surface (the "black" cells)-see Fig. 3.44A.

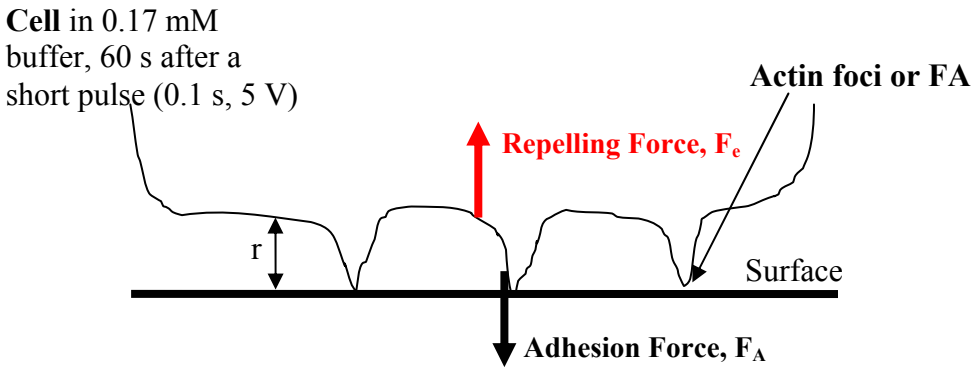

Fig. 4. 6 Schematic representation of a cell in dilute phosphate buffer localized at an equilibrium distance *r*, where the two opposite forces are equals. The black thin arrow indicates a stable focal site.

Anyway, the repelling forces (F_e), in opposition to the adhesion forces (F_A), localize the cell at an equilibrium distance *r* from the ITO surface (Fig. 4.6), even from the beginning of its spreading (the "white" cells do not change their brightness contrast during spreading), deducing that the "feets" (actin foci or FA) are very thin.

The gray level of RICM images allows us to estimate that the distance between the most part of ventral cell membrane and the ITO surfaces to be 60-80 nm. Using the eq. 4.7, and ignoring the repulsion between ITO and the membrane of the "feets" we have:

$$F_e = 4\pi \cdot 110 \cdot 5.6 \cdot 10^{-15} \frac{\psi(r) e^{-\kappa r}}{r} > F_A \qquad \text{Eq. 4.27}$$

For $r = 70$ nm, $S = 110\ \mu m^2$ (the averaged surface area for a spread cell) we obtain the force of adherence being:

$$F_A > 9.54\ \text{nN/cell} \qquad \text{Eq. 4.28}$$

By shear flow experiments on glass coverslip, Decave et al. (Decave, 2003) found that for a shear stress of $\sigma = 2.5$ Pa (N/m^2), 50% of cells detach to the surface, in SB. This value corresponds to a peeling force, $F_P = 2.5 \cdot 110 \cdot 10^{-12}$ N ~ 0.3 nN, which represents the necessary force to break the actin foci at the edge of the cell undergoing the shear flow.

Cell adhesion at intermediate ionic strength

The range and energy of electrostatic forces can be modulated by the ionic concentration. This phenomenon is purely passive, contrary to spreading, which requires actin polymerization. Fig. 3.24 shows that the relationship between the percentage of cells attached and the ionic concentration is very sharp. The experimental data can be fitted with a kinetic model incorporating the dependence of the repulsive electrostatic energy with the cell-surface distance modeled by the DLVO theory (Atkins, 2006). This model is explained in Materials and Methods (Eq. 2.54). The situation is similar to colloid flocculation, where particle interaction is also strongly modulated by repulsive interactions. It should be noted that divalent ions are more effective than monovalent ones, which is due to two effects. First, at equal ionic concentration, divalent ions have a higher ionic strength than monovalent ones and thus divalent ions in the diffuse layer would better screen out immobilized electrostatic charges at the surface. Second, divalent ions, if they adsorb specifically in the Stern layer, are more strongly attached to the

immobile charges at the surface and would, thus, reduce twice the negative surface charge than the monovalent ones.

Equation 2.59 depends on four coefficients, related to the kinetics of cell spreading at high ionic strength (a), the contribution of electrostatic repulsion energy to the activation barrier (c), the link between the ionic strength and the Debye length (b) and the cell-surface distance where the activation barrier is set (d). Fitting the percentage of attached cells as a function of a single salt concentration can not unambiguously resolve a, b, c and d. We therefore calculated *b* (Materials and Methods) and imposed that *a* and *d* be the same for SB and $CaCl_2$ salt solutions. For a least square adjustment of the experimental data with equation 2.59, the following values of the coefficients were obtained: a = 11 ± 1.5, d = 0.03 ± 0.01 nm and c = 35 ± 2 and 18 ± 3 for SB and $CaCl_2$ salt solutions, respectively (Hoppe, 1983).

This allows the calculation of the magnitude of the electrostatic energy U_0, which is therefore about 35 kT in SB, which explains that cells can reach the surface at physiological ionic concentrations. The association rate at physiological SB concentration is $a/\tau = 1.1 \pm 0.15$ min^{-1}, which is similar to the association rate constant estimated from shear stress detachment experiments by Décavé et al. (Decave, 2002). The small value of *d* suggests that adhesive molecules at the surface of *Dictyostelium* cells come in close contact with the surface.

4.4 Synchronization of cellular adhesion

Synchronization by ion diffusion

In order to synchronize cell attachment, two methods are proposed and investigated in this study. In the first one, the ionic environment of the cells is modulated by diffusion. Good synchronization in physiological conditions is provided (8±3 s) by a fast rise in ionic concentration, which is promoted by a reduced lower chamber thickness (e = 264 µm) and an increase in the concentration of the diffusing solution. However, this time interval turns out to be insufficient for a good synchronization of biochemical processes in a cell population. Indeed, the period of actin polymerization oscillation is about 8 s (see subchapter 3.1).

Additionally, the way the upper compartment is filled influences the results. Indeed, when we pushed a 17 mM SB solution on the polycarbonate membrane, the injection helped to reduce the lag time (t = 24±4 instead of 46±2) but also most of the suspended cells were displaced in the created convection flux. Moreover, if the membrane is wetted by pouring gently 300 µL of 0.17 mM SB (the cells are still levitating) before injection of 300µL 34 mM SB, the lag time is reduced to t = 17±2. The moistening of the membrane favours the convection flow, the injection through a liquid being much more efficient than directly on the dry membrane. Also, the lag time and asynchrony depend on the angle of injection.

Like above, an injection of the concentrated buffer reduces the lag time. Practically, we poured 300 µL 0.17 mM SB gently on the membrane in a such a way as the cells were still levitating in the lower chamber. Then, we injected 300µL SB into the upper chamber, the final concentration of the solution being approximately 8.5 mM. The lag time was t = 126±4 s instead of 142±3 s and the percentage of suspended cells that were displaced in the created convection flux was less than 20 % due to the increased distance between the membrane and the cells. Moreover, if one uses the same approach with 300 µL 34 mM SB, one reduces the lag time even more (t = 60±5). The asynchrony for the cells which had not been displaced by the flux was then, $\Delta t = 10 \pm 2$.

Synchronization by an electrical pulse

The second method involves four phenomena in the electrolyte near the conductive ITO surface, when a positive potential is applied: water oxidation produces protons that (1) coordinate and interact with negative groups of the ITO surface and cells and (2) diffuse away from the ITO surface and change the ionic concentration around the levitating cells. Negatively charged objects are therefore rapidly attracted to the surface where (3) chemical reactions can take place. Additionally, an electrophoretic transport (EP) occurs (4).

The behavior of negatively charged fluorescent beads (Fig. 3.47 and Fig. 3.48), illustrates two effects of an electric pulse: attraction and formation of covalent bonds with the surface. The attraction of the carboxylic beads, even when the pulse was applied for 4 seconds, and a high concentration of protons was reached (pH = 2-3) at the ITO surface,

inversing the surface charge in a positive one, suggests that the carboxylic groups were not neutralized. This could explain why the surface charge of the cells does not significantly vary during 0.1 seconds 5 V electrical pulse (negative phosphate groups are less basic than the carboxyl ones and additionally, all amine groups are protonated even at physiological pH).

After the pulse, a fraction of the attracted beads remained at the surface while others were pushed away, since they did not have enough time to reach the surface or to react with. Similarly, in 0.17 mM phosphate sucrose buffer, cells approach the surface, and form molecular contacts during the 0.1 s pulse (Fig. 3.44). These contacts trigger periodic actin polymerization resulting in cell spreading, visualized by RICM as white contact areas ("white" cells). It should be noted that under these low ionic concentration conditions, the cell body remains about 100 nm above the substrate, which suggests the existence of long adhesive structures extending from the cell down to the surface. For the cells in 0.017 mM phosphate sucrose buffer, we did not observed the apparition of the "white" cells, maybe because the adhesive structures are not long enough or could not resist at an equilibrium distance higher than 250 nm. They underwent huge repelling force in this dilute medium.

Longer exposure to the pulse (more than 0.1s for a 5 V pulse, see Fig. 3.41 and Fig. 3.42) is likely to induce membrane cytoskeleton rupture, resulting in large dark contact area devoid of LimE. Adjusting the pulse time allows us to minimize cell damage. The cell-surface contact zone formed during a long voltage pulse (and only during pulse application) was significantly darker, as observed by RICM, than those formed later in the same diluted buffer solution ("white" cells). Interestingly, cells formed dark contacts immediately after the voltage was raised (< 60 ms, see Fig. 3.45 at t = 0.05 s dark cells appeared) and only during pulse application. In contrast, white contacts appeared visible by RICM on a period of 5 to 15 s after a 0.1 s pulse and with a period of 20 to 30 s after a 0.05 s pulse.

Furthermore, most cells violently attached after an electric pulse (in concentrated or diluted buffer) did not move away from the initial contact zone formed during the voltage pulse, even when the ionic concentration was raised to physiological values (for the cells initially in dilute buffer), as if the cells were stuck to the ITO surface and the

membrane components bound to the surface groups (see Fig. 4.7B, right, red arrow). Some minutes later (depending on the potential applied and its duration), cells eventually moved away from this zone, living behind them black zones, perhaps some membrane fragments (Fig. 4.7B, right). Altogether, these observations suggest that the formation of H^+ ions at the ITO surface is able to trigger close contact with the surface but also could damages the cell membrane.

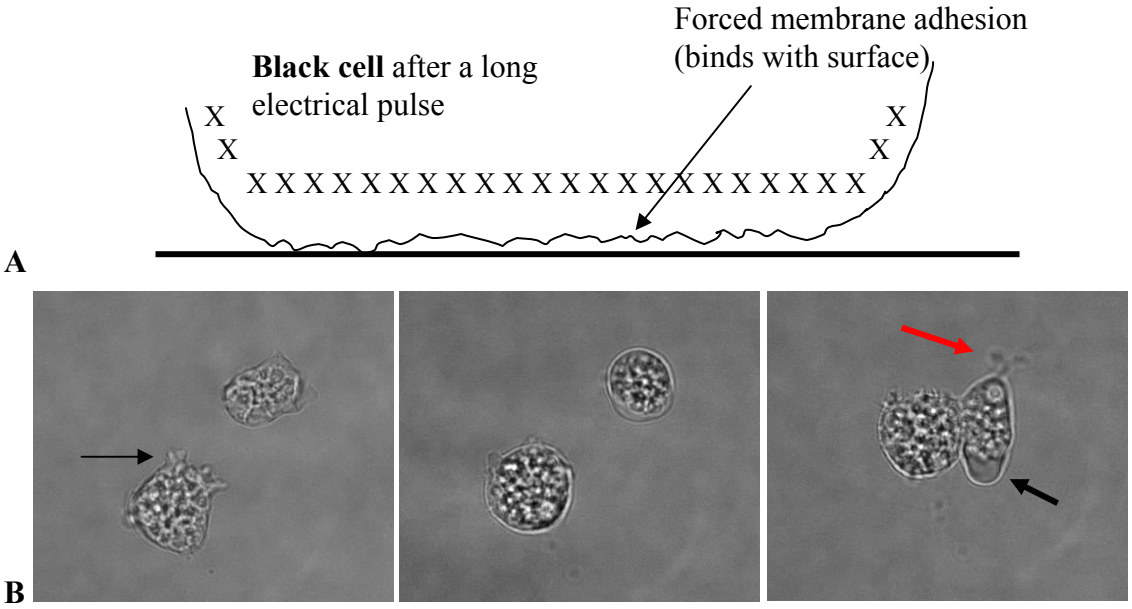

Fig. 4.7 A. Schematic representation of a cell which was violently attached (2 V/Ref. for 1 minute). Actin cytoskeleton is represented by X and is drawn separated from the membrane. **B**. Phase Contrast images of the cells submitted to 2 V/Ref. for 1 minute, in 1.7 mM phosphate sucrose buffer. **Left**: the dynamic adhering cells (one filipodia is pointed by the black arrow) before pulse application. **Centre**: immobile round cells 1 minute after the pulse. **Right**: 5 minutes after the pulse. One cell (the left one) moved from initial place. The other one is trying to move but it seems to be stuck by a membrane fragment (red arrow) which is bound to the surface. A pseudopodium can be seen forming at the opposite way pointed by the black arrow. After breaking a part of a membrane on the surface, the cell moves normally.

In order to estimate the effect of the pulse on the local ion concentration, we assume only Faradaic current and a proton diffusion coefficient ($D=10^{-4}$ $cm^2 \cdot s^{-1}$). The protons diffuse over a distance of 100 µm during a 1 s pulse at $4 \cdot 10^{-5}$: $(Dt)^{0.5} = (10^{-4} \cdot 1)^{0.5}$ = 0.01 cm. The resulting concentration, $6 \cdot 10^{-5}$ M, is insufficient to screen out electrostatic interactions (Fig. 3.24). Therefore, the molecular phenomenon that explains spreading is the neutralization of surface charges by protons. The applied positive potential is thus likely to change the surface charge from negative to neutral value or even more, to a

positive one. This hypothesis is supported by experimental measurements of the zeta potentials of ITO surfaces contacting solutions with the same concentration but with different pH (Table 3.7). The state of the surface charge therefore varies very rapidly during the pulse. Proton accumulation at the surface dissipates quasi-instantly after the pulse ($t = d^2/D \approx 10^{-6}$ s over d = 100 nm, for protons) and therefore, the molecular event leading to cell spreading must occur during this time. Triggering adhesion with an electric pulse allows defining precisely when and for how long the cells have access to the surface.

Two mechanisms of membrane movement during the pulse application were proposed: cell deformation (Fig. 4.8A) and entire cell displacement (Fig. 4.8B).

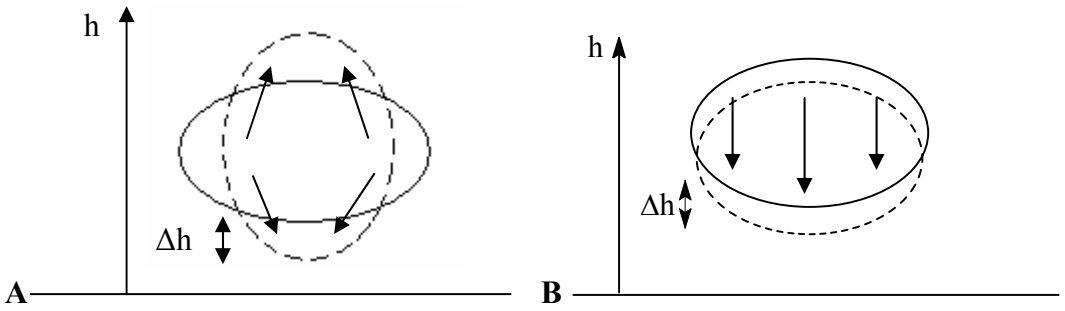

Fig. 4. 8 A. Schematic representations of a cell membrane dynamics during an electrical pulse. **A.** Cell deformation associated with ventral surface area decrease. **B.** Entire cell displacement. The black arrows indicate the cytoplasm movement.

The only movement of the ventral part of the membrane was excluded because would necessitate the cell volume variation that could not be sustained by cell membrane transport of the water in such short time. The same phenomenon applies for the "hidden" membrane. Another possibility would be the internal vesicles, which could fuse with the cell membrane, but this is also a time requiring process. Anyway, the latter process could occur after pulse application period (in membrane recovery).

Immediately after a voltage pulse, the cells, which undergo a membrane deformation during the pulse, decrease their previous activity (see Fig. 4.1B), retract its protrusions by actin depolymerization and reduce ventral surface area (all of these are very clearly observed by Phase Contrast). It is very probable that the mechanisms ruling these processes, should be similar of those described by Dalous et al. (Dalous, 2008) who submitted adherent cells to changes in flow direction. They observed reversal of cell

polarity and actin-myosin cytoskeleton reorganization for *Dictyostelium* cells undergoing mechanical stimulations from alternating directions.

In the same time, the pulse-induced contact between the cell and the surface triggers ordered actin polymerization cycles that accompany cell spreading and correspond to those described for a cell spreading in SB (Fig. 3.49, Fig. 3.50). Because of the limiting resolution and contrast of RICM, we detect only the formation of effective contacts leading to cell spreading and cannot exclude whether the cell forms transient contacts before (see Fig. 4.1B). In fact, Bongrand and co-workers have shown that transient single molecular contacts can be formed between cells and a surface before spreading (Pierres, 1996; Pierres, 1998a,b). Triggering cell-surface contact by an electric pulse, allows defining the onset time for contact-induced signaling. The beginning of the first actin polymerization event starts around 2 s after the pulse and peaks about 10 s after the pulse. Such a fast reaction to contact is advantageous for efficient phagocytosis.

Perspectives

The contact of cells with a solid surface is a complex process and triggers important intracellular signalization pathways, which finally lead to actin polymerization, leading to cell spreading, polarization, motility, proliferation and eventually differentiation. The number of proteins involved in cell adhesion is quite large and involves a plethora of molecular interactions. To *Dictyostelium discoideum* several plasma membrane proteins have been identified that mediate such adhesion. Some of these proteins are similar to integrins, which mediate interaction of mammalian cells with extracellular matrix proteins (see Chapter Introduction). *D. discoideum* also possesses many proteins known to be part of adhesion structures in higher eukaryotes, such as talin, paxillin, coronin, Src-like kinase, which stimulate actin polymerization or link the attachment of actin microfilaments to the plasma membrane.

Despite our knowledge of many elements that play a role in adhesion, their *temporal hierarchy and spatial organization* is only partially understood. It is challenging **to identify the successive formation of protein complexes** leading to stable cell-surface contacts (Fig. 4. 9).

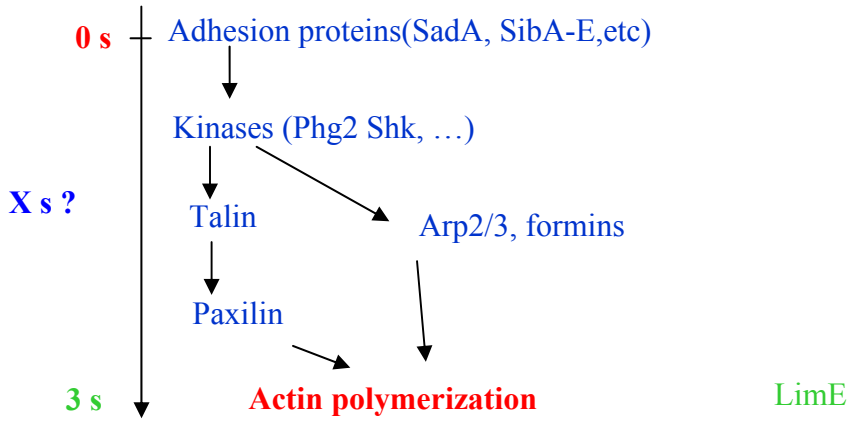

Fig. 4.9 Schematic representation of time scale of a presumed successive formation of protein complexes; we determined that actin starts to polymerize after approximately 3 s after we forced the cells to adhere (0 s). For other protein complexes we indicated 'x' s, inferior to 3, which follow to be found.

We showed that pulse-induced surface contact allows synchronizing molecular events associated to cell-surface adhesion and spreading in a cell population and in conclusion, it provides a novel method to study contact induced signaling at the

molecular level (see Chapter Results). Additionally, we determined that all process starting with first stable cell-surface contact (time 0, pulse application) ending with actin polymerization takes approximately 3 seconds (see Fig. 3.50, red arrow). Making a double fluorescent mark (e.g. LimE and paxilin), we can study the kinetical analysis of other fluorescent proteins recruited at adhesion sites, such as talin, paxillin, coronin, Src-like kinase, determining in the same time their temporal hierarchy.

Synchronizing cell-surface contact is a prerequisite for **the preparation of cell material enriched in protein complexes** active at a given time after contact. Designing an experimental device like in Figure 4.10, permits us to synchronously attach the cells by applying a 5 V pulse during 0.1 seconds and after 'x' seconds to permeabilize (for example, reversing the current polarity and applying a millisecond high negative pulse or injecting a liquid thqt contains a detergent) the cells and finally to recover the molecules whose concentration may change during cell spreading. For instance, PIP_3 or IP_3 production, protein phosphorylation or dephosphorylation could be monitored after the electrical pulse.

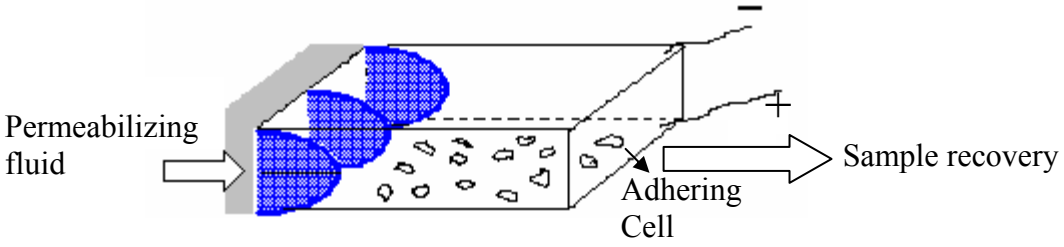

Fig. 4.10 Schematic representation of an experimental device which allows to access at different stages of chain signalization. Reversing the current polarity and applying a millisecond high negative pulse or injecting a liquid that contains a detergent, at *t* seconds after the pulse onset, allow us to access at different stages of chain signalization.

Other perspectives are the **analysis of drug-treated or mutant cells** (Mam, Phg3, talin null, Myosin null, PTEN null, etc.) in order to establish the role of different proteins in adhesion process.

We can measure the ability of mutants to form new contact points after having forced to contact the surface during an electric pulse. As for AX_2 cells (see Fig.3.52) we can count the number of mutant cells that exhibit the first fluorescent event peak after an electrical pulse application within one-second interval. In this way, we can test their

response to contact and analyze actin polymerization kinetics in order to check the role of restricted gene in signaling pathways.

By measuring the percentage of adhering mutant cells in 10 minutes as a function of phosphate buffer concentration (see Fig. 3.24), compared to the parental strain, we can test the ability of mutants to reach the surface and form stable contacts. This entails the capacity of protrusions emission and the presence of active adherence molecules at the cell surface.

Another perspective is **to localize in space the cellular adhesion** (in order to localize the first stable surface-cell contacts which trigger internal signaling), either by constructing discrete conductive patterns (Fig. 4.11A) or by chemical deposition of a continuous conductive layer with a non-uniform morphology (Fig. 4.11B). In the later case, the cell will contact the surface on the highest part of the conductive material. In this way, we will know where and when the first contact area is formed. Then, we can study how and when a new actin foci form from this point.

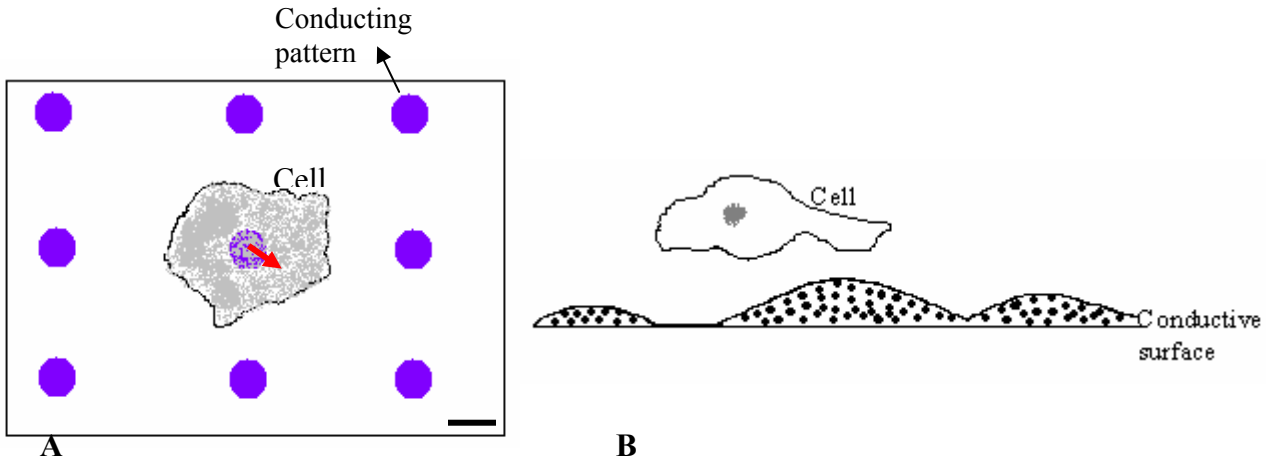

Fig. 4. 11 Schematic representation of (**A**) an experimental device which would allow us to localize the cell contacts with a conductive pattern; the red arrow indicates the onset of a new actin polymerization activity and of (**B**) a continuous conductive surface (spoted area) obtained by non-uniform chemical deposition of a conductive material (which bears a negative charge) on glass; after the electrical pulse, the levitating cell (in dilute medium) will contact the surface in the highest point of it. Scale bar in (**A**) 2 µm.

It could be of interest to aply these techniques to higher eukaryotic cells.

We also intend to search for **materials with a more negative zeta potential** in order to use less diluted buffers. Grater the negative surface charge is, a smaller Debye length is needed to obtain the same effect on cell levitation.

Cell contact with the substrate is likely to change the impedance of the ITO-electrolyte system. Therefore, we intend **to monitor by impedance measurements the synchronous cell spreading** triggered by electrical pulse. In addition, the resistance increase allows to estimate the relative area covered by actin foci, assuming that they behave like insulate.

We have seen how the cells are affected by the exposure during more than 1 minute to a low (or high) pH. A very interesting perspective for **drug delivery** is the possibility to explode liposomes close to the surface of microelectrodes locally implanted. Additionally, microelectrode surface could be made of biomaterials with high catalyst properties for electrolysis such as platinum or gold.

Bibliography:

Alberts B., Johnson A., Lewis J., Raff M., Roberts K., and Walter P., 2008, Molecular Biology of the cell, Ed. Garland Science, 5th edition.

Alon G., De Dominico G., 1987, High voltage stimulations: An integrated approach to Clinical Electrotherapy, 1st Ed. Hixton.

Armstrong D. W., Schulte G., Schneiderheinze J. M., Westenberg D. J., 1999, Separating microbes in the manner of molecules. 1. Capillary electrokinetic approaches., Anal. Chem., 71, 5465.

Atkins P., de Paula J., 2006, Physical Chemistry, Oxford University Press, Oxford.

Aubry L., Firtel R., 1999, Integration of signaling networks that regulate Dictyostelium differentiation, Annu. Rev. Cell. Dev. Biol., 15, 446.

Balaban N. Q., Schwarz U. S., Riveline D., Goichberg P., Tzur G., Sabanay I., Mahalu D., Safran S., Bershadsky A., Addadi L., Geiger B., 2001, Force and focal adhesion assembly: a close relationship studied using elastic micropatterned substrates, Nature Cell Biology, 3, 466 – 472.

Bamburg J. R., McGough A. and Ono S., 1999, Putting a new twist on actin: ADF/cofilins modulate actin dynamics, trends in Cell Biology, 9, 364.

Bard A. J., Faulkner L. R., 1980, Electrochemical Methods. Fundamentals and Applications, John Wiley and Sons Ed.

Barentin C., Sawada Y., Rieu J. P., 2006, An iterative method to calculate forces exerted by single cells and multicellular assemblies from the detection of deformations of flexible substrates, Eur. Biophys. J., 35, 328–339.

Barker, A. T., Jaffe, L. F., Vanable Jr, J. W., 1982, The glabrous epidermis of cavies contains a powerful battery, Am. J. Physiol., 242, 358-366.

Beebe S. J., Schoenbach K. H., 2005, Nanosecond pulsed electric fields: a new stimulus to activate intracellular signaling, J. Biomed. Biotechnol., 297.

Bereiter-Han J., Fox C. H. and Thorell B., 1979, Quantitative refection contrast microscopy of living cells, J Cell Biol, 82, 767-779.

Bereiter-Han J., Vesely P., 1998, Cell Biology: A laboratory handbook, second edition, vol 3 - Refection interference microscopy, 54-63.

Bernard M., Busnot F., 1996, Usuel de chimie générale et minérale. Ed. Dunod.

Block M. R., C. Badowski, A. Millon-Fremillon, D. Bouvard, A. P. Bouin, E. Faurobert, D. Gerber-Scokaert, E. Planus, and C. Albiges-Rizo, 2008, Podosome-type adhesions and focal adhesions, so alike yet so different, Eur J Cell Biol, 87:491-506.

Blumenthal S., Clark G. B., Roux S. J., 2004, Biochemical and immunological characterization of pea nuclear intermediate filament proteins, Planta, 218, 6, 965.

Borisy G. G. and Svitkina T. M., 2000, Actin machinery: pushing the envelope, Current Opinion in Cell Biology, 12:104–112.

Boulbitch, A., R. Simson, D. A. Simson, R. Merkel, W. Hackl, M. Barmann, and E. Sackmann, 2000, Shape instability of a biomembrane driven by a local softening of the underlying actin cortex. Phys Rev E Stat Phys Plasmas Fluids Relat Interdiscip Topics 62:3974-3985.

Brar S. and Siu C., 1993, Characterization of the cell adhesion molecule gp24 in Dictyostelium discoideum. Mediation of cell-cell adhesion via a Ca(2+)-dependent mechanism. J. Biol. Chem, 268, 24902.

Bretschneider T., Diez S., Anderson K., Heuser J., Clarke M., Muller-Taubenberger A., Kohler J. and Gerisch G., 2004, Dynamic actin patterns and Arp2/3 assembly at the substrate-attached surface of motile cells, Curr. Biol., 14, 1-10.

Bretschneider T., Jonkman J., Kohler J., Medalia O., Barisic K., Weber I., Stelzer E. H. K., Baumeister W., Gerisch G., 2002, Dynamic organization of the actin system in the motile cells of Dictyostelium, Journal of Muscle Research and Cell Motility 23: 639–649.

Bretschneider, T., K. Anderson, M. Ecke, A. Muller-Taubenberger, B. Schroth-Diez, H. C. Ishikawa-Ankerhold, and G. Gerisch, 2009, The three-dimensional dynamics of actin waves, a model of cytoskeletal self-organization, Biophys. J., 96:2888-2900.

Bretschneider, T., S. Diez, K. Anderson, J. Heuser, M. Clarke, A. Muller-Taubenberger, J. Kohler, and G. Gerisch, 2004, Dynamic actin patterns and Arp2/3 assembly at the substrate-attached surface of motile cells. Curr Biol 14:1-10.

Bukharova, T., G. Weijer, L. Bosgraaf, D. Dormann, P. J. van Haastert, and C. J. Weijer, 2005, Paxillin is required for cell-substrate adhesion, cell sorting and slug migration during Dictyostelium development. J Cell Sci 118:4295-4310.

Burridge K. and Chrzanowska-Wodnicka M., 1996, Focal adhesions, contractility, and signaling, Annu. Rev. Cell Dev. Biol., 12:463–519.

Carlier Marie-France, C. Le Clainche, S. Wiesner, and D. Pantaloni, 2003, Actin-based motility: from molecules to movement, BioEssays 25:336–345.

Catterall W. A., 1995, Structure and function of voltage-gated ion channels. Annu. Rev. Biochem., 64, 493–531.

Chalfie M., Tu Y., Euskirchen G., Ward W. W. and Prasher D. C., 1994, Green fluorescent protein as marker for gene expression, Science, 263, 802, 5.

Chamaraux F., S. Fache, F. Bruckert, and B. Fourcade, 2005, Kinetics of cell spreading, Phys Rev Lett, 94, 158102.

Chen C. F. and Katz E. R., 2000, Mediation of cell-substratum adhesion by RasG in Dictyostelium, Journal of Cellular Biochemistry, 79:139–149.

Chi Pak W., Flynn K. C. and Bamburg J. R., 2008, Actin-binding proteins take the reins in growth cones, Nature Reviews Neuroscience 9, 136-147.

Chia C. P., 1996, A 130-kDa plasma membrane glycoprotein involved in Dictyostelium phagocitosis, Exp. Cell. Res., 227, 182.

Choi, C. K., M. Vicente-Manzanares, J. Zareno, L. A. Whitmore, A. Mogilner, and A. R. Horwitz, 2008, Actin and alpha-actinin orchestrate the assembly and maturation of nascent adhesions in a myosin II motor-independent manner, Nat Cell Biol., 10:1039-1050.

Condeelis J., 1993, Life at the leading edge: The Formation of Cell Protrusions, Annu. Rev. Cell Biol. 9:411-44.

Cornillon S, Froquet R. and Cosson P., 2008, Involvement of Sib proteins in the regulation of cellular adhesion in Dictystelium Discoideum, Eukaryotic Cell, 7,9, 1600.

Cornillon S, Gebbie L., Benghezal M., Nair P., Keller S., Wehrle-Haller B., Charette S. J., Bruckert F., Letourneur F. and Cosson P., 2006, An adhesion molecule in free-living Dictystelium amoebae with integrin β features., EMBO reports, 7,6, 617.

Cornillon S., Pech E., Benghezal M, Ravanel K., Gaynor E., Letourneur F., Bruckert F., Cosson P., 2000, Phg1p is a nine-transmembrane protein superfamily member involved in Dictyostelium adhesion and phagocytosis, J. Biol. Chem., 275, 34287.

Curran A. R., Engelman D. M., 2003, Sequence motifs, polar interactions and conformational changes in helical membrane proteins, Curr. Opin. Struct. Biol, 13, 412.

Dalous J., Burghardt E., Taubenberger-M. A., Bruckert F., Gerisch G., Bretschneider T., 2008, Reversal of cell polarity and actin-myosin cytoskeleton reorganization und chemical stimulation, Biophys. J., 94, 1063-1074.

de Hostos E.L., Bradtke B., Lottspeich F., Guggenheim R. and Gerisch G., 1991, Coronin, an actin binding protein of Dictyostelium discoideum localized to cell surface projections, has sequence similarities to G protein subunits, The EMBO Journal, 10, 13, 4097-4104.

Decave, E., D. Garrivier, Y. Brechet, B. Fourcade, and F. Bruckert, 2002, Shear flow-induced detachment kinetics of Dictyostelium discoideum cells from solid substrate. Biophys. J., 82:2383-2395.

Decave, E., D. Rieu, J. Dalous, S. Fache, Y. Brechet, B. Fourcade, M. Satre, and F. Bruckert, 2003, Shear flow-induced motility of Dictyostelium discoideum cells on solid substrate. J Cell Sci 116:4331-4343.

Del Alamo, J. C., R. Meili, B. Alonso-Latorre, J. Rodriguez-Rodriguez, A. Aliseda, R. A. Firtel, and J. C. Lasheras, 2007, Spatio-temporal analysis of eukaryotic cell motility by improved force cytometry. Proc Natl Acad Sci U S A 104:13343-13348.

Delgado A. V., Gonzales-Caballero F., Hunter R. J., Koopal L. K., Lyklema J., 2005, Measurement and interpretation of Electrokinetic Phenomena, Pure Appl. Chem., 77, p. 1753.

Delon I., and Brown N. H., 2007, Integrins and the actin cytoskeleton, Curr Opin Cell Biol., 19, 43-50.

Denker, S. P., Barber, D. L., 2002, Cell migration requires both ion translocation and cytoskeletal anchoring by the Na-H exchanger NHE1, J. Cell. Biol., 159, 1087.

Dickinson R. B., Purich D. L., 2002, Clamped-Filament Elongation Model for Actin-Based Motors, Biophys J., 82, 605-617.

Dictybase, About Dictyostelium. http://dictybase.org

Diez S., Gerisch G., Anderson K., Müller-Taubenberger A., and Bretschneider T., 2005, Subsecond reorganization of the actin network in cell motility and chemotaxis, PNAS, 102, 21, 7601-7606.

Docoslis A., Kalogerakis N., Behie L. A., 1999, Dielectrophoretic forces can be safely used to retain viable cells in perfusion cultures of animal cells, Cytotechnology, 30,133.

Doherty G. J., McMahon H. T., 2008, Mediation, modulation and consequences of membrane – cytoskeleton interactions, Annual Review of Biophysics, 37, 65.

Dubin-Thaler, B. J., J. M. Hofman, Y. Cai, H. Xenias, I. Spielman, A. V. Shneidman, L. A. David, H. G. Dobereiner, C. H. Wiggins, and M. P. Sheetz, 2008, Quantification of cell edge velocities and traction forces reveals distinct motility modules during cell spreading. PLoS ONE 3:e3735.

Dumontier M., Höcht P., Mintert U., Faix J., 2000, Rac1 GTPases control filopodia formation, cell motility, endocytosis, cytokinesis and development in Dictyostelium, Journal of Cell Science, 113, 2253-2265.

Duran M. B., Rahman A., Colten M., and Brazill D., 2009 Dictyostelium discoideum paxillin regulates actin-based processes, Protist, 160, 221-232.

Eddy R. J., Han J., Sauterer R. A., Condeelis J. S., 1996, A major agonist-regulated capping activity in Dictyostelium is due to the capping protein, cap32/34, Biochimica et Biophysica Acta, 1314: 247-259.

Eichinger L., Lee S. S. and Schleicher M., Dictyostelium as model system for studies of the actin cytoskeleton by molecular genetics, 1999, Microscopy research and technique, 47, 124.

Eichinger L., Pachebat J. A., Glockner G., Rajandream M. A., Sucgang R., Berriman M., Song J., Olsen R., Szafranski K., Xu Q. and all., 2005. The genome of the social amoeba Dictyostelium discoideum. Nature. 435 (7038):34-57.

Evans E., Ritchie K. and Merkel R., 1995, Sensitive force technique to probe molecular adhesion and structural linkage at biological interfaces, Biophys. J., 68, 7, 2580.

Fache, S., J. Dalous, M. Engelund, C. Hansen, F. Chamaraux, B. Fourcade, M. Satre, P. Devreotes, F. Bruckert, 2005, Calcium mobilization stimulates Dictyostelium discoideum shear-flow-induced cell motility. J Cell Sci 118:3445-3457.

Fey P., Stephens S., Titus M. A. and Chisholm L., 2002, SadA, a novel adhesion receptor in Dictystelium, J. Cell Biol., 159, 6, 1109.

Franek A., Anna Polak A., Kucharzewski M., 2000, Modern application of high voltage stimulation for enhanced healing of venous crural ulceration, Medical Engineering and Physics, 22, 647.

Friedl P., Borgman S., Bröcker Eva-B., 2001, Amoeboid leukocyte crawling through extracellular matrix: lessons from the Dictyostelium paradigm of cell movement, Journal of Leukocyte Biology, 70, 491-509.

Frixione E, 2000, Recurring views on the structure and function of the cytoskeleton: 300-year epic, Cell motility and cytoskeleton, 46, 2, 73.

Fromherz P., 2008, Joining microelectronics and microionics: Nerve cells and brain tissue on semiconductor chips, Solid-state electronics, 52, 9, 1364-1373.

Fuhr G., Glasser H., Muller T., Schnelle T., 1994, Cell manipulation and cultivation under AC electric-field influence in highly conductive culture media, Biochim. Biophys. Acta Gen. Subj., 1201, 353.

Fujiwara I., Takahashi S. Tadakuma H., Funatsu T. and Ishiwata S., 2002, Microscopic analysis of polymerization dynamics with individual actin filaments, Nature Cell Biology, 4, 667.

Fukui Y., de Hostos E., Yumura S., Kitanishi-Yumura T., and Inoué S., 1999, Architectural Dynamics of F-Actin in Eupodia Suggests Their Role in Invasive Locomotion in Dictyostelium, Experimental Cell Research, 249, 33–45.

Fukui Y., Uyeda T. Q. P., Kitayama C., and Inoué S., 2000, How well can an amoebae climb?, PNAS, 97, 18, 10020-10025.

Fukui Y., Uyeda T., Kitayama C. and Inoue S., 2000, How hell can an amoebae climb?, PNAS, 97, 10020.

Garrivier, D., E. Decave, Y. Brechet, F. Bruckert, and B. Fourcade, 2002, Peeling model for cell detachment, Eur Phys J E Soft Matter 8:79-97.

Gascoyne P. R. C., Wang X. B., Huang Y., Becker F. F., 1997, Dielectrophoretic separation of cancer cells from blood, IEEE Transactions on industry applications, 33, 670.

Gebbie L., Benghezal M., Cornillon S., Froquet R., Cherix N., Malbouyres M., Lefkir Y., Grangeasse C., Fache S., Dalous J., Brückert F., Letourneur F., and Cosson P., 2004, Phg2, a Kinase involved in adhesion and focal site modeling in Dictyostelium, Molecular Biology of the Cell, 15, 3915–3925.

Geiger, B., Bershadsky, A., Pankov, R., and Yamada, K. M., 2001, Transmembrane crosstalk between the extracellular matrix-cytoskeleton crosstalk. Nat Rev Mol Cell Biol 2, 793-805.

Gentil G., Philippin G., and Bokelmann U., 2007, Signal enhancement in electronic detection of DNA hybridization, Phys. Rev., 75.

Gerisch G., Albrecht R., De Hostos E., Wallraff E., Heizer C., Kreitmeier M., Muller-Taubenberger A., 1993, Actin-associated proteins in motility and chemotaxis of Dictyostelium cells, Symp Soc Exp Biol., 47, 297-315.

Gerisch, G., T. Bretschneider, A. Muller-Taubenberger, E. Simmeth, M. Ecke, S. Diez, and K. Anderson, 2004, Mobile actin clusters and traveling waves in cells recovering from actin depolymerization. Biophys J., 87:3493-3503.

Giannone, G., B. J. Dubin-Thaler, H. G. Dobereiner, N. Kieffer, A. R. Bresnick, and M. P. Sheetz, 2004, Periodic lamellipodial contractions correlate with rearward actin waves. Cell 116:431-443.

Gingell D., Fornes J. A., 1976, Interaction of red blood cells with a polarized electrode, Biophys. J., 16, 1131.

Gingell D., Vince S., 1982, Cell-glass separation depends on salt concentration and valency: measurements on Dictyostelium amoebae by finite aperture interferometry, J. Cell. Sci., 54, 299.

Glasser H., Fuhr G., 1998, Cultivation of cells under strong ac-electric field— differentiation between heating and trans-membrane potential effects. Bioelectrochem. Bioenerg., 47, 301.

Goldman D. E., 1943, Potential, impedance, and rectification in membranes, The Journal of General Physiology, 37-60.

Gouaux E., MacKinnon R., 2005, Principles of selective ion transport in channels and pumps, Science, 310, 1461-1465.

Guo R, Pu X. P., Jin O. Y., Li X. R., Luo P., Yang Y. P., 2002, Capillary electrophoretic determination of apoptosis of rat cerebellar granule cells induced by 1-methyl-4-phenyl pyridium ion, Electrophoresis, 23,1110.

Han Y. H., Chung C. Y., Wessels D., Stephens S., Titus M. A., Soll D. R., and Firtel R. A., 2002, Requirement of a vasodilator-stimulated phosphoprotein family member for cell adhesion, the formation of filopodia, and chemotaxis in Dictyostelium, Journal of Biological Chemistry, 277, 51, 49877-49887.

Heid P., Geiger J., Wessels D., Voss E. and Soll D. R., 2005, Computer-assisted analysis of filipod formation and the role of myosin II heavy chain phosphorylation in Dictyostelium, J. Cell. Sci., 118, 2225.

Hiemenz P.C., Rajagopalan R., 1997, Principles of Colloid and Surface Chemistry, 3 Ed., Marcel Dekker, New York, 462.

Hoppe W., Lohmann W., Markl H., Ziegler H., 1983, Biophysics, Springer Verlag, Berlin.

Hunter R.J., 1981, Zeta Potential in Colloid Science, Academic Press, New York.

Israelachvili J. N., 1992, Intermolecular and surface forces, London: Academic Press, 2nd Ed.

Jacquez J. A., 1971, A generalization of the Goldman equation, including the effect of electrogenic pump, Mathematical Biosciences, 12, 185-196.

Jiang, X., D. A. Bruzewicz, A. P. Wong, M. Piel, and G. M. Whitesides. 2005. Directing cell migration with asymmetric micropatterns. Proc Natl Acad Sci U S A 102:975-978.

Kabsch W., Mannherz H. G., Suck D., Pai E. F., Holmes K. C., 1990, Atomic structure of the actin: DNase I complex, Nature, 347, 37.

Kanduser M., Miklavcic D., Pavlin M., 2009, Mechanisms involved in gene electrotransfer using high and low voltage pulses-an in vitro study, Bioelectrochemistry, 74, 265.

Keller S., M. Socol, S. Fache, M. Weidenhaupt, D. Delabouglise, P. Grandemange, F. Chamaraux, B. Fourcade, and F. Bruckert, 2009, Dictyostelium discoideum spreading on solid surface: morphology and kinetics. Submitted at Eur. Biophys. J.

Killich T., Plath P. J., Wei X., Bultmann H., Rensing L. and Vicker M. G., 1993, The locomotion, shape and pseudopodial dynamics of unstimulated Dictyostelium cells are not random, Journal of Cell Science, 106, 1005-1013.

Killich, T., P. J. Plath, X. Wei, H. Bultmann, L. Rensing, and M. G. Vicker, 1993, The locomotion, shape and pseudopodial dynamics of unstimulated Dictyostelium cells are not random. J Cell Sci., 106, 1005-1013.

Lahann J., Mitragotri S., Tran T., Kaido H., Sundaram J., Choi I., Hoffer S., Somorjai G, Langer R., 2003, A Reversibly Switching Surface, Science, 299, 371.

Lakshminarayanaiah N. and Murayama K., 1975, Estimation of surface charges in some biological membranes, J. Membrane Biol., 23, 279.

Lee, J., A. Ishihara, G. Oxford, B. Johnson, and K. Jacobson. 1999. Regulation of cell movement is mediated by stretch-activated calcium channels. Nature 400:382-386.

Lodish H., Berk A., Zipursky L. S., 2001, Molecular Cell Biology (4th ed.), New York, W. H. Freeman and Company.

Mali P., Bhattacharjee N., Searson P. C., 2006, Electrochemically Programmed Release of Biomolecules and Nanoparticles, Nano Lett., 6, 1250.

Marcy Y., Prost J., Carlier M. F., and Sykes C., 2004, Forces generated during actin-based propulsion: A direct measurement by micromanipulation, PNAS, 101, 16, 5992-5997.

Markx G. H., Talary M. S., Pethig R., 1994, Separation of viable and non-viable yeast using dielectrophoresis, J. Biotechnol., 32, 29.

McCaig, C. D., Rajnicek, A. M., Song, B. and Zhao, M., 2005, Controlling cell behaviour electrically: current views and future potential, Physiol. Rev. 85, 943–978.

Medalia O., Beck M., Ecke M., Weber I., Neujahr R., Baumeister W., and Gerisch G., 2007, Organization of actin networks in intact filopodia, Current Biology 17, 79–84.

Mehrishi J. N., Bauer J., 2002, Electrophoresis of cells and the biological relevance of surface charge, Electrophoresis, 23, 1984-1994.

Merkel, R., R. Simson, D. A. Simson, M. Hohenadl, A. Boulbitch, E. Wallraff, and E. Sackmann. 2000. A micromechanic study of cell polarity and plasma membrane cell body coupling in Dictyostelium. Biophys J 79:707-719.

Millhauser G. L., Salpeter E. E., Oswald R. E., 1988, Diffusion models of ion-channels gating and the origin of power-low distributions from single-channel recording, Proc. Natl. Acad. Sci. USA, 88, 1503-1507.

Moniakis J., Funamoto S., Fukuzawa M., Meisenhelder J., Araki T., Abe T., Meili R., Hunter T., Williams J., Firtel R. A., 2001, An SH2-domain-containing kinase negatively regulates the phosphatidylinositol-3 kinase pathway, Genes&Development, 15, 687-698.

Moore E., O'Connell D., Galvin P., 2006, Surface characterization of indium-tin electrode films for use a conducting substrate in DNA sensor development, Thin Solid Films, 515, 4, 2612.

Moran M. T., Caroll W. M., Selezneva I., Gorelov A., Rochev Y., 2006, Cell growth and detachment from protein-coated PNIPAAm-based copolymers, J. of Biomed. Mat. Res., 870.

Nag D. K., Tikhonenko I., Soga I. and Koonce M. P., 2008, Disruption of Four Kinesin Genes in Dictyostelium, BMC Cell Biol, 9, 21.

Nellen W., Silan C., Firtel R. A., 1984, DNA-mediated transformation in Dictyostelium discoideum : Regulated expression of an actin gene fusion, Mol. Cell. Biol., 4, 2890.

Neujahr R., Heizer C., Gerisch G., 1997, Myosin II-independent processes in mitotic cells of Dictyostelium discoideum: redistribution of the nuclei, re-arrangement of the actin system and formation of the cleavage furrow, J. Cell. Sci., 110, 123.

Neumann E., Schaefer-Ridder M., Wang Y., Hofscheineder P. H., 1982, Gene transfer into mouse lyoma cells by electroporation in high electric fields, EMBO J., 1, 841.

Niewohner J., Weber I., Maniak M., Muller-Taubenberger A. and Gerisch G., 1997, Talin-null cells of Dictyostelium are strongly defective in adhesion to particle and substrate surfaces and slightly impaired in cytokinesis, J. Cell. Biol., 138, 349-361.

Nobes C. D. and Hall A., 1999, Rho GTPases Control polarity, protrusion, and adhesion during cell movement, The Journal of Cell Biology, 144, 6, 1235-1244.

Nuccitelli R., Chen X., Pakkhonov A. C., Baldin W. H., Skeikh S., Pomocter J. L., Ren W., Osgood C., Swanson R. J., Kolb J. F., Beebe S. J., Schoenbach K. H., 2009, A new pulsed power field therapy for melanoma disrupts the tumor's blood supply and causes complete remission without recurrences, Int. J. Cancer, in print.

O'Shea P., Walters J., Ridge J., Wainright M. and Trinci A. P. J., 1990, Zeta potential measurements of cell wall preparations from Regnellidium diphyllum and Nymphoides peltata, Plant, Cell and Environement, 13, 447.

Ormö M., Cubitt A. B., Kallio K., Gross L. A., Tsien R. Y. and Remington S. J., 1996, Crystal structure of the Aequorea victoria green fluorescent protein, Science, 273, 1392, 5.

Overbeek J.T.G., 1984, Interparticle forces in colloid science, Powder Technology, 1984, 195-208.

Para A., Krischke M., Merlot S., Shen Z., Oberholzer M., Lee S., Briggs S., and Firtel R. A., 2009, Dictyostelium Dock180-related RacGEFs regulate the actin cytoskeleton during cell motility, Molecular Biology of the Cell, 20, 699–707.

Parks, G.A., 1965, The isoelectric points of solid oxides, solid hydroxides and aqueous complex systems, Chem. Rev. 65, 177.

Patel H., König I., Tsujioka M., Frame M. C., Anderson K. I. and Brunton V. G., 2008, The multi-FERM-domain-containing protein FrmA is required for turnover of paxillin-adhesion sites during cell migration of Dictyostelium, Journal of Cell Science, 121, 1159-1164

Pierre A.C., 1998, Introduction to Sol-Gel Processing, Kluwer, Norwell, MA.

Pierres, A., A. M. Benoliel, and P. Bongrand, 1998a, Use of a laminar flow chamber to study the rate of bond formation and dissociation between surface-bound adhesion molecules: effect of applied force and distance between surfaces, Faraday Discuss., 321-330; discussion 331-343.

Pierres, A., A. M. Benoliel, and P. Bongrand, 1998b, Studying receptor-mediated cell adhesion at the single molecule level. Cell Adhes Commun 5:375-395.

Pierres, A., A. M. Benoliel, P. Bongrand, and P. A. van der Merwe., 1996, Determination of the lifetime and force dependence of interactions of single bonds between surface-attached CD2 and CD48 adhesion molecules. Proc Natl Acad Sci U. S. A., 93, 15114-15118.

Podolski J. L., Steck T. L., 1990, Length distribution of F-actin in Dictyostelium discoideum, J. Biol. Chem., 265, 1312.

Pollard T. D., Borisy G. G., 2003, Cellular motility driven by assembly and disassembly of actin filaments, Cell, 112, 453.

Portinga A. T., Bos R., Busscher H. J., 2001, Reversibility of Bacterial Adhesion at an Electrode Surface, Langmuir, 17, 2851.

Prasher D. C., Eckenrode V. K., Ward W. W., Predendergast F. G. and Cormier M. J., 1992, Primary structure of the Aequorea victoria green-fluorescent protein, Gene, 111, 229, 33.

Rajnicek A. M., Foubister L. E., McCaig C. D., 2008, Alignment of corneal and lens epithelial cells by co-operative effects of substratum topography and DC electric fields, Biomaterials, 29, 2082.

Raper, K. B., 1935, Dictyostelium discoideum, a new species of slime mold from decaying forest leaves, J. Agr. Res., 50, 135-147.

Ridley J. A., Self A. J., Kasmi F., Paterson H. F., Hall A., Marshall J. C., Ellis C., 1993, rho familyGTPase activating proteins p190, bcr and rhoGAP show distinct specificities in vitro and in vivo, The EMBO Journal, 12, 13, 5151.

Riske K. A., Dimova R., 2005, Electro-Deformation and Poration of Giant Vesicles Viewed with High Temporal Resolution, Biophys. J.,88, 1143.

Riske K. A., Dimova R., 2006, Electric Pulses Induce Cylindrical Deformations on Giant Vesicles in Salt Solutions, Biophys. J.,91, 1778.

Riveline, D., E. Zamir, N. Q. Balaban, U. S. Schwarz, T. Ishizaki, S. Narumiya, Z. Kam, B. Geiger, and A. D. Bershadsky. 2001. Focal contacts as mechanosensors: externally applied local mechanical force induces growth of focal contacts by an mDia1-dependent and ROCK-independent mechanism. J Cell Biol 153:1175-1186.

Robert C. W., 1987, Handbook of Chemistry and Physics, Boca Raton, Florida.

Robinson R., Stokes R. H., 1970, Electrolyte solutions, Ed. Butterworths.

Russ M., Croft D., Ali O., Martinez R., and Steimle P. A., 2006, Myosin heavy-chain kinase A from Dictyostelium possesses a novel actin-binding domain that cross-links actin filaments, Biochem J., 395, 373-383.

Sameshima M., Y. Kishi, M. Osumi, R. Minamikawa-Tachino, D. Mahadeo and D. A. Cotter, 2001, The formation of actin rods composed of actin tubules in Dictyostelium discoideum spores, Journal of Structural Biology, 136, 7–19.

Schafer D. A., Welch M. D., Machesky L. M., Bridgman P. C., Meyer S. M., and Cooper J. A., 1998, Visualization and Molecular Analysis of Actin Assembly in Living Cells, Journal of Cell Biology, 143, 7, 1919-1930.

Schneider M., Schroth S., Schilm J., Michaelis A., 2009, Micro-EIS of anodic thin films on titanium for capacitor applications, Electrochimica Acta, 54(9), 2663.

Schneider N., Weber I., Faix J., Prassler J., Taubenberger A. M., Kohler J., Burghardt E., Gerisch G., Marriott G., 2003, A Lim protein involved in the progression of cytokinesis and regulation of the mitotic spindle, Cell Motil. Cytoskeleton 56, 130.

Schwartz M. A., 2001, Integrin signaling revisited, Trends Cell Biol., 11, 466.

Sept D., Xu J., Pollard T. D., and McCammon J. A., 1999, Annealing accounts for the length of actin filaments formed by spontaneous polymerization, Biophys. J., 77, 2911-2919.

Sheetz M. P., 2001, Cell control by membrane-cytoskeleton adhesion, Nat. Rev. Mol. Cell Biol., 2, 392.

Shenderov, A. D., and M. P. Sheetz, 1997, Inversely correlated cycles in speed and turning in an ameba: an oscillatory model of cell locomotion, Biophys J., 72:2382-2389.

Shimomura O., Johnson F. H. and Saiga Y., 1962, Extraction, purification and properties of aequorin, a bioluminescent protein from the luminous hydromedusan, Aequorea, J. Cell. Comp. Physiol., 59, 223, 39.

Simon K. A., Burton E. A., Han Y., Li J., Huang A., Luk Y. Y., 2007, Enhancing cell adhesion and confinement by gradient nanotopography, J. Am. Chem. Soc., 129, 4892.

Steffen A., Faix J., Resch G. P., Linkner J., Wehland J., Small V. J., Rottner K., and Stradal T. E.B., 2006, Filopodia formation in the absence of functional WAVE- and Arp2/3-complexes, Molecular Biology of the Cell, 17, 2581–2591.

Tang C. S., Dusseiller M., Makohliso S., Heuschkel M., Sharma S., Keller B., Voros J., 2006, Dynamic, electronically switchable surfaces for membrane protein microarrays Anal Chem 78, 711.

Teissie J., Golzio M., Rols M. P., 2005, Mechanisms of cell membrane electropermeabilization: a minireview of our present (lack of ?) knowledge, Biochim. Biophys. Acta., 3, 270.

Teissie J., Rols M. P., 1986, Fusion of mammalian cells in culture is obtained by creating the contact between cells after their electropermeabilization, Biochem. Biophys. Res. Commun., 140, 258.

Theriot J. A, 1997, Accelerating on a Treadmill: ADF/Cofilin Promotes Rapid Actin Filament Turnover in the Dynamic Cytoskeleton, Journal of Cell Biology, 136, 6, 1165–1168.

Thery, M., A. Pepin, E. Dressaire, Y. Chen, and M. Bornens, 2006b, Cell distribution of stress fibres in response to the geometry of the adhesive environment. Cell Motil Cytoskeleton 63:341-355.

Thery, M., V. Racine, M. Piel, A. Pepin, A. Dimitrov, Y. Chen, J. B. Sibarita, and M. Bornens, 2006a, Anisotropy of cell adhesive microenvironment governs cell internal organization and orientation of polarity. Proc Natl Acad Sci U S A 103:19771-19776.

Tobias S. M., 2002, Investigation of Short-Range surface forces to develop self –organizing devices, Msc. Degree.

Traynor D., Kessin R. H., Williams J. G., 1992, Chemotactic sorting to cAMP in the multicelular stages of Dictyostelium development, Proc. Natl. Acad. Sci., 89, 8303.

Trommler A, Gingell D.and Wolf H., 1985, Red blood experience electrostatic repulsion but make molecular adhesion with glass, Biophys. J.,48, 835.

Tsong T. Y., 1992, Molecular recognition and processing of periodic signals in cells: study of activation of membrane ATPases by alternating electric fields, Biochim. Biophys. Acta, 1113, 53–70.

Tsujioka M., Yoshida K., Nagasaki A., Yonemura S., Müller-Taubenberger A., and Uyeda T. Q. P., 2008, Overlapping functions of the two talin homologues in Dictyostelium, Eukaryotic cell, 7, 5, 906–916.

Tyler M. S., 2000, Developmental Biology: A guide for experimental study, 2nd ed. Sunderland (MA), 31-34.

Tzvetkova-Chevolleau, T., E. Yoxall, D. Fuard, F. Bruckert, P. Schiavone, and M. Weidenhaupt, 2009, Microscale adhesion patterns for the precise localization of amoeba. Microelectronic Engineering, 86, 1845-1487.

Uchida K. and Yumura S., 1999, Novel cellular tracks of migrating Dictyostelium cells, Europ. J. Cell Biol., 78, 757-766.

Uchida K., Yumura S., 2004, Dynamics of novel feet of Dictyostelium cells during migration, J. Cell Science, 117, 1443.

Uchida, K. S., and S. Yumura., 2004, Dynamics of novel feet of Dictyostelium cells during migration. J Cell Sci 117:1443-1455.

Uchida, K. S., T. Kitanishi-Yumura, and S. Yumura, 2003, Myosin II contributes to the posterior contraction and the anterior extension during the retraction phase in migrating Dictyostelium cells. J Cell Sci 116:51-60.

Uchida, K. S., T. Kitanishi-Yumura, and S. Yumura, 2003, Myosin II contributes to the posterior contraction and the anterior extension during the retraction phase in migrating Dictyostelium cells. J Cell Sci 116:51-60.

Ueda M., Graf R., Macwilliams H. K., Schiliwa M. and Euteneur U., 1997, Centrosome positioning and directionality of cell movements, Proc. Natl. Acad. Sci., 94, 9674.

Vicente-Manzanares M., Choi C. K., and Horwitz A. R., 2009, Integrins in cell migration--the actin connection, J Cell Sci, 122:199-206.

Vicker, M. G., 2000, Reaction-diffusion waves of actin filament polymerization/depolymerization in Dictyostelium pseudopodium extension and cell locomotion, Biophys. Chem., 84:87-98.

Vicker, M. G., 2002a, Eukaryotic cell locomotion depends on the propagation of self-organized reaction-diffusion waves and oscillations of actin filament assembly. Exp Cell Res 275:54-66.

Vicker, M. G., 2002b, F-actin assembly in Dictyostelium cell locomotion and shape oscillations propagates as a self-organized reaction-diffusion wave. FEBS Lett 510, 5-9.

Vigeant M., Ford R. M., 1997, Interaction between motile E. coli and glass in media with various ionic strength, as observed with a three-dimensional-tracking microscope, Appl. Envir. Microbiol., 3474-3479.

Voldman J., 2006, Electrical forces for microscale cell manipulation, Annu. Rev. Biomed. Eng., 8, 425.

Wang X. B., Huang Y., Gascoyne, P. R. C., Becker F. F., 1995, Dielectrophoretic manipulation of particles, Industry Application Conference, 2, 1358.

Wang X., Kharitonov A. B., Katz E., Villner I., 2003, Potential-controlled molecular machinery of bipyridinium monolayer-functionalized surfaces: an electrochemical and contact angle analysis, Chem. Commun., 1542.

Washizu M., 1992, Manipulation of biological objects in micromachined structures, Micro Electro Mechanical Systems, 4, 196.

Watts D. J., Ashworth J. M., 1970, Growth of myxamoebae of the cellular slime mould Dictyostelium discoideum in axenic culture, Biochem. J., 119, 171.

Weber, I., E. Wallraff, R. Albrecht, and G. Gerisch, 1995, Motility and substratum adhesion of Dictyostelium wild-type and cytoskeletal mutant cells: a study by RICM/bright-field double-view image analysis. J Cell Sci 108:1519-1530.

Wessels, D., E. Voss, N. Von Bergen, R. Burns, J. Stites, and D. R. Soll, 1998, A computer-assisted system for reconstructing and interpreting the dynamic three-dimensional relationships of the outer surface, nucleus and pseudopods of crawling cells. Cell Motil Cytoskeleton 41:225-246.

Wolf H. and Gingell D., 1983, Conformational response of glycocalyx to ionic strength and interaction with modified glass surfaces: study of live red cells by interferometry, J. Cell. Sci., 63, p. 101.

Yang J., Huang Y. ,Wang X. B., Becker F. F., Gascoyne P. R. C., 2000, Differential analysis of human leukocytes by dielectrophoretic field-flow-fractionation, Biophys. J., 78, 2680.

Yeo W. S., Yousaf M. N. and Mrksich M., 2003, Dynamic interfaces between cells and surfaces: electoactive substrates that sequentially release and attach cells, J Am Chem Soc 125,14994.

Yousaf M. N., Houseman B. T., and Mrksich M., 2001, Using electroactive substrates to pattern the attachment of two different cell populations, PNAS, 98, 11, 5993.

Yumura S., Kitanishi-Yumura T., 1990, Fluorescence-mediated visualization of actin and myosin filaments in the contractile membrane-cytoskeleton complex of Dictyostelium discoideum, Cell Struct. Funct., 15, 355-364.

Yumura, S., 1993. Reorganization of actin and myosin II in Dictyostelium amoeba during stimulation by cAMP. Cell Struct Funct 18:379-388.

Zang J. H., Cavet G., Sabry J. H., Wagner P., Moores S. L., Spudich J. A., 1997, On the role of myosin II in cytokinesis: division of Dictyostelium cells under adhesive and nonadhesive conditions, Mol. Biol. Cell, 8, 2617.

Zhao M., Jin T., McCaig C. D., Forrester J. V. and Devreotes P. N., 2002b, Genetic analysis of the role of G protein–coupled receptor signaling in electrotaxis, J. Cell Biol., 157, 6, 921.

Zhao M., Pu J., Forrester V. J., McCaig C. D., 2002a, Membrane lipids, EGF receptors, and intracellular signals colocalize and are polarized in epithelial cells moving directionally in a physiological electric field, The FASEB J.

Zhao M., Song B., Pu J., Wada T., Reid B., Tai G., Wang F., Guo A., Walczysko P., Gu Y. Sasaki T., Suzuki A., Forrester J. V., Bourne H. R., Devreotes P. N., McCaig C. D. and Penninger J. M., 2006, Electrical signals control wound healing through phosphatidylinositol-3-OH kinase-g and PTEN, Nature, 442, 457.

Abstract

Cell synchronization is important for the analysis of molecular events involved in cell spreading and motility. Electrostatic interactions between cells and surfaces were investigated in order to synchronize the first step in cell adhesion. LimE-GFP marked *Dictyostelium discoideum* cells were used for fluorescent tracking of actin polymerization events. Oscillating LimE fluorescent peaks were observed for individual cells in standard phosphate buffer during spreading. At low ionic concentration (phosphate sucrose buffer 0.17 mM), cells levitate over the conductive surfaces (Indium Tin Oxide, ITO) due to electrostatic repulsion. An electrochemical device was designed in order to apply an overpotential pulse (+2.5 V/Ag,AgCl) during 0.1 s to the ITO surface. In these conditions, protons are produced by water oxidation, which reduce the ITO negative surface charge and thus, attracting the levitating cells simultaneously. Consequently, these irreversible contacts with the surface triggered the onset of cell spreading. For 37 from 47 studied cells (80%), successive fluorescent peaks appear, more or less regularly spaced in time, showing an oscillating actin polymerization activity. Remarkably, no maxima appeared before 7 s after the pulse application. Moreover, *29* cells from *37* (79%) had the first peak within 4 seconds interval, between 7.5 s and 11.5 s after the pulse. Therefore, we obtained synchronization of the spreading of a cell population for the first time thanks to an electrochemical method.

Keywords: Cell synchronization, ITO, Optical Microscopy, Overpotential.

Résumé

La synchronisation des cellules est importante pour l'analyse des processus moléculaires impliqués dans l'étalement et la motilité. Les interactions électrostatiques entre les cellules et les surfaces ont été étudiées dans le but de synchroniser la première étape de l'adhésion cellulaire. Les cellules *Dictyostelium discoideum* marquées avec LimE-GFP ont été utilisées pour le suivi en fluorescence des événements de polymérisation de l'actine. Des pics de fluorescence ont été observés pour les cellules individuelles pendant l'étalement en tampon phosphate. Dans une solution de concentration faible (0.17 mM tampon phosphate sucrose) les cellules lévitent au dessous des surfaces conductrices (Indium Tin Oxide, ITO), à cause de la répulsion électrostatique. Un dispositif électrochimique a été construit dans le but d'appliquer un pulse électrique (+2.5 V/Ag,AgCl) sur une surface de ITO pendant 0,1 secondes. Dans ces conditions, l'oxydation de l'eau produit des protons qui réduisent la charge de surface négative de l'ITO et ainsi, les cellules sont attirées simultanément. Ces contacts irréversibles avec la surface déclenchent l'étalement cellulaire. Pour 37 parmi les 47 cellules étudiées (80%), apparaissent des pics de fluorescences successives plus au moins réguliers en temps, montrant une activité de polymérisation de l'actine oscillante. Remarquablement, aucun pic de fluorescence n'apparaît dans les 7 premières secondes d'après l'application du pulse. De plus, 29 des cellules parmi les 37 ont eu le premier pic dans un intervalle de 4 secondes, entre 7,5 et 11,5 secondes après le pulse. Ainsi, nous avons obtenu, pour la première fois, la synchronisation de l'étalement cellulaire d'un groupe de cellules grâce à une méthode électrochimique.

Mots-clés: Synchronisation cellulaire, ITO, Microscopie Optique, Pulse Electrique.